

**Propagation and Control of Geometric Variation in
Engineering Structural Design and Analysis**

by

J. D. Benzaken

B.S. Aerospace Engineering, California State University Long Beach, 2013

B.S. Applied Mathematics, California State University Long Beach, 2013

B.A. Physics, California State University Long Beach, 2013

M.S. Applied Mathematics, University of Colorado, Boulder, 2018

A thesis submitted to the
Faculty of the Graduate School of the
University of Colorado in partial fulfillment
of the requirements for the degree of
Doctor of Philosophy
Department of Applied Mathematics

2018

This thesis entitled:
Propagation and Control of Geometric Variation in Engineering Structural Design and Analysis
written by J. D. Benzaken
has been approved for the Department of Applied Mathematics

Prof. John A. Evans

Prof. Stephen Becker

Date _____

The final copy of this thesis has been examined by the signatories, and we find that both the content and the form meet acceptable presentation standards of scholarly work in the above mentioned discipline.

Benzaken, J. D. (Ph.D., Applied Mathematics)

Propagation and Control of Geometric Variation in Engineering Structural Design and Analysis

Thesis directed by Prof. John A. Evans

In this dissertation, we present a methodology for understanding the propagation and control of geometric variation in engineering design and analysis. This work is comprised of two major components: (i) novel discretizations and associated solution strategies for rapid numerical solution over geometric parametrizations of the linear and nonlinear thin-shell equations, and (ii) efficient surrogate modeling techniques and algorithms towards the control of geometric variation. While the methodologies presented are in the setting of structural mechanics, particularly Nitsche's method in the context of linearized membranes, Kirchhoff-Love plates, and Kirchhoff-Love shells, they are applicable to any system of parametric partial differential equations. We present a design space exploration framework that elucidates design parameter sensitivities used to inform initial and early-stage design and a novel tolerance allocation algorithm for the assessment and control of geometric variation on system performance. Both of these methodologies rely on surrogate modeling techniques where various designs throughout the design space considered are sampled and used in the construction of approximations to the system response. The design space exploration paradigm enables the visualization of a full system response through the surrogate model approximation. The tolerance allocation algorithm poses a set of optimization problems over this surrogate model restricted to nested hyperrectangles represents the effect of prescribing design tolerances, where the maximizer of this restricted function depicts the worst-case member, i.e. design. The loci of these tolerance hyperrectangles with maximizers attaining the performance constraint represents the boundary to the feasible region of allocatable tolerances. The boundary of the feasible set is elucidated as an immersed manifold of codimension one, over which optimization routines exist and are employed to efficiently determine an optimal feasible tolerance with respect to a user-specified measure. Examples of these methodologies for problems of various complexities are presented.

Dedication

To myself. Throughout my life I have always put myself second, even in cases which have consequently inconvenienced myself. This one is for you, Joe, you did good work.

Acknowledgements

First and foremost, I would like to thank my advisor Dr. John A. Evans for his patience, guidance, and support throughout my graduate school career. Your brilliance, dedication, and curiosity towards the progression of Applied Mathematics are an inspiration and a reminder as to why I pursued this field. Next, I would like to thank my fellow graduate students in the Computational Mechanics and Geometry Lab who have been there with tremendous support both inside and outside of school, you guys rock and I wish you all of the successes in your future endeavors! Next, I would like to thank my family for their support throughout my graduate school career. Beginning with my sister, Talia Benzaken, we started our doctoral programs at the same time and were there for each other throughout the trials of graduate school and have both made it through with our reciprocating system of support from day one. Thank you to my mom, Lori Caputi, and dad, Eliahu Benzaken, for believing in me and seeing me to success through this program. I also want to thank my stepfather, Tony Caputi, and stepmother, Carol Adams, who have served as a second set of parents for me with tremendous, unwavering support throughout my life. Finally, I would like to thank all of the graduate students around the world for their dedication to their passions, whatever they may be. Graduate school is a difficult path to follow but regardless of the associated challenges you have decided to pursue what you love and that is something to be commended.

Contents

Chapter	
1 Introduction	1
2 Fundamentals of Isogeometric Analysis	8
2.1 Isogeometric Analysis	9
3 Differential Geometry	16
4 Continuum Mechanics	25
5 Functional Analysis	34
5.1 Existence, Uniqueness, and Error Estimation	35
5.2 Trace Inequalities, Poincaré Inequalities, and Inverse Estimates	37
5.3 Green’s Identity	42
6 Problems	44
6.1 Linear Elasticity	44
6.1.1 The Linear Elastic Formulation	45
6.1.2 Work and Energy	45
6.1.3 The Euler-Lagrange Equations and the Variational Formulation	46
6.1.4 The Strong Formulation for Linear Elasticity	48
6.1.5 Nitsche’s Variational Form for Linear Elasticity	49
6.1.6 Consistency and Symmetry of Nitsche’s Method for Linear Elasticity	50

6.1.7	Continuity and Coercivity of Nitsche's Method for Linear Elasticity	51
6.1.8	A Priori Error Estimates	53
6.2	Kirchhoff-Love Plate	54
6.2.1	Kirchhoff-Love plate formulation	54
6.2.2	Work and Energy	54
6.2.3	The Euler-Lagrange Equations and the Variational Formulation	56
6.2.4	The Strong Formulation for the Kirchhoff-Love Plate	60
6.2.5	Nitsche's Variational Form for the Kirchhoff-Love Plate	62
6.2.6	Consistency and Symmetry of Nitsche's Method for the Kirchhoff-Love Plate	63
6.2.7	Continuity and Coercivity of Nitsche's Method for the Kirchhoff-Love Plate .	64
6.2.8	A Priori Error Estimates	68
6.3	Linearized Kirchhoff-Love Shell	69
6.3.1	Kirchhoff-Love shell formulation	69
6.3.2	Work and Energy	69
6.3.3	The Euler-Lagrange Equations and the Variational Formulation	72
6.3.4	The Strong Formulation for the Kirchhoff-Love Shell	76
6.3.5	Nitsche's Variational Form for the Linearized Kirchhoff-Love Shell	78
6.3.6	Consistency of Nitsche's Method	80
6.3.7	Continuity and Coercivity of Nitsche's Method for the linearized Kirchhoff- Love Shell	83
6.3.8	A Priori Error Estimates	87
6.4	Numerical Results	88
6.4.1	The Shell Obstacle Course	88
7	Design Space Exploration	93
7.1	Parametric Partial Differential Equations & Families of Geometries	93
7.2	Design Space Collocation for Parametrized IGA	97

7.2.1	Nodal Solution Manifold Representation	99
7.2.2	Modal Solution Manifold Representation	102
7.2.3	Design Space Sampling and Numerical Integration	105
7.2.4	Numerical Results	112
7.2.5	Flat L-Bracket	119
7.2.6	Wind Turbine Blade	126
8	Physics-Informed Tolerance Allocation	141
8.1	Problem Statement	141
8.1.1	A Low-Rank, Separated Representation for System Performance	143
8.1.2	Construction of the Tolerance Search Space	145
8.1.3	Tolerance Measures	146
8.1.4	Manifold Traversal	148
8.1.5	Algorithm Pseudocode	151
8.2	Numerical Tests	152
8.2.1	Application to Linear Elasticity	157
8.2.2	Two-dimensional plate with hole	157
8.2.3	Six-dimensional plate with hole	164
8.2.4	17-dimensional L-Bracket	166
9	Multigrid Methods	173
9.1	Fundamentals of Isogeometric Multigrid Methods	173
9.2	Numerical Tests	178
10	Conclusion	181
	Bibliography	187

Tables

Table

7.1	A comparison between the Gauss-Legendre, Clenshaw-Curtis, and Kronrod-Patterson quadrature schemes considered in this dissertation.	106
7.2	Results for the Scordelis-Lo roof with a Nodal solution manifold representation using a full tensor-product interpolation scheme with the Gauss-Legendre quadrature nodes. In the table below, ℓ is the level parameter, p_ℓ is the polynomial order of the Lagrange basis used to represent the solution manifold, n_ℓ is the number of interpolation points used to attain the specified representation, and n_{dof} is the number of basis functions in $\mathcal{Q}_{p_\ell}(\mathcal{D}_{\text{roof}})$	135
7.3	Results for the Scordelis-Lo roof with a Modal solution manifold representation using a tensor-product Gauss-Legendre quadrature scheme for numerical computation of the pseudospectral coefficients. In the table below, ℓ is the level parameter, p_ℓ is the polynomial order of the Legendre basis used to represent the solution manifold, n_ℓ is the number of quadrature points used to attain the specified representation, and n_{dof} is the number of basis functions in $\mathcal{Q}_{p_\ell}(\mathcal{D}_{\text{roof}})$	135

7.4 Results for the Scordelis-Lo roof with a modal solution manifold representation using sparse, delayed Kronrod-Patterson and Clenshaw-Curtis schemes for the computation of the sparse pseudospectral coefficients in the isotropic Legendre basis. In the table below, ℓ denotes the level parameter, n_ℓ is the number of function evaluations required to accurately capture the pseudospectral coefficients, and n_{dof} is the number of basis functions in $\mathcal{P}_{p_\ell}(\mathcal{D}_{roof})$ 136

7.5 Results for the Scordelis-Lo roof with a modal solution manifold representation using an isotropic Legendre basis with a tensor-product univariate Gauss-Legendre quadrature scheme. In the table below, ℓ denotes the level parameter, n_ℓ is the number of function evaluations required to accurately capture the pseudospectral coefficients, and n_{dof} is the number of basis functions in $\mathcal{P}_{p_\ell}(\mathcal{D}_{roof})$ 137

7.6 Optimization of the functional presented in this section using the full IGA model throughout the design space. 137

7.7 Optimization of the functional presented in this section for varying level and α_i for a tensor-product, interpolating surrogate model. 138

7.8 Functional optimization for varying level and α_i for a sparse, isotropic surrogate model. 139

7.9 Results for the Flat L-Bracket with a modal solution manifold representation of the $\mathcal{D}_{L,minor}$ using the sparse, delayed Kronrod-Patterson with an isotropic Legendre basis. In the table below, ℓ denotes the level parameter, n_{dof} are the number of basis functions contained in $\mathcal{P}_{p_\ell}(\mathcal{D}_{L,minor})$ and n_ℓ are the number of function evaluations required to accurately capture the pseudospectral coefficients. 140

7.10 Results for the Flat L-Bracket with a modal solution manifold representation of the $\mathcal{D}_{L,extreme}$ using the sparse, delayed Kronrod-Patterson with an isotropic Legendre basis. In the table below, ℓ denotes the level parameter, n_{dof} are the number of basis functions contained in $\mathcal{P}_{p_\ell}(\mathcal{D}_{L,extreme})$ and n_ℓ are the number of function evaluations required to accurately capture the pseudospectral coefficients. 140

7.11	Results for an NREL 5MW with a nodal discretization of the design space using tensor-product Gauss-Legendre nodes. These results use 10 randomly chosen design variables and compares the isogeometric solution to the solution predicted by the nodal surrogate design space representation. In the table below, ℓ denotes the level parameter, n_{dof} are the number of basis functions contained in $\mathcal{Q}_{p_\ell}(\mathcal{D}_{turb})$ and n_ℓ are the number of function evaluations.	140
8.1	The strain energy and maximum stress surrogate modeling errors for the two-dimensional plate with hole problem constructed from $N = 100$ samples and $N_c = 500$	160
8.2	Tolerance values obtained using a dense sampling of the tolerance hyperrectangle. These values are treated as the “exact” optima and are used in our subsequent results. Bold numbers indicate values lying on the boundary of the hyperrectangle.	161
8.3	Errors and convergence behavior of the tolerance allocation algorithm for the 1-norm.	163
8.4	Errors and convergence behavior of the tolerance allocation algorithm for the μ -norm.	163
8.5	Errors and convergence behavior of the tolerance allocation algorithm for the -1 -norm.	164
8.6	The maximum stress surrogate modeling errors for the six-dimensional plate with hole problem constructed from $N = 1500$ samples and $N_c = 500$	166
8.7	Tolerance values obtained using a rank 20, degree 4 SR constructed from 7500 samples of the maximum stress between the top and bottom of the plate with hole. These values are treated as the “exact” optima and are used in our subsequent results. Bold numbers indicate values lying on the boundary of the hyperrectangle.	167
8.8	Errors and convergence behavior of the tolerance allocation algorithm for the 1-norm.	167
8.9	Errors and convergence behavior of the tolerance allocation algorithm for the μ -norm.	168
8.10	Errors and convergence behavior of the tolerance allocation algorithm for the -1 -norm.	169
8.11	The maximum stress surrogate modeling errors for the six-dimensional plate with hole problem constructed from $N = 13500$ samples and $N_c = 500$	170

- 8.12 Tolerance values obtained using a rank 20, degree 4 SR constructed from 7500 samples. These values are treated as the “exact” optima and are used in our subsequent results. Bold numbers indicate values lying on the boundary of the hyperrectangle. . 171
- 8.13 Errors and convergence behavior of the tolerance allocation algorithm for the 1-norm.171
- 8.14 Errors and convergence behavior of the tolerance allocation algorithm for the μ -norm.172
- 8.15 Errors and convergence behavior of the tolerance allocation algorithm for the -1 -norm.172

Figures

Figure

- 2.1 The constant, linear, quadratic, and cubic B-spline basis functions (left). A bicubic B-spline basis function is constructed through a tensor product of 1D splines (right). 10
- 2.2 An example NURBS curve (left) and NURBS surface (right) with their corresponding control meshes. 11
- 2.3 The set of cubic Bernstein polynomials is shown in the left figure. In the right figure, the set of B-spline basis functions described by the knot vector $\Xi = \{0, 0, 0, 0, 1, 2, 2, 3, 3, 3, 3\}$ is shown on the top. Below that, the B-spline basis functions restricted to the 2^{nd} element are shown, along with the scaled Bernstein polynomials which span the B-spline basis. For example, $\hat{R}_4(\xi)|_{\Omega^2} = \frac{1}{4}B_1(\xi) + \frac{1}{2}B_2(\xi) + B_3(\xi) + \frac{1}{2}B_4(\xi)$, where the coefficients arise through Bézier extraction. 14
- 2.4 2^{nd} -order B-spline basis before Bézier Extraction (left) and after Bézier Extraction (right) which it is cast in the Bernstein polynomial basis. 15
- 2.5 Bézier extraction defines the notion of an “element” in the isogeometric paradigm, where quadrature can be used for numerical integration in an element-wise fashion. First, the physical Bézier element Ω^e is “pulled back” to the parametric domain through the geometric mapping $\mathbf{x}(\boldsymbol{\xi})$. Thereafter, an affine mapping pulls the parametric element $\hat{\Omega}^e$ to the parent element $\tilde{\Omega}$, where the element stiffness matrix is formed after integration. 15

6.1	The Linear Elasticity problem domain with boundary conditions. All entities are shown in the positive convention.	45
6.2	The problem setup and conventions for the Kirchhoff-Love plate problem.	55
6.3	An arbitrary shell domain. All positive conventions for degrees of freedom and applied loadings are depicted.	70
6.4	The Scordelis-Lo Roof problem setup and configuration.	89
6.5	The Scordelis-Lo Roof displacement criterion is shown across the range of refinements considered in this paper (left). The z -displacement field is shown on the contour plot (right).	89
6.6	The Pinched Cylinder problem setup and configuration.	90
6.7	The Pinched Cylinder displacement criterion shown across the range of refinements considered in this paper (left). The y -displacement field is shown on the contour plot (right).	91
6.8	The Pinched Hemisphere problem setup and configuration.	92
6.9	The Pinched Hemisphere displacement criterion shown across the range of refinements considered in this paper (left). The z -displacement field is shown on the contour plot (right). Note this is symmetric to the x -displacement field due to the symmetry of the loading configuration.	92
7.1	The Scordelis-Lo Roof Family	94
7.2	A representative sample of Scordelis-Lo Roof geometries belonging to the same family. Notice that after defining the appropriate mapping $\mathbf{x}_{\mu_i}(\boldsymbol{\xi})$, the same parametric domain can be mapped to various geometries seamlessly.	95
7.3	A representative tensor-product Lagrange interpolating basis function (left) and an interpolatory representation of the function $f(x, y) = \sin(\pi x) \sin(\pi y) - e^{-x^2 - 4y^2}$ using equispaced nodes and tensor-product Lagrange polynomials (right).	101

- 7.4 The 1st row of the figure shows the Legendre polynomial basis sets for $p = 2$ and $p = 3$. The 2nd row shows the 1-dimensional pseudospectral approximation of $f(x) = \cos(\pi x/2)$ using the above sets of Legendre polynomials, requiring 5 points and 9 points, respectively, for accurate integration using the univariate Clenshaw-Curtis quadrature rule over the domain $\mathcal{D} = (-1, 1)$. The 3rd row shows the pseudospectral representation of the function $f(x, y) = e^{-x^2-y^2}$ using a tensor-product Clenshaw-Curtis quadrature rule in a tensor-product Legendre basis, requiring 25 points and 81 points respectively, resulting in 2nd and 3rd degree tensor-product polynomial approximations over the domain $\mathcal{D} = (-1, 1)^2$. The 4th row shows the pseudospectral representation of the function $f(x, y)$ using a Delayed Smolyak Clenshaw-Curtis quadrature rule in the isotropic Legendre basis, requiring 13 points and 29 points respectively, resulting in 2nd and 3rd degree isotropic polynomial approximations over the domain $\mathcal{D} = (-1, 1)^2$ 104
- 7.5 Two-dimensional tensor-product Clenshaw-Curtis (left) and Gauss-Legendre (right) quadrature rules for the integration domain $\mathcal{D} = (-1, 1)^2$. The ℓ th-level Clenshaw-Curtis quadrature rule is capable of integrating $f \in \mathcal{Q}_{p_\ell}(\mathcal{D})$ with $p_\ell = 2^{\ell-1} + 1$ for $\ell > 1$ exactly while each Gauss-Legendre grid level ℓ is capable of integrating $f \in \mathcal{Q}_{p_\ell}(\mathcal{D})$ with $p_\ell = 2\ell - 1$ exactly. 107
- 7.6 Smolyak collocation schemes for the delayed, two-dimensional Clenshaw-Curtis (left) and Kronrod-Patterson (right) quadrature rules for the integration domain $\mathcal{D} = (-1, 1)^2$. Both delayed Clenshaw-Curtis and Kronrod-Patterson grids are capable of integrating $f \in \mathcal{P}_{p_\ell}(\mathcal{D})$ with $p_\ell = 2\ell - 1$ exactly. Note that the nestedness of the Clenshaw-Curtis naturally permits Smolyak implementation, contrary to the Gauss-Legendre scheme which requires the Kronrod extension and Patterson's recursion. . . 110

- 7.7 The computational domain of the Scordelis-Lo Roof. For sake of computational expense, only a quarter of the roof is modeled with symmetry boundary conditions. Therefore, refinement with respect to this geometry occurs only in this quadrant. This particular geometry has 16 elements. 113
- 7.8 The “nominal” Scordelis-Lo roof geometry. A sparse, level 5 Kronrod-Patterson grid is used to compute the pseudospectral coefficients of the surrogate displacement field in the isotropic Legendre basis. 114
- 7.9 An admissible geometry to the design space specified above. In this particular example, a full (tensor-product), level 5 Gauss-Legendre grid is used to construct a nodal representation of the displacement field using a tensor-product Lagrange basis in the design space. 115
- 7.10 The L^2 error in the displacement field for the various surrogate models considered applied to the Scordelis-Lo roof problem. The first half of each legend entry refers to the sampling scheme employed while the second half refers to the surrogate model used. Note here that TP denotes “Tensor-Product”, GL denotes “Gauss-Legendre”, KP denotes “Kronrod-Patterson”, and CC denotes “Clenshaw-Curtis”. Additionally, “Nodal” indicates the use of the Lagrange polynomials as an interpolating basis while “Modal” denotes the use of the Legendre orthogonal polynomials. 118
- 7.11 The energy error in the displacement field for the various surrogate models considered applied to the Scordelis-Lo roof problem. The first half of each legend entry refers to the sampling scheme employed while the second half refers to the surrogate model used. Note here that TP denotes “Tensor-Product”, GL denotes “Gauss-Legendre”, KP denotes “Kronrod-Patterson”, and CC denotes “Clenshaw-Curtis”. Additionally, “Nodal” indicates the use of the Lagrange polynomials as an interpolating basis while “Modal” denotes the use of the Legendre orthogonal polynomials. 118

7.12	The design parameters associated with the Flat L-Bracket problem (left) and the patches associated with implementing a multi-patch isogeometric linear-elastic solver (right).	121
7.13	The boundary conditions and applied loading used in the L-Bracket problem. The lower and center L-Bracket holes are constrained with homogeneous Dirichlet boundary conditions. The loading on the remaining hole is cosine distributed for $-\pi/4 \leq \theta \leq 3\pi/4$ and is applied as a Neumann traction.	122
7.14	A sample geometry contained within $\mathcal{P}_{p_\ell}(\mathcal{D}_{L,\text{minor}})$ (left) along with the resulting Von Mises stress field (right).	124
7.15	A sample geometry within $\mathcal{P}_{p_\ell}(\mathcal{D}_{L,\text{extreme}})$ (left) along with the resulting Von Mises stress field (right).	124
7.16	Simplified composite layup used for wind turbine optimization. Green color (top) indicates base uni-directional carbon across entire blade, blue color (middle) indicates root buildup of SNLTriax, and purple color (bottom) indicates spar cap region made up of additional uni-directional carbon.	127
7.17	The basic layout of the isogeometric PDO framework, laid out in Grasshopper 3D, a visual programming plugin for Rhino, configured for iterative use.	128
7.18	The isogeometric PDO framework configured for use with the design space exploration methodology, including analysis-heavy, iterative offline stage (top) and GUI-driven, rapidly evaluated design exploration stage (bottom).	129
7.19	The chord line describing design space of an NREL 5MW wind turbine blade, $\mathcal{D}_{\text{turb}}$. The chord line as a function of radial location is constructed using a piecewise quadratic B-spline. The two red control points in the dashed box, \mathbf{P}_5 and \mathbf{P}_7 are the design parameters for the turbine blade, which are free to move within the box. The B-spline curve shown is the nominal configuration for the turbine blade.	131
7.20	A sample geometry contained in $\mathcal{D}_{\text{turb}}$. This design has a tip wise shift in the maximal chord location.	131

7.21	A sample geometry contained in $\mathcal{D}_{\text{turb}}$. This design has a smaller maximal chord location.	132
7.22	In the left plots, we present representative chord lines associated with geometries admissible to $\mathcal{D}_{\text{turb}}$. The blue lines correspond to the nominal turbine geometry while the red lines are the chord lines associated with a turbine geometry present in the design space under consideration. In the right column of plots, the corresponding strain fields for the exact IGA solution, as well as the nodal surrogate model for levels 1 through 4, are shown.	133
8.1	An example manifold with a graphical illustration of the differential geometric tools presented in this section.	149
8.2	(left) Two-dimensional plate with hole geometric configuration where variations of the horizontal and vertical positions of the hole are considered. (center) The loading and boundary conditions associated with the plate with hole problem. A uniform loading of $P = 30$ MPa is applied to the right and the left side of the plate has zero-displacement boundary conditions. (right) Von Mises stress distribution in the plate with hole in the nominal configuration.	158
8.3	The white asterisk at $\mu_h = 0$ and $\mu_k = 0$ denotes the nominal configuration of the two-dimensional plate with hole problem. The three colored rectangles depict three different tolerance hyperrectangles, $\tau^{(i)}$, with hollow markers that indicate the location where the maximum of the restricted system performance $\mathcal{Q}(\mu_h, \mu_k) _{\mathcal{D}_{\hat{\mu}}(\tau^{(i)})}$ is attained. The red contour line denotes the loci of τ , that is the immersed manifold, such that $\mathcal{G}(\tau_h, \tau_k) = \mathcal{Q}_{\text{allow}}$. Refer to the online article for the colorized figure.	161
8.4	The one-dimensional manifold corresponding to the level set of $\mathcal{G}(\tau) = \mathcal{Q}_{\text{allow,SE}}$ for strain energy with (left) the tolerance measure $\mathcal{F}_1(\tau)$, (center) the tolerance measure $\mathcal{F}_{\mu}(\tau)$, and (right) the tolerance measure $\mathcal{F}_{-1}(\tau)$. The black asterisk denotes the location of $\hat{\tau}$ with respect to this norm.	162

8.5	The one-dimensional manifold corresponding to the level set of $\mathcal{G}(\boldsymbol{\tau}) = \mathcal{Q}_{\text{allow},M}$ for maximum stress with (left) the tolerance measure $\mathcal{F}_1(\boldsymbol{\tau})$, (center) the tolerance measure $\mathcal{F}_\mu(\boldsymbol{\tau})$, and (right) the tolerance measure $\mathcal{F}_{-1}(\boldsymbol{\tau})$. The black asterisk denotes the location of $\hat{\boldsymbol{\tau}}$ with respect to this norm.	162
8.6	Six-dimensional plate with hole geometric configuration where variations of the horizontal and vertical positions of the hole, plate height and width, and hole radius and eccentricity are considered.	164
8.7	(left) The 17-dimensional L-Bracket configuration where the various design parameters are shown. (center) The loading and boundary conditions associated with the L-Bracket problem. A uniform bearing pressure of $P = 30$ MPa is applied to the top-right hole while the other two holes have zero-displacement boundary conditions. (right) Von Mises stress distribution in the L-Bracket in the nominal configuration. .	170
9.1	Convergence behavior and displacement plot for the rectangular Kirchhoff-Love plate system using a $V(1,1)$ scheme.	179
9.2	Convergence rates and plot of $\ \mathbf{e}\ _{L^2}$ at various levels of refinement for the rectangular Kirchhoff-Love plate using FMG(1,1,1) scheme.	179
9.3	Convergence behavior and displacement plot for the parallelogram Kirchhoff-Love plate system using a $V(1,1)$ scheme.	180

Chapter 1

Introduction

The field of Computer-Aided Engineering (CAE) and Computer-Aided Design (CAD) has fostered a grandiose vision with regards to the progression of engineering design and analysis protocols, suggesting engineering systems can be iteratively optimized to obey specified performance constraints such as cost and load-bearing capability. However, the realization of this vision has been severely inhibited due to the growing demand for complex engineering systems along with the design-through-analysis bottleneck, that is, the apparent disconnect between design and analysis. Presently, iterative engineering optimization routines employ computational system models with highly simplified physics and geometry. The resulting designs are then physically prototyped and undergo extensive testing. Consequently, the lack of high-fidelity models in the design iterations commonly results in an over-designed, sub-optimal final product.

Isogeometric analysis (IGA) is a computational approach that offers the possibility of integrating finite element analysis (FEA) into conventional computer aided design (CAD) tools [9, 32, 68]. In IGA, the geometric entities described by CAD software, namely NURBS and T-splines, serve as the basis for all subsequent engineering analyses. As the same geometric descriptions are used for both the FEA and CAD, models may be designed, tested, and adjusted in one integrated stage. This is in direct contrast with current practices in engineering analyses and simulations.

As IGA provides a seamless integration between FEA and CAD, it constitutes an ideal analysis technology for design optimization. However, it is still very expensive to utilize full-order design and analysis models in an IGA-based design optimization loop. In early stage design, the

phrase “design optimization” is platitudinous in that the problem of finding the “optimal design” is not well-defined. In fact, a primary objective of early stage design is to identify suitable optimization criteria in addition to design constraints. To clarify, the “initial guess” or nominal design input to the engineering design cycle is typically ill-informed or chosen arbitrarily.

Design constraints which govern design optimization routines are not known or well-understood and cannot be determined without a design space exploration framework. Determination of such criteria requires an understanding of how design parameters affect system response and ultimately performance. Furthermore, successfully posing an optimization problem requires an understanding of how design parameter perturbations affect the resulting displacement field. With this in mind, a framework enabling a designer to explore full system response in real-time would be invaluable.

This design paradigm is referred to as “design space exploration” throughout this dissertation, since it presents a framework in which one can “explore” the displacement field as a function of these design parameters in a neighborhood of a nominal design through a surrogate model. This methodology arises through a unification of techniques emerging from the Uncertainty Quantification (UQ) community [118, 12, 104, 86, 96, 39] with isogeometric analysis [32, 68, 9] and parametric modeling [57, 16, 85, 66, 40] in a deterministic fashion. This is accomplished by sampling the solution at a set of designs in a subset of the solution space during an offline stage. An intelligent sampling scheme combined with sparse collocation provides a means to dramatically reduce this computational cost [7, 89, 88, 52]. Afterwards, the model is constructed by either fitting an interpolating polynomial to sampled data or constructing a spectral representation of the polynomial in this neighborhood. It should be emphasized that with our design space exploration framework, a designer can visualize the full system response. That is, a designer can visualize the solution field across the physical domain for a particular geometry in the design space. This is in contrast with state-of-the-art design space exploration frameworks which only allow a designer to examine pre-selected quantities of interest.

Following the design stage, manufacturing processes require extensive supervision to ensure the final product performs some intended task within specified performance constraints. Through-

out the engineering design cycle and the service lifetime of the assembled product, it is expected that uncertainty due to manufacturing processes, fatigue, modeling assumptions, etc. will affect the overall system performance. Regardless of these uncertainties, the product is still expected to successfully perform its intended task.

Geometric variations which occur during manufacturing or from erosion throughout its life span adversely affect part performance. These effects on performance are rarely, if ever, considered during assembly design in a rigorous, analytical manner. Instead, manufacturing tolerances are somewhat arbitrarily prescribed which typically only address the issue of goodness-of-fit between parts in an assembly. Monte-Carlo methods are typically employed in efforts to ascertain the certainty of fit in a statistical sense [27, 64]. Thereafter, parts which are not in compliance with these tolerances are recycled or discarded imposing additional costs on manufacturing processes. On the other hand, wear and tear throughout the part life span deteriorates performance. These issues are often addressed in an a posteriori manner namely, measurements are periodically collected throughout the part life cycle and are used to assess the overall condition of the system. In this manner, the status of the engineering system is not well-understood until thorough subsequent analyses are conducted which, if not performed in a timely manner, may result in catastrophic failure.

In this dissertation, we also present a methodology for determining spaces of admissible design parameters, e.g. tolerances, a priori, given acceptable performance metrics. This allows the engineer to know, simply through measurement, the compliance of the system with regards to performance constraints. Additionally, this methodology allows for the implementation of systems which can detect their own non-compliance. This is accomplished by parameterizing the solution to partial differential equations, and relevant quantities of interest therein, as a function of design. We leverage isogeometric analysis and a flavor of the surrogate modeling methodology emerging from our design space exploration technology to accomplish this.

Thereafter, Monte-Carlo samples are taken throughout this parametric domain about some nominal design and subsequently, a surrogate model to the solution is constructed. A set of do-

main restrictions over this surrogate model effectively emulates tolerances by permitting geometric deviations within some hyperrectangle about the nominal design. An optimization problem posed over the restricted surrogate yields the worst offender of the elements contained within a given hyperrectangle. The “largest” hyperrectangle such that the worst offender remains within the prescribed performance constraint is an optimal tolerance to allocate, which naturally has a strong dependence on the norm used to measure tolerances in the hyperrectangle.

The problem herein is interpreted as a manifold optimization. This manifold is of dimension one less than the number of design parameters used in the geometric parameterization. Moreover, it represents the loci of hyperrectangles whose worst offender is equivalent to the performance constraint that is considered. Provided a weighted norm that is informed by considerations such as design sensitivities or manufacturing costs, the point with the largest value in this measure is considered optimal. Furthermore, we employ manifold gradient ascent and manifold conjugate gradients optimization routines to determine this optimal value.

The primary theme of this dissertation pertains to surrogate model construction. Regardless of surrogate modeling strategy employed, it is understood that in general more solution realizations at higher fidelities is directly correlated to a more accurate surrogate predictive modeling capabilities. Obtaining a large number of samples isn’t generally feasible due to the large increase in computational complexity. Therefore, we resort to geometric multigrid methods to alleviate the associated computational expense of linear system solution. These methods are well-understood in the context of finite elements and in this dissertation we extend these techniques to the isogeometric analysis setting.

Although the techniques and methodologies considered in this dissertation extend naturally to a wide variety of physical phenomena, we primarily focus on structural mechanics. In particular, we consider a geometrically-linear elastic model of membranes, thin plates, and in general, thin shells. We spend a significant portion of this dissertation providing derivations and analyses associated with physically-consistent boundary condition enforcement, since this is a non-trivial manner in the general NURBS setting. The goal of this is to devise a numerical methodology leading

to a symmetric, positive-definite system without excessive ill-conditioning while maintaining this physical consistency.

Nitsche’s method as originally introduced in [87] allows us to achieve this goal, but its application to shell problems is nontrivial in part because of the fourth-order nature of the shell equations. Throughout this dissertation, we present a thorough analysis of Nitsche’s method applied to problems in continuum mechanics. We present our derivations in a unified manner with the intention that these techniques can be applied to more complex PDEs with relative ease. The approach we take in this dissertation provides tight estimates for penalty parameters as well as a priori error estimates. This consequently provides a robust and stable method of computing penalty parameters which avert issues of discrepancies due to numerical roundoff. Additionally, we present the physically-correct boundary conditions with respect to an underlying energy principle. To the best of the authors’ knowledge, this has not been accomplished in the context of the linearized Kirchhoff-Love shell, where modified tractions and corner forces must be introduced to preserve the physical consistency with the system energy. This is particularly important for problem configurations containing free or symmetric boundary conditions. The exposition here is limited to linear elasticity and for simplicity, we only consider a linear, isotropic constitutive model corresponding to a plane stress state. Extending these models to a linear, anisotropic material model are anticipated to be fairly straight-forward while the extension to geometric and material nonlinearities are relegated to future work.

In contrast to a standard Galerkin method, where Dirichlet boundary conditions are enforced strongly in the trial space and the homogeneous counterpart enforced strongly in the test space, Nitsche’s method utilizes a weak enforcement of Dirichlet boundary conditions. Methods for the weak enforcement of Dirichlet boundary conditions are commonly used for B-spline and subdivision finite elements [58, 101, 28]. One common approach, the classical penalty method require a penalty parameter selection that, without a rigorous analysis, may lead to an overly stiff, ill-conditioned system or a poor enforcement of boundary conditions. On the other hand, Lagrange multipliers are another approach used for weak-enforcement of Dirichlet boundary conditions [49]. However,

this method results in a saddle point system which are generally more difficult to solve [49]. The symmetric Nitsche formulations considered herein can be interpreted as residual-based, stabilized Lagrange multiplier methods where the Lagrange multiplier is determined algebraically via a static condensation of the saddle point system. To this end, the resulting formulation is an agglomeration of the penalty and the Lagrange multiplier methods. In particular, the symmetric Nitsche formulations utilize penalty parameters which are computed optimally through trace inequality constants, averting the aforementioned concerns of ill-conditioning of the discrete system or poor enforcement of boundary conditions entirely. Moreover, the residual-based, stabilized Lagrange multiplier yields a variational form that has a corresponding positive-definite system.

The fundamental crux of Nitsche’s method is the retention of consistency terms and the addition of symmetrizing terms to a standard penalty method. The consistency terms restore the high-order accuracy of the method by rendering the variational form consistent with the original strong form. These terms are obtained by the relaxation of the homogeneous Dirichlet boundary conditions on the test space. The symmetrizing terms ensure the bilinear form is symmetric. Lastly, the penalty terms ensure the bilinear form is definite and enforces Dirichlet boundary conditions. The symmetrizing residual-based terms are obtained through the symmetric counterpart of the Dirichlet consistency terms while the residual-based penalty terms enforce Dirichlet boundary conditions through additional penalty parameters.

In all three problems considered, we begin exposition through the variational form arising through the Euler-Lagrange equations, particularly the stationary point of the first variation of the system Lagrangian. Through this variational form, we perform integration by parts to determine the underlying strong formulation of the PDE for which the variational form, provided enough regularity, satisfies. The strong formulation elucidates the appropriate boundary conditions which must be applied to maintain energetic conjugacy. Additionally, this process provides the appropriate consistency, and symmetrizing, terms required in the Nitsche formulation. Thereafter, we posit the Nitsche formulation followed by a proof of consistency with the inferred strong formulation as well as the proposed symmetry of the associated bilinear form. This is followed by proofs of continuity

and coercivity of the bilinear form, additionally providing estimates for optimal penalty parameters selection which preserve conditioning of the resulting discrete system. We conclude each section with a presentation of a priori error estimates that ultimately demonstrate the optimal convergence of the method.

The remainder of this dissertation proceeds as follows. In Chapter 2, we outline the fundamentals of isogeometric analysis. In particular, how geometric entities are represented in this setting and how analysis over these geometries is conducted thereafter. Chapter 3, presents the notation and necessary differential geometry used throughout the exposition of this dissertation. Chapter 4, we provide a short review of continuum mechanics and present the problem-dependent strain measures posed over a differentiable manifold. Chapter 5 provides the necessary theorems and functional analysis tools that will be used throughout our proofs of properties arising in Nitsche's formulation. Chapter 6 is comprised of three major sections. The first of which goes through a detailed derivation of Nitsche's method for the linear elastic membrane. The second section performs a similar exposition and analysis of Nitsche's method but for the Kirchhoff-Love plate, a fourth-ordered PDE. The last section combines the previous two problems posed over a Riemannian manifold known as the Kirchhoff-Love shell. Chapter 7 provides the necessary ingredients for constructing a design space exploration framework for a real-time visualization of system response with respect to perturbations in design parameters. Chapter 8 provides a discussion of the novel physics-informed tolerance allocation algorithm through a similar surrogate model construction to that of the design space exploration algorithm. Finally, Chapter 10 provides some concluding remarks on the contributions of this dissertation to the scientific community.

Chapter 2

Fundamentals of Isogeometric Analysis

Simulating structural mechanics is natural in the IGA setting. This is due to the intrinsic mesh present in CAD geometries, permitting an exact geometrical representation in contrast to conventional finite elements, where the mesh is generated as an approximation to the geometry. In the finite element setting, features of great importance in engineering, such as fillets, holes, and corners, are removed from the CAD geometry before constructing the analysis mesh. This is typically done because of the inability to easily create a mesh which accurately captures the physical effects of these features. However, this over-simplification likely results in unrealistic peak stresses which are commonly smoothed through an averaging process or imposing an enormous margin of safety to compensate. The results from these analyses are furthermore used to inform subsequent design stages. Consequently, the result of the engineering design cycle is a sub-optimal, over-designed product. Isogeometric analysis mitigates this issue through the underlying analysis mesh which can readily describe such engineering features and capture the corresponding stress and strain distributions throughout the same CAD geometry.

These features in the Isogeometric method are made possible through a clever choice of basis for analysis, particularly the same basis used to represent the geometry. Most engineering and free-form CAD software suites use the **Non-Uniform Rational B-Spline** (NURBS) basis for constructing geometry. This choice is favorable over other basis functions, since NURBS permit local control of feature manipulation, are arbitrarily continuous without induced oscillations due to polynomial degree elevation (compared to interpolatory polynomials), and form a partition of

unity which enables this basis a suitable choice for analysis. For an elaborate presentation of NURBS entities and manipulation, see [93]. More recently, the advent of T-splines have served as a generalization to NURBS which permit Isogeometric analysis on “water-tight” geometries of arbitrary complexity [110, 109, 43, 77]. However, for simplicity of exposition, we restrict our discussion here to B-Splines and NURBS.

2.1 Isogeometric Analysis

A d -dimensional NURBS function is a projective transformation of a B-spline function in one higher spatial dimension. Therefore, to motivate the discussion of IGA, we first present the construction of the B-spline basis. We generate B-spline basis functions in a parametric fashion by first constructing a **knot vector** which describes the support and continuity of the set of resulting basis functions. A knot vector is a non-decreasing set of real numbers $\Xi = \{\xi^1, \xi^2, \dots, \xi^{n+p+1}\}$ where n is the number of basis functions and p is the polynomial degree. We assume without loss of generality that $\xi^1 = 0$ and $\xi^{n+p+1} = 1$. In IGA, we typically employ an **open knot vector** such that the first and last knots are repeated $p+1$ times. This ensures that the basis will interpolate the geometry at the boundaries in one-dimension, or the corners in higher dimensions, and enforcing C^0 -continuity across parametric patches. The knot vector, along with the **Cox-deBoor formula** shown below, defines the univariate B-spline basis functions for intermediate $\xi \in (0, 1)$:

$$\begin{aligned} \hat{N}_{i,p}(\xi) &= \frac{\xi - \xi^i}{\xi^{i+p} - \xi^i} \hat{N}_{i,p-1}(\xi) + \frac{\xi^{i+p+1} - \xi}{\xi^{i+p+1} - \xi^{i+1}} \hat{N}_{i+1,p-1}(\xi) \\ \hat{N}_{i,0}(\xi) &= \begin{cases} 1, & \xi^i \leq \xi < \xi^{i+1} \\ 0, & \text{elsewhere} \end{cases} \end{aligned} \quad (2.1)$$

The multivariate B-spline basis is obtained through a tensor product of one-dimensional basis functions. In particular, to define the d_p -dimensional B-spline basis functions for multi-indices $\mathbf{i} = (i_1, i_2, \dots, i_{d_p})$ and $\mathbf{p} = (p_1, p_2, \dots, p_{d_p})$ representing basis function number and polynomial degree respectively, we write:

$$\hat{N}_{\mathbf{i},\mathbf{p}}(\boldsymbol{\xi}) = \bigotimes_{j=1}^{d_p} \hat{N}_{i_j,p_j}(\xi^j) \quad \forall \boldsymbol{\xi} \in \hat{\Omega} \quad (2.2)$$

where $\hat{\Omega} = (0, 1)^{d_p}$ is the so-called **parametric domain**. One-dimensional B-spline basis functions of various degree, as well as a representative two-dimensional basis function, are shown in Figure 2.1 below.

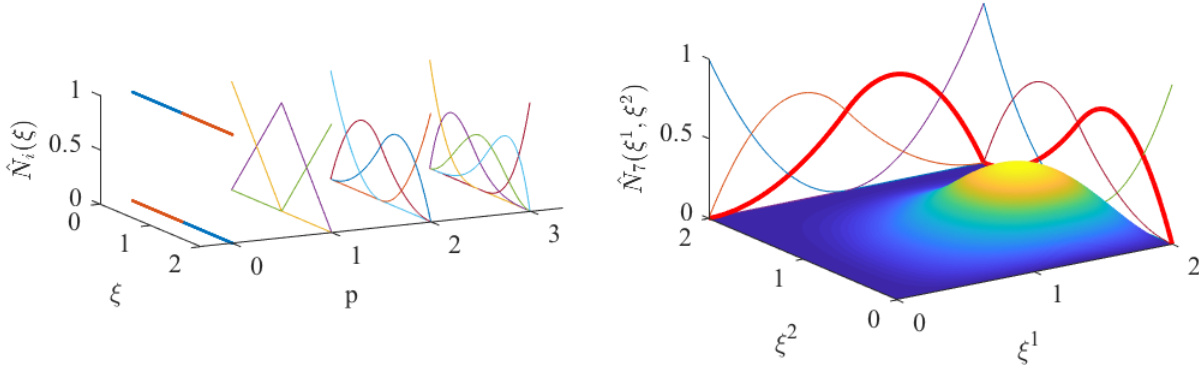


Figure 2.1: The constant, linear, quadratic, and cubic B-spline basis functions (left). A bicubic B-spline basis function is constructed through a tensor product of 1D splines (right).

Before proceeding to geometry definition in this setting, we must first discuss the construction of the NURBS basis from the B-spline basis presented. Given a set of $n_{\text{basis}} = \prod_{i=1}^{d_p} n_i$ d_p -dimensional B-spline basis functions and a set of n_{basis} NURBS **weights**, $w_i \in \mathbb{R}^+$, we define the corresponding set of d_p -dimensional NURBS basis functions via:

$$\hat{R}_{\mathbf{i},\mathbf{p}}(\boldsymbol{\xi}) = \frac{w_i \hat{N}_{\mathbf{i},\mathbf{p}}(\boldsymbol{\xi})}{w(\boldsymbol{\xi})}, \quad \text{where} \quad w(\boldsymbol{\xi}) = \sum_{\mathbf{i}} w_i \hat{N}_{\mathbf{i},\mathbf{p}}(\boldsymbol{\xi}) \quad (2.3)$$

The function $w(\boldsymbol{\xi})$ is known as the **weighting function**. As previously mentioned, a d_p -dimensional NURBS entity is constructed in $d_p + 1$ dimensions and then projected into a d_p dimensional space; the NURBS weights are in fact the $(d_p + 1)^{\text{th}}$ -component of the control mesh in the projective space.

Now, in order to construct geometry using this basis and subsequently perform analysis on this geometry, we construct the **control mesh**, a network of n_{basis} **control points** in d_s -dimensions

which, together with the complete set of NURBS basis functions, construct a d_s -dimensional geometry $\Omega \subset \mathbb{R}^{d_s}$ which will serve as our **physical domain**. More specifically, given a set of NURBS control points \mathbf{P}_i and weights w_i , the parametric representation of the geometry $\mathbf{x}(\boldsymbol{\xi}): \hat{\Omega} \rightarrow \Omega$ is given by:

$$\mathbf{x}(\boldsymbol{\xi}) = \sum_{\mathbf{i}} \mathbf{P}_{\mathbf{i}} \hat{R}_{\mathbf{i}}(\boldsymbol{\xi}) \quad \forall \boldsymbol{\xi} \in \hat{\Omega} \quad (2.4)$$

Note we have dropped the subscript \mathbf{p} for notational ease, and we will proceed to do so henceforth. Before doing so, it is worthwhile to note that through an analogous procedure, we are capable of constructing tensor product basis functions of anisotropic polynomial degrees by varying the multi-index \mathbf{p} accordingly.

At this juncture, it is useful to delineate between the two different notions of dimension we have introduced heretofore. The dimension d_p refers to the **parametric dimension** (e.g., $d_p = 1$ for a curve, $d_p = 2$ for a surface, and $d_p = 3$ for a volume). Alternatively, the dimension d_s refers to the **spatial dimension**. It is required that $d_p \leq d_s$. For instance, a surface ($d_p = 2$) may be embedded within \mathbb{R}^3 but not within \mathbb{R}^1 . Figure 2.2 shows an example of a NURBS curve in two-dimensional space and a two-dimensional NURBS surface in three-dimensional space.

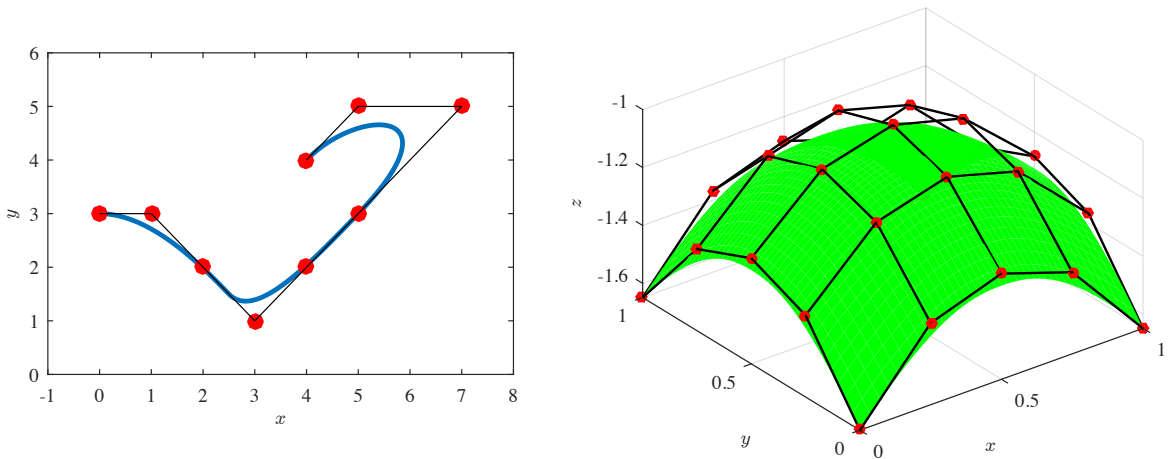


Figure 2.2: An example NURBS curve (left) and NURBS surface (right) with their corresponding control meshes.

Once the geometry has been constructed, IGA follows analogously to a standard Bubnov-Galerkin method. In particular, we seek a finite-dimensional approximation to a solution of a system of partial differential equations (PDEs). For simplicity, consider a general boundary-value problem (BVP) of the form:

$$\begin{aligned}\mathcal{L}(\mathbf{u}) &= \mathcal{F} \quad \forall \mathbf{x} \in \Omega \\ \mathcal{B}(\mathbf{u}) &= \mathcal{G} \quad \forall \mathbf{x} \in \Gamma\end{aligned}\tag{2.5}$$

where $\mathcal{L}(\cdot)$ is a differential operator, possibly nonlinear, $\mathcal{B}(\cdot)$ is a boundary operator, and $\Gamma = \partial\Omega$. Both operators act on the unknown solution field $\mathbf{u} : \Omega \rightarrow \mathbb{R}^d$. In the context of structural mechanics, \mathbf{u} typically denotes the displacement field and $d = 2$ or 3 .

As the PDE system is typically cast over a spatial variable, we require an appropriate space of basis functions defined in physical space in which to express the solution. To arrive at such a space, we leverage the isoparametric concept provided by the isogeometric analysis paradigm to uniquely relate topologically equivalent parametric and physical domains. The isoparametric concept is elucidated through the notion of the **pull back** and **push forward** operations which explicitly describe how the physical variable \mathbf{x} is related to the parametric variable $\boldsymbol{\xi}$ through the geometric mapping:

$$\text{push forward: } \mathbf{x} = \mathbf{x}(\boldsymbol{\xi}) \quad \text{pull back: } \boldsymbol{\xi} = \mathbf{x}^{-1}(\mathbf{x})\tag{2.6}$$

Hence, the NURBS basis functions defined in the parametric domain also define splines in the physical domain as directed by the geometric mapping (2.4):

$$R_{\mathbf{i}}(\mathbf{x}) = \hat{R}_{\mathbf{i}}(\mathbf{x}^{-1}(\mathbf{x})) \quad \text{and} \quad \hat{R}_{\mathbf{i}}(\boldsymbol{\xi}) = R_{\mathbf{i}}(\mathbf{x}(\boldsymbol{\xi}))\tag{2.7}$$

In IGA, we use the same basis for geometric design and analysis, so we seek a discrete solution of the form:

$$\mathbf{u}^h(\mathbf{x}) = \sum_{\mathbf{i}} \mathbf{d}_{\mathbf{i}} R_{\mathbf{i}}(\mathbf{x}) \quad (2.8)$$

where the terms $\mathbf{d}_{\mathbf{i}} \in \mathbb{R}^d$ are referred to as **control variables**. With the admissible trial functions defined, we invoke Galerkin’s method by multiplying the PDE system by a corresponding NURBS weighting function, integrating by parts, strongly enforcing Dirichlet boundary conditions, and weakly enforcing Neumann boundary conditions. This yields a residual system of the form:

$$\mathbf{R}(\mathbf{d}) = \mathbf{0} \quad (2.9)$$

where \mathbf{R} is a vector of residuals and \mathbf{d} is a solution vector of control variables. In the linear setting, this equation reduces further to the linear system:

$$\mathbf{Kd} = \mathbf{F} \quad (2.10)$$

where \mathbf{K} is the system stiffness matrix and \mathbf{F} is the system forcing vector. To assemble and solve this system, finite elements are constructed through a process known as “Bézier extraction” where a transformation, referred to as the extraction operator, is constructed that describes the B-spline basis locally in terms of the Bernstein polynomials. These elements are then assembled in a global stiffness matrix and a global system solve is performed to obtain the displacement vector. The p^{th} -degree Bernstein polynomials over $[0, 1]$ are generated through the Cox-deBoor formula (2.1) with the open knot vector of length $2p + 2$, containing only the points 0 and 1, each repeated $p + 1$ times. The cubic Bernstein polynomial set is shown below in Figure 2.3, in addition to a pictorial representation of Bézier extraction.

Bézier extraction is accomplished by repeatedly inserting knots in the global knot vector until each knot appears p times, where p is the polynomial order of the basis. Moreover, each knot interval becomes a Bézier element on which we can perform analysis. This process with the resulting **unscaled** Bernstein basis is shown in Figure 2.4 below for the knot vector $\Xi = \{0, 0, 0, 1, 2, 3, 3, 3\}$ for a quadratic basis.

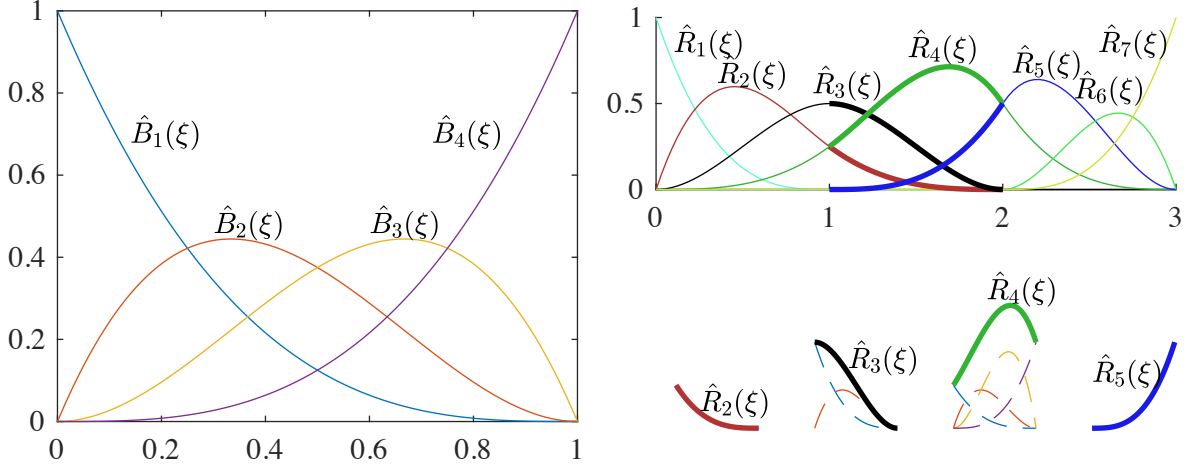


Figure 2.3: The set of cubic Bernstein polynomials is shown in the left figure. In the right figure, the set of B-spline basis functions described by the knot vector $\Xi = \{0, 0, 0, 0, 1, 2, 2, 3, 3, 3\}$ is shown on the top. Below that, the B-spline basis functions restricted to the 2^{nd} element are shown, along with the scaled Bernstein polynomials which span the B-spline basis. For example, $\hat{R}_4(\xi)|_{\Omega^2} = \frac{1}{4}B_1(\xi) + \frac{1}{2}B_2(\xi) + B_3(\xi) + \frac{1}{2}B_4(\xi)$, where the coefficients arise through Bézier extraction.

After performing Bézier extraction, the global control points are re-expressed as local control points which construct the **Bézier control polygon** and provide a Bézier representation of the original geometric entity. In addition to Bézier extraction, knot insertion is the primary method in which we can refine the isogeometric mesh, since inserting knots into the global knot vector increases the resolution of the parametric domain.

The process of Bézier extraction for both NURBS and T-splines are presented in [17, 108]. Once the notion of an “element” has been defined, the element formation and assembly routines follow in a similar fashion to the conventional finite element method. In particular, each physical element is “pulled back” to the parametric domain through the inverse geometric mapping (2.6), followed by an affine transformation to the parent element, where Gaussian quadrature is then used for numerical integration. Moreover, Figure 2.5 illustrates this process. For an in-depth overview of the isogeometric method and its implementation, the reader is referred to [32, Chapter 3].

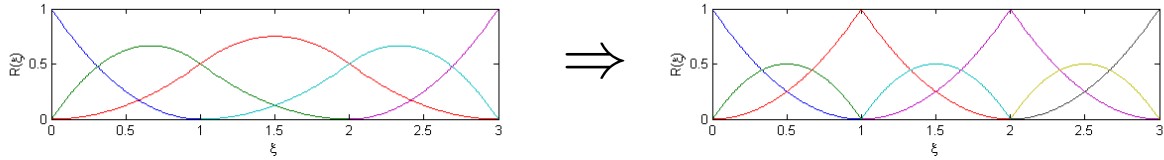


Figure 2.4: 2^{nd} -order B-spline basis before Bézier Extraction (left) and after Bézier Extraction (right) which it is cast in the Bernstein polynomial basis.

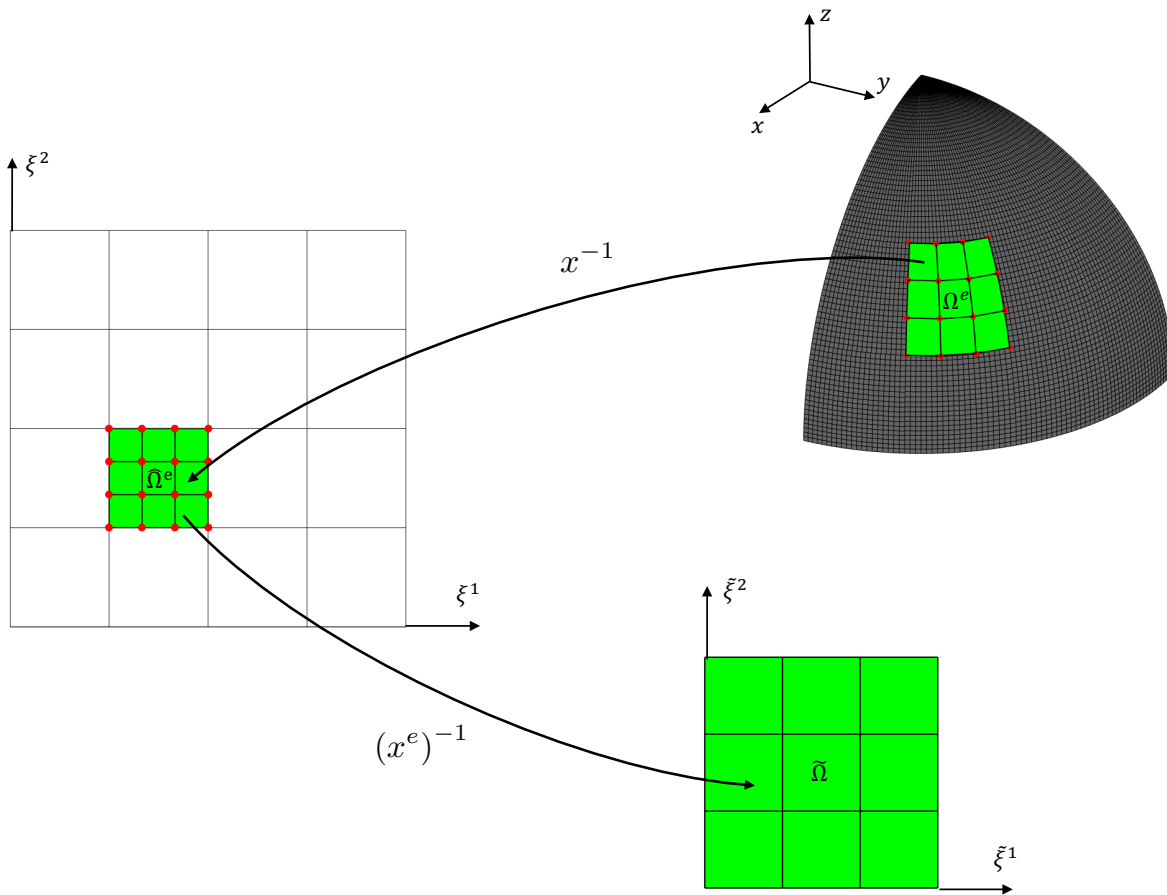


Figure 2.5: Bézier extraction defines the notion of an “element” in the isogeometric paradigm, where quadrature can be used for numerical integration in an element-wise fashion. First, the physical Bézier element Ω^e is “pulled back” to the parametric domain through the geometric mapping $\mathbf{x}(\boldsymbol{\xi})$. Thereafter, an affine mapping pulls the parametric element $\hat{\Omega}^e$ to the parent element $\tilde{\Omega}$, where the element stiffness matrix is formed after integration.

Chapter 3

Differential Geometry

The models we consider herein idealize the three-dimensional elastic body $\mathcal{B} \subset \mathbb{R}^3$ into a two-dimensional manifold $\Omega \subset \mathbb{R}^3$, commonly referred to as the midsurface. The boundary of the midsurface is denoted $\Gamma = \partial\Omega \subset \mathbb{R}^3$. The midsurface is typically chosen to be the surface midway through the thickness of the shell. If the elastic body is of uniform thickness η with homogeneous material properties, this surface coincides with the neutral plane, that is, the plane which undergoes no compressive or tensile forces due to bending. We parametrize Ω in terms of the variables $\boldsymbol{\xi} = (\xi^1, \xi^2)$ in the parametric domain $\hat{\Omega} \subset \mathbb{R}^2$ and utilize the physical push-forward mapping \boldsymbol{x} .

The formulation of the equations for linearized Kirchhoff-Love shells requires extensive use of differential geometry to effectively describe the physics. In the following, we use Einstein notation, i.e. repeated high-low indices have an induced summation. Latin indices, e.g., i, j, k , take values 1, 2, and 3 while Greek indices, e.g., α, β, λ , take values 1 and 2. Moreover, a comma preceding an index denotes derivative with respect to that index in contrast to a vertical bar, indicating the covariant derivative. Although our discussions of other PDEs, particularly linear elasticity and the Kirchhoff-Love plate, do not require as much machinery, we attempt to express all the equations in a uniform manner using a consistent notation. To this end, we interpret a problem in \mathbb{R}^2 as a flat manifold in \mathbb{R}^3 throughout the dissertation.

In the general setting, \boldsymbol{x} is not-affine, with possible intrinsic curvatures present in the immersed manifold Ω . These curvatures are necessary to effectively describe general shell structures

however present difficulty in analysis since there is no natural **global** coordinate system to reference the shell kinematic equations. Therefore, we resort to using **local** coordinate frames to perform analyses. The isogeometric paradigm permits a natural implementation of parametric coordinate frames for analysis. The in-plane vectors of the coordinate frame, along with its derivatives, are given by higher-ordered derivatives of the geometric mapping.

$$\mathbf{a}_\alpha(\xi^1, \xi^2) = \mathbf{x}_{,\alpha}, \quad \mathbf{a}_{\alpha,\beta}(\xi^1, \xi^2) = \mathbf{x}_{,\alpha\beta}, \quad \text{and} \quad \mathbf{a}_{\alpha,\beta\lambda}(\xi^1, \xi^2) = \mathbf{x}_{,\alpha\beta\lambda} \quad (3.1)$$

Note that many of these derivatives are symmetric due to the differentiability of \mathbf{x} . We henceforth drop the explicit dependence of (ξ^1, ξ^2) for notational brevity. Parametric scaling and skewing due to \mathbf{x} present complications in vector measurements through a standard Euclidean inner product. The **first fundamental form**, also known as the **metric tensor**, encapsulates these geometric properties pertaining to vector norms in the parametric coordinate frame. The metric tensor is given by

$$\underline{\underline{a}} = a_{\alpha\beta} \mathbf{a}^\alpha \otimes \mathbf{a}^\beta = a^{\alpha\beta} \mathbf{a}_\alpha \otimes \mathbf{a}_\beta \quad (3.2)$$

where these tensorial components are computed through various inner products of the parametric basis vectors as

$$a_{\alpha\beta} = \mathbf{a}_\alpha \cdot \mathbf{a}_\beta \quad \text{and} \quad a^{\alpha\beta} = \mathbf{a}^\alpha \cdot \mathbf{a}^\beta. \quad (3.3)$$

Note that the metric tensor is symmetric, since the Euclidean inner product, ‘ \cdot ’, is symmetric, i.e., $a_{\alpha\beta} = a_{\beta\alpha}$. The terms $a_{\alpha\beta}$ and $a^{\alpha\beta}$ are referred to as the **covariant** and **contravariant** components of the metric tensor. In contrast to the standard Cartesian basis, where $\mathbf{e}_i \equiv \mathbf{e}^i$, covariant and contravariant entities are not necessarily identical hence must be differentiated from one another throughout our exposition. Henceforth, lowered indices denote covariant quantities while raised indices indicate contravariant ones.

Intuitively, the metric tensor serves as an identity operator in the vector space described by this curvilinear coordinate system:

$$\underline{\underline{a}} \mathbf{a}_\mu = \left(a_{\alpha\beta} \mathbf{a}^\alpha \otimes \mathbf{a}^\beta \right) \mathbf{a}_\mu = a_{\alpha\beta} \mathbf{a}^\alpha \otimes \delta_\mu^\beta = a_{\alpha\mu} \mathbf{a}^\alpha = \mathbf{a}_\mu. \quad (3.4)$$

Here we have made use of the **right composition** tensor operation between the metric tensor and one of its basis vectors. This property holds in an analogous manner for contravariant vectors composed with the metric tensor. Furthermore, the metric tensor provides a mechanism for converting covariant quantities into contravariant ones, or vice versa, colloquially referred to herein as “index raising” and “index lowering”, respectively. This is a consequence of the inverse relationship between the covariant and contravariant components, namely

$$[a^{\alpha\beta}] = [a_{\alpha\beta}]^{-1}. \quad (3.5)$$

where “[.]” denotes the matrix of the respective components. Therefore, we can construct the corresponding contravariant basis vectors through the index raising operation

$$\mathbf{a}^\alpha = a^{\alpha\mu} \mathbf{a}_\mu. \quad (3.6)$$

Note that necessarily, the covariant and contravariant basis vectors satisfy the Kronecker delta relationship, that is

$$\mathbf{a}^\alpha \cdot \mathbf{a}_\beta = \delta_\beta^\alpha \quad (3.7)$$

where the Kronecker delta symbol is defined via

$$\delta_\beta^\alpha = \begin{cases} 1, & \alpha = \beta \\ 0, & \text{else} \end{cases}. \quad (3.8)$$

The in-plane covariant vectors define a basis for the tangent bundle of the manifold, and through the exterior product we can define a surface normal director

$$\mathbf{a}_3 = \frac{\mathbf{a}_1 \times \mathbf{a}_2}{\|\mathbf{a}_1 \times \mathbf{a}_2\|_2} \quad (3.9)$$

where $\|\cdot\|_2$ is the standard Euclidean norm. Note, by this definition, that (i) the normal director is always orthogonal to the in-plane vectors and (ii) the normal director always has unit length. Therefore necessarily, the covariant and contravariant normal directors are identical (e.g., $\mathbf{a}_3 \equiv \mathbf{a}^3$). We will also require derivatives of these basis vectors for geometric computation. However, the derivatives of the normal director are more involved, due to their construction and normalization. The first and second derivatives are given by

$$\mathbf{a}_{3,\beta} = \frac{\hat{a}_{,\beta}}{\tilde{a}} - \frac{\tilde{a}_{,\beta}}{\tilde{a}} \mathbf{a}_3 \quad \text{and} \quad \mathbf{a}_{3,\beta\lambda} = \frac{\mathbf{a}_{,\beta\lambda}}{\tilde{a}} - \frac{\tilde{a}_{,\lambda}\hat{a}_{,\beta}}{(\tilde{a})^2} - \frac{(\tilde{a}_{,\beta}\mathbf{a}_{3,\lambda} + \tilde{a}_{,\beta\lambda}\mathbf{a}_3)}{\tilde{a}} + \frac{\tilde{a}_{,\beta}\tilde{a}_{,\lambda}\mathbf{a}_3}{(\tilde{a})^2} \quad (3.10)$$

where

$$\begin{aligned} \hat{a} &= \mathbf{a}_1 \times \mathbf{a}_2 \\ \hat{a}_{,\beta} &= \mathbf{a}_{1,\beta} \times \mathbf{a}_2 + \mathbf{a}_1 \times \mathbf{a}_{2,\beta} \\ \hat{a}_{,\beta\lambda} &= \mathbf{a}_{1,\beta\lambda} \times \mathbf{a}_2 + \mathbf{a}_{1,\beta} \times \mathbf{a}_{2,\lambda} + \mathbf{a}_{1,\lambda} \times \mathbf{a}_{2,\beta} + \mathbf{a}_1 \times \mathbf{a}_{2,\beta\lambda} \end{aligned} \quad (3.11)$$

and

$$\begin{aligned} \tilde{a} &= \|\mathbf{a}_1 \times \mathbf{a}_2\|_2 \\ \tilde{a}_{,\beta} &= \hat{a}_{,\beta} \cdot \mathbf{a}_3 \\ \tilde{a}_{,\beta\lambda} &= \hat{a}_{,\beta\lambda} \cdot \mathbf{a}_3 + \hat{a}_{,\beta} \cdot \mathbf{a}_{3,\lambda} \end{aligned} \quad (3.12)$$

Note that $\mathbf{a}_{3,3} = 0$ by the inextensibility of the normal director hence $\mathbf{a}_{3,\alpha}$ lies solely in the manifold. Together, these three vectors define a complete curvilinear coordinate system for \mathbb{R}^3 in which we perform most of our subsequent analyses. Proceeding forward, we introduce notation to differentiate between manifold quantities, that is, quantities residing in the manifold, from those existing in the full, three-dimensional space. In particular, \bullet and $\underline{\bullet}$ will be used to denote manifold

quantities, that is, quantities that can be expressed through a linear combination of vectors lying in-plane of the manifold, with the number of underlines indicating the order of the tensor.

For instance, we define \underline{n} be the outward-facing unit normal and \underline{t} be the positively-oriented, counter-clockwise unit tangent vector to Γ . Note that \underline{n} is normal to Γ and should not be confused with the midsurface normal director \mathbf{a}_3 , which coincidentally also dictates the positive orientation of \underline{t} . These boundary quantities are defined via the non-normalized normal and tangent vectors denotes $\underline{\nu}$ and \underline{s} , respectively

$$\underline{n} = \frac{\underline{\nu}}{\|\underline{\nu}\|_2}, \quad \underline{\nu} = \nu_\alpha \mathbf{a}^\alpha \quad \text{and} \quad \underline{t} = \frac{\underline{s}}{\|\underline{s}\|_2}, \quad \underline{s} = s_\alpha \mathbf{a}^\alpha \quad (3.13)$$

and analogously for higher-ordered tensors such as the metric tensor (3.2).

On the other hand, **bold-faced text** denotes quantities residing in three-dimensional space. For example,

$$\underline{\underline{u}} = \tilde{u}_\alpha \mathbf{a}^\alpha \quad \text{and} \quad \mathbf{u} = \underline{u} + \tilde{u}_3 \mathbf{a}^3 \quad (3.14)$$

In addition, curvilinear tensorial components are denoted via $\tilde{\bullet}$ while the Cartesian counterparts are left unaccented. To this end, it is convenient to define the basis transformation operators for relating these entities. In particular the operators that maps Cartesian components to covariant, curvilinear ones, and vice versa:

$$\begin{array}{cc} \text{Covariant Transformation} & \text{Contravariant Transformation} \\ \hline \Lambda_j^i = \mathbf{e}_i \cdot \mathbf{a}^j & V_j^i = \mathbf{a}^i \cdot \mathbf{e}_j \end{array} \quad (3.15)$$

For example, if $\mathbf{u} = u_i \mathbf{e}^i = \tilde{u}_i \mathbf{a}^i$, then $\tilde{u}_i = \Lambda_i^j u_j$. On the other hand, if $\mathbf{u} = u_i \mathbf{e}^i = \tilde{u}_i \mathbf{a}^i$, then $u_i = V_i^j \tilde{u}_j$. Indeed, these two transformations are inverses as seen by:

$$\Lambda_k^i V_i^j = (\mathbf{e}^i \cdot \mathbf{a}_k) (\mathbf{a}^j \cdot \mathbf{e}_i) = \mathbf{a}^j \cdot (\mathbf{e}^i \cdot \mathbf{a}_k) \mathbf{e}_i = \mathbf{a}^j \cdot \mathbf{a}_k = \delta_k^j. \quad (3.16)$$

Before proceeding with further derivation, we present the following Kronecker relationship

that is used generously throughout this, and later, sections. In particular, this relationship relates covariant and contravariant tensor components through a sign change on a product rule. In particular,

$$(\mathbf{a}^\alpha \cdot \mathbf{a}_\beta)_{,\lambda} = (\delta_\beta^\alpha)_{,\lambda} \quad \Rightarrow \quad \mathbf{a}^\alpha \cdot \mathbf{a}_{\beta,\lambda} = -\mathbf{a}^\alpha_{,\lambda} \cdot \mathbf{a}_\beta \quad (3.17)$$

and similarly for \mathbf{a}_3 .

Since we now have the mathematical machinery to compute lengths, and areas, in the parametric frame, the natural next step is to develop the machinery to compute various derivatives in this frame. Through this notation, we define the **surface gradient** [18, §95], the gradient of a scalar, vector, or tensor quantity along the manifold, via

$$\begin{aligned} \text{Scalar:} \quad \underline{\nabla} u &= u_{,\alpha} \mathbf{a}^\alpha \\ \text{Vector:} \quad \underline{\nabla} \mathbf{u} &= \mathbf{u}_{,\alpha} \otimes \mathbf{a}^\alpha \\ \text{Tensor:} \quad \underline{\nabla} \mathbf{T} &= \mathbf{T}_{,\alpha} \otimes \mathbf{a}^\alpha \end{aligned} \quad (3.18)$$

We can thus express the directional derivative along a manifold coordinate through the **left** or **right compositions** of the following tensor relationships

$$\begin{aligned} \text{Scalar:} \quad \underline{\nabla} u \cdot \mathbf{a}_\alpha & \\ \text{Vector:} \quad \mathbf{u}_{,\alpha} &= (\underline{\nabla} \mathbf{u}) \mathbf{a}_\alpha \\ \text{Tensor:} \quad \mathbf{T}_{,\alpha} &= (\underline{\nabla} \mathbf{T}) \mathbf{a}_\alpha \end{aligned} \quad (3.19)$$

This elucidates the definition of **surface divergence** for vector and tensor-valued fields as the trace of the surface gradient via

$$\begin{aligned} \text{Vector:} \quad \underline{\nabla} \cdot \mathbf{u} &= \mathbf{u}_{,\alpha} \cdot \mathbf{a}^\alpha = \mathbf{a}^\alpha \cdot (\underline{\nabla} \mathbf{u}) \cdot \mathbf{a}_\alpha \\ \text{Tensor:} \quad \underline{\nabla} \cdot \mathbf{T} &= \mathbf{T}_{,\alpha} \cdot \mathbf{a}^\alpha = \mathbf{a}^\alpha \cdot (\underline{\nabla} \mathbf{T}) \cdot \mathbf{a}_\alpha \end{aligned} \quad (3.20)$$

The “.” operation denotes the standard Euclidean “dot” product, which is analogously defined for higher ordered tensors, e.g., “:” operation for 2^{nd} -ordered tensors, etc, all of which fall in the tensor operation of **contraction**. We reserve this notation purely for operations between tensor

entities resulting in a scalar, with the exception of tensor divergence. In all other instances, we use the left and right composition operations. These operations together are used to describe the PDEs presented in the following sections that are considered throughout this dissertation.

The intrinsic curvature present in the general manifold causes the locally defined basis to vary at each point (ξ^1, ξ^2) . Intuitively, the components of a vector represented in the basis defined at the point $\xi_0 \in \hat{\Omega}$ do not describe the same vector in terms of the basis at some other point $\xi_1 \in \hat{\Omega}$. Consequently, the concept of parallel transport is no longer naturally present in the new basis and the Cartesian notion of component-wise differentiation of vectors is no longer valid. To motivate the forthcoming derivations, we consider the derivative of a vector \mathbf{u} expressed in our newly-constructed frame:

$$\begin{aligned}
\mathbf{u}_{,\beta} &= (\tilde{u}_\alpha \mathbf{a}^\alpha + u_3 \mathbf{a}^3)_{,\beta} \\
&= \tilde{u}_{\alpha,\beta} \mathbf{a}^\alpha + \tilde{u}_\alpha \mathbf{a}_{,\beta}^\alpha + \tilde{u}_{3,\beta} \mathbf{a}^3 + \tilde{u}_3 \mathbf{a}_{,\beta}^3 \\
&= \tilde{u}_{\alpha,\beta} \mathbf{a}^\alpha + \tilde{u}_\lambda \left((\mathbf{a}_{,\beta}^\lambda \cdot \mathbf{a}_\alpha) \mathbf{a}^\alpha + (\mathbf{a}_{,\beta}^\lambda \cdot \mathbf{a}_3) \mathbf{a}^3 \right) + \tilde{u}_{3,\beta} \mathbf{a}^3 + \tilde{u}_3 (\mathbf{a}_{,\beta}^3 \cdot \mathbf{a}_\alpha) \mathbf{a}^\alpha \\
&= \left[\tilde{u}_{\alpha,\beta} + \tilde{u}_\lambda (\mathbf{a}_{,\beta}^\lambda \cdot \mathbf{a}_\alpha) + \tilde{u}_3 (\mathbf{a}_{,\beta}^3 \cdot \mathbf{a}_\alpha) \right] \mathbf{a}^\alpha + \left[\tilde{u}_\lambda (\mathbf{a}_{,\beta}^\lambda \cdot \mathbf{a}_3) + \tilde{u}_{3,\beta} \right] \mathbf{a}^3 \tag{3.21} \\
&= \left[\tilde{u}_{\alpha,\beta} - \tilde{u}_\lambda (\mathbf{a}^\lambda \cdot \mathbf{a}_{\alpha,\beta}) - \tilde{u}_3 (\mathbf{a}^3 \cdot \mathbf{a}_{\alpha,\beta}) \right] \mathbf{a}^\alpha + \left[\tilde{u}_\lambda (a^{\lambda\mu} \mathbf{a}_{\mu,\beta} \cdot \mathbf{a}_3) + \tilde{u}_{3,\beta} \right] \mathbf{a}^3 \\
&= \left[\tilde{u}_{\alpha,\beta} - \Gamma_{\alpha\beta}^\lambda \tilde{u}_\lambda - \tilde{u}_3 b_{\alpha\beta} \right] \mathbf{a}^\alpha + \left[\tilde{u}_\lambda (a^{\lambda\mu} b_{\mu\beta}) + \tilde{u}_{3,\beta} \right] \mathbf{a}^3 \\
&= [\tilde{u}_{\alpha|\beta} - b_{\alpha\beta} \tilde{u}_3] \mathbf{a}^\alpha + [b_\beta^\lambda \tilde{u}_\lambda + \tilde{u}_{3,\beta}] \mathbf{a}^3
\end{aligned}$$

Several terms have been introduced, in the derivation above. The terms $\Gamma_{\alpha\beta}^\lambda$ are known as the **Christoffel symbols of the second kind** which quantify how the basis changes in plane with respect to either parametric direction. Since a manifold is not a linear space, the Christoffel symbols define an **affine connection**, that is, the affine deviation between two nearby tangent spaces on a manifold. These entities are defined via

$$\Gamma_{\alpha\beta}^\lambda = \mathbf{a}^\lambda \cdot \mathbf{a}_{\alpha,\beta} \tag{3.22}$$

and appear in the **covariant derivative** of tensorial components, denoted via ‘|’ in the index

position. For example,

$$\tilde{u}_{\alpha|\beta} = \tilde{u}_{\alpha,\beta} - \Gamma_{\alpha\beta}^{\lambda} \tilde{u}_{\lambda} \quad (3.23)$$

The covariant derivative is the curvilinear analogue of the derivative of Cartesian vector components namely, it describes how the covariant components lying in the $\mathbf{a}_1\mathbf{a}_2$ -plane change with respect to either parametric direction.

While the metric tensor provides a notion of length and distance in the curvilinear frame, the term $b_{\alpha\beta}$, known as the **second fundamental form** or **curvature tensor**, describes intrinsic curvature in the manifold by measuring the rotational changes in \mathbf{a}_3 . The covariant components of the second fundamental form are given by:

$$b_{\alpha\beta} = \mathbf{a}_3 \cdot \mathbf{a}_{\alpha,\beta} = -\mathbf{a}_{3,\beta} \cdot \mathbf{a}_{\alpha}. \quad (3.24)$$

Note that the covariant components of the second fundamental form are symmetric i.e. $b_{\alpha\beta} = b_{\beta\alpha}$. Equivalently, the second fundamental form can be expressed in terms of mixed covariant-contravariant components. These components can be obtained through the index raising operation. For example, the mixed contravariant-covariant components of the second fundamental form are given by:

$$b^{\alpha}_{\beta} = a^{\alpha\mu} b_{\mu\beta} \quad (3.25)$$

Here we have implicitly introduced the notation of the “.” in the index position, that establishes an ordering in indexed quantities. This is helpful for tensor construction as well as left and right composition operations which are used extensively in the derivations of the linearized Kirchhoff-Love shell. Lastly, the covariant components of the **third fundamental form** provide an alternative measure of curvature and are given by:

$$c_{\alpha\beta} = b_{\alpha\mu} b^{\mu}_{\beta} \quad (3.26)$$

The notion of the covariant derivative generalizes to higher-ordered tensors as well. For example, consider the derivative of the curvature tensor

$$\begin{aligned}
\mathbf{b}_{,\lambda} &= \left(b_{\alpha\beta} \mathbf{a}^\alpha \otimes \mathbf{a}^\beta \right)_{,\lambda} \\
&= b_{\alpha\beta,\lambda} \mathbf{a}^\alpha \otimes \mathbf{a}^\beta + b_{\alpha\beta} \mathbf{a}_{,\lambda}^\alpha \otimes \mathbf{a}^\beta + b_{\alpha\beta} \mathbf{a}^\alpha \otimes \mathbf{a}_{,\lambda}^\beta \\
&= b_{\alpha\beta,\lambda} \mathbf{a}^\alpha \otimes \mathbf{a}^\beta + b_{\mu\beta} \left[\left(\mathbf{a}_{,\lambda}^\mu \cdot \mathbf{a}_\alpha \right) \mathbf{a}^\alpha + \left(\mathbf{a}_{,\lambda}^\mu \cdot \mathbf{a}_3 \right) \mathbf{a}^3 \right] \otimes \mathbf{a}^\beta \\
&\quad + b_{\alpha\mu} \mathbf{a}^\alpha \otimes \left[\left(\mathbf{a}_{,\lambda}^\mu \cdot \mathbf{a}_\beta \right) \mathbf{a}^\beta + \left(\mathbf{a}_{,\lambda}^\mu \cdot \mathbf{a}_3 \right) \mathbf{a}^3 \right] \\
&= \left(b_{\alpha\beta,\lambda} - \Gamma_{\alpha\lambda}^\mu b_{\mu\beta} - \Gamma_{\beta\lambda}^\mu b_{\alpha\mu} \right) \mathbf{a}^\alpha \otimes \mathbf{a}^\beta + b_{,\lambda}^\mu b_{\mu\beta} \mathbf{a}^3 \otimes \mathbf{a}^\beta + b_{,\lambda}^\mu b_{\alpha\mu} \mathbf{a}^\alpha \otimes \mathbf{a}^3 \\
&= b_{\alpha\beta|\lambda} \mathbf{a}^\alpha \otimes \mathbf{a}^\beta + c_{\lambda\beta} \mathbf{a}^3 \otimes \mathbf{a}^\beta + c_{\alpha\lambda} \mathbf{a}^\alpha \otimes \mathbf{a}^3
\end{aligned} \tag{3.27}$$

Note that similar expressions exist for tensors expressed in mixed and contravariant components, however there is typically a sign change associated with the index position in the covariant derivative and a metric tensor for out-of-plane components. For instance,

$$b_{,\beta|\lambda}^\alpha = b_{\beta,\lambda}^\alpha + \Gamma_{\mu\lambda}^\alpha b_{,\beta}^\mu - \Gamma_{\beta\lambda}^\mu b_{\alpha\mu} \tag{3.28}$$

and similarly for tensors of higher order. In the setting of Cartesian analyses, many of these differential geometric entities vanish since the parametric basis coincides with the standard basis. However for the study of PDEs posed over a manifold, these entities are of great importance for both analysis and implementation.

Chapter 4

Continuum Mechanics

Before proceeding forth with more complex derivations of Nitsche’s method, we digress to a brief discussion of continuum mechanics, particularly the stress and strain measures employed as well as the notation which will be carried throughout the remainder of the dissertation.

Continuum mechanics is grounded in elasticity theory where strain measures, constitutive relationships, and Newton’s 2^{nd} law serve as a surrogate to the displacement field \mathbf{u} . Namely, derivatives of the displacement field represent strains which, with a constitutive relationship, determine internal stresses due to external loadings. A wide range of strain measures exist however for shell theory, and more generally finite element theory, the Green-Lagrange strain measure is typically employed. This choice is made since the Green-Lagrange strain tensor and the 2^{nd} Kirchhoff-Piola stress tensor are energetically conjugate which has a natural foundation in variational formulations which seek the displacement configuration that minimizes the potential energy.

The differential geometric discussion in Chapter 3 pertains to the two-dimensional “midsurface” of the shell body. However, to obtain accurate strain measurements, we need a parameterization of the linear elastic body \mathcal{B} itself. To this end, we are able to arrive at a parametrization of any structural member considered in this dissertation through the following relationships:

$$\begin{aligned} \text{Linear Elasticity:} \quad & \mathbf{X}_{LE}(\xi^1, \xi^2) = \mathbf{x}(\xi^1, \xi^2) \\ \text{Kirchhoff-Love Plate:} \quad & \mathbf{X}_{KLP}(\xi^1, \xi^2, \xi^3) = \mathbf{x}(\xi^1, \xi^2) + \xi^3 \mathbf{e}^3(\xi^1, \xi^2) \\ \text{Kirchhoff-Love Shell:} \quad & \mathbf{X}_{KLS}(\xi^1, \xi^2, \xi^3) = \mathbf{x}(\xi^1, \xi^2) + \xi^3 \mathbf{a}^3(\xi^1, \xi^2) \end{aligned} \tag{4.1}$$

where $\mathbf{x}(\xi^1, \xi^2)$ is the push-forward parametrization of the structural member, describing the mid-surface of the body while ξ^3 is the parametric variable designating the through-thickness direction of the elastic body along the midsurface normal director. Note that the linear elasticity model is equivalent to \mathbf{x} because we assume through all of our structural analyses that these members are in a **plane stress** state. In particular, through-thickness stresses are negligible in comparison to the in-plane counterpart. Analogously to the exposition of Chapter 3, we can define a curvilinear frame for the elastic body which we will utilize in the computation of stresses and strains. For example, these vectors are given for the Kirchhoff-Love shell by:

$$\mathbf{g}_\alpha = \frac{\partial \mathbf{X}}{\partial \xi^\alpha} = \mathbf{a}_\alpha + \xi^3 \mathbf{a}_{3,\alpha} = \left(\delta_\alpha^\beta - \xi^3 b_{\cdot\alpha}^\beta \right) \mathbf{a}_\beta \quad \text{and} \quad \mathbf{g}_3 = \frac{\partial \mathbf{X}}{\partial \xi^3} = \mathbf{a}_3 \quad (4.2)$$

and therefore, the covariant components of the metric tensor associated with this parametrization is given via

$$g_{\alpha\beta} = \mathbf{g}_\alpha \cdot \mathbf{g}_\beta \quad \text{and} \quad g_{33} = 1 \quad \text{and} \quad g_{\alpha 3} = g_{3\alpha} = 0 \quad (4.3)$$

Proceeding forward with our strain measure, we assume there exists a smooth, bijective mapping $\tilde{\mathbf{X}}(\boldsymbol{\xi}) = \tilde{\mathbf{X}}(\mathbf{X}(\boldsymbol{\xi}))$ between $\tilde{\mathbf{X}}$, the deformed configuration $\tilde{\mathcal{B}}$, and \mathbf{X} , the undeformed configuration \mathcal{B} . Through the derivatives of this mapping, we obtain the entity known as the **deformation gradient** which is given by:

$$\mathbf{F} \equiv \frac{\partial \tilde{\mathbf{X}}}{\partial \mathbf{X}} = \frac{\partial \tilde{\mathbf{X}}}{\partial \xi^i} \frac{\partial \xi^i}{\partial \mathbf{X}} = \tilde{\mathbf{g}}_i \otimes \mathbf{g}^i. \quad (4.4)$$

While one may utilize any other pair of conjugate stress-strain measures, herein we consider the Green-Lagrange strain measure given by:

$$\mathbf{E} = \frac{1}{2} (\mathbf{R} - \mathbf{I}) = \frac{1}{2} (\mathbf{F}^T \mathbf{F} - \mathbf{I}) \quad (4.5)$$

where $\mathbf{R} = \mathbf{F}^T \mathbf{F}$ is the **Right Cauchy strain tensor**. Utilizing (4.4) we obtain:

$$\mathbf{E} = \frac{1}{2} ((\mathbf{g}^i \otimes \tilde{\mathbf{g}}_i)(\tilde{\mathbf{g}}_j \otimes \mathbf{g}^j) - \mathbf{I}) = \frac{1}{2} (g_{ij} - \tilde{g}_{ij}) \mathbf{g}^i \otimes \mathbf{g}^j \equiv E_{ij} \mathbf{g}^i \otimes \mathbf{g}^j. \quad (4.6)$$

Observe that the coefficients E_{ij} are in fact a function of the, yet to be defined, displacement field \mathbf{U} . In particular,

$$\tilde{\mathbf{g}}_i = \frac{\partial \tilde{\mathbf{X}}}{\partial \xi^i} = \frac{\partial (\mathbf{X} + \mathbf{U})}{\partial \xi^i} = \mathbf{g}_i + \mathbf{U}_{,i} \quad (4.7)$$

and moreover, utilizing (4.7) with (4.3) and substituting into (4.6), the Green-Lagrange strain tensor coefficients reduce to

$$E_{ij}(\mathbf{U}) = \frac{1}{2} \left(\frac{\partial \mathbf{U}}{\partial \xi^i} \cdot \mathbf{g}_j + \frac{\partial \mathbf{U}}{\partial \xi^j} \cdot \mathbf{g}_i + \frac{\partial \mathbf{U}}{\partial \xi^i} \cdot \frac{\partial \mathbf{U}}{\partial \xi^j} \right) \approx \frac{1}{2} \left(\frac{\partial \mathbf{U}}{\partial \xi^i} \cdot \mathbf{g}_j + \frac{\partial \mathbf{U}}{\partial \xi^j} \cdot \mathbf{g}_i \right) \quad (4.8)$$

where the nonlinear dependencies have been neglected, effectively linearizing the tensor coefficients. For notational ease in forthcoming derivations, we introduce the **symmetrized gradient** of the displacement field, which is in fact equivalent to the **linearized Green-Lagrange strain tensor**

$$\varepsilon_{ij}(\mathbf{U}) \equiv \underline{\nabla} \mathbf{U} = \frac{1}{2} \left(\frac{\partial \mathbf{U}}{\partial \xi^i} \cdot \mathbf{g}_j + \frac{\partial \mathbf{U}}{\partial \xi^j} \cdot \mathbf{g}_i \right). \quad (4.9)$$

Our theory of elastic models proceeds with the **Reissner-Mindlin kinematical assumption**, that is the displacement field of the entire elastic body takes the form of a translational midsurface displacement and a through-thickness midsurface rotation. In particular,

$$\begin{aligned} \text{Linear Elasticity:} \quad & \mathbf{U}_{LE}(\xi^1, \xi^2, \xi^3) = \underline{\mathbf{u}}(\xi^1, \xi^2) \\ \text{Kirchhoff-Love Plate:} \quad & \mathbf{U}_{KLP}(\xi^1, \xi^2, \xi^3) = u_3(\xi^1, \xi^2) \mathbf{a}^3 + \xi^3 \underline{\theta}(\xi^1, \xi^2) \\ \text{Kirchhoff-Love Shell:} \quad & \mathbf{U}_{KLS}(\xi^1, \xi^2, \xi^3) = \mathbf{u}(\xi^1, \xi^2) + \xi^3 \underline{\theta}(\xi^1, \xi^2) \end{aligned} \quad (4.10)$$

where $\mathbf{u}(\xi^1, \xi^2)$ is a translational displacement of the midsurface while $\underline{\theta}(\xi^1, \xi^2) = \tilde{\theta}_\lambda \mathbf{a}^\lambda$ is a rotational displacement of the midsurface normal director \mathbf{a}^3 . It is worth mentioning that the rotational displacement $\underline{\theta}$ can be represented by a surface tensor due to the inextensibility of the midsurface normal director \mathbf{a}^3 . Note, we only use $\underline{\theta}$ as a variable to enforce the Kirchhoff-Love constraint in

the following sections, it is not present in the numerical implementation. Furthermore, note that the Kirchhoff-Love shell is the agglomeration of the linear-elastic and plate displacement profiles defined over a curved manifold, a theme that is carried throughout our derivations allowing us to establish theory of these elastic models in a hierarchical manner.

We now proceed with deriving the corresponding strain measures from these prescribed displacement profiles. In particular, we substitute each of the displacement fields (4.10) into (4.9). We demonstrate this explicitly here only for the Kirchhoff-Love shell, since it encompasses both the linear-elastic setting and the Kirchhoff-Love plate. Observe,

$$\begin{aligned}
\varepsilon_{\alpha\beta}(\mathbf{U}_{KLS}) &= \frac{1}{2} [\mathbf{U}_{,\alpha} \cdot \mathbf{g}_\beta + \mathbf{U}_{,\beta} \cdot \mathbf{g}_\alpha] \\
&= \frac{1}{2} \left[(\mathbf{u}_{,\alpha} + \xi^3 \underline{\theta}_{,\alpha}) \cdot (\delta_\beta^\lambda - \xi^3 b_{,\beta}^\lambda) \mathbf{a}_\lambda + (\mathbf{u}_{,\beta} + \xi^3 \underline{\theta}_{,\beta}) \cdot (\delta_\alpha^\lambda - \xi^3 b_{,\alpha}^\lambda) \mathbf{a}_\lambda \right] \\
&= \frac{1}{2} (\mathbf{u}_{,\alpha} \cdot \mathbf{a}_\beta + \mathbf{u}_{,\beta} \cdot \mathbf{a}_\alpha) + \frac{\xi}{2} (\underline{\theta}_{,\alpha} \cdot \mathbf{a}_\beta + \underline{\theta}_{,\beta} \cdot \mathbf{a}_\alpha - \mathbf{u}_{,\alpha} \cdot b_{,\beta}^\lambda \mathbf{a}_\lambda - \mathbf{u}_{,\beta} \cdot b_{,\alpha}^\lambda \mathbf{a}_\lambda) \\
&\quad - \frac{(\xi^3)^2}{2} (\underline{\theta}_{,\alpha} \cdot b_{,\beta}^\lambda \mathbf{a}_\lambda + \underline{\theta}_{,\beta} \cdot b_{,\alpha}^\lambda \mathbf{a}_\lambda) \\
&= \gamma_{\alpha\beta}(\mathbf{u}) + \xi^3 \kappa_{\alpha\beta}(\mathbf{u}, \underline{\theta}) + (\xi^3)^2 \chi_{\alpha\beta}(\underline{\theta}).
\end{aligned} \tag{4.11}$$

Given a displacement field \mathbf{u} , the tensorial components $\gamma_{\alpha\beta}(\mathbf{u})$ correspond to membrane strains in the shell body, the components $\kappa_{\alpha\beta}(\mathbf{u})$ correspond to bending strains in the shell body, and the components $\chi_{\alpha\beta}(\mathbf{u})$ correspond to through-thickness shearing strains due to nonlinear material normal deformations. As we will demonstrate shortly, we express the rotational degrees of freedom in terms of the translational displacement field i.e. $\underline{\theta} = \underline{\theta}(\mathbf{u})$, through the Kirchhoff-Love assumption that the deformed midsurface normal director remains orthogonal to the deformed midsurface. An additional Kirchhoff-Love assumption is that the deformed midsurface normal director is **straight**, hence we discard the term $\chi_{\alpha\beta}(\mathbf{u})$, which is nonlinear in ξ^3 .

We now derive the tensor form of the membrane and bending strains for later use in devising a Galerkin Nitsche formulation. Proceeding forward, we have for the membrane strain:

$$\begin{aligned}
\gamma_{\alpha\beta}(\mathbf{u}) &= \frac{1}{2} [\mathbf{u}_{,\alpha} \cdot \mathbf{a}_\beta + \mathbf{u}_{,\beta} \cdot \mathbf{a}_\alpha] \\
&= \frac{1}{2} [((\nabla \mathbf{u}) \mathbf{a}_\alpha) \cdot \mathbf{a}_\beta + ((\nabla \mathbf{u}) \mathbf{a}_\beta) \cdot \mathbf{a}_\alpha] \\
&= \frac{1}{2} [\mathbf{a}_\alpha \cdot (\nabla \mathbf{u})^T \cdot \mathbf{a}_\beta + \mathbf{a}_\alpha \cdot (\nabla \mathbf{u}) \cdot \mathbf{a}_\beta] \\
&= \mathbf{a}_\alpha \cdot \frac{1}{2} [(\nabla \mathbf{u})^T + (\nabla \mathbf{u})] \cdot \mathbf{a}_\beta.
\end{aligned} \tag{4.12}$$

Hence the membrane strain tensor is given by:

$$\underline{\underline{\gamma}}(\mathbf{u}) = \nabla^s \mathbf{u} = \frac{1}{2} [(\nabla \mathbf{u})^T + (\nabla \mathbf{u})]. \tag{4.13}$$

Furthermore, the bending strain:

$$\begin{aligned}
\kappa_{\alpha\beta}(\mathbf{u}, \underline{\theta}) &= \frac{1}{2} [\underline{\theta}_{,\alpha} \cdot \mathbf{a}_\beta + \underline{\theta}_{,\beta} \cdot \mathbf{a}_\alpha - \mathbf{u}_{,\alpha} \cdot b_{,\beta}^\lambda \mathbf{a}_\lambda - \mathbf{u}_{,\beta} \cdot b_{,\alpha}^\lambda \mathbf{a}_\lambda] \\
&= \frac{1}{2} [((\nabla \underline{\theta}) \mathbf{a}_\alpha) \cdot \mathbf{a}_\beta + ((\nabla \underline{\theta}) \mathbf{a}_\beta) \cdot \mathbf{a}_\alpha - ((\nabla \mathbf{u}) \mathbf{a}_\alpha) \cdot (\underline{\underline{b}} \mathbf{a}_\beta) - ((\nabla \mathbf{u}) \mathbf{a}_\beta) \cdot (\underline{\underline{b}} \mathbf{a}_\alpha)] \\
&= \frac{1}{2} [\mathbf{a}_\alpha \cdot (\nabla \underline{\theta})^T \cdot \mathbf{a}_\beta + \mathbf{a}_\alpha \cdot (\nabla \underline{\theta}) \cdot \mathbf{a}_\beta - \mathbf{a}_\alpha \cdot (\nabla \mathbf{u})^T \underline{\underline{b}} \cdot \mathbf{a}_\beta - \mathbf{a}_\alpha \cdot \underline{\underline{b}}^T (\nabla \mathbf{u}) \cdot \mathbf{a}_\beta] \\
&= \mathbf{a}_\alpha \cdot \frac{1}{2} [(\nabla \underline{\theta})^T + (\nabla \underline{\theta}) - (\nabla \mathbf{u})^T \underline{\underline{b}} - \underline{\underline{b}}^T (\nabla \mathbf{u})] \cdot \mathbf{a}_\beta
\end{aligned} \tag{4.14}$$

Therefore, the bending strain tensor is given by:

$$\underline{\underline{\kappa}}(\mathbf{u}) = \nabla^s \underline{\theta} - \frac{1}{2} [(\nabla \mathbf{u})^T \underline{\underline{b}} + \underline{\underline{b}}^T (\nabla \mathbf{u})] \tag{4.15}$$

The transverse shearing strain components are given via:

$$\begin{aligned}
\zeta_\alpha(\mathbf{U}_{KLS}) &= \varepsilon_{\alpha 3}(\mathbf{U}_{KLS}) \\
&= \frac{1}{2} (\mathbf{U}_{,\alpha} \cdot \mathbf{g}_3 + \mathbf{U}_{,3} \cdot \mathbf{g}_\alpha) \\
&= \frac{1}{2} [(\mathbf{u}_{,\alpha} + \xi^3 \underline{\theta}_{,\alpha}) \cdot \mathbf{a}_3 + \underline{\theta} \cdot (\delta_\alpha^\lambda - \xi^3 b_{,\alpha}^\lambda) \mathbf{a}_\lambda].
\end{aligned} \tag{4.16}$$

Note that since $\underline{\theta} = \theta_\alpha \mathbf{a}^\alpha$ it follows that:

$$\underline{\theta}_{,\alpha} \cdot \mathbf{a}_3 = (\theta_{\lambda,\alpha} \mathbf{a}^\lambda + b_{,\lambda}^\mu \theta_\mu \mathbf{a}^3) \cdot \mathbf{a}_3 = b_{,\lambda}^\mu \theta_\mu \tag{4.17}$$

hence (4.16) reduces to:

$$\underline{\underline{\zeta}}(\mathbf{U}_{KLS}) = \frac{1}{2} (\mathbf{a}_3^T (\nabla \mathbf{u}) + \underline{\theta}) \otimes \mathbf{a}^3. \quad (4.18)$$

Lastly, note the out-of-plane strains vanish due to the inextensibility of the midsurface normal director imposed in our parametrization:

$$\varepsilon_{33}(\mathbf{U}_{KLS}) = \mathbf{U}_{,3} \cdot \mathbf{g}_3 = \underline{\theta} \cdot \mathbf{a}_3 = 0. \quad (4.19)$$

Repeating this process for the remaining linear elastic membrane and Kirchhoff-Love plate gives rise to the following summarizing table of strains:

	Linear Elasticity	Kirchhoff-Love Plate	Kirchhoff-Love Shell
in-plane	$\underline{\nabla}^s \underline{u}$	$\xi^3 \underline{\nabla}^s \underline{\theta}$	$\underline{\nabla}^s \mathbf{u} + \frac{\xi^3}{2} \underline{\nabla}^s \underline{\theta} - \frac{\xi^3}{2} \left((\underline{\nabla} \mathbf{u})^T \underline{\underline{b}} + \underline{\underline{b}}^T (\underline{\nabla} \mathbf{u}) \right)$
transverse shear	0	$\frac{1}{2} (\underline{\nabla} u_3 + \underline{\theta})$	$\frac{1}{2} (\mathbf{a}_3^T (\underline{\nabla} \mathbf{u}) + \underline{\theta})$
out-of-plane	0	0	0

(4.20)

However, we are unfinished with the derivation of the strains. The Kirchhoff-Love kinematical assumption is that material normals remain straight and normal to the deformed material, e.g. $\zeta_\alpha = \varepsilon_{\alpha 3} = \varepsilon_{3\alpha} = 0$. This introduces a constraint on the rotational degrees of freedom as follows

Kirchhoff-Love Plate	Kirchhoff-Love Shell
$\underline{\theta} = -\underline{\nabla} u_3$	$\underline{\theta} = -\mathbf{a}_3^T (\underline{\nabla} \mathbf{u})$

(4.21)

which we then substitute back into (4.20) and, through algebraic simplification, we obtain the following strain fields:

Linear Elasticity	Kirchhoff-Love Plate	Kirchhoff-Love Shell
$\underline{\nabla}^s \underline{u}$	$-\xi^3 \underline{\nabla}^s \underline{\nabla} u_3$	$\underline{\nabla}^s \mathbf{u} - \frac{\xi^3}{2} \left(\mathbf{a}_3^T (\underline{\nabla} \underline{\nabla} \mathbf{u}) + (\underline{\nabla} \underline{\nabla} \mathbf{u})^T \mathbf{a}_3 \right)$

(4.22)

where, $\underline{\nabla} \underline{\nabla} \mathbf{u} = \mathbf{u}_{,\alpha\beta} \otimes \mathbf{a}^\alpha \otimes \mathbf{a}^\beta - \Gamma_{\alpha\beta}^\lambda \mathbf{u}_{,\lambda} \otimes \mathbf{a}^\alpha \otimes \mathbf{a}^\beta$, and with a slight abuse of notation, we define $(\underline{\nabla} \underline{\nabla} \mathbf{u})^T = \mathbf{a}^\alpha \otimes \mathbf{a}^\beta \otimes \mathbf{u}_{,\alpha\beta} - \mathbf{a}^\alpha \otimes \mathbf{a}^\beta \otimes \Gamma_{\alpha\beta}^\lambda \mathbf{u}_{,\lambda}$ for our Cartesian displacement field.

Since a boundary rotation does not necessarily coincide with a normal derivate due to intrinsic manifold curvatures in the shell setting, in order to maintain energetic conjugacy throughout our derivations, it is necessary to define the following boundary quantities:

$$\begin{array}{cc} \text{Normal Rotation} & \text{Twisting Rotation} \\ \hline \theta_n(\mathbf{u}) := \underline{\theta}(\mathbf{u}) \cdot \underline{n} & \theta_t(\mathbf{u}) := \underline{\theta}(\mathbf{u}) \cdot \underline{t} \end{array} \quad (4.23)$$

We are then able to develop a unified notation which we define in the context of the shell but employ throughout our discussion of these three models. The linear elasticity model provides the strain field associated with in-plane displacements due to in-plane loadings, i.e. membrane action. On the other hand, our Kirchhoff-Love plate model provides the strain field associated with transverse displacements due to transverse loadings, i.e. bending action. Therefore, we define the membrane and bending tensors via:

$$\begin{array}{cc} \text{Membrane Strain} & \text{Bending Strain} \\ \hline \underline{\underline{\gamma}}(\mathbf{u}) := \underline{\nabla}^s \mathbf{u} & \underline{\underline{\kappa}}(\mathbf{u}) := -\frac{1}{2} \left(\mathbf{a}_3^T (\underline{\nabla} \underline{\nabla} \mathbf{u}) + (\underline{\nabla} \underline{\nabla} \mathbf{u})^T \mathbf{a}_3 \right). \end{array} \quad (4.24)$$

Note that in the case of zero curvature, the membrane and bending strain tensors of the Kirchhoff-Love shell coincide with the linear elastic and Kirchhoff-Love plate models, respectively, precisely how we've defined the flat counterparts to these tensors. In particular, $\underline{\underline{\gamma}}^{(\text{flat})}(\mathbf{u}) := \underline{\nabla}^s \mathbf{u}$ and $\underline{\underline{\kappa}}^{(\text{flat})}(\mathbf{u}) := -\underline{\nabla}^s \underline{\nabla} u_3$. Therefore, it is expected that studying the behavior of these simpler models will aid us in inferring behavior of the entire Kirchhoff-Love shell. From these definitions, it follows that we can decompose the Green-Lagrange strain tensor into a membrane component lying in the midsurface model and a bending component which varies linearly through-thickness. In particular:

$$\underline{\underline{\varepsilon}}(\mathbf{u}) = \underline{\underline{\gamma}}(\mathbf{u}) + \xi^3 \underline{\underline{\kappa}}(\mathbf{u}). \quad (4.25)$$

At this point, it is worthwhile to define the energetically-conjugate stresses for both the membrane and bending strain tensors. Since both of these quantities require a material law in their definition, we present the following linear constitutive model which we employ in our mathematics:

$$\mathbb{C} = \mathbb{C}^{\alpha\beta\lambda\mu} \mathbf{a}_\alpha \otimes \mathbf{a}_\beta \otimes \mathbf{a}_\lambda \otimes \mathbf{a}_\mu \quad \text{where} \quad \mathbb{C}^{\alpha\beta\lambda\mu} = \frac{E}{2(1+\nu)} \left(a^{\alpha\lambda} a^{\beta\mu} + a^{\alpha\mu} a^{\beta\lambda} + \frac{2\nu}{1-\nu} a^{\alpha\beta} a^{\lambda\mu} \right) \quad (4.26)$$

where E is Young's modulus and ν is Poisson's ratio. Note here we have adopted the blackboard notation for the constitutive law, since it is a fourth-order tensor, and although it is a surface entity, four underlines is overbearing. Through this constitutive law we can define the strain energy as a function of displacement. In particular, the strain energy is the integral of the stress-strain contraction over the three-dimensional body. Substituting (4.25) into this relationship yields:

$$\begin{aligned} \|\|\mathbf{u}\|\|^2 &:= \frac{1}{2} \int_{\mathcal{B}} \boldsymbol{\sigma}(\mathbf{u}) : \boldsymbol{\varepsilon}(\mathbf{u}) \, d\mathcal{B} \\ &= \frac{1}{2} \int_{\mathcal{B}} \boldsymbol{\varepsilon}(\mathbf{u}) : \mathbb{C} : \boldsymbol{\varepsilon}(\mathbf{u}) \, d\mathcal{B} \\ &= \frac{1}{2} \int_{\mathcal{B}} \left(\underline{\underline{\gamma}}(\mathbf{u}) + \xi^3 \underline{\underline{\kappa}}(\mathbf{u}) \right) : \mathbb{C} : \left(\underline{\underline{\gamma}}(\mathbf{u}) + \xi^3 \underline{\underline{\kappa}}(\mathbf{u}) \right) \, d\mathcal{B} \\ &= \frac{1}{2} \left[\int_{\mathcal{B}} \underline{\underline{\gamma}}(\mathbf{u}) : \mathbb{C} : \underline{\underline{\gamma}}(\mathbf{u}) \, d\mathcal{B} + 2 \int_{\mathcal{B}} \xi^3 \underline{\underline{\gamma}}(\mathbf{u}) : \mathbb{C} : \underline{\underline{\kappa}}(\mathbf{u}) \, d\mathcal{B} + \int_{\mathcal{B}} (\xi^3)^2 \underline{\underline{\kappa}}(\mathbf{u}) : \mathbb{C} : \underline{\underline{\kappa}}(\mathbf{u}) \, d\mathcal{B} \right] \\ &= \frac{1}{2} \left[\int_{\Omega} \left[\int_{-\eta/2}^{\eta/2} \underline{\underline{\gamma}}(\mathbf{u}) : \mathbb{C} : \underline{\underline{\gamma}}(\mathbf{u}) \, d\xi^3 \right] d\Omega + 2 \int_{\Omega} \left[\int_{-\eta/2}^{\eta/2} \xi^3 \underline{\underline{\gamma}}(\mathbf{u}) : \mathbb{C} : \underline{\underline{\kappa}}(\mathbf{u}) \, d\xi^3 \right] d\Omega \right. \\ &\quad \left. + \int_{\Omega} \left[\int_{-\eta/2}^{\eta/2} (\xi^3)^2 \underline{\underline{\kappa}}(\mathbf{u}) : \mathbb{C} : \underline{\underline{\kappa}}(\mathbf{u}) \, d\xi^3 \right] d\Omega \right] \\ &= \frac{1}{2} \left[\eta \int_{\Omega} \underline{\underline{\gamma}}(\mathbf{u}) : \mathbb{C} : \underline{\underline{\gamma}}(\mathbf{u}) \, d\Omega + \frac{\eta^3}{12} \int_{\Omega} \underline{\underline{\kappa}}(\mathbf{u}) : \mathbb{C} : \underline{\underline{\kappa}}(\mathbf{u}) \, d\Omega \right] \\ &= \frac{1}{2} \int_{\Omega} \underline{\underline{\gamma}}(\mathbf{u}) : \mathbb{C}_M : \underline{\underline{\gamma}}(\mathbf{u}) \, d\Omega + \frac{1}{2} \int_{\Omega} \underline{\underline{\kappa}}(\mathbf{u}) : \mathbb{C}_B : \underline{\underline{\kappa}}(\mathbf{u}) \, d\Omega \\ &= \underbrace{\frac{1}{2} \int_{\Omega} \underline{\underline{A}}(\mathbf{u}) : \underline{\underline{\gamma}}(\mathbf{u}) \, d\Omega}_{\text{membrane energy}} + \underbrace{\frac{1}{2} \int_{\Omega} \underline{\underline{B}}(\mathbf{u}) : \underline{\underline{\kappa}}(\mathbf{u}) \, d\Omega}_{\text{bending energy}} \end{aligned} \quad (4.27)$$

Here we have defined the membrane and bending stresses via the relationships:

$$\begin{array}{cc}
\text{Membrane Stress} & \text{Bending Stress} \\
\hline
\underline{\underline{A}}(\mathbf{u}) := \mathbb{C}_A : \underline{\underline{\gamma}}(\mathbf{u}) & \underline{\underline{B}}(\mathbf{u}) := \mathbb{C}_B : \underline{\underline{\kappa}}(\mathbf{u})
\end{array} \tag{4.28}$$

where we have defined the constitutive laws for membrane and bending action as $\mathbb{C}_A = \eta\mathbb{C}$ and $\mathbb{C}_B = \frac{\eta^3}{12}\mathbb{C}$. Note that the cross-integrals between the the bending strain and membrane stress as well as the membrane strain and the bending stress vanish due to the integration through-thickness of a linear ξ^3 . We can use these relationships to define the energy norms for membrane and bending responses as:

$$\begin{array}{cc}
\text{Membrane Energy} & \text{Bending Energy} \\
\hline
\|\mathbf{u}\|_A^2 := \int_{\Omega} \underline{\underline{A}}(\mathbf{u}) : \underline{\underline{\gamma}}(\mathbf{u}) \, d\Omega & \|\mathbf{u}\|_B^2 := \int_{\Omega} \underline{\underline{B}}(\mathbf{u}) : \underline{\underline{\kappa}}(\mathbf{u}) \, d\Omega.
\end{array} \tag{4.29}$$

These quantities are physically twice the true energy however the definitions in this form simplify later exposition. In the following sections, we will use these energies with the principle of virtual work and the Euler-Lagrange equations to arrive at weak formulations for the PDEs considered. Moreover, we will also utilize these energies in the demonstration of continuity, coercivity, and error estimates for the proposed variational forms.

Chapter 5

Functional Analysis

Throughout this dissertation, we rely on tools emerging from functional analysis to state, derive, and prove properties of numerical methods. In this chapter, we provide the necessary ingredients for use in later chapters. Before proceeding with theorems used in later sections, we establish the notation that will be used throughout this dissertation. Let \mathcal{M} denote an arbitrary differentiable manifold immersed in \mathbb{R}^3 . Then, let $L^2(\mathcal{M})$ be the space of square-integrable functions defined over this manifold and $\mathbf{L}^2(\mathcal{M}) := (L^2(\mathcal{M}))^d$ be the vectorial counterpart where $d = 2$ or $d = 3$ in this dissertation. For an arbitrary function $\mathbf{v} \in \mathbf{L}^2(\mathcal{M})$, the L^2 -norm is given by

$$\|\mathbf{v}\|_{0,\mathcal{M}} := \left(\int_{\Omega} \mathbf{v} \cdot \mathbf{v} \, d\Omega \right)^{1/2} \quad (5.1)$$

Let $H^k(\mathcal{M})$ denote the space of functions in $L^2(\mathcal{M})$ whose k^{th} -order derivatives belong to $L^2(\mathcal{M})$ as well, where these derivatives are defined in (3.18). Similarly, we define $\mathbf{H}^k(\mathcal{M}) := (H^k(\mathcal{M}))^d$ as its vectorial counterpart. This Sobolev space is endowed with the standard Sobolev norm

$$\|\mathbf{v}\|_{k,\mathcal{M}} := \left(\sum_{i=0}^k \|\nabla^i \mathbf{v}\|_{0,\mathcal{M}}^2 \right)^{1/2} \quad (5.2)$$

where the notion of contraction in the case of these higher-order tensors arising through high-ordered Sobolev norms generalizes naturally through a Frobenius norm. Note here that we have implicitly adopted the convention that $H^0(\mathcal{M}) \equiv L^2(\mathcal{M})$, and analogously for the vectorial counterparts. Lastly, we denote the k Sobolev semi-norm via $|\cdot|_{k,\mathcal{M}}$. Fractional-order Sobolev spaces are utilized

throughout this dissertation and are defined in a distributional sense. Note that all of these concepts extend to the manifold boundary $\partial\mathcal{M}$ naturally.

5.1 Existence, Uniqueness, and Error Estimation

Theorem 1 (Lax-Milgram Theorem). *Assume that*

$$a(\cdot, \cdot): \mathcal{U} \times \mathcal{U} \rightarrow \mathbb{R} \quad (5.3)$$

is a bilinear mapping, for which there exists constants $C_{cont}, C_{coer} > 0$ such that for $\mathbf{u}, \mathbf{v} \in \mathcal{U}$

$$a(\mathbf{v}, \mathbf{u}) \leq C_{cont} \|\mathbf{v}\|_{\mathcal{U}} \|\mathbf{u}\|_{\mathcal{U}} \quad (5.4)$$

and

$$a(\mathbf{v}, \mathbf{v}) \geq C_{coer} \|\mathbf{v}\|_{\mathcal{U}}^2 \quad (5.5)$$

Then, for $\mathbf{f}: \mathcal{U} \rightarrow \mathbb{R}$ a bounded linear functional on \mathcal{U} , there exists a unique element $\mathbf{u} \in \mathcal{U}$ such that

$$a(\mathbf{v}, \mathbf{u}) = (\mathbf{f}, \mathbf{v}) \quad (5.6)$$

for all $\mathbf{v} \in \mathcal{U}$.

The Lax-Milgram Theorem is ubiquitous to proving the existence and uniqueness of a weak solution. Its proof can be found in many places, for instance [48]. Throughout this dissertation, we use lemmas to demonstrate that the bilinear form under consideration is indeed equivalent to some norm and, through Lax-Milgram, ensures the existence and uniqueness of a weak solution with respect to the norm $\|\cdot\|_{\mathcal{V}}$.

Theorem 2 (Galerkin Orthogonality). *Suppose that the unique solution $\mathbf{u} \in \mathcal{U}$ satisfies the following relationship*

$$a(\mathbf{v}, \mathbf{u}) = \ell(\mathbf{v}, \mathbf{f}) \quad (5.7)$$

for all $\mathbf{v} \in \mathcal{V}$ and let $\mathbf{u}^h \in \mathcal{U}^h \subset \mathcal{U}$ be such that

$$a(\mathbf{v}^h, \mathbf{u}^h) = \ell(\mathbf{v}^h, \mathbf{f}) \quad (5.8)$$

for all $\mathbf{v}^h \in \mathcal{V}^h \subset \mathcal{V}$. Then it follows that

$$a(\mathbf{v}, \mathbf{u} - \mathbf{u}^h) = 0 \quad (5.9)$$

Proof. Since (5.7) holds for all $\mathbf{v} \in \mathcal{V}$. Let $\mathbf{v} = \mathbf{v}^h$ and subtract (5.8) from (5.7) to obtain the desired result. \square

Additionally, we prove **a priori** error estimates based on the following theorem regarding best-approximation by utilizing Theorem 1 and Theorem 2:

Theorem 3 (Approximation Theorem). *Let \mathbf{u}^h be the unique solution to $a(\cdot, \cdot)$ as postulated in Theorem 1 and suppose the conditions therein hold. Then,*

$$\|\mathbf{u} - \mathbf{u}^h\|_{\mathcal{U}} \leq \left(1 + \frac{C_{cont}}{C_{coer}}\right) \inf_{\mathbf{v}^h \in \mathcal{U}^h} \|\mathbf{u} - \mathbf{v}^h\|_{\mathcal{U}}. \quad (5.10)$$

Proof. By the orthogonality of the mesh-dependent bilinear form $a(\cdot, \cdot)$, it follows that that

$$\begin{aligned} \|\mathbf{v}^h - \mathbf{u}^h\|_{\mathcal{U}}^2 &\leq \frac{1}{C_{coer}} a(\mathbf{v}^h - \mathbf{u}^h, \mathbf{v}^h - \mathbf{u}^h) \\ &= \frac{1}{C_{coer}} a(\mathbf{v}^h - \mathbf{u}^h, \mathbf{v}^h - \mathbf{u}) \\ &\leq \frac{C_{cont}}{C_{coer}} \|\mathbf{v}^h - \mathbf{u}^h\|_{\mathcal{U}} \|\mathbf{v}^h - \mathbf{u}^h\|_{\mathcal{U}} \end{aligned} \quad (5.11)$$

hence,

$$\|\mathbf{v}^h - \mathbf{u}^h\|_{\mathcal{U}} \leq \frac{C_{cont}}{C_{coer}} \|\mathbf{v}^h - \mathbf{u}^h\|_{\mathcal{U}}. \quad (5.12)$$

Then by the triangle inequality,

$$\begin{aligned} \|\mathbf{u} - \mathbf{u}^h\|_{\mathcal{U}} &\leq \inf_{\mathbf{v}^h \in \mathcal{U}} \left(\|\mathbf{u} - \mathbf{v}^h\|_{\mathcal{U}} + \|\mathbf{v}^h - \mathbf{u}^h\|_{\mathcal{U}} \right) \\ &\leq \left(1 + \frac{C_{cont}}{C_{coer}} \right) \inf_{\mathbf{v}^h \in \mathcal{U}} \|\mathbf{u}^h - \mathbf{v}^h\|_{\mathcal{U}}. \end{aligned} \quad (5.13)$$

□

5.2 Trace Inequalities, Poincaré Inequalities, and Inverse Estimates

Trace inequalities provide upper bounds to boundary quantities by their mesh-scaled, interior counterparts for finite-dimensional quantities. The trace inequalities considered in this dissertation for $h > 0$ take the form

$$\|D_{\Gamma}^n \mathbf{u}^h\|_{0,\Gamma}^2 \leq \frac{C_{tr}}{h} \|D_{\Omega}^n \mathbf{u}^h\|_{0,\Omega}^2 \quad (5.14)$$

where C_{tr} is the trace inequality constant independent of h and $n \geq 0$ is the order of the differential operator. The differential operators D_{Γ} and D_{Ω} are defined over the domain boundary and the interior, respectively. The following eight trace inequalities will be used throughout this dissertation in proving coercivity and a priori error estimates for the various PDEs considered.

1. A trace inequality bounding the membrane stress on the boundary by the membrane stress on the interior of the form

$$\|\underline{\underline{A}}(\mathbf{u}^h)\|_{0,\Gamma}^2 \leq \frac{C_{tr,A}}{h} \|\underline{\underline{A}}(\mathbf{u}^h)\|_{0,\Omega}^2 \quad (5.15)$$

where $C_{tr,A}$ is the trace inequality constant that is independent of mesh size.

2. A trace inequality bounding the bending stress on the boundary by the bending stress on the interior of the form

$$\|\underline{\underline{B}}(\mathbf{u}^h)\|_{0,\Gamma}^2 \leq \frac{C_{tr,B}}{h} \|\underline{\underline{B}}(\mathbf{u}^h)\|_{0,\Omega}^2 \quad (5.16)$$

where $C_{tr,B}$ is the trace inequality constant that is independent of mesh size.

3. A trace inequality bounding derivatives of the bending moment on the boundary by derivatives of the bending moment on the interior of the form

$$\|T_3(\mathbf{u}^h)\|_{0,\Gamma}^2 \leq \frac{C_{tr,T}}{h} \|T_3(\mathbf{u}^h)\|_{0,\Omega}^2 \quad (5.17)$$

where $C_{tr,T}$ is the trace inequality constant that is independent of mesh size and the term $T_3(\mathbf{u})$ is a modified transverse shearing, much like a gradient of the bending stress, that will be introduced in later sections.

4. A trace inequality bounding the displacement field on the boundary by the displacement field on the interior of the form

$$\|\mathbf{u}^h\|_{0,\Gamma}^2 \leq \frac{C_{tr,u\Omega}}{h} \|\mathbf{u}^h\|_{0,\Omega}^2 \quad (5.18)$$

where $C_{tr,u\Omega}$ is the trace inequality constant that is independent of mesh size.

5. A trace inequality bounding the rotational displacement field on the boundary by the derivative of the displacement field on the interior of the form

$$\|\theta_n(\mathbf{u}^h)\|_{0,\Gamma}^2 \leq \frac{C_{tr,\theta}}{h} \|\mathbf{u}^h\|_{1,\Omega}^2 \quad (5.19)$$

where $C_{tr,\theta}$ is the trace inequality constant that is independent of mesh size.

6. A trace inequality bounding a pointwise evaluation of the twisting moment over the set $\chi_C \in \Gamma$ by the norm of the twisting moment on the boundary of the form

$$\left| M_{nt}(\mathbf{u}^h) \right|_{\chi_C}^2 \leq \frac{C_{tr,M}}{h} \|M_{nt}(\mathbf{u}^h)\|_{0,\Gamma}^2 \quad (5.20)$$

where $C_{tr,M}$ is the trace inequality constant that is independent of mesh size. Note that this trace inequality constant is known a priori as is demonstrated in [121].

7. A trace inequality bounding a pointwise evaluation of the transverse displacement over the set $\chi_C \in \Gamma$ by the norm of the transverse displacement on the boundary of the form

$$\left| \mathbf{u}^h \right|_{\chi_C}^2 \leq \frac{C_{tr, u_\Gamma}}{h} \|\mathbf{u}^h\|_{0, \Gamma}^2 \quad (5.21)$$

where C_{tr, u_Γ} is the trace inequality constant that is independent of mesh size. Note that this trace inequality constant is known a priori as is demonstrated in [121].

8. A trace inequality bounding the pointwise evaluation of a function over the set χ_C by the L^2 norm and the H^1 -seminorm in Γ of the form

$$u_3 \Big|_{\chi_C}^2 \leq C_{tr, \chi} \left(\frac{1}{h} \|u_3\|_{0, \Gamma}^2 + h |u_3|_{1, \Gamma}^2 \right) \quad (5.22)$$

where $C_{tr, \chi}$ is the trace inequality constant that is independent of mesh size. Note that this trace inequality constant holds for the infinite-dimensional setting, unlike the previous inequalities, due to the presence of the H^1 -seminorm which guarantees existence by the trace theorem for Sobolev spaces.

9. A trace inequality bounding the L^2 norm of a function over Γ by the L^2 norm and the H^1 -seminorm in Ω of the form

$$\|\mathbf{u}\|_{0, \Gamma}^2 \leq C_{tr, 0} \left(\frac{1}{h} \|\mathbf{u}\|_{0, \Omega}^2 + h |\mathbf{u}|_{1, \Omega}^2 \right) \quad (5.23)$$

where $C_{tr, 0}$ is the trace inequality constant that is independent of mesh size. Note that this trace inequality constant holds for the infinite-dimensional setting, unlike the previous inequalities, due to the presence of the H^1 -seminorm. The detailed proof of this inequality can be found in [47].

In a similar spirit, we can bound finite-dimensional derivative quantities by derivatives of a lower order through **inverse inequalities**. The inverse inequalities considered in in this dissertation

for $h > 0$ take the form

$$\|D_\Omega^n \mathbf{u}^h\|_{0,\Omega}^2 \leq \frac{C_{inv}}{h^{2j}} \|D_\Omega^{n-j} \mathbf{u}^h\|_{0,\Omega}^2 \quad (5.24)$$

where C_{inv} is the inverse inequality constant independent of h and $n \geq j \geq 0$. The following inverse inequality is employed in our proofs of coercivity and a priori error estimates.

1. An inverse inequality bounding the modified shear on the interior by the bending energy on the interior of the form

$$\|T_3(\mathbf{u}^h)\|_{0,\Omega}^2 \leq \frac{C_{inv,T}}{h^2} \|\underline{\underline{B}}(\mathbf{u}^h)\|_{0,\Omega}^2 \quad (5.25)$$

Ultimately, we would like to relate these quantities to the membrane and bending energies which motivates the auxiliary bounds on the constitutive law

$$E \leq \|\mathbb{C}\|_{0,\Omega} \leq 2E. \quad (5.26)$$

We can then bound the membrane stress, and membrane energy, from above by

$$\|\underline{\underline{A}}(\mathbf{u})\|_{0,\Omega}^2 \leq 2E\eta \|\mathbf{u}\|_A^2 \leq (2E\eta)^2 |\mathbf{u}|_{1,\Omega}^2 \quad (5.27)$$

and a similar bound for the bending stress, and bending energy, from above by

$$\|\underline{\underline{B}}(\mathbf{u})\|_{0,\Omega}^2 \leq \frac{E\eta^3}{6} \|\mathbf{u}\|_B^2 \leq \left(\frac{E\eta^3}{6}\right)^2 |\mathbf{u}|_{2,\Omega}^2. \quad (5.28)$$

Furthermore, the constitutive laws for membrane and bending stress-strain relationships follow by a simple thickness scaling. In particular, through a Poincaré-type inequality, we have the following

1. A Poincaré-type bound for the membrane energy by the H^1 -norm

$$E\eta \|\mathbf{u}\|_{1,\Omega}^2 \leq C_{poin,A} \|\mathbf{u}\|_A^2 \quad (5.29)$$

where $C_{poin,A}$ is a positive constant that is independent of h , E , and η .

2. A Poincaré-type bound for the bending energy by the H^2 -norm

$$\frac{E\eta^3}{12} \|\mathbf{u}\|_{2,\Omega}^2 \leq C_{poin,B} \|\mathbf{u}\|_B^2 \quad (5.30)$$

where $C_{poin,B}$ is a positive constant that is independent of h , E , and η .

Often times, we require a combination of these inequalities while demonstrating continuity, coercivity, and a priori error estimates for the PDEs considered. Moreover, since these constants appear in estimates of the penalty parameters used for Dirichlet boundary condition enforcement, we would like an approach for their efficient computation. Therefore, these inequalities can be generalized and an optimal constant can be determined through the following generalized eigenvalue problem:

$$\mathbf{M}\mathbf{u} = \lambda \mathbf{N}\mathbf{u} \quad (5.31)$$

where

$$\|D_\Gamma^n \mathbf{u}^h\|_{0,\Gamma}^2 = \langle \mathbf{u}, \mathbf{M}\mathbf{u} \rangle_{0,\Gamma}^2 \quad \text{and} \quad \|D_\Omega^{n-j} \mathbf{u}^h\|_{0,\Omega}^2 = \langle \mathbf{u}, \mathbf{N}\mathbf{u} \rangle_{0,\Omega}^2 \quad (5.32)$$

with $\mathbf{u} = \{\mathbf{u}_i\}_i$ the degrees of freedom used in a discretization of the form $\mathbf{u}^h = \sum_i \mathbf{u}_i N_i$.

The trace inequality constant can be bounded from below by the maximal eigenvalue of (5.31). This can be seen clearly by the corresponding generalized Rayleigh quotient:

$$\frac{\|D_\Gamma^n \mathbf{u}^h\|_{0,\Gamma}^2}{\|D_\Omega^{n-j} \mathbf{u}^h\|_{0,\Omega}^2} = \frac{\langle \mathbf{u}, \mathbf{M}\mathbf{u} \rangle_{0,\Gamma}^2}{\langle \mathbf{u}, \mathbf{N}\mathbf{u} \rangle_{0,\Omega}^2} \leq \lambda \leq \frac{C_{trace}(\Omega, p) C_{AB}(E, \eta)}{h^{2j+1}} \quad (5.33)$$

where $C_{AB}(E, \eta)$ is some constant dependent on Young's modulus and thickness arising through the constitutive relationship. Note that although we denote this optimal constant $C_{trace}(\Omega, p)$, it is understood that there may implicitly be several trace estimate, inverse inequality, and Poincaré inequality constants present as well, hence the dependence on both geometric configuration and

polynomial degree of discretization. This inequality demonstrates that $C_{trace}(\Omega, p)$ is bounded from below by the maximal eigenvalue and that $\lambda = \mathcal{O}(h^{2j+1}C_{AB}(E, \eta))$.

For small problems, this trace inequality constant can be approximated with good accuracy by explicitly constructing and solving (5.31) with relatively low computational expense. This constant may then be scaled according to the mesh-dependent scaling for problems of larger size, e.g. $C_{trace}(\Omega, p) = h^{2j+1}\lambda C_{AB}(E, \eta)$. For clarity, we explicitly outline the h -dependence of the eigenvalues for the explicit trace inequalities considered herein, as well as the dependence on Young's modulus and the thickness. An excellent source for explicit trace inequality constants can be found in [47] where, in addition to a more-thorough exposition of the mathematics presented, alternative approaches to determining the constants are provided including various measures of geometric mappings. Additionally, inverse estimates and Poincaré inequalities, presented above and utilized in later sections, are presented in great depth and motivated by several examples in [61].

5.3 Green's Identity

Green's identities are used gratuitously in this dissertation and moreover must be cast over a differentiable manifold in this setting. Before proceeding with the physical derivations in the main portions of this dissertation, we present this identity that we employ throughout these sections, over a general, symmetric tensor $\underline{\underline{M}}$.

$$\begin{aligned}
\int_{\Omega} \underline{\underline{M}} : (\nabla^s \mathbf{v}) \, d\Omega &= \int_{\Omega} \underline{\underline{M}} : (\nabla \mathbf{v}) \, d\Omega \\
&= \int_{\Omega} \underline{\underline{M}} : (\nabla \underline{v}) \, d\Omega + \int_{\Omega} \underline{\underline{M}} : (\nabla (v_3 \mathbf{a}^3)) \, d\Omega \\
&= \int_{\Omega} M^{\alpha\beta} v_{\alpha|\beta} \, d\Omega - \int_{\Omega} M^{\alpha\beta} b_{\alpha\beta} v_3 \, d\Omega \\
&= \int_{\Omega} \left(M^{\alpha\beta} v_{\alpha} \right)_{|\beta} \, d\Omega - \int_{\Omega} M^{\alpha\beta} v_{\alpha} \, d\Omega - \int_{\Omega} M^{\alpha\beta} b_{\alpha\beta} v_3 \, d\Omega \tag{5.34} \\
&= \int_{\Gamma} M^{\alpha\beta} v_{\alpha} n_{\beta} \, d\Gamma - \int_{\Omega} M^{\alpha\beta} v_{\alpha} \, d\Omega - \int_{\Omega} M^{\alpha\beta} b_{\alpha\beta} v_3 \, d\Omega \\
&= \underbrace{\int_{\Gamma} \underline{n} \underline{\underline{M}} \underline{v} \, d\Gamma}_{\text{in-plane}} - \underbrace{\int_{\Omega} (\nabla \cdot \underline{\underline{M}}) \underline{v} \, d\Omega}_{\text{out-of-plane}} - \int_{\Omega} (\underline{\underline{M}} : \underline{b}) v_3 \, d\Omega
\end{aligned}$$

where the out-of-plane contributions arise because

$$(\nabla \mathbf{a}_3) = \mathbf{a}_{3,\alpha} \otimes \mathbf{a}^{\alpha} = (\mathbf{a}_{3,\alpha} \cdot \mathbf{a}^{\beta}) \mathbf{a}_{\beta} \otimes \mathbf{a}^{\alpha} = -(\mathbf{a}_3 \cdot \mathbf{a}^{\beta}, \alpha) \mathbf{a}_{\beta} \otimes \mathbf{a}^{\alpha} = -b_{\alpha}^{\beta} \mathbf{a}_{\beta} \otimes \mathbf{a}^{\alpha} = -\underline{\underline{b}} \tag{5.35}$$

Chapter 6

Problems

In this chapter, we present the three PDEs problems that are considered throughout the remainder of this dissertation. These include (i) the linear-elastic member in a plane stress state, (ii) the linearized Kirchhoff-Love plate, and (iii) the linearized Kirchhoff-Love shell. Moreover, we derive a Nitsche formulation for each of these PDEs. In the case of isogeometric analysis with NURBS defined through an open knot vector, the additional boundary terms vanish due to strong homogeneous enforcement of Dirichlet boundary conditions in the test space. However, in the case of uniform B-splines, and more generally Catmull-Clark subdivision surfaces, these additional terms play a crucial role in analysis, discretization, and implementation.

6.1 Linear Elasticity

This problem covers a wide variety of physical phenomena and serves as an excellent demonstration of design space exploration and tolerance allocation tools in later chapters. We begin this, and subsequent, sections with the variational form and infer the underlying strong form through the Euler-Lagrange equations. While linear elasticity can be discussed in higher dimensions, we only consider this PDE in the two-dimensional setting. In particular, this section presents Nitsche's method in the context of vector-valued degrees of freedom as well as PDEs which arise through an energy principle.

6.1.1 The Linear Elastic Formulation

Linear elasticity is used to model the structural response of structural members subject to in-plane loading. Moreover, in this setting it is assumed that strains are small and hence the linearized Green-Lagrange strain tensor and a linear constitutive model are sufficiently accurate. Two-dimensional linear elasticity is capable of idealizing three-dimensional elasticity in two scenarios, **plane strain** and **plane stress**. In the setting of the former, the out-of-plane direction is much larger than the in-plane directions, e.g. a dam or a tunnel, while in the case of the latter the member is a three-dimensional planar body with small thickness.

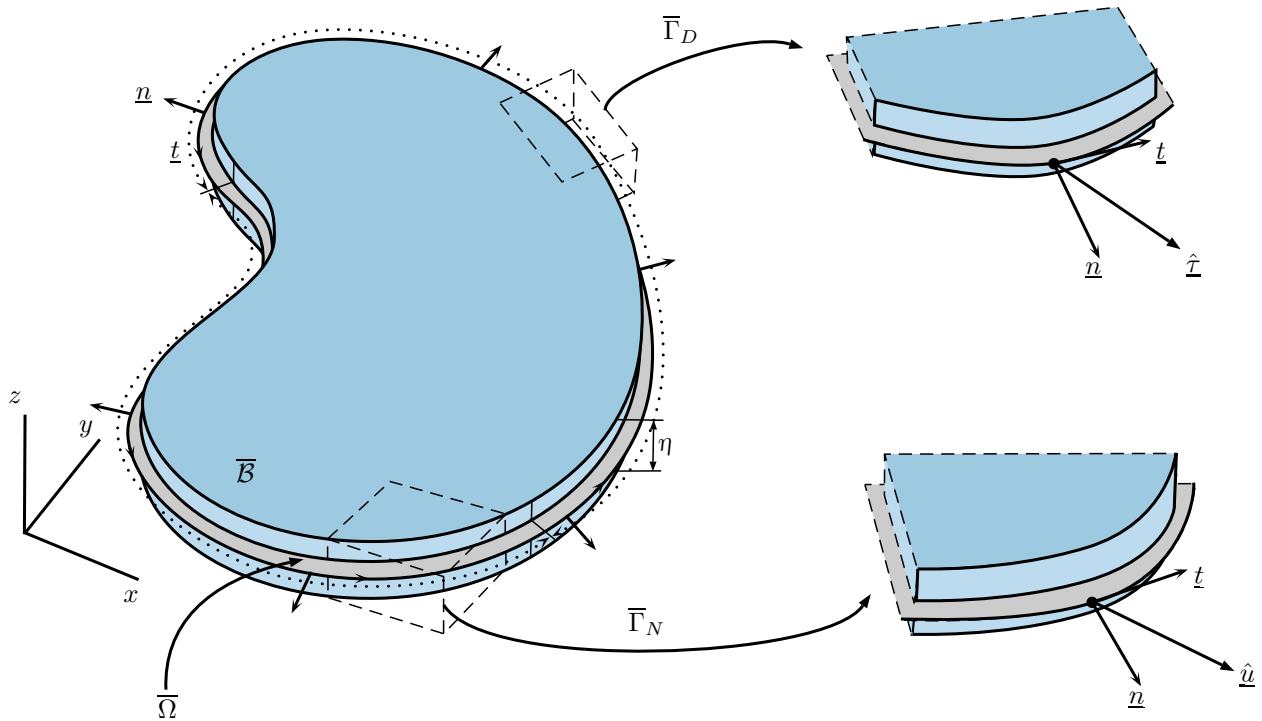


Figure 6.1: The Linear Elasticity problem domain with boundary conditions. All entities are shown in the positive convention.

6.1.2 Work and Energy

For the construction of our trial and test spaces, the bilinear form arises from the symmetrized gradient, that is, the linearized Green-Lagrange strain tensor, hence we require that at least one

derivative be integrable in the interior of the domain. Moreover, we will begin by enforcing Dirichlet boundary conditions strongly in the trial space and their homogeneous counterparts strongly enforced in the trial space. Heuristically, the trial and test spaces can be viewed as the spaces of admissible and virtual displacements which are defined as:

$$\begin{aligned}\mathcal{U}_{LE} &:= \left\{ \underline{u}: \Omega \rightarrow \mathbb{R}^2: \underline{u} \in \mathbf{H}^1(\Omega) \text{ and } \underline{u}|_{\Gamma_D} = \hat{\underline{u}} \right\} \\ \mathcal{V}_{LE} &:= \left\{ \underline{v}: \Omega \rightarrow \mathbb{R}^2: \underline{v} \in \mathbf{H}^1(\Omega) \text{ and } \underline{v}|_{\Gamma_D} = \underline{0} \right\}.\end{aligned}\tag{6.1}$$

Note that in the setting of linear elasticity, we have both Dirichlet and Neumann boundary conditions. The former is an applied displacement, often zero, whereas the latter is a boundary traction, that is, an in-plane loading along the boundary. The internal energy of the system is given via

$$\Pi_{int,LE}(\underline{u}) = \frac{1}{2} \|\underline{u}\|_A^2\tag{6.2}$$

and the external work done on the system is given via

$$\begin{aligned}W_{ext,LE}(\underline{u}) &= \int_{\mathcal{B}} \underline{f} \cdot \underline{u} \, d\mathcal{B} + \int_{\partial\mathcal{B}} \hat{\underline{\tau}} \cdot \underline{u} \, d(\partial\mathcal{B}) \\ &= \eta \int_{\Omega} \underline{f} \cdot \underline{u} \, d\Omega + \eta \int_{\Gamma_N} \hat{\underline{\tau}} \cdot \underline{u} \, d\Gamma\end{aligned}\tag{6.3}$$

where \underline{f} is an in-plane loading or body force on the planar member and $\hat{\underline{\tau}}$ is the boundary traction.

For this system to be in static equilibrium, it must follow that these two entities be equal to one another and that the displacement configuration corresponds to a minimal potential energy. To obtain this, we will require the Lagrangian of the system given by

$$\mathcal{L}_{LE}(\underline{u}) = W_{ext,LE}(\underline{u}) - \Pi_{int,LE}(\underline{u})\tag{6.4}$$

6.1.3 The Euler-Lagrange Equations and the Variational Formulation

To arrive at the variational formulation for linear elasticity, we must take a variation of the Lagrangian and find the stationary solution which corresponds to the minimum potential energy

configuration

$$\begin{aligned} \delta \mathcal{L}_{LE}(\underline{u}) &= \delta W_{ext,LE}(\underline{u}) - \delta \Pi_{int,LE}(\underline{u}) \\ &= \eta \int_{\Omega} \underline{f} \cdot \delta \underline{u} \, d\Omega + \eta \int_{\Gamma_N} \hat{\underline{\tau}} \cdot \delta \underline{u} \, d\Gamma - \int_{\Omega} \underline{\underline{A}}(\underline{u}) : \underline{\underline{\gamma}}(\delta \underline{u}) \, d\Omega \end{aligned} \quad (6.5)$$

which follows immediately by the linearity of our constitutive model. The variational form is the extremal value of the Lagrangian corresponding to the root of the first variation. Therefore letting $\underline{v} = \delta \underline{u}$ and utilizing our stress-strain relationship, we have the following variational form:

$$\int_{\Omega} \underline{\underline{\gamma}}(\underline{v}) : \mathbb{C}_A : \underline{\underline{\gamma}}(\underline{u}) \, d\Omega = \eta \int_{\Omega} \underline{f} \cdot \underline{v} \, d\Omega + \eta \int_{\Gamma_N} \hat{\underline{\tau}} \cdot \underline{v} \, d\Gamma \quad (6.6)$$

therefore, canceling the η on both sides of the equation, we arrive at the following infinite-dimensional variational form for linear elasticity:

Variational Formulation for Linear Elasticity

Find $\underline{u} \in \mathcal{U}_{LE}$ such that

$$a_{LE}(\underline{v}, \underline{u}) = \ell_{LE}(\underline{v}) \quad (6.7)$$

for all $\underline{v} \in \mathcal{V}_{LE}$ where

$$\begin{aligned} a_{LE}(\underline{v}, \underline{u}) &= \eta \int_{\Omega} \mathbb{C}^{\alpha\beta\lambda\mu} \gamma_{\alpha\beta}(\underline{v}) \gamma_{\lambda\mu}(\underline{u}) \, d\Omega \\ \ell_{LE}(\underline{v}) &= \eta \int_{\Omega} \underline{f} \cdot \underline{v} \, d\Omega + \eta \int_{\Gamma_N} \hat{\underline{\tau}} \cdot \underline{v} \, d\Gamma. \end{aligned} \quad (6.8)$$

With the presentation of this weak formulation, we have the following lemma regarding the existence and uniqueness of the weak solution $\underline{u} \in \mathcal{U}_{LE}$.

Lemma 4. *Suppose that for the Lebesgue measure $\lambda(\cdot)$ and Lebesgue-measurable sets Γ_D and $\lambda(\Gamma_D) > 0$. Then there exists a unique weak solution to (6.7). If $\lambda(\Gamma_D) = \emptyset$, the solution is unique up to a constant.*

Proof. We want to show that $a_{LE}(\cdot, \cdot)$ induces a norm on \mathcal{V}_{LE} . Let $\underline{v}, \underline{w} \in \mathcal{V}_{LE}$. To demonstrate that $a_{LE}(\cdot, \cdot)$ is a norm on \mathcal{V}_{LE} , we must show it satisfies the properties of being a norm. Since

$a_{LE}(\cdot, \cdot)$ is a seminorm, it satisfies properties (a), (b), and (c) of:

$$\begin{aligned}
(a) \quad a_{LE}(\alpha \underline{v}, \alpha \underline{v}) &= |\alpha|^2 a_{LE}(\underline{v}, \underline{v}) \text{ for } \alpha \in \mathbb{R} && \text{(absolute homogeneity)} \\
(b) \quad a_{LE}(\underline{v} + \underline{w}, \underline{v} + \underline{w}) &\leq a_{LE}(\underline{v}, \underline{v}) + a_{LE}(\underline{w}, \underline{w}) && \text{(subadditivity)} \\
(c) \quad a_{LE}(\underline{v}, \underline{v}) &> 0 && \text{(non-negativity)} \\
(d) \quad a_{LE}(\underline{v}, \underline{v}) = 0 &\Leftrightarrow \underline{v} \equiv \underline{0} && \text{(definiteness)}
\end{aligned} \tag{6.9}$$

The question of whether a constant lies in the kernel of $a_{LE}(\cdot, \cdot)$ rendering the bilinear form indefinite. Therefore, we consider the scenario of the solution field $\underline{v}_C = C$ for some $C \in \mathbb{R}$. We will demonstrate that the only value of this constant with $a_{LE}(\underline{v}_C, \underline{v}_C) = 0$ is $C = 0$.

Suppose $\lambda(\Gamma_D) > 0$. Then $\underline{v}_C = 0$ on Γ_D and hence $\underline{v} = C = 0$. Moreover $a_{LE}(\underline{v}_C, \underline{v}_C) = 0 \Leftrightarrow \underline{v}_C \equiv 0$. Therefore, the definiteness of the bilinear form is ensured and $a_{LE}(\cdot, \cdot)$ indeed induces a norm on \mathcal{V} . The existence and uniqueness of the weak solution follows from Theorem 1.

In the case where $\lambda(\Gamma_D) = \emptyset$, C is not uniquely defined however all other displacement fields are, hence the solution is unique up to C . \square

Here we have strongly enforced our Dirichlet boundary conditions which we strive to release in the implementation of Nitsche's method for linear elasticity. However, before we can state Nitsche's method for linear elasticity, we must first infer the underlying strong formulation.

6.1.4 The Strong Formulation for Linear Elasticity

To obtain the underlying strong formulation for linear elasticity, we must essentially “reverse” integrate-by-parts¹ the variational form defined in (6.7). Following this procedure for the bilinear form yields

$$\int_{\Omega} \underline{\underline{A}}(\underline{v}) : \underline{\underline{\gamma}}(\underline{u}) \, d\Omega = \int_{\Gamma} \underline{\underline{\tau}}(\underline{u}) \cdot \underline{v} \, d\Gamma - \int_{\Omega} \left(\nabla \cdot \underline{\underline{A}}(\underline{u}) \right) \cdot \underline{v} \, d\Omega \tag{6.10}$$

¹ This operation is simply integration by parts however we refer to it as “reverse” because we are effectively returning the differential operators to the trial function, the opposite procedure of obtaining a variational formulation from the strong form of a PDE

where the boundary traction here is defined as $\underline{\tau}(\underline{u}) = \underline{\underline{A}}(\underline{u})\underline{n}$. Then, combining this result with the linear form $\ell_{LE}(\underline{v})$ yields

$$\begin{aligned} 0 &= a_{LE}(\underline{v}, \underline{u}) - \ell_{LE}(\underline{v}) \\ &= \int_{\Gamma_N} [\underline{\tau}(\underline{u}) - \hat{\underline{\tau}}] \cdot \underline{v} \, d\Gamma - \int_{\Omega} [\underline{\nabla} \cdot \underline{\underline{A}}(\underline{u}) + \underline{f}] \cdot \underline{v} \, d\Omega. \end{aligned} \quad (6.11)$$

The remaining boundary integral over the Dirichlet boundary vanishes due to the strong-homogeneous enforcement of Dirichlet boundaries in the test space. However as we will see, this is what will become our consistency term in Nitsche's method. The strong formulation for linear elasticity, which we have inferred from the variational form, is expressed as

Strong Formulation for Linear Elasticity

Find $\underline{u} : \Omega \rightarrow \mathbb{R}^2$ such that:

$$\begin{aligned} -\underline{\nabla} \cdot \underline{\underline{A}}(\underline{u}) &= \underline{f} \quad \text{in } \Omega \\ \underline{u} &= \hat{\underline{u}} \quad \text{on } \Gamma_D \\ \underline{\tau}(\underline{u}) &= \hat{\underline{\tau}} \quad \text{on } \Gamma_N \end{aligned} \quad (6.12)$$

We now have the ability to express Nitsche's method for linear elasticity, given this strong form of the PDE.

6.1.5 Nitsche's Variational Form for Linear Elasticity

To begin our derivation of Nitsche's method for linear elasticity, we define the following discrete spaces of admissible and virtual displacements which release the strong-enforcement of Dirichlet boundary conditions:

$$\mathcal{V}_{LE}^h \equiv \mathcal{U}_{LE}^h := \left\{ \underline{u}^h : \Omega \rightarrow \mathbb{R}^2 : \underline{\tau}(\underline{u}^h) \in \mathbf{L}^2(\Gamma_D) \text{ and } \underline{u}^h(\xi^1, \xi^2) = \sum_{i=1}^n c_i N_i(\xi^1, \xi^2) \right\} \quad (6.13)$$

With the definition of these discrete spaces, we can express the discrete Galerkin formulation for Nitsche's method as follows:

Find $\underline{u}^h \in \mathcal{U}_{LE}^h$ such that

$$a_{LE}^h(\underline{v}^h, \underline{u}^h) = \ell_{LE}^h(\underline{v}^h) \quad (6.14)$$

for all $\underline{v}^h \in \mathcal{V}_{LE}^h$ where

$$\begin{aligned} a_{LE}^h(\underline{v}^h, \underline{u}^h) &= a_{LE}(\underline{v}^h, \underline{u}^h) - \underbrace{\int_{\Gamma_D} \boldsymbol{\tau}(\underline{u}^h) \cdot \underline{v}^h \, d\Gamma}_{\text{Consistency Term}} - \underbrace{\int_{\Gamma_D} \boldsymbol{\tau}(\underline{v}^h) \cdot \underline{u}^h \, d\Gamma}_{\text{Symmetry Term}} + \underbrace{\frac{2\eta EC_{pen}}{h} \int_{\Gamma_D} \underline{v}^h \cdot \underline{u}^h \, d\Gamma}_{\text{Penalty Term}} \\ \ell_{LE}^h(\underline{v}^h) &= \ell_{LE}(\underline{v}^h) - \underbrace{\int_{\Gamma_D} \boldsymbol{\tau}(\underline{v}^h) \cdot \hat{\underline{u}} \, d\Gamma}_{\text{Symmetry Term}} + \underbrace{\frac{2\eta EC_{pen}}{h} \int_{\Gamma_D} \underline{v}^h \cdot \hat{\underline{u}} \, d\Gamma}_{\text{Penalty Term}} \end{aligned} \quad (6.15)$$

6.1.6 Consistency and Symmetry of Nitsche's Method for Linear Elasticity

The symmetry of the discrete bilinear form arising through Nitsche's method (6.14) is obvious. We have the following lemma which details the proof of consistency of $a_{LE}^h(\cdot, \cdot)$ with the strong form of the original PDE, provided the exact solution \underline{u} to (6.7) satisfies an additional regularity condition:

Lemma 5. *Suppose that the unique weak solution \underline{u} of (6.7) satisfies the regularity condition $\underline{u} \in \mathbf{H}^{3/2+\varepsilon}(\Omega)$ for some $\varepsilon > 0$. Then:*

$$a_{LE}^h(\underline{v}^h, \underline{u}) = \ell_{LE}^h(\underline{v}^h) \quad (6.16)$$

for all $\underline{v}^h \in \mathcal{V}_{LE}^h$.

Proof. The result follows immediately through integration by parts. Observe that:

$$\begin{aligned}
a_{LE}^h(\underline{v}^h, \underline{u}) - \ell_{LE}^h(\underline{v}^h) &= \int_{\Omega} \underline{A}(\underline{u}) : \underline{\alpha}(\underline{v}^h) \, d\Omega - \int_{\Gamma_D} \underline{\tau}(\underline{u}) \cdot \underline{v}^h \, d\Gamma - \int_{\Gamma_D} \underline{\tau}(\underline{v}^h) \cdot [\underline{u} - \hat{\underline{u}}] \, d\Gamma \\
&\quad + \frac{2\eta EC_{pen}}{h} \int_{\Gamma_D} \underline{v}^h \cdot [\underline{u} - \hat{\underline{u}}] \, d\Gamma - \int_{\Omega} \underline{f} \cdot \underline{v}^h \, d\Omega - \int_{\Gamma_N} \hat{\underline{\tau}} \cdot \underline{v}^h \, d\Gamma \\
&= \int_{\Gamma_N} [\underline{\tau}(\underline{u}) - \hat{\underline{\tau}}] \cdot \underline{v}^h \, d\Gamma - \int_{\Omega} [\underline{f} + \nabla \cdot \underline{A}(\underline{u})] \cdot \underline{v}^h \, d\Omega - \int_{\Gamma_D} \underline{\tau}(\underline{v}^h) \cdot [\underline{u} - \hat{\underline{u}}] \, d\Gamma \\
&\quad + \frac{2\eta EC_{pen}}{h} \int_{\Gamma_D} \underline{v}^h \cdot [\underline{u} - \hat{\underline{u}}] \, d\Gamma.
\end{aligned} \tag{6.17}$$

Hence the bilinear form is consistent with the strong form of linear elasticity. \square

6.1.7 Continuity and Coercivity of Nitsche's Method for Linear Elasticity

To preface this section, we define the mesh-dependent norm with which we prove continuity, coercivity, and later error estimates:

$$\|\underline{v}\|_{\mathcal{U}_{LE}^h}^2 := \|\underline{v}\|_A^2 + \frac{2\eta EC_{pen}}{h} \|\underline{v}\|_{0,\Gamma}^2 + \frac{h}{2\eta E} \|\underline{\tau}(\underline{v})\|_{0,\Gamma}^2. \tag{6.18}$$

Note that (6.18) is indeed a norm over \mathcal{V}_{LE}^h , and moreover \mathcal{U}_{LE}^h , since $\|\cdot\|_A$ is a seminorm with only a constant in the kernel and the L^2 boundary term enforces that this mode must be zero for the norm to vanish. Additionally, by (5.15) and (5.27), this norm satisfies the following relationship $\forall \underline{v}^h \in \mathcal{V}_{LE}^h$ with $C_\ell^{-1} \geq 1 + C_{tr,A}$:

$$\begin{aligned}
\|\underline{v}^h\|_{\mathcal{U}_{LE}^h}^2 &\leq \left\| \left\| \underline{v}^h \right\| \right\|_A^2 + \frac{2\eta EC_{pen}}{h} \|\underline{v}^h\|_{0,\Gamma}^2 + \frac{C_{tr,A}}{2\eta E} \|A(\underline{v}^h)\|_{0,\Omega}^2 \\
&\leq (1 + C_{tr,A}) \left\| \left\| \underline{v}^h \right\| \right\|_A^2 + \frac{2\eta EC_{pen}}{h} \|\underline{v}^h\|_{0,\Gamma}^2 \\
&\leq \frac{1}{C_\ell} \left(\left\| \left\| \underline{v}^h \right\| \right\|_A^2 + \frac{2\eta EC_{pen}}{h} \|\underline{v}^h\|_{0,\Gamma}^2 \right).
\end{aligned} \tag{6.19}$$

Now that we have demonstrated that $\|\cdot\|_{\mathcal{U}_{LE}^h}$ is indeed a norm, we are able to prove the continuity, that is the boundedness, of the mesh-dependent bilinear form $a_{LE}^h(\cdot, \cdot)$ in the following lemma:

Lemma 6. *The following continuity statement holds:*

$$a_{LE}^h(\underline{v}^h, \underline{w}) \leq C_{cont,LE} \|\underline{v}^h\|_{\mathcal{U}_{LE}^h} \|\underline{w}\|_{\mathcal{U}_{LE}^h} \quad (6.20)$$

for all $\underline{v}^h \in \mathcal{V}_{LE}^h$ and $\underline{w} \in \mathbf{H}^{3/2+\varepsilon}(\Omega)$ for some $\varepsilon > 0$.

Proof. To prove the continuity estimate, we first write

$$a_{LE}^h(\underline{v}^h, \underline{w}) = a_{LE}(\underline{v}^h, \underline{w}) - \int_{\Gamma_D} \boldsymbol{\tau}(\underline{w}) \cdot \underline{v}^h \, d\Gamma - \int_{\Gamma_D} \boldsymbol{\tau}(\underline{v}^h) \cdot \underline{w} \, d\Gamma + \frac{2\eta EC_{pen}}{h} \int_{\Gamma_D} \underline{v}^h \cdot \underline{w} \, d\Gamma \quad (6.21)$$

Observe we can bound

$$a_{LE}^h(\underline{v}^h, \underline{w}) = a_{LE}(\underline{v}^h, \underline{w}) + \frac{2\eta EC_{pen}}{h} \int_{\Gamma_D} \underline{v}^h \cdot \underline{w} \, d\Gamma \leq \|\underline{v}^h\|_{\mathcal{U}_{LE}^h} \|\underline{w}\|_{\mathcal{U}_{LE}^h} \quad (6.22)$$

and the remaining terms via

$$\begin{aligned} \int_{\Gamma_D} \boldsymbol{\tau}(\underline{w}) \cdot \underline{v}^h \, d\Gamma &\leq \|\boldsymbol{\tau}(\underline{w})\|_{0,\Gamma} \|\underline{v}^h\|_{0,\Gamma} \\ &\leq \sqrt{\frac{1}{h} \|\underline{v}^h\|_{0,\Gamma}^2} \sqrt{h \|\boldsymbol{\tau}(\underline{w})\|_{0,\Gamma}^2} \\ &\leq \|\underline{v}^h\|_{\mathcal{U}_{LE}^h} \|\underline{w}\|_{\mathcal{U}_{LE}^h} \end{aligned} \quad (6.23)$$

Clearly, this inequality holds for the symmetric counterpart. Collecting these inequalities yields

$$a_{LE}^h(\underline{v}^h, \underline{w}) \leq C_{cont,LE} \|\underline{v}^h\|_{\mathcal{U}_{LE}^h} \|\underline{w}\|_{\mathcal{U}_{LE}^h} \quad (6.24)$$

with $C_{cont,LE} = 3$.

□

Next, we prove the coercivity of the bilinear form with respect to $\|\cdot\|_{\mathcal{U}_{LE}^h}$ in the following lemma

Lemma 7. *The following coercivity statement holds:*

$$a_{LE}^h(\underline{v}^h, \underline{v}^h) \geq C_{coer,LE} \|\underline{v}^h\|_{\mathcal{U}_{LE}^h}^2, \quad \forall \underline{v}^h \in \mathcal{V}_{LE}^h \quad (6.25)$$

Proof. Let $\underline{v}^h \in \mathcal{V}_{LE}^h$, $\varepsilon > 2C_{tr,A}$, and observe that by Cauchy-Schwarz and Young's inequalities, it follows that

$$\int_{\Gamma_D} \underline{\tau}(\underline{v}^h) \cdot \underline{v}^h \, d\Gamma \leq \|\underline{\tau}(\underline{v}^h)\|_{0,\Gamma} \|\underline{v}^h\|_{0,\Gamma} \leq \left(\frac{h}{4\varepsilon\eta E} \|\underline{\tau}(\underline{v}^h)\|_{0,\Gamma}^2 + \frac{\varepsilon\eta E}{h} \|\underline{v}^h\|_{0,\Gamma}^2 \right). \quad (6.26)$$

Therefore, combining (6.26) with (5.15), and (5.27) for $C_{pen,LE} > \frac{1}{2} + 2C_{tr,A}$ we have the following

$$\begin{aligned} a_{LE}^h(\underline{v}^h, \underline{v}^h) &= \left\| \underline{v}^h \right\|_A^2 - 2 \int_{\Gamma_D} \underline{\tau}(\underline{v}^h) \cdot \underline{v}^h \, d\Gamma + \frac{2\eta EC_{pen}}{h} \|\underline{v}^h\|_{0,\Gamma}^2 \\ &\geq \left\| \underline{v}^h \right\|_A^2 - \left(\frac{h}{2\varepsilon\eta E} \|\underline{\tau}(\underline{v}^h)\|_{0,\Gamma}^2 + \frac{2\varepsilon\eta E}{h} \|\underline{v}^h\|_{0,\Gamma}^2 \right) + \frac{2\eta EC_{pen}}{h} \|\underline{v}^h\|_{0,\Gamma}^2 \\ &\geq \left(1 - \frac{C_{tr,A}}{\varepsilon} \right) \left\| \underline{v}^h \right\|_A^2 + \frac{2\eta E (C_{pen} - \varepsilon)}{h} \|\underline{v}^h\|_{0,\Gamma}^2 \\ &\geq \frac{1}{2} \left(\left\| \underline{v}^h \right\|_A^2 + \frac{2\eta EC_{pen}}{h} \|\underline{v}^h\|_{0,\Gamma}^2 \right) \\ &\geq C_{coer,LE} \|\underline{v}^h\|_{\mathcal{U}_{LE}^h}^2 \end{aligned} \quad (6.27)$$

where $C_{coer,LE} = \frac{1}{2} (1 + C_{tr,A})^{-1}$ and we have made use of (6.19) in the last inequality. □

6.1.8 A Priori Error Estimates

Before proceeding with discretization-dependent approximation theorems, we have the following corollary to Theorem 3.

Corollary 8. *Let \underline{u} and \underline{u}^h denote the unique solutions of problems (6.7) and (6.14), respectively. Furthermore, suppose the hypotheses of Theorem 1 and Theorem 3 are satisfied. Then,*

$$\|\underline{u} - \underline{u}^h\|_{\mathcal{U}_{LE}^h} \leq (7 + 6C_{tr,A}) \inf_{\underline{w}^h \in \mathcal{U}_{LE}^h} \|\underline{u} - \underline{w}^h\|_{\mathcal{U}_{LE}^h}. \quad (6.28)$$

Proof. Recall Theorem 3 and the estimate provided therein. Then the result follows immediately by the continuity and coercivity constants defined in Lemma 6 and Lemma 7 and the consistency inherent to Nitsche's variational formulation for linear elasticity. □

6.2 Kirchhoff-Love Plate

Now that we have covered Nitsche’s method for vector-valued degrees of freedom in the context of an energy principle, we can extend this experience to the Kirchhoff-Love plate. In this scenario, we will discuss and derive what are known as the **ersatz** forces which will also arise in the setting of the Kirchhoff-Love shell. These modified shear forces will change Nitsche’s variational formulation by introducing the correct, physically-consistent boundary integrals into the system. Moreover, in the context of the Kirchhoff-Love shell with zero curvature, this problem is the orthogonal counterpart to the linear-elastic relationships presented in the previous section.

6.2.1 Kirchhoff-Love plate formulation

Plate models simulate the structural response of a three-dimensional elastic planar body subject to transverse loading. Moreover, these models are idealized by representing the plate by the midsurface and handling through-thickness effects in a linear fashion by assuming such in the parametrization of the elastic body as well as the displacement profile. When known a priori, the midsurface is chosen to be the neutral plane, that is, the plane which undergoes no compressive or tensile forces due to bending, otherwise it is the surface midway through the thickness of the plate.

6.2.2 Work and Energy

Before proceeding to the Euler-Lagrange equations, we must define the appropriate spaces of admissible and virtual displacements. In this scenario, we will require that at least **two** derivatives be integrable in the interior and one on the boundary of the domain. This suggests a subspace of $H^2(\Omega)$ will be a suitable choice, where the boundary regularity is ensured by the trace Theorem for Sobolev spaces [cite](#). For the variational formulation, we once again enforce our Dirichlet boundary conditions strongly in both function spaces, with the homogeneous counterpart in the test space. These spaces are defined as:

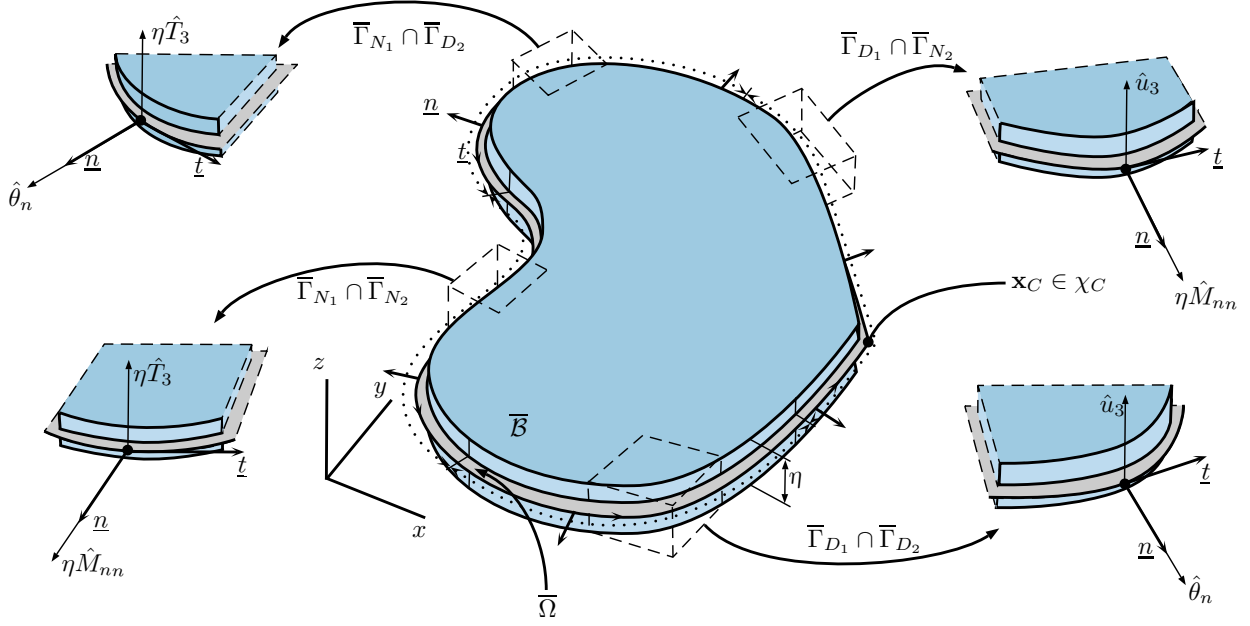


Figure 6.2: The problem setup and conventions for the Kirchhoff-Love plate problem.

$$\begin{aligned} \mathcal{U}_{KLP} &:= \left\{ u_3 : \Omega \rightarrow \mathbb{R} : u_3 \in H^2(\Omega), u_3|_{\Gamma_{D_1}} = \hat{u}_3, \text{ and } \theta_n(u_3)|_{\Gamma_{D_2}} = \hat{\theta}_n \right\} \\ \mathcal{V}_{KLP} &:= \left\{ v_3 : \Omega \rightarrow \mathbb{R} : v_3 \in H^2(\Omega), v_3|_{\Gamma_{D_1}} = 0, \text{ and } \theta_n(v_3)|_{\Gamma_{D_2}} = 0 \right\}. \end{aligned} \quad (6.29)$$

In this instance, there are portions of the boundary which will have either displacements, rotations, or both constrained, while other portions will have the energetically-conjugate applied tractions. Therefore, we decompose these conditions into Dirichlet and Neumann parts, i.e. $\Gamma = \overline{\Gamma_D} \cup \overline{\Gamma_N}$, respectively. Moreover, we can further decompose these conditions as $\Gamma_D = \Gamma_{D_1} \cup \Gamma_{D_2}$ and $\Gamma_N = \Gamma_{N_1} \cup \Gamma_{N_2}$ such that $\Gamma_{D_\alpha} \cap \Gamma_{N_\alpha} = \emptyset$ for $\alpha = 1, 2$. Physically, Γ_{D_1} is the boundary with a fixed displacement, Γ_{D_2} is the boundary with a fixed rotation, Γ_{N_1} is the boundary with applied shear forces, and Γ_{N_2} is the boundary with an applied bending moment. Similarly, we can define $\Gamma_1 := \Gamma_{D_1} \cup \Gamma_{N_1}$ and $\Gamma_2 = \Gamma_{D_2} \cup \Gamma_{N_2}$. Note that necessarily, $\Gamma = \overline{\Gamma_1} = \overline{\Gamma_2}$. Physically, displacements and work-conjugate applied shear forces are elements of Γ_1 while rotations and work-conjugate applied moments are elements of Γ_2 . The internal energy of the system is given via

$$\Pi_{int,KLP}(u_3) = \frac{1}{2} \| \| u_3 \| \|_B^2 \quad (6.30)$$

and the external work done on the system is given via

$$\begin{aligned}
W_{ext,KLP}(u_3) &= \int_{\mathcal{B}} f_3 u_3 \, d\mathcal{B} + \int_{\partial\mathcal{B}} \tau_3 u_3 \, d(\partial\mathcal{B}) + \int_{\partial\mathcal{B}} \hat{\underline{B}} \cdot \underline{\theta}(u_3) \, d(\partial\mathcal{B}) \\
&= \eta \int_{\Omega} f_3 u_3 \, d\Omega + \eta \int_{\Gamma_N} \tau_3 u_3 \, d\Gamma + \eta \int_{\Gamma_N} \hat{B}_{nt} \theta_t(u_3) \, d\Gamma + \eta \int_{\Gamma_N} \hat{B}_{nn} \theta_n(u_3) \, d\Gamma
\end{aligned} \tag{6.31}$$

where f_3 is the transverse loading or body force of the plate, τ_3 is the applied transverse boundary shearing, and $\hat{\underline{B}} = \hat{B}_{nn}\underline{n} + \hat{B}_{nt}\underline{t}$ is the applied moment with \hat{B}_{nn} the bending component and \hat{B}_{nt} the twisting moment. For this system to be in static equilibrium, it must follow that these two entities be equal to one another and that the potential energy configuration is minimal. Therefore, the Lagrangian of this system is given via

$$\mathcal{L}_{KLP}(u_3) = W_{ext,KLP}(u_3) - \Pi_{int,KLP}(u_3) \tag{6.32}$$

6.2.3 The Euler-Lagrange Equations and the Variational Formulation

To arrive at the variational formulation for linear elasticity, we must take a variation of the Lagrangian and find the stationary solution which corresponds to the minimum potential energy configuration

$$\begin{aligned}
\delta\mathcal{L}_{KLP}(u_3) &= \delta W_{ext,KLP}(u_3) - \delta\Pi_{int,KLP}(u_3) \\
&= \eta \int_{\Omega} f_3 (\delta u_3) \, d\Omega + \eta \int_{\Gamma_N} \tau_3 (\delta u_3) \, d\Gamma + \eta \int_{\Gamma_N} \hat{B}_{nt} \theta_t(\delta u_3) \, d\Gamma + \eta \int_{\Gamma_N} \hat{B}_{nn} \theta_n(\delta u_3) \, d\Gamma \\
&\quad - \int_{\Omega} \underline{\underline{B}}(u_3) : \underline{\underline{\kappa}}(\delta u_3) \, d\Omega
\end{aligned} \tag{6.33}$$

which follows immediately by the linearity of our constitutive model. The variational form is the extremal value of the Lagrangian corresponding to the root of the variation. Therefore letting $v_3 = \delta u_3$ and utilizing our stress-strain relationship, we have the following variational form

$$\int_{\Omega} \underline{\underline{\kappa}}(v_3) : \mathbb{C}_B : \underline{\underline{\kappa}}(u_3) \, d\Omega = \eta \int_{\Omega} f v_3 \, d\Omega + \eta \int_{\Gamma_N} \tau_3 v_3 \, d\Gamma - \eta \int_{\Gamma_N} \hat{B}_{nt} \frac{\partial v_3}{\partial t} \, d\Gamma + \eta \int_{\Gamma_N} \hat{B}_{nn} \theta_n(v_3) \, d\Gamma \quad (6.34)$$

where we have utilized (4.21) with (4.23) to obtain $\theta_t(v_3)$ explicitly in terms of the transverse displacement field.

At this point, formally posing the infinite-dimensional variational form of the Kirchhoff-Love plate is slightly problematic. Namely, we are dealing with a 4th-ordered PDE which allows us to enforce **two** boundary conditions along the boundary. However, to satisfy the energy associated with the variational form, we require the satisfaction of **three** boundary conditions as shown by the right-hand side of (6.34). This paradox was first solved by Kirchhoff who was able to show that the tangential derivative along the boundary is in fact dependent on the transverse displacement. He did this by integrating the tangential derivative by parts along the boundary to introduce a modified shear term coined the **ersatz force**. We demonstrate the construction of these forces here

$$\int_{\Gamma_N} \hat{B}_{nt} \frac{\partial v_3}{\partial t} \, d\Gamma = \hat{B}_{nt} v_3 \Big|_{\chi_C} - \int_{\Gamma_N} v_3 \frac{\partial \hat{B}_{nt}}{\partial t} \, d\Gamma \quad (6.35)$$

which allows us to express our variational form as

$$\begin{aligned} \int_{\Omega} \underline{\underline{\kappa}}(v_3) : \mathbb{C}_B : \underline{\underline{\kappa}}(u_3) \, d\Omega &= \eta \int_{\Omega} f v_3 \, d\Omega + \eta \int_{\Gamma_{N_1}} \left(\tau_3 + \frac{\partial \hat{B}_{nt}}{\partial t} \right) v_3 \, d\Gamma \\ &\quad - \hat{B}_{nt} v_3 \Big|_{\chi_{C_N}} + \eta \int_{\Gamma_{N_2}} \hat{B}_{nn} \theta_n(v_3) \, d\Gamma \end{aligned} \quad (6.36)$$

where, after introduction of the ersatz force, we are capable of splitting the Γ_1 and Γ_2 boundaries by energetically-conjugate displacements v_3 and rotations $\theta_n(v_3)$, respectively.

In this equation, we have presented χ_C which are the set of non-differentiable loci, e.g. corners, of Γ_1 , in addition to the set $\partial\Gamma_{N_1} \cup \partial\Gamma_{D_1}$, e.g. the contour endpoints of Γ_{D_1} and Γ_{D_2} , respectively. We will require subsets of χ_C in the derivation of Nitsche's method, which we define here. Namely, (i) $\chi_{C_N} := \chi_C \cap \Gamma_{N_1}$ and (ii) $\chi_{C_D} := \chi_C \cap \Gamma_{D_1}$. The notation $\cdot|_{\chi_C}$ should be

understood as an integral evaluation. In particular, if $\boldsymbol{x} \in \text{int}(\chi_C)$, the evaluation has both “left” and “right” points, while contour endpoints only have their evaluation from the interior.

Intuitively, this evaluation adds **corner forces** to the non-differentiable points which prevent an artificial lifting of the response surface. As we will present in the strong form of the Kirchhoff-Love plate, and later the Kirchhoff-Love shell, we weakly impose the constraint $B_{nt}^+(v_3) = B_{nt}^-(v_3)$ on $\text{int}(\chi_{C_N})$ which nullifies the application of these corner forces where two edges of the same BC type meet. Therefore, the only portion of the boundary where these corner forces truly appear are those which the boundary condition transitions from a Neumann-1 type to Dirichlet-1 type, or vice-versa. The variational form is now well-posed requiring the satisfaction of only two boundary conditions. Therefore, the infinite-dimensional Kirchhoff-Love plate problem statement is written as

Variational Formulation for the Kirchhoff-Love Plate

Find $u_3 \in \mathcal{U}_{KLP}$ such that

$$a_{KLP}(v_3, u_3) = \ell_{KLP}(v_3) \quad (6.37)$$

for all $v_3 \in \mathcal{V}_{KLP}$ where

$$\begin{aligned} a_{KLP}(v_3, u_3) &= \frac{\eta^3}{12} \int_{\Omega} \mathbb{C}^{\alpha\beta\lambda\mu} \beta_{\alpha\beta}(v_3) \beta_{\lambda\mu}(u_3) \, d\Omega \\ \ell_{KLP}(v_3) &= \eta \int_{\Omega} f_3 v_3 \, d\Omega + \eta \int_{\Gamma_{N_1}} \hat{T}_3 v_3 \, d\Gamma - \eta \hat{B}_{nt} v_3 \Big|_{\chi_{C_N}} + \eta \int_{\Gamma_{N_2}} \hat{B}_{nn} \theta_n(v_3) \, d\Gamma. \end{aligned} \quad (6.38)$$

Here we have introduced the following notation for obtaining the applied ersatz force \hat{T}_3 through its relation to the physically-intuitive loadings of applied shear and twisting moment in the variational formulation

$$\hat{T}_3 = \tau_3 + \underline{\nabla} \hat{B}_{nt} \cdot \underline{t}. \quad (6.39)$$

With the presentation of this weak formulation, we have the following lemma regarding the existence and uniqueness of the weak solution $u_3 \in \mathcal{U}_{KLP}$:

Lemma 9. *Suppose that for the Lebesgue measure $\lambda(\cdot)$ and Lebesgue-measurable sets Γ_{D_1} and Γ_{D_2} , one of the following hold:*

(i) $\lambda(\Gamma_{D_1}) > 0$ and Γ_{D_1} is not colinear

(ii) $\lambda(\Gamma_{D_1}) > 0$, $\lambda(\Gamma_{D_2}) > 0$, and $\lambda(\Gamma_{D_1} \cap \Gamma_{D_2}) > 0$

Then there exists a unique weak solution to (6.37). If $\lambda(\Gamma_{D_1}) = \emptyset$, then the solution is unique up to a constant.

Proof. We want to show that $a_{KLP}(\cdot, \cdot)$ induces a norm on \mathcal{V}_{KLP} . KLPt $\underline{v}, \underline{w} \in \mathcal{V}_{KLP}$. To demonstrate that $a_{KLP}(\cdot, \cdot)$ is a norm on \mathcal{V}_{KLP} , we must show it satisfies the properties of being a norm. Since $a_{KLP}(\cdot, \cdot)$ is a seminorm, it satisfies properties (a), (b), and (c) of:

$$\begin{aligned}
 (a) \quad a_{KLP}(\alpha \underline{v}, \alpha \underline{v}) &= |\alpha|^2 a_{KLP}(\underline{v}, \underline{v}) \text{ for } \alpha \in \mathbb{R} && \text{(absolute homogeneity)} \\
 (b) \quad a_{KLP}(\underline{v} + \underline{w}, \underline{v} + \underline{w}) &\leq a_{KLP}(\underline{v}, \underline{v}) + a_{KLP}(\underline{w}, \underline{w}) && \text{(subadditivity)} \\
 (c) \quad a_{KLP}(\underline{v}, \underline{v}) &> 0 && \text{(non-negativity)} \\
 (d) \quad a_{KLP}(\underline{v}, \underline{v}) = 0 &\leftrightarrow \underline{v} \equiv \underline{0} && \text{(definiteness)}
 \end{aligned} \tag{6.40}$$

All that must be shown is that (d) is also true which we accomplish by considering cases (i) and (ii) above independently. Both cases rely on demonstrating the function $v_3(\xi^1, \xi^2) = c_1 + c_2 \xi^1 + c_3 \xi^2$, which violates (d), yield a nonsingular Vandermonde system.

(i) Suppose $\Gamma_{D_1} \neq \emptyset$ and Γ_{D_1} is not colinear. Then $\exists \{(\xi_1^1, \xi_1^2), (\xi_2^1, \xi_2^2), (\xi_3^1, \xi_3^2)\} \in \Gamma_{D_1}$ that are not colinear from which we obtain the following Vandermonde system:

$$\begin{bmatrix} 1 & \xi_1^1 & \xi_1^2 \\ 1 & \xi_2^1 & \xi_2^2 \\ 1 & \xi_3^1 & \xi_3^2 \end{bmatrix} \begin{pmatrix} c_1 \\ c_2 \\ c_3 \end{pmatrix} = \begin{pmatrix} 0 \\ 0 \\ 0 \end{pmatrix} \tag{6.41}$$

Note that since the points are not all colinear, the system is nonsingular and thus the only solution is $c_1 = c_2 = c_3 = 0$.

(ii) Suppose $\Gamma_{D_1} \neq \emptyset$, $\Gamma_{D_2} \neq \emptyset$, and $\Gamma_{D_1} \cap \Gamma_{D_2} \neq \emptyset$. We define the closed, smooth, connected set with nonzero measure $\mathcal{Q} \subset \Gamma_{D_1} \cap \Gamma_{D_2}$. Then, select $\{(\xi_1^1, \xi_1^2), (\xi_2^1, \xi_2^2)\}$ as the endpoints of \mathcal{Q} . Then by the intermediate value theorem, $\exists (\xi_3^1, \xi_3^2) \in \mathcal{Q}$ such that the boundary normal $\underline{n}(\xi_3^1, \xi_3^2) = \alpha [(\xi_1^2 - \xi_2^2) \mathbf{a}_1 + (\xi_2^1 - \xi_1^1) \mathbf{a}_2]$ for some $\alpha \in \mathbb{R} \setminus \{0\}$. From these three points, we arrive at the following Vandermonde system:

$$\begin{bmatrix} 1 & \xi_1^1 & \xi_1^2 \\ 1 & \xi_2^1 & \xi_2^2 \\ 0 & n_1 & n_2 \end{bmatrix} \begin{pmatrix} c_1 \\ c_2 \\ c_3 \end{pmatrix} = \begin{bmatrix} 1 & \xi_1^1 & \xi_1^2 \\ 1 & \xi_2^1 & \xi_2^2 \\ 0 & \xi_1^2 - \xi_2^2 & \xi_2^1 - \xi_1^1 \end{bmatrix} \begin{pmatrix} c_1 \\ c_2 \\ c_3 \end{pmatrix} = \begin{pmatrix} 0 \\ 0 \\ 0 \end{pmatrix} \quad (6.42)$$

The determinant of this Vandermonde system is:

$$(\xi_1^1 - \xi_2^1)^2 + (\xi_1^2 - \xi_2^2)^2 > 0 \quad (6.43)$$

hence the system is nonsingular and the only solution is given by $c_1 = c_2 = c_3 = 0$.

Therefore, the definiteness of the bilinear form is ensured and $a_{KLP}(\cdot, \cdot)$ is indeed a norm on \mathcal{V} .

The existence and uniqueness of the weak solution follows from Theorem 1.

In the case where $\lambda(\Gamma_{D_1}) = \emptyset$, then $\Gamma = \Gamma_{D_2}$ and the problem reduces to that of the linear-elastic problem which was proved to have a solution unique up to a constant in Lemma 4. \square

Once again, we have strongly enforced our Dirichlet boundary conditions which we strive to release in the implementation of Nitsche's method. However, before we can state Nitsche's method for the Kirchhoff-Love plate, we must first infer the underlying strong formulation from the variational form (6.37).

6.2.4 The Strong Formulation for the Kirchhoff-Love Plate

Following an analogous procedure to what was performed in the context of linear elasticity we obtain

$$\begin{aligned}
\int_{\Omega} \underline{\underline{B}}(u_3) : \underline{\underline{\kappa}}(v_3) \, d\Omega &= - \int_{\Omega} \underline{\underline{B}}(u_3) : \nabla^s \nabla v_3 \, d\Omega \\
&= - \int_{\Gamma} \left(\underline{n} \underline{\underline{B}}(u_3) \right) \cdot \nabla v_3 \, d\Gamma + \int_{\Omega} \left(\nabla \cdot \underline{\underline{B}}(u_3) \right) \cdot \nabla v_3 \, d\Omega \\
&= \int_{\Gamma_2} B_{nn}(u_3) \theta_n(v_3) \, d\Gamma - \int_{\Gamma_1} B_{nt}(u_3) \frac{\partial v_3}{\partial t} \, d\Gamma + \int_{\Gamma_1} v_3 \left(\nabla \cdot \underline{\underline{B}}(u_3) \right) \underline{n} \, d\Gamma \\
&\quad - \int_{\Omega} \nabla \cdot \left(\nabla \cdot \underline{\underline{B}}(u_3) \right) v_3 \, d\Omega \\
&= \int_{\Gamma_2} B_{nn}(u_3) \theta_n(v_3) \, d\Gamma - B_{nt}(u_3) v_3|_{\chi_C} + \int_{\Gamma_1} v_3 T_3(u_3) \, d\Gamma \\
&\quad - \int_{\Omega} \nabla \cdot \left(\nabla \cdot \underline{\underline{B}}(u_3) \right) v_3 \, d\Omega
\end{aligned} \tag{6.44}$$

where we have utilized (4.23) and have introduced the following boundary quantities:

$$\begin{aligned}
B_{nn}(u_3) &= \underline{n} \underline{\underline{B}}(u_3) \underline{n} && \text{(Normal traction)} \\
B_{nt}(u_3) &= \underline{n} \underline{\underline{B}}(u_3) \underline{t} && \text{(Tangential traction)} \\
T_3(u_3) &= \left(\nabla \cdot \underline{\underline{B}}(u_3) \right) \underline{n} + \nabla B_{nt}(u_3) \cdot \underline{t} && \text{(Ersatz traction)}
\end{aligned} \tag{6.45}$$

Note that the ‘‘corner’’ evaluation here has become χ_C because the integration by parts was carried throughout Γ . Then, combining this result with the linear form $\ell_{KLP}(v)$ yields

$$\begin{aligned}
0 &= a_{KLP}(v_3, u_3) - \ell_{KLP}(v_3) \\
&= - \int_{\Omega} \left[\nabla \cdot \left(\nabla \cdot \underline{\underline{B}}(u_3) \right) + \eta f \right] v_3 \, d\Omega - \left[B_{nt}(u_3) - \eta \hat{B}_{nt} \right] v_3 \Big|_{\chi_{CN}} + \int_{\Gamma_{N_1}} v_3 \left[T_3(u_3) - \hat{T}_3 \right] \, d\Gamma \\
&\quad + \int_{\Gamma_{N_2}} \left[B_{nn}(u_3) - \eta \hat{B}_{nn} \right] \theta_n(v_3) \, d\Gamma
\end{aligned} \tag{6.46}$$

The remaining boundary integrals over the Dirichlet-1 and Dirichlet-2 boundaries and over χ_{CD} vanish due to strong homogeneous enforcement in the test space. However as we will demonstrate later, these terms will become the consistency terms in Nitsche’s method. Therefore, the strong formulation for Kirchhoff-Love plate is expressed as:

Strong Formulation for the Kirchhoff-Love Plate

Find $u_3 : \Omega \rightarrow \mathbb{R}$ such that:

$$\begin{aligned}
 -\underline{\nabla} \cdot \left(\underline{\nabla} \cdot \underline{\underline{B}}(u_3) \right) &= \eta f_3 && \text{in } \Omega \\
 u_3 &= \hat{u}_3 && \text{on } \Gamma_{D_1} \\
 \theta_n(v_3) &= \hat{\theta}_n && \text{on } \Gamma_{D_2} \\
 T_3(u_3) &= \eta \hat{T}_3 && \text{on } \Gamma_{N_1} \\
 B_{nn}(u_3) &= \eta \hat{B}_{nn} && \text{on } \Gamma_{N_2} \\
 B_{nt}(u_3) &= \eta \hat{B}_{nt} && \text{on } \chi_{C_N} \\
 B_{nt}^+(u_3) &= B_{nt}^-(u_3) && \text{on int } (\chi_{C_N})
 \end{aligned} \tag{6.47}$$

We now have the ability to express Nitsche's method for linear elasticity given the inferred strong form of the PDE.

6.2.5 Nitsche's Variational Form for the Kirchhoff-Love Plate

To begin our derivation of Nitsche's method for the Kirchhoff-Love plate, we define the following discrete spaces of admissible and virtual displacements which release the strong-enforcement of Dirichlet boundary conditions

$$\begin{aligned}
 \mathcal{V}_{KLP}^h &\equiv \mathcal{U}_{KLP}^h \\
 &:= \left\{ u_3^h \in H^2(\Omega) : T_3(u_3^h) \in L^2(\Gamma_{D_1}), B_{nn}(u_3^h) \in L^2(\Gamma_{D_2}), u_3^h(\xi^1, \xi^2) = \sum_{i=1}^n c_i N_i(\xi^1, \xi^2) \right\}.
 \end{aligned} \tag{6.48}$$

With the definition of these discrete spaces, we can express the discrete Galerkin formulation for Nitsche's method as follows:

Nitsche's Method for the Kirchhoff-Love Plate

Find $u_3^h \in \mathcal{U}_{KLP}^h$ such that

$$a_{KLP}^h(v_3^h, u_3^h) = \ell_{KLP}^h(v_3^h) \quad (6.49)$$

for all $v_3^h \in \mathcal{V}_{KLP}^h$ where:

$$\begin{aligned}
 a_{KLP}^h(v_3^h, u_3^h) &= a_{KLP}(v_3^h, u_3^h) - \underbrace{\int_{\Gamma_{D_1}} v_3^h T_3(u_3^h) d\Gamma - \int_{\Gamma_{D_2}} B_{nn}(u_3^h) \theta_n(v_3^h) d\Gamma + B_{nt}(u_3^h) v_3^h \Big|_{\chi_{CD}}}_{\text{Consistency Terms}} \\
 &\quad - \underbrace{\int_{\Gamma_{D_1}} u_3^h T_3(v_3^h) d\Gamma - \int_{\Gamma_{D_2}} B_{nn}(v_3^h) \theta_n(u_3^h) d\Gamma + B_{nt}(v_3^h) u_3^h \Big|_{\chi_{CD}}}_{\text{Symmetry Terms}} \\
 &\quad + \underbrace{\frac{\eta^3 EC_{pen,1}}{6h^3} \int_{\Gamma_{D_1}} v_3^h u_3^h d\Gamma + \frac{\eta^3 EC_{pen,2}}{6h} \int_{\Gamma_{D_2}} \theta_n(v_3^h) \theta_n(u_3^h) d\Gamma}_{\text{Penalty Terms}} \\
 \ell_{KLP}^h(v_3^h) &= \ell_{KLP}(v_3^h) - \underbrace{\int_{\Gamma_{D_1}} \hat{u}_3 T_3(v_3^h) d\Gamma - \int_{\Gamma_{D_2}} B_{nn}(v_3^h) \hat{\theta}_n d\Gamma + B_{nt}(v_3^h) \hat{u}_3 \Big|_{\chi_{CD}}}_{\text{Symmetry Terms}} \\
 &\quad + \underbrace{\frac{\eta^3 EC_{pen,1}}{6h^3} \int_{\Gamma_{D_1}} v_3^h \hat{u}_3 d\Gamma + \frac{\eta^3 EC_{pen,2}}{6h} \int_{\Gamma_{D_2}} \theta_n(v_3^h) \hat{\theta}_n d\Gamma}_{\text{Penalty Terms}}
 \end{aligned} \quad (6.50)$$

6.2.6 Consistency and Symmetry of Nitsche's Method for the Kirchhoff-Love Plate

Once again, the symmetry of the discrete bilinear form arising through Nitsche's method (6.49) is obvious. We have the following lemma which details the proof of consistency of $a_{KLP}^h(\cdot, \cdot)$ with the strong form of the original PDE, provided the exact solution u_3 to (6.37) satisfies an additional regularity condition:

Lemma 10. *Suppose that the unique weak solution u_3 of (6.37) satisfies the regularity conditions $T_3(u_3) \in L^2(\Gamma_{D_1})$ and $\theta_n(u_3) \in L^2(\Gamma_{D_2})$. Then:*

$$a_{KLP}^h(v_3^h, u_3) = \ell_{KLP}^h(v_3^h) \quad (6.51)$$

for all $v_3^h \in \mathcal{V}_{KLP}^h$.

Proof. The result follows immediately through two applications of integration by parts which are performed explicitly in (6.46). Observe that:

$$\begin{aligned}
a_{KLP}^h(v_3^h, u_3) - \ell_{KLP}^h(v_3^h) &= \int_{\Omega} \underline{\underline{B}}(u_3) : \underline{\underline{\kappa}}(v_3^h) \, d\Omega - \int_{\Gamma_{D_1}} v_3^h T_3(u_3) \, d\Gamma - \int_{\Gamma_{D_2}} B_{nn}(u_3) \theta_n(v_3^h) \, d\Gamma \\
&\quad + B_{nt}(u_3) v_3^h \Big|_{\chi_{CD}} - \int_{\Gamma_{D_1}} T_3(v_3^h) [u_3 - \hat{u}_3] \, d\Gamma + B_{nt}(v_3^h) [u_3 - \hat{u}_3] \Big|_{\chi_{CD}} \\
&\quad - \int_{\Gamma_{D_2}} B_{nn}(v_3^h) [\theta_n(u_3) - \hat{\theta}_n] \, d\Gamma + \frac{\eta^3 EC_{pen,1}}{6h^3} \int_{\Gamma_{D_1}} v_3^h [u_3 - \hat{u}_3] \, d\Gamma \\
&\quad + \frac{\eta^3 EC_{pen,2}}{6h} \int_{\Gamma_{D_2}} \theta_n(v_3^h) [\theta_n(u_3) - \hat{\theta}_n] \, d\Gamma - \eta \int_{\Omega} f_3 v_3^h \, d\Omega \\
&\quad - \eta \int_{\Gamma_{N_1}} \hat{T}_3 v_3^h \, d\Gamma + \eta \hat{B}_{nt} v_3^h \Big|_{\chi_{CN}} - \eta \int_{\Gamma_{N_2}} \hat{B}_{nn} \theta_n(v_3^h) \, d\Gamma \\
&= - \int_{\Omega} [\nabla \cdot (\nabla \cdot \underline{\underline{B}}(u_3)) + \eta f_3] v_3^h \, d\Omega - \int_{\Gamma_{D_1}} T_3(v_3^h) [u_3 - \hat{u}_3] \, d\Gamma \\
&\quad + B_{nt}(v_3^h) [u_3 - \hat{u}_3] \Big|_{\chi_{CD}} - \int_{\Gamma_{D_2}} B_{nn}(v_3^h) [\theta_n(u_3) - \hat{\theta}_n] \, d\Gamma \\
&\quad + \frac{\eta^3 EC_{pen,1}}{6h^3} \int_{\Gamma_{D_1}} v_3^h [u_3 - \hat{u}_3] \, d\Gamma + \int_{\Gamma_{N_1}} [T_3(u_3) - \eta \hat{T}_3] v_3^h \, d\Gamma \\
&\quad + \frac{\eta^3 EC_{pen,2}}{6h} \int_{\Gamma_{D_2}} \theta_n(v_3^h) [\theta_n(u_3) - \hat{\theta}_n] \, d\Gamma \\
&\quad - [B_{nt}(u_3) - \eta \hat{B}_{nt}] v_3^h \Big|_{\chi_{CN}} + \int_{\Gamma_{N_2}} [B_{nn}(u_3) - \eta \hat{B}_{nn}] \theta_n(v_3^h) \, d\Gamma \\
&= 0
\end{aligned} \tag{6.52}$$

Hence the bilinear form is consistent with the strong form of the Kirchhoff-Love plate. \square

6.2.7 Continuity and Coercivity of Nitsche's Method for the Kirchhoff-Love Plate

To preface this section, we define the mesh-dependent norm with which we prove continuity, coercivity, and later error estimates:

$$\begin{aligned}
\|v_3\|_{\mathcal{U}_{KLP}^h}^2 &:= \|\|v_3\|\|_B^2 + \frac{\eta^3 EC_{pen,1}}{6h^3} \|v_3\|_{0,\Gamma}^2 + \frac{\eta^3 EC_{pen,2}}{6h} \|\theta_n(v_3)\|_{0,\Gamma}^2 + \frac{6h^3}{\eta^3 E} \|T_3(v_3)\|_{0,\Gamma}^2 \\
&+ \frac{6h}{\eta^3 E} \|B_{nn}(v_3)\|_{0,\Gamma}^2 + \frac{6h^2}{\eta^3 E} |B_{nt}(v_3)|^2 \Big|_{\chi_C} + \frac{\eta^3 E}{6h^2} |v_3|^2 \Big|_{\chi_C}.
\end{aligned} \tag{6.53}$$

Note that (6.53) is indeed a norm over \mathcal{U}_{KLP}^h , and moreover \mathcal{V}_{KLP}^h , since $\|\cdot\|_B$ is a seminorm with a constant and a linear in the kernel and the L^2 penalty terms enforce such modes to be zero for the norm to vanish. Additionally, by (5.16), (5.17), (5.20), (5.21), (5.25), and (5.28), this norm satisfies the following relationship $\forall v_3^h \in \mathcal{V}_{KLP}^h$ with $C_\ell^{-1} \geq 1 + \max \left[C_{tr,T} C_{inv,T} + (1 + C_{tr,M}) C_{tr,B}, \frac{C_{tr,u_\Gamma}}{C_{pen,1}} \right]$:

$$\begin{aligned}
\|v_3^h\|_{\mathcal{U}_{KLP}^h}^2 &\leq \|\|v_3^h\|\|_B^2 + \frac{\eta^3 EC_{pen,1}}{6h^3} \|v_3^h\|_{0,\Gamma}^2 + \frac{\eta^3 EC_{pen,2}}{6h} \|\theta_n(v_3^h)\|_{0,\Gamma}^2 + \frac{6h^2 C_{tr,T}}{\eta^3 E} \|T_3(v_3^h)\|_{0,\Omega}^2 \\
&+ \frac{6C_{tr,B}}{\eta^3 E} \|\underline{B}(v_3^h)\|_{0,\Omega}^2 + \frac{6h C_{tr,M}}{\eta^3 E} \|\underline{B}(v_3^h)\|_{0,\Gamma}^2 + \frac{\eta^3 EC_{tr,u_\Gamma}}{6h^3} \|v_3^h\|_{0,\Gamma}^2 \\
&\leq (1 + C_{tr,T} C_{inv,T} + (1 + C_{tr,M}) C_{tr,B}) \|\|v_3^h\|\|_B^2 + \frac{\eta^3 EC_{pen,2}}{6h} \|\theta_n(v_3^h)\|_{0,\Gamma}^2 \\
&+ \frac{\eta^3 E}{6h^3} (C_{pen,1} + C_{tr,u_\Gamma}) \|v_3^h\|_{0,\Gamma}^2 \\
&\leq \frac{1}{C_\ell} \left(\|\|v_3^h\|\|_B^2 + \frac{\eta^3 EC_{pen,2}}{6h} \|\theta_n(v_3^h)\|_{0,\Gamma}^2 + \frac{\eta^3 EC_{pen,1}}{6h^3} \|v_3^h\|_{0,\Gamma}^2 \right).
\end{aligned} \tag{6.54}$$

Now that we have demonstrated that $\|\cdot\|_{\mathcal{U}_{KLP}^h}$ is indeed a norm, we are able to prove the continuity, that is the boundedness, of the mesh-dependent bilinear form $a_{KLP}^h(\cdot, \cdot)$ in the following lemma:

Lemma 11. *The following continuity statement holds:*

$$a_{KLP}^h(v_3^h, w_3) \leq C_{cont,KLP} \|v_3^h\|_{\mathcal{U}_{KLP}^h} \|w_3\|_{\mathcal{U}_{KLP}^h} \tag{6.55}$$

for all $v_3^h \in \mathcal{V}_{KLP}^h$ and w_3 such that $T_3(w_3) \in L^2(\Gamma_{D_1})$ and $B_{nn}(w_3) \in L^2(\Gamma_{D_2})$.

Proof. To prove the continuity estimate, we first write:

$$\begin{aligned}
a_{KLP}^h(v_3^h, w_3) &= a_{KLP}(v_3^h, w_3) + \int_{\Gamma_{D_1}} v_3^h T_3(w_3) \, d\Gamma + \int_{\Gamma_{D_2}} B_{nn}(w_3) \theta_n(v_3^h) \, d\Gamma - B_{nt}(w_3) v_3^h \Big|_{\chi_C} \\
&\quad + \int_{\Gamma_{D_1}} w_3 T_3(v_3^h) \, d\Gamma + \int_{\Gamma_{D_2}} B_{nn}(v_3^h) \theta_n(w_3) \, d\Gamma - B_{nt}(v_3^h) w_3 \Big|_{\chi_C} \\
&\quad + \frac{\eta^3 EC_{pen,1}}{6h^3} \int_{\Gamma_{D_1}} v_3^h w_3 \, d\Gamma + \frac{\eta^3 EC_{pen,2}}{6h} \int_{\Gamma_{D_2}} \theta_n(v_3^h) \theta_n(w_3) \, d\Gamma.
\end{aligned} \tag{6.56}$$

Observe we can bound:

$$a_{KLP}(v_3^h, w_3) + \frac{\eta^3 EC_{pen,1}}{6h^3} \int_{\Gamma_{D_1}} v_3^h w_3 \, d\Gamma + \frac{\eta^3 EC_{pen,2}}{6h} \int_{\Gamma_{D_2}} \theta_n(v_3^h) \theta_n(w_3) \, d\Gamma \leq \|v_3^h\|_{\mathcal{U}_{KLP}^h} \|w_3\|_{\mathcal{U}_{KLP}^h}. \tag{6.57}$$

Next, we bound the remaining terms via:

$$\begin{aligned}
\int_{\Gamma_{D_1}} v_3^h T_3(w_3) \, d\Gamma &\leq \|v_3^h\|_{0,\Gamma} \|T_3(w_3)\|_{0,\Gamma} \\
&\leq \sqrt{\frac{1}{h^3} \|v_3^h\|_{0,\Gamma}^2} \sqrt{h^3 \|T_3(w_3)\|_{0,\Gamma}^2} \\
&\leq \|v_3^h\|_{\mathcal{U}_{KLP}^h} \|w_3\|_{\mathcal{U}_{KLP}^h}
\end{aligned} \tag{6.58}$$

and

$$\begin{aligned}
\int_{\Gamma_{D_2}} B_{nn}(v_3^h) \theta_n(w_3) \, d\Gamma &\leq \|B_{nn}(v_3^h)\|_{0,\Gamma} \|\theta_n(w_3)\|_{0,\Gamma} \\
&\leq \sqrt{h \|B_{nn}(v_3^h)\|_{0,\Gamma}^2} \sqrt{\frac{1}{h} \|\theta_n(w_3)\|_{0,\Gamma}^2} \\
&\leq \|v_3^h\|_{\mathcal{U}_{KLP}^h} \|w_3\|_{\mathcal{U}_{KLP}^h}
\end{aligned} \tag{6.59}$$

and lastly, the boundary evaluation via:

$$\begin{aligned}
B_{nt}(w_3) v_3^h \Big|_{\chi_C} &\leq \left(|B_{nt}(w_3)| \Big|_{\chi_C} \right) \left(|v_3^h| \Big|_{\chi_C} \right) \\
&\leq \sqrt{h^2 |B_{nt}(w_3)|^2 \Big|_{\chi_C}} \sqrt{\frac{1}{h^2} |v_3^h|^2 \Big|_{\chi_C}} \\
&\leq \|v_3^h\|_{\mathcal{U}_{KLP}^h} \|w_3\|_{\mathcal{U}_{KLP}^h}.
\end{aligned} \tag{6.60}$$

Clearly, these inequalities hold for the symmetric counterpart of these terms. Collecting these inequalities yields:

$$a_{KLP}^h(v_3^h, w_3) \leq C_{cont,KLP} \|v_3^h\|_{\mathcal{U}_{KLP}^h} \|w_3\|_{\mathcal{U}_{KLP}^h} \quad (6.61)$$

with $C_{cont,KLP} = 7$.

□

Next, we prove the coercivity of the bilinear form with respect to $\|\cdot\|_{\mathcal{U}_{KLP}^h}$ in the following lemma:

Lemma 12. *The following coercivity statement holds:*

$$a_{KLP}^h(v_3^h, v_3^h) \geq C_{coer,KLP} \|v_3^h\|_{\mathcal{U}_{KLP}^h}^2, \quad \forall v_3^h \in \mathcal{V}_{KLP}^h \quad (6.62)$$

Proof. Let $v_3^h \in \mathcal{V}_{KLP}^h$, $\varepsilon_1 > 6C_{tr,T}C_{inv,T}$, $\varepsilon_2 > 6C_{tr,B}$, $\varepsilon_3 > 6C_{tr,M}C_{inv,B}$, and observe that by Cauchy-Schwarz and Young's inequalities:

$$\int_{\Gamma_{D_1}} v_3^h T_3(v_3^h) \, d\Gamma \leq \|v_3^h\|_{0,\Gamma} \|T_3(v_3^h)\|_{0,\Gamma} \leq \frac{\eta^3 E \varepsilon_1}{12h^3} \|v_3^h\|_{0,\Gamma}^2 + \frac{3h^3}{\eta^3 E \varepsilon_1} \|T_3(v_3^h)\|_{0,\Gamma}^2 \quad (6.63)$$

and

$$\int_{\Gamma_{D_2}} B_{nn}(v_3^h) \theta_n(v_3^h) \, d\Gamma \leq \|B_{nn}(v_3^h)\|_{0,\Gamma} \|\theta_n(v_3^h)\|_{0,\Gamma} \leq \frac{3h}{\eta^3 E \varepsilon_2} \|B_{nn}(v_3^h)\|_{0,\Gamma}^2 + \frac{\eta^3 E \varepsilon_2}{12h} \|\theta_n(v_3^h)\|_{0,\Gamma}^2 \quad (6.64)$$

Utilizing (5.20) and (5.21), we obtain the following estimate for the boundary evaluation:

$$B_{nt}(v_3^h) v_3^h \Big|_{\chi_C} \leq \left(\left| B_{nt}(v_3^h) \right|_{\chi_C}^2 \right) \left(\left| v_3^h \right|_{\chi_C}^2 \right) \leq \frac{3h C_{tr,M}}{\eta^3 E \varepsilon_3} \|B_{nt}(v_3^h)\|_{0,\Gamma}^2 + \frac{\eta^3 E \varepsilon_3 C_{tr,u\Gamma}}{12h^3} \|v_3^h\|_{0,\Gamma}^2 \quad (6.65)$$

Therefore, utilizing (6.63), (6.64), (6.65), (5.16) through (5.21), (5.25), and for $C_{pen,1} > 1/2 + 6C_{tr,T}C_{inv,T} + 6C_{tr,M}C_{tr,B}C_{tr,u\Gamma}$ and $C_{pen,2} > 1/2 + 6C_{tr,B}$, we have the following:

$$\begin{aligned}
a_{KLP}^h(v_3^h, v_3^h) &\geq \left\| \|v_3^h\|_B^2 - 2 \int_{\Gamma_{D_1}} v_3^h T_3(v_3^h) d\Gamma - 2 \int_{\Gamma_{D_2}} B_{nn}(v_3^h) \theta_n(v_3^h) d\Gamma - 2 B_{nt}(v_3^h) v_3^h \right\|_{\chi_C} \\
&\quad + \frac{\eta^3 E C_{pen,1}}{6h^3} \|v_3^h\|_{0,\Gamma}^2 + \frac{\eta^3 E C_{pen,2}}{6h} \|\theta_n(v_3^h)\|_{0,\Gamma}^2 \\
&\geq \left\| \|v_3^h\|_B^2 - \left(\frac{\eta^3 E \varepsilon_1}{6h^3} \|v_3^h\|_{0,\Gamma}^2 + \frac{6h^3}{\eta^3 E \varepsilon_1} \|T_3(v_3^h)\|_{0,\Gamma}^2 \right) \right. \\
&\quad - \left(\frac{6h}{\eta^3 E \varepsilon_2} \|B_{nn}(v_3^h)\|_{0,\Gamma}^2 + \frac{\eta^3 E \varepsilon_2}{6h} \|\theta_n(v_3^h)\|_{0,\Gamma}^2 \right) \\
&\quad - \left(\frac{6h C_{tr,M}}{\eta^3 E \varepsilon_3} \|B_{nt}(v_3^h)\|_{0,\Gamma}^2 + \frac{\eta^3 E \varepsilon_3 C_{tr,u\Gamma}}{6h^3} \|v_3^h\|_{0,\Gamma}^2 \right) \\
&\quad + \frac{\eta^3 E C_{pen,1}}{6h^3} \|v_3^h\|_{0,\Gamma}^2 + \frac{\eta^3 E C_{pen,2}}{6h} \|\theta_n(v_3^h)\|_{0,\Gamma}^2 \\
&\geq \left(1 - \frac{C_{tr,T} C_{inv,T}}{\varepsilon_1} - \frac{C_{tr,B}}{\varepsilon_2} - \frac{C_{tr,M} C_{tr,B}}{\varepsilon_3} \right) \left\| \|v_3^h\|_B^2 \right. \\
&\quad + \frac{\eta^3 E (C_{pen,1} - \varepsilon_1 - \varepsilon_3 C_{tr,u\Gamma})}{6h^3} \|v_3^h\|_{0,\Gamma}^2 + \frac{\eta^3 E (C_{pen,2} - \varepsilon_2)}{6h} \|\theta_n(v_3^h)\|_{0,\Gamma}^2 \\
&\geq \frac{1}{2} \left(\left\| \|v_3^h\|_B^2 + \frac{\eta^3 E C_{pen,1}}{6h^3} \|v_3^h\|_{0,\Gamma}^2 + \frac{\eta^3 E C_{pen,2}}{6h} \|\theta_n(v_3^h)\|_{0,\Gamma}^2 \right) \right. \\
&\geq C_{coer,KLP} \|v_3^h\|_{\mathcal{U}_{KLP}^h}^2
\end{aligned} \tag{6.66}$$

where $C_{coer,KLP} = \frac{1}{2} \left(1 + \max \left[C_{tr,T} C_{inv,T} + (1 + C_{tr,M}) C_{tr,B}, \frac{C_{tr,u\Gamma}}{C_{pen,1}} \right] \right)^{-1}$ and we have made use of (6.54) in the last inequality. \square

6.2.8 A Priori Error Estimates

Before proceeding with discretization-dependent approximation theorems, we have the following corollary to Theorem 3.

Corollary 13. *Let u_3 and u_3^h denote the unique solutions of problems (6.37) and (6.49), respectively. Furthermore, suppose the hypotheses of Theorem 1 and Theorem 3 are satisfied. Then,*

$$\|u_3 - u_3^h\|_{\mathcal{U}_{KLP}^h} \leq \left(15 + 14 \max \left[C_{tr,T} C_{inv,T} + (1 + C_{tr,M}) C_{tr,B}, \frac{C_{tr,u\Gamma}}{C_{pen,1}} \right] \right) \inf_{w_3^h \in \mathcal{U}_{KLP}^h} \|u_3 - w_3^h\|_{\mathcal{U}_{KLP}^h}. \tag{6.67}$$

Proof. Recall Theorem 3 and the estimate provided therein. Then the result follows immediately by the continuity and coercivity constants defined in Lemma 11 and Lemma 12 and the consistency inherent to Nitsche’s variational formulation for the Kirchhoff-Love plate.

□

6.3 Linearized Kirchhoff-Love Shell

In the previous two sections, we have independently derived and devised Nitsche’s method for the problems of linear elasticity and the Kirchhoff-Love plate. Herein, we employ the techniques presented in those sections to arrive at Nitsche’s method for the Kirchhoff-Love shell. In this setting, the presence of intrinsic curvatures introduces a coupling between membrane and bending displacement modes.

6.3.1 Kirchhoff-Love shell formulation

Shell models simulate the structural response of a three-dimensional immersed manifold subject to both in-plane and out-of-plane loadings. These models are similarly idealized through a midsurface model with linearized through-thickness displacement profiles. Moreover, the Kirchhoff-Love shell paradigm assumes there is no transverse shearing strain through-thickness which leads linear elasticity-type PDE over the in-plane displacements, a Kirchhoff-Love plate-type PDE over the out-of-plane displacements, and a coupling between the two due to intrinsic curvatures present in the curved manifold.

6.3.2 Work and Energy

As we will see in the following derivations, the displacement solution field for the Kirchhoff-Love shell require that at least one derivative be integrable along the convective manifold coordinates while at least two derivatives be integrable in the direction of the midsurface normal director, in the interior of Ω . Moreover, we will require that at least one derivative be integrable on the boundary Γ . We then strongly enforce the Dirichlet boundary conditions for displacements and

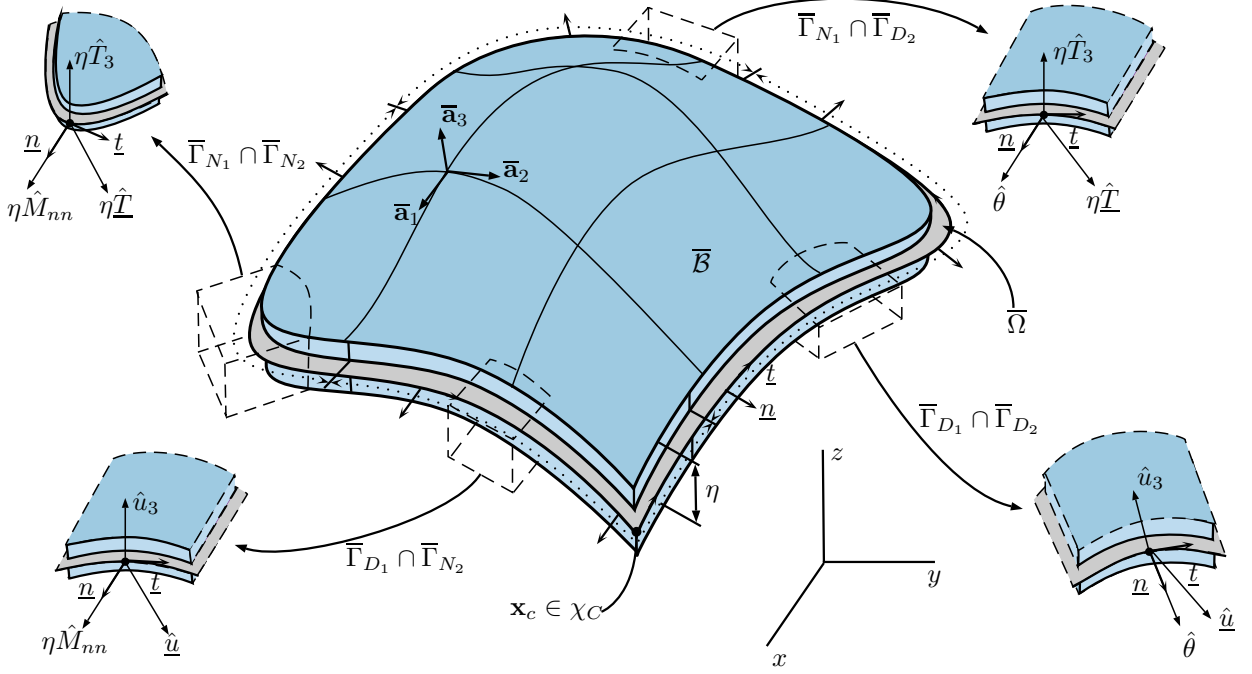


Figure 6.3: An arbitrary shell domain. All positive conventions for degrees of freedom and applied loadings are depicted.

rotations while weakly enforcing the Neumann boundary conditions. However, these derivatives are not classical derivatives since they are over a manifold. Therefore, to define our spaces of admissible test and trial functions, we must first define the auxiliary spaces $\hat{\mathcal{M}}$ and \mathcal{M} which imposes the appropriate regularity on classical derivatives and the required smoothness associated with the geometric mapping, respectively. Let

$$\hat{\mathcal{M}} := H^1(\hat{\Omega}) \times H^1(\hat{\Omega}) \times H^2(\hat{\Omega}) \quad (6.68)$$

and

$$\mathcal{M} := \left\{ \mathbf{u}: \Omega \rightarrow \mathbb{R}^3: \mathbf{u} \circ \mathbf{x} \in \hat{\mathcal{M}} \text{ and } \mathbf{x} \in H^2(\hat{\Omega}) \times H^2(\hat{\Omega}) \times H^3(\hat{\Omega}) \right\} \quad (6.69)$$

Then, we formally define the spaces of admissible and virtual displacements as

$$\begin{aligned}
\mathcal{U}_{KLS} &:= \left\{ \mathbf{u} \in \mathcal{M} : \mathbf{u}|_{\Gamma_{D_1}} = \hat{\mathbf{u}} \text{ and } \theta_n(\mathbf{u})|_{\Gamma_{D_2}} = \hat{\theta}_n \right\} \\
\mathcal{V}_{KLS} &:= \left\{ \mathbf{v} \in \mathcal{M} : \mathbf{v}|_{\Gamma_{D_1}} = \mathbf{0} \text{ and } \theta_n(\mathbf{v})|_{\Gamma_{D_2}} = 0 \right\}.
\end{aligned} \tag{6.70}$$

The energy balance of the system between internal energies and external loadings yields a weak formulation through the principle of virtual work for the Kirchhoff-Love shell. As in the case of the flat plate, there are portions of the boundary which will have either displacements, rotations, or both constrained, while other portions will have the energetically-conjugate applied tractions. Therefore, we decompose these conditions into Dirichlet and Neumann parts, i.e. $\Gamma = \overline{\Gamma_D} \cup \overline{\Gamma_N}$, respectively. Moreover, we can further decompose these conditions as $\Gamma_D = \Gamma_{D_1} \cup \Gamma_{D_2}$ and $\Gamma_N = \Gamma_{N_1} \cup \Gamma_{N_2}$ such that $\Gamma_{D_\alpha} \cap \Gamma_{N_\alpha} = \emptyset$ for $\alpha = 1, 2$. Physically, Γ_{D_1} is the boundary with a fixed displacement, Γ_{D_2} is the boundary with a fixed rotation, Γ_{N_1} is the boundary with applied shear forces, and Γ_{N_2} is the boundary with an applied bending moment. Similarly, we can define $\Gamma_1 := \Gamma_{D_1} \cup \Gamma_{N_1}$ and $\Gamma_2 = \Gamma_{D_2} \cup \Gamma_{N_2}$. Note that necessarily, $\Gamma = \overline{\Gamma_1} = \overline{\Gamma_2}$. Physically, displacements and work-conjugate applied shear forces are elements of Γ_1 while rotations and work-conjugate applied moments are elements of Γ_2 . Given a displacement field \mathbf{u} , the internal energy of the system is given by

$$\Pi_{int,KLS}(\mathbf{u}) = \frac{1}{2} \|\mathbf{u}\|_A^2 + \frac{1}{2} \|\mathbf{u}\|_B^2 \tag{6.71}$$

and the external work done on the system is given by

$$\begin{aligned}
W_{ext,KLS}(\mathbf{u}) &= \int_{\mathcal{B}} \mathbf{f} \cdot \mathbf{u} \, d\mathcal{B} + \int_{\partial\mathcal{B}} \hat{\boldsymbol{\tau}} \cdot \mathbf{u} \, d(\partial\mathcal{B}) + \int_{\partial\mathcal{B}} \hat{\underline{B}} \cdot \underline{\theta}(\mathbf{u}) \, d(\partial\mathcal{B}) \\
&= \eta \int_{\Omega} \mathbf{f} \cdot \mathbf{u} \, d\Omega + \eta \int_{\Gamma_N} \hat{\boldsymbol{\tau}} \cdot \underline{\mathbf{u}} \, d\Gamma + \eta \int_{\Gamma_N} \tau_3 u_3 \, d\Gamma + \eta \int_{\Gamma_N} \hat{B}_{nt} \theta_t(\mathbf{u}) \, d\Gamma \\
&\quad + \eta \int_{\Gamma_N} \hat{B}_{nn} \theta_n(\mathbf{u}) \, d\Gamma.
\end{aligned} \tag{6.72}$$

Here $\mathbf{f} = \underline{\mathbf{f}} + f_3 \mathbf{a}^3$ is a distributed loading, $\hat{\boldsymbol{\tau}} = \hat{\boldsymbol{\tau}} + \tau_3 \mathbf{a}_3$ is the boundary traction, and $\hat{\underline{B}} = \hat{B}_{nn} \underline{n} + \hat{B}_{nt} \underline{t}$ is the applied moment. Moreover, τ_3 is an applied transverse shear force, $\underline{\tau}$ is an in-plane membrane loading, \hat{B}_{nt} is an applied twisting moment, and \hat{B}_{nn} is an applied bending

moment. For the shell system to be in static equilibrium, the internal energy must equal the external work. Furthermore, the system must assume a minimal potential energy configuration. The Lagrangian of the system is given by:

$$\mathcal{L}_{KLS}(\mathbf{u}) = W_{ext,KLS}(\mathbf{u}) - \Pi_{int,KLS}(\mathbf{u}). \quad (6.73)$$

6.3.3 The Euler-Lagrange Equations and the Variational Formulation

To arrive at the variational formulation of the Kirchhoff-Love shell, we must take a variation of this Lagrangian and find the stationary solution which corresponds to the minimum potential energy configuration:

$$\begin{aligned} \delta \mathcal{L}_{KLS}(\mathbf{u}) &= \delta W_{ext,KLS}(\mathbf{u}) - \delta \Pi_{int,KLS}(\mathbf{u}) \\ &= \eta \int_{\Omega} \mathbf{f} \cdot \delta \mathbf{u} \, d\Omega + \eta \int_{\Gamma_N} \underline{\tau} \cdot \delta \underline{v} \, d\Gamma + \eta \int_{\Gamma_N} \tau_3 (\delta u_3) \, d\Gamma + \eta \int_{\Gamma_N} \hat{B}_{nt} \theta_t(\delta \mathbf{u}) \, d\Gamma \\ &\quad + \eta \int_{\Gamma_N} \hat{B}_{nn} \theta_n(\delta \mathbf{u}) \, d\Gamma - \int_{\Omega} \underline{\underline{A}}(\mathbf{u}) : \underline{\underline{\gamma}}(\delta \mathbf{u}) \, d\Omega - \int_{\Omega} \underline{\underline{B}}(\mathbf{u}) : \underline{\underline{\kappa}}(\delta \mathbf{u}) \, d\Omega \end{aligned} \quad (6.74)$$

which follows immediately by the linearity of our constitutive model. The variational form is the extremal value of the Lagrangian corresponding to the root of the variation. Therefore letting $\mathbf{v} = \delta \mathbf{u}$ and utilizing our stress-strain relationship, we have the following variational form:

$$\begin{aligned} \int_{\Omega} \underline{\underline{A}}(\mathbf{u}) : \underline{\underline{\gamma}}(\mathbf{v}) \, d\Omega + \int_{\Omega} \underline{\underline{B}}(\mathbf{u}) : \underline{\underline{\kappa}}(\mathbf{v}) \, d\Omega &= \eta \int_{\Omega} \mathbf{f} \cdot \mathbf{v} \, d\Omega + \eta \int_{\Gamma_N} \underline{\tau} \cdot \underline{v} \, d\Gamma + \eta \int_{\Gamma_N} \tau_3 v_3 \, d\Gamma \\ &\quad - \eta \int_{\Gamma_N} \hat{B}_{nt} \left[(\underline{\nabla} \mathbf{v})^T \mathbf{a}_3 \right] \cdot \underline{t} \, d\Gamma + \eta \int_{\Gamma_N} \hat{B}_{nn} \theta_n(\mathbf{v}) \, d\Gamma \end{aligned} \quad (6.75)$$

where we have utilized (4.23) to obtain $\theta_t(\mathbf{v})$ explicitly in terms of the displacement field.

Similar to (6.34), we only have the ability to enforce two boundary conditions while this variational formulation requires the enforcement of three boundary conditions: displacement, tangential derivatives, and normal derivatives. Analogously to the Kirchhoff-Love plate, we must construct

the equivalent **ersatz forces** for the Kirchhoff-Love shell where in this scenario the boundary integration by parts of the tangential derivative introduces a modified shearing term with both in-plane and transverse contributions. Observe, using integration by parts along $\partial\Gamma$

$$\int_{\Gamma_N} \hat{B}_{nt} \left[(\nabla \mathbf{v})^T \mathbf{a}_3 \right] \cdot \underline{t} \, d\Gamma = \hat{B}_{nt} v_3 \Big|_{\chi_{C_N}} - \int_{\Gamma_N} v_3 \left(\nabla \hat{B}_{nt} \cdot \underline{t} \right) \, d\Gamma + \int_{\Gamma_N} \hat{B}_{nt} \underline{v} \underline{b} \underline{t} \, d\Gamma \quad (6.76)$$

where the last term follows since $\nabla \mathbf{a}_3 = -\underline{b}$.

Therefore, the tangential boundary rotation is in fact energetically-conjugate to the boundary displacement. Therefore, this quantity is a Γ_1 -entity, in contrast to the normal rotation which is a Γ_2 -entity. Analogous to the plate setting, we have presented χ_C which are the set of non-differentiable loci, e.g. corners, of Γ_1 , in addition to the set $\partial\Gamma_{N_1} \cup \partial\Gamma_{D_1}$, e.g. the contour endpoints of Γ_{D_1} and Γ_{D_2} , respectively. We will require subsets of χ_C in the derivation of Nitsche's method, which we define here. Namely, (i) $\chi_{C_N} := \chi_C \cap \Gamma_{N_1}$ and (ii) $\chi_{C_D} := \chi_C \cap \Gamma_{D_1}$. The notation $\cdot|_{\chi_C}$ should be understood as an integral evaluation. In particular, if $\mathbf{x} \in \text{int}(\chi_C)$, the evaluation has both “left” and “right” points, while contour endpoints only have their evaluation from the interior.

Intuitively, this evaluation adds **corner forces** to the non-differentiable points which prevent an artificial lifting of the response surface. As we will present in the strong form of the Kirchhoff-Love plate, we weakly impose the constraint $B_{nt}^+(v_3) = B_{nt}^-(v_3)$ on $\text{int}(\chi_{C_N})$ which nullifies the application of these corner forces where two edges of the same BC type meet. Therefore, the only portion of the boundary where these corner forces truly appear are those which the boundary condition transitions from a Neumann-1 type to Dirichlet-1 type, or vice-versa. The variational form is now well-posed requiring the satisfaction of only two boundary conditions. Therefore, the infinite-dimensional Kirchhoff-Love plate problem statement is written as With the presentation of these forces, we can concisely write the variational form as

$$\begin{aligned} \int_{\Omega} \underline{A}(\mathbf{u}) : \underline{\gamma}(\mathbf{v}) \, d\Omega + \int_{\Omega} \underline{B}(\mathbf{u}) : \underline{\kappa}(\mathbf{v}) \, d\Omega = \eta \int_{\Omega} \mathbf{f} \cdot \mathbf{v} \, d\Omega + \eta \int_{\Gamma_{N_1}} \hat{\mathbf{T}} \cdot \mathbf{v} \, d\Gamma - \eta \hat{B}_{nt} v_3 \Big|_{\chi_C} \\ + \eta \int_{\Gamma_{N_2}} \hat{B}_{nn} \theta_n(\mathbf{v}) \, d\Gamma. \end{aligned} \quad (6.77)$$

Here we have introduced the **applied ersatz force** which is defined as

$$\hat{\mathbf{T}} = \underbrace{\left[\tau_3 + \nabla \hat{B}_{nt} \cdot \underline{t} \right]}_{\hat{t}_3} \mathbf{a}_3 + \underbrace{\hat{t} - \hat{B}_{nt} \underline{b} \cdot \underline{t}}_{\hat{\underline{t}}}. \quad (6.78)$$

The full tensor form of the membrane and bending strains will prove useful for the necessary mathematical manipulations to arrive at a Nitsche’s method for the Kirchhoff-Love shell. Namely, Green’s identities extend naturally to the manifold setting wherein the differential operators behave in an analogous manner to a general region in \mathbb{R}^2 . It should be noted that $\underline{\underline{\gamma}}(\mathbf{u})$ and $\underline{\underline{\kappa}}(\mathbf{u})$ are **not** “truly” surface tensors in the form that they are written in (4.24). This is because they contain differential operators that, after acting upon the convective coordinate system, introduce out-of-plane contributions. However, in the context of shells, and more generally energy principles, we **always** contract these tensors with constitutive models which are surface tensors. Therefore, these out-of-plane tensor components arising through differentiation will vanish due to their mutual orthogonality.

The infinite-dimensional Kirchhoff-Love shell problem statement is written as:

Variational Formulation for the Kirchhoff-Love Shell

Find $\mathbf{u} \in \mathcal{U}_{KLS}$ such that

$$a_{KLS}(\mathbf{v}, \mathbf{u}) = a_{LE}(\mathbf{v}, \mathbf{u}) + a_{KLP}(\mathbf{v}, \mathbf{u}) = \ell_{KLS}(\mathbf{v}) \quad (6.79)$$

for all $\mathbf{v} \in \mathcal{V}_{KLS}$ where

$$a_{LE}(\mathbf{v}, \mathbf{u}) = \eta \int_{\Omega} \mathbb{C}^{\alpha\beta\lambda\mu} \gamma_{\alpha\beta}(\mathbf{v}) \gamma_{\lambda\mu}(\mathbf{u}) \, d\Omega \quad (6.80)$$

$$a_{KLP}(\mathbf{v}, \mathbf{u}) = \frac{\eta^3}{12} \int_{\Omega} \mathbb{C}^{\alpha\beta\lambda\mu} \kappa_{\alpha\beta}(\mathbf{v}) \kappa_{\lambda\mu}(\mathbf{u}) \, d\Omega \quad (6.81)$$

and

$$\ell_{KLS}(\mathbf{v}) = \eta \int_{\Omega} \mathbf{f} \cdot \mathbf{v} \, d\Omega + \eta \int_{\Gamma_{N_1}} \hat{\mathbf{T}} \cdot \mathbf{v} \, d\Gamma - \eta \hat{B}_{nt} v_3 \Big|_{\chi_{CN}} + \eta \int_{\Gamma_{N_2}} \hat{B}_{nn} \theta_n(\mathbf{v}) \, d\Gamma. \quad (6.82)$$

With the presentation of this weak formulation, we have the following theorem regarding the existence and uniqueness of the weak solution $\mathbf{u} \in \mathcal{U}_{KLS}$.

Lemma 14. *Suppose that for the Lebesgue measure $\lambda(\cdot)$ and Lebesgue-measurable sets Γ_{D_1} and Γ_{D_2} , one of the following hold:*

$$(i) \lambda(\Gamma_{D_1}) > 0 \text{ and } \underline{\underline{b}}(\Gamma_{D_1}) \neq 0$$

$$(ii) \lambda(\Gamma_{D_1}) > 0, \lambda(\Gamma_{D_2}) > 0, \text{ and } \lambda(\Gamma_{D_1} \cap \Gamma_{D_2}) > 0$$

Then there exists a unique weak solution to (6.79). If $\lambda(\Gamma_{D_1}) = \emptyset$, then the solution is unique up to a constant.

Proof. The proof follows through the combination of Lemma 4 and Lemma 9. In particular, $\underline{\underline{b}}(\Gamma_{D_1}) \neq 0$ ensures that Γ_{D_1} is not colinear and the proof follows immediately. \square

6.3.4 The Strong Formulation for the Kirchhoff-Love Shell

We apply (5.34) to the shell equations. Beginning with the membrane energy, and dropping the explicit dependence on \mathbf{u} for notational brevity, we have for every $\mathbf{v} \in \mathcal{V}_{KLS}$:

$$\int_{\Omega} \underline{\underline{A}} : \underline{\underline{\kappa}}(\mathbf{v}) \, d\Omega = \int_{\Gamma} \underline{n} \underline{\underline{A}} \underline{v} \, d\Gamma - \int_{\Omega} (\underline{\nabla} \cdot \underline{\underline{A}}) \underline{v} \, d\Omega - \int_{\Omega} (\underline{\underline{A}} : \underline{\underline{b}}) v_3 \, d\Omega. \quad (6.83)$$

The bending energy is more involved, regardless, the same procedure is followed

$$\begin{aligned} \int_{\Omega} \underline{\underline{B}} : \underline{\underline{\kappa}}(\mathbf{v}) \, d\Omega &= -\frac{1}{2} \int_{\Omega} \underline{\underline{B}} : \left(\mathbf{a}_3^T (\underline{\nabla} \underline{\nabla} \mathbf{v}) + (\underline{\nabla} \underline{\nabla} \mathbf{v})^T \mathbf{a}_3 \right) \, d\Omega \\ &= - \int_{\Omega} \underline{\underline{B}} : \underline{\nabla} (\mathbf{a}_3^T (\underline{\nabla} \mathbf{v})) \, d\Omega - \int_{\Omega} (\underline{\underline{b}} \underline{\underline{B}}) : (\underline{\nabla} \mathbf{v}) \, d\Omega \\ &= \int_{\Gamma} B_{nn} \theta_n(\mathbf{v}) \, d\Gamma - \int_{\Gamma} B_{nt} \theta_t(\mathbf{v}) \, d\Gamma + \int_{\Omega} (\underline{\nabla} \cdot \underline{\underline{B}}) \cdot (\mathbf{a}_3^T (\underline{\nabla} \mathbf{v})) \, d\Omega \\ &\quad - \int_{\Gamma} \underline{n} (\underline{\underline{b}} \underline{\underline{B}}) \underline{v} \, d\Gamma + \int_{\Omega} (\underline{\nabla} \cdot (\underline{\underline{b}} \underline{\underline{B}})) \underline{v} \, d\Omega + \int_{\Omega} (\underline{\underline{B}} : \underline{\underline{c}}) v_3 \, d\Omega \\ &= \int_{\Gamma} B_{nn} \theta_n(\mathbf{v}) \, d\Gamma - B_{nt} v_3 \Big|_{\chi_C} - \int_{\Gamma} B_{nt} (\underline{\underline{b}} \underline{\underline{t}}) \underline{v} \, d\Gamma + \int_{\Gamma} (\underline{\nabla} B_{nt} \cdot \underline{\underline{t}}) v_3 \, d\Gamma \\ &\quad + \int_{\Omega} (\underline{\nabla} \cdot \underline{\underline{B}}) \cdot \underline{\nabla} v_3 \, d\Omega + \int_{\Omega} \underline{\underline{b}} (\underline{\nabla} \cdot \underline{\underline{B}}) \underline{v} \, d\Omega - \int_{\Gamma} \underline{n} (\underline{\underline{b}} \underline{\underline{B}}) \underline{v} \, d\Gamma \\ &\quad + \int_{\Omega} (\underline{\nabla} \cdot (\underline{\underline{b}} \underline{\underline{B}})) \underline{v} \, d\Omega + \int_{\Omega} (\underline{\underline{B}} : \underline{\underline{c}}) v_3 \, d\Omega \\ &= \int_{\Gamma} B_{nn} \theta_n(\mathbf{v}) \, d\Gamma - B_{nt} v_3 \Big|_{\chi_C} + \int_{\Gamma} \left[\underline{n} (\underline{\nabla} \cdot \underline{\underline{B}}) + (\underline{\nabla} B_{nt} \cdot \underline{\underline{t}}) \right] v_3 \, d\Gamma \\ &\quad + \int_{\Omega} \left[\underline{\underline{B}} : \underline{\underline{c}} - \underline{\nabla} \cdot (\underline{\nabla} \cdot \underline{\underline{B}}) \right] v_3 \, d\Omega + \int_{\Omega} \underline{\underline{b}} (\underline{\nabla} \cdot \underline{\underline{B}}) \underline{v} \, d\Omega \\ &\quad - \int_{\Gamma} \left[B_{nt} (\underline{\underline{b}} \underline{\underline{t}}) + \underline{n} (\underline{\underline{b}} \underline{\underline{B}}) \right] \underline{v} \, d\Gamma + \int_{\Omega} (\underline{\nabla} \cdot (\underline{\underline{b}} \underline{\underline{B}})) \underline{v} \, d\Omega \end{aligned} \quad (6.84)$$

Combining these two results yields the following relationship

$$\begin{aligned}
\int_{\Omega} \underline{\underline{A}} : \underline{\underline{\gamma}}(\mathbf{v}) \, d\Omega + \int_{\Omega} \underline{\underline{B}} : \underline{\underline{\kappa}}(\mathbf{v}) \, d\Omega &= \int_{\Gamma_2} B_{nn} \theta_n(\mathbf{v}) \, d\Gamma - B_{nt} v_3 \Big|_{\chi_C} \\
&+ \int_{\Gamma_1} \left[\underline{n} \left(\underline{\nabla} \cdot \underline{\underline{B}} \right) + \left(\underline{\nabla} B_{nt} \cdot \underline{t} \right) \right] v_3 \, d\Gamma \\
&+ \int_{\Gamma_1} \left[\underline{n} \left(\underline{\underline{A}} - \underline{b} \underline{\underline{B}} \right) - B_{nt} \left(\underline{b} \underline{t} \right) \right] \underline{v} \, d\Gamma \\
&+ \int_{\Omega} \left[\underline{\underline{B}} : \underline{c} - \underline{\nabla} \cdot \left(\underline{\nabla} \cdot \underline{\underline{B}} \right) - \underline{\underline{A}} : \underline{b} \right] v_3 \, d\Omega \\
&+ \int_{\Omega} \left[\underline{\nabla} \cdot \left(\underline{b} \underline{\underline{B}} \right) + \underline{b} \left(\underline{\nabla} \cdot \underline{\underline{B}} \right) - \underline{\nabla} \cdot \underline{\underline{A}} \right] \underline{v} \, d\Omega \\
&= \int_{\Gamma_2} B_{nn} \theta_n(\mathbf{v}) \, d\Gamma - B_{nt} v_3 \Big|_{\chi_C} + \int_{\Gamma_1} \mathbf{T}(\mathbf{v}) \cdot \mathbf{v} \, d\Gamma \\
&+ \int_{\Omega} \left[\underline{\underline{B}} : \underline{c} - \underline{\nabla} \cdot \left(\underline{\nabla} \cdot \underline{\underline{B}} \right) - \underline{\underline{A}} : \underline{b} \right] v_3 \, d\Omega \\
&+ \int_{\Omega} \left[\underline{\nabla} \cdot \left(\underline{b} \underline{\underline{B}} \right) + \underline{b} \left(\underline{\nabla} \cdot \underline{\underline{B}} \right) - \underline{\nabla} \cdot \underline{\underline{A}} \right] \cdot \underline{v} \, d\Omega.
\end{aligned} \tag{6.85}$$

We have also presented the equations using the following boundary quantities:

$$\begin{aligned}
B_{nn}(\mathbf{u}) &= \underline{n} \underline{\underline{B}} \underline{n} && \text{(Bending traction)} \\
B_{nt}(\mathbf{u}) &= \underline{n} \underline{\underline{B}} \underline{t} && \text{(Twisting traction)} \\
\mathbf{T}(\mathbf{u}) &= \underbrace{\left[\underline{n} \left(\underline{\nabla} \cdot \underline{\underline{B}} \right) + \left(\underline{\nabla} B_{nt} \cdot \underline{t} \right) \right]}_{T_3(\mathbf{u})} \mathbf{a}_3 + \underbrace{\left[\underline{n} \left(\underline{\underline{A}} - \underline{b} \underline{\underline{B}} \right) - B_{nt} \left(\underline{b} \underline{t} \right) \right]}_{T(\mathbf{u})} && \text{(Ersatz traction)}
\end{aligned} \tag{6.86}$$

Note that the ‘‘corner’’ evaluation here has become χ_C because the integration by parts was carried throughout Γ . Then, combining this result with the linear form $\ell_{KLS}(\mathbf{v})$ yields

$$\begin{aligned}
0 &= a_{KLS}(\mathbf{v}, \mathbf{u}) - \ell_{KLS}(\mathbf{v}) \\
&= \int_{\Gamma_1} \left[\mathbf{T}(\mathbf{v}) - \eta \hat{\mathbf{T}} \right] \cdot \mathbf{v} \, d\Gamma - \left[B_{nt} - \eta \hat{B}_{nt} \right] v_3 \Big|_{\chi_C} + \int_{\Omega} \left[\underline{\underline{B}} : \underline{c} - \underline{\nabla} \cdot \left(\underline{\nabla} \cdot \underline{\underline{B}} \right) - \underline{\underline{A}} : \underline{b} - f_3 \right] v_3 \, d\Omega \\
&+ \int_{\Gamma_2} \left[B_{nn} \theta_n(\mathbf{v}) - \eta \hat{B}_{nn} \right] \, d\Gamma + \int_{\Omega} \left[\left(\left\{ \underline{\nabla} \cdot \left(\underline{\underline{B}} \underline{b} \right) + \left(\underline{\nabla} \cdot \underline{\underline{B}} \right) \underline{b} - \underline{\nabla} \cdot \underline{\underline{A}} \right\} \cdot \mathbf{a}_\alpha \right) \mathbf{a}^\alpha - \underline{f} \right] \cdot \underline{v} \, d\Omega.
\end{aligned} \tag{6.87}$$

The remaining boundary integrals over the Dirichlet-1 and Dirichlet-2 boundaries and over χ_{C_D} vanish due to strong homogeneous enforcement in the test space. However as is demonstrated

shortly, these terms become the consistency terms in Nitsche's method. Therefore, the following strong form is inferred from the "reverse" integration by parts of the weak formulation above:

Strong Formulation for the Kirchhoff-Love Shell

Find $\mathbf{u}: \Omega \rightarrow \mathbb{R}^3$ such that

$$\begin{aligned}
 \left[\underline{\nabla} \cdot \left(\underline{b} \underline{B}(\mathbf{u}) \right) + \underline{b} \left(\underline{\nabla} \cdot \underline{B}(\mathbf{u}) \right) - \underline{\nabla} \cdot \underline{A}(\mathbf{u}) \right] \cdot \mathbf{a}_\alpha &= \eta f_\alpha && \text{in } \Omega \\
 \underline{B}(\mathbf{u}) : \underline{c} - \underline{\nabla} \cdot \left(\underline{\nabla} \cdot \underline{B}(\mathbf{u}) \right) - \underline{A}(\mathbf{u}) : \underline{b} &= \eta f_3 && \text{in } \Omega \\
 \mathbf{u} &= \hat{\mathbf{u}} && \text{on } \Gamma_{D_1} \\
 \theta_n(\mathbf{u}) &= \hat{\theta}_n && \text{on } \Gamma_{D_2} \\
 \mathbf{T}(\mathbf{u}) &= \eta \hat{\mathbf{T}} && \text{on } \Gamma_{N_1} \\
 B_{nn}(\mathbf{u}) &= \eta \hat{B}_{nn} && \text{on } \Gamma_{N_2} \\
 B_{nt}(\mathbf{u}) &= \eta \hat{B}_{nt} && \text{on } \chi_{C_N} \\
 B_{nt}^+(\mathbf{u}) &= B_{nt}^-(\mathbf{u}) && \text{on } \text{int}(\chi_{C_N})
 \end{aligned} \tag{6.88}$$

As in the plate setting, for physical reasons it is convenient to split the domain boundary into four disjoint parts $\Gamma = \Gamma_C \cup \Gamma_{SS} \cup \Gamma_S \cup \Gamma_F$ each with zero BCs. Here, Γ_C is the clamped portion of the boundary, Γ_{SS} is the simply-supported portion of the boundary, Γ_S is the symmetric portion of the boundary, and Γ_F is the free portion of the boundary. Then the boundary conditions we wish to prescribe are given via:

$$\begin{aligned}
 \text{(clamped)} \quad \mathbf{u} = \mathbf{0}, \quad \theta_n(\mathbf{u}) = 0, &&& \text{on } \Gamma_C = \Gamma_{D_1} \cap \Gamma_{D_2} \\
 \text{(simply-supported)} \quad \mathbf{u} = \mathbf{0}, &&& B_{nn}(\mathbf{u}) = 0, \quad \text{on } \Gamma_{SS} = \Gamma_{D_1} \cap \Gamma_{N_2} \\
 \text{(symmetric)} \quad \theta_n(\mathbf{u}) = 0, \quad \mathbf{T}(\mathbf{u}) = \mathbf{0}, &&& \text{on } \Gamma_S = \Gamma_{N_1} \cap \Gamma_{D_2} \\
 \text{(free)} \quad \mathbf{T}(\mathbf{u}) = \mathbf{0}, \quad B_{nn}(\mathbf{u}) = 0, &&& \text{on } \Gamma_F = \Gamma_{N_1} \cap \Gamma_{N_2}
 \end{aligned} \tag{6.89}$$

6.3.5 Nitsche's Variational Form for the Linearized Kirchhoff-Love Shell

To begin the derivation of Nitsche's method for the linearized Kirchhoff-Love shell, we define the following discrete spaces of admissible and virtual displacements which accordingly release the

strong-enforcement of the Dirichlet boundary conditions

$$\begin{aligned} \mathcal{V}_{KLS}^h &\equiv \mathcal{U}_{KLS}^h \\ &:= \left\{ \mathbf{u}^h \in \mathcal{M}: \mathbf{T}(\mathbf{u}^h) \in \mathbf{L}^2(\Gamma_{D_1}), B_{nn}(\mathbf{u}^h) \in L^2(\Gamma_{D_2}), \text{ and } \mathbf{u}^h(\mathbf{x}) = \sum_{i=1}^n \mathbf{c}_i N_i(\mathbf{x}) \right\}. \end{aligned} \tag{6.90}$$

We now present the following discrete formulation for the Kirchhoff-Love shell:

Nitsche's Method for the Linearized Kirchhoff-Love Shell

Find $\mathbf{u}^h \in \mathcal{U}_{KLS}^h$ such that

$$a_{KLS}^h(\mathbf{v}^h, \mathbf{u}^h) = \ell_{KLS}^h(\mathbf{v}^h) \quad (6.91)$$

for all $\mathbf{v}^h \in \mathcal{V}_{KLS}^h$ where

$$\begin{aligned} a_{KLS}^h(\mathbf{v}^h, \mathbf{u}^h) &= a_{KLS}(\mathbf{v}^h, \mathbf{u}^h) \\ &\quad \underbrace{- \int_{\Gamma_{D_2}} B_{nn}(\mathbf{u}^h) \theta_n(\mathbf{v}^h) d\Gamma + B_{nt}(\mathbf{u}^h) v_3^h \Big|_{\chi_{CD}} - \int_{\Gamma_{D_1}} \underline{T}(\mathbf{u}^h) \cdot \underline{v}^h d\Gamma - \int_{\Gamma_{D_1}} T_3(\mathbf{u}^h) v_3^h d\Gamma}_{\text{Consistency Terms}} \\ &\quad \underbrace{- \int_{\Gamma_{D_2}} B_{nn}(\mathbf{v}^h) \theta_n(\mathbf{u}^h) d\Gamma + B_{nt}(\mathbf{v}^h) u_3^h \Big|_{\chi_{CD}} - \int_{\Gamma_{D_1}} \underline{T}(\mathbf{v}^h) \cdot \underline{u}^h d\Gamma - \int_{\Gamma_{D_1}} T_3(\mathbf{v}^h) u_3^h d\Gamma}_{\text{Symmetry Terms}} \\ &\quad \underbrace{+ \frac{\eta EC_{pen,1}}{h} \left(2 \int_{\Gamma_{D_1}} \underline{u}^h \cdot \underline{v}^h d\Gamma + \frac{\eta^2}{6h^2} \int_{\Gamma_{D_1}} u_3^h v_3^h d\Gamma \right) + \frac{\eta^3 EC_{pen,2}}{6h} \int_{\Gamma_{D_2}} \theta_n(\mathbf{u}^h) \theta_n(\mathbf{v}^h) d\Gamma}_{\text{Penalty Terms}} \end{aligned} \quad (6.92)$$

and

$$\begin{aligned} \ell_{KLS}^h(\mathbf{v}^h) &= \ell_{KLS}(\mathbf{v}^h) \\ &\quad \underbrace{- \int_{\Gamma_{D_2}} B_{nn}(\mathbf{v}^h) \hat{\theta}_n d\Gamma + B_{nt}(\mathbf{v}^h) \hat{u}_3 \Big|_{\chi_{CD}} - \int_{\Gamma_{D_1}} \underline{T}(\mathbf{v}^h) \cdot \hat{\underline{u}} d\Gamma - \int_{\Gamma_{D_1}} T_3(\mathbf{v}^h) \hat{u}_3 d\Gamma}_{\text{Symmetry Terms}} \\ &\quad \underbrace{+ \frac{\eta EC_{pen,1}}{h} \left(2 \int_{\Gamma_{D_1}} \hat{\underline{u}} \cdot \underline{v}^h d\Gamma + \frac{\eta^2}{6h^2} \int_{\Gamma_{D_1}} \hat{u}_3 v_3^h d\Gamma \right) + \frac{\eta^3 EC_{pen,2}}{6h} \int_{\Gamma_{D_2}} \hat{\theta}_n \theta_n(\mathbf{v}^h) d\Gamma}_{\text{Penalty Terms}} \end{aligned} \quad (6.93)$$

6.3.6 Consistency of Nitsche's Method

Once again, the symmetry of the discrete bilinear form arising through Nitsche's method (6.91) is obvious. We have the following lemma which details the proof of consistency of $a_{KLS}^h(\cdot, \cdot)$ with the original strong form of the PDE, provided the exact solution \mathbf{u} satisfies a reasonable

regularity condition.

Lemma 15. *Suppose the unique solution \mathbf{u} of (6.91) is sufficiently regular such that $\mathbf{T}(\mathbf{u}) \in \mathbf{L}^2(\Gamma_{D_1})$ and $B_{nn}(\mathbf{u}) \in L^2(\Gamma_{D_2})$. Then:*

$$a_{KLS}^h(\mathbf{v}^h, \mathbf{u}) = \ell_{KLS}^h(\mathbf{v}^h) \quad (6.94)$$

for all $\mathbf{v}^h \in \mathcal{V}_{KLS}^h$

Proof. By a process identical to those performed in (6.83) - (6.85), it follows that:

$$\begin{aligned}
a_{KLS}^h(\mathbf{u}, \mathbf{v}^h) - \ell_{KLS}^h(\mathbf{v}^h) &= \int_{\Omega} \underline{\underline{B}}(\mathbf{u}) : \underline{\underline{\kappa}}(\mathbf{v}^h) \, d\Omega + \int_{\Omega} \underline{\underline{A}}(\mathbf{u}) : \underline{\underline{\gamma}}(\mathbf{v}^h) \, d\Omega - \int_{\Gamma_{D_2}} B_{nn}(\mathbf{u}) \theta_n(\mathbf{v}^h) \, d\Gamma \\
&\quad - \int_{\Gamma_{D_1}} \underline{\mathbf{T}}(\mathbf{u}) \cdot \underline{\mathbf{v}}^h \, d\Gamma - \int_{\Gamma_{D_1}} T_3(\mathbf{u}) v_3^h \, d\Gamma + B_{nt}(\mathbf{v}^h) [u_3 - \hat{u}_3] \Big|_{\chi_{CD}} \\
&\quad - \int_{\Gamma_{D_2}} B_{nn}(\mathbf{v}^h) [\theta_n(\mathbf{u}) - \hat{\theta}_n] \, d\Gamma - \int_{\Gamma_{D_1}} \mathbf{T}(\mathbf{v}^h) \cdot [\mathbf{u} - \hat{\mathbf{u}}] \, d\Gamma \\
&\quad + \frac{\eta EC_{pen,1}}{h} \left(2 \int_{\Gamma_{D_1}} [\underline{\mathbf{u}} - \hat{\underline{\mathbf{u}}}] \cdot \underline{\mathbf{v}}^h \, d\Gamma + \frac{\eta^2}{6h^2} \int_{\Gamma_{D_1}} [u_3 - \hat{u}_3] v_3^h \, d\Gamma \right) \\
&\quad + \frac{\eta^3 EC_{pen,2}}{6h} \int_{\Gamma_{D_2}} [\theta_n(\mathbf{u}) - \hat{\theta}_n] \theta_n(\mathbf{v}^h) \, d\Gamma - \eta \int_{\Omega} \mathbf{f} \cdot \mathbf{v}^h \, d\Omega \\
&\quad - \eta \int_{\Gamma_{N_1}} \hat{\mathbf{T}} \cdot \mathbf{v}^h \, d\Gamma - \eta \int_{\Gamma_{N_2}} \hat{B}_{nn} \theta_n(\mathbf{v}^h) \, d\Gamma + B_{nt}(\mathbf{u}) v_3^h \Big|_{\chi_{CD}} \\
&= \int_{\Omega} \left[\underline{\underline{B}}(\mathbf{u}) : \underline{\underline{c}} - \nabla \cdot \nabla \cdot \underline{\underline{B}}(\mathbf{u}) - \underline{\underline{A}}(\mathbf{u}) : \underline{\underline{b}} - \eta f_3 \right] v_3^h \, d\Omega + \eta \hat{B}_{nt}(\mathbf{u}) v_3 \Big|_{\chi_{CN}} \\
&\quad + \int_{\Omega} \left[\left\{ \nabla \cdot \left(\underline{\underline{B}}(\mathbf{u}) \underline{\underline{b}} \right) + \left(\nabla \cdot \underline{\underline{B}}(\mathbf{u}) \right) \underline{\underline{b}} - \nabla \cdot \underline{\underline{A}}(\mathbf{u}) \right\} \cdot \mathbf{a}_\alpha - \eta f_\alpha \right] \left(\underline{\mathbf{v}}^h \right)^\alpha \, d\Omega \\
&\quad + B_{nt}(\mathbf{v}^h) [u_3 - \hat{u}^h] \Big|_{\chi_{CD}} - \int_{\Gamma_{D_1}} \mathbf{T}(\mathbf{v}^h) \cdot [\mathbf{u} - \hat{\mathbf{u}}] \, d\Gamma \\
&\quad + \int_{\Gamma_{N_1}} \left[\mathbf{T}(\mathbf{u}) - \eta \hat{\mathbf{T}} \right] \cdot \mathbf{v}^h \, d\Gamma + \int_{\Gamma_{N_2}} \left[B_{nn}(\mathbf{u}) - \eta \hat{B}_{nn} \right] \theta_n(\mathbf{v}^h) \, d\Gamma \\
&\quad + \frac{\eta EC_{pen,1}}{h} \left(2 \int_{\Gamma_{D_1}} [\underline{\mathbf{u}} - \hat{\underline{\mathbf{u}}}] \cdot \underline{\mathbf{v}}^h \, d\Gamma + \frac{\eta^2}{6h^2} \int_{\Gamma_{D_1}} [u_3 - \hat{u}^h] \cdot \mathbf{v}^h \, d\Gamma \right) \\
&\quad + \frac{\eta^3 EC_{pen,2}}{6h} \int_{\Gamma_{D_2}} [\theta_n(\mathbf{u}) - \hat{\theta}_n] \theta_n(\mathbf{v}^h) \, d\Gamma \\
&\quad - \int_{\Gamma_{D_2}} B_{nn}(\mathbf{v}^h) [\theta_n(\mathbf{u}) - \hat{\theta}_n] \, d\Gamma + [B_{nt}(\mathbf{u}) - \eta \hat{B}_{nt}] v_3^h \Big|_{\chi_{CN}} \\
&= 0
\end{aligned} \tag{6.95}$$

Hence the consistency with (6.88) is proven.

□

6.3.7 Continuity and Coercivity of Nitsche's Method for the linearized Kirchhoff-Love Shell

To preface this section, we define the mesh-dependent norm with which we prove continuity, coercivity, and later error estimates:

$$\begin{aligned} \|\mathbf{v}\|_{\mathcal{U}_{KLS}^h}^2 &:= \|\mathbf{v}\|_A^2 + \|\mathbf{v}\|_B^2 + \frac{\eta EC_{pen,1}}{h} \left(2\|\underline{v}\|_{0,\Gamma}^2 + \frac{\eta^2}{6h^2} \|v_3\|_{0,\Gamma}^2 \right) + \frac{\eta^3 EC_{pen,2}}{6h} \|\theta_n(\mathbf{v})\|_{0,\Gamma}^2 \\ &\quad + \frac{6h^3}{\eta^3 E} \|T_3(\mathbf{v})\|_{0,\Gamma}^2 + \frac{h}{2\eta E} \|\underline{T}(\mathbf{v})\|_{0,\Gamma}^2 + \frac{6h}{\eta^3 E} \|B_{nn}(\mathbf{v})\|_{0,\Gamma}^2 + \frac{6h^2}{\eta^3 E} |B_{nt}(\mathbf{v})|^2 \Big|_{\chi_C} \\ &\quad + \frac{\eta^3 E}{6h^2} |v_3|^2 \Big|_{\chi_C} \end{aligned} \quad (6.96)$$

Note that (6.96) is indeed a norm over \mathcal{V}_{KLS}^h since it is a combination of $\|\cdot\|_{\mathcal{U}_{LE}^h}$ and $\|\cdot\|_{\mathcal{U}_{KLP}^h}$. Additionally, by (5.15), (5.16), (5.17), (5.20), and (5.25), this norm satisfies the following relationship $\forall \mathbf{v}^h \in \mathcal{V}_{KLS}^h$ with $C_\ell^{-1} \geq 1 + \max \left[C_{tr,A}, C_{tr,T} C_{inv,T} + \left(\frac{\eta^2}{6} \|\underline{b}\|_{0,\Omega}^2 + 1 + C_{tr,M} \right) C_{tr,B}, \frac{C_{tr,u_\Gamma}}{C_{pen,1}} \right]$:

$$\begin{aligned} \|\mathbf{v}^h\|_{\mathcal{U}_{KLS}^h}^2 &\leq \|\mathbf{v}^h\|_A^2 + \|\mathbf{v}^h\|_B^2 + \frac{\eta EC_{pen,1}}{h} \left(2\|\underline{v}^h\|_{0,\Gamma}^2 + \frac{\eta^2}{6h^2} \|v_3^h\|_{0,\Gamma}^2 \right) + \frac{\eta^3 EC_{pen,2}}{6h} \|\theta_n(\mathbf{v}^h)\|_{0,\Gamma}^2 \\ &\quad + \frac{6h^2 C_{tr,T}}{\eta^3 E} \|T_3(\mathbf{v}^h)\|_{0,\Omega}^2 \\ &\quad + \frac{C_{tr,A}}{2\eta E} \|\underline{A}(\mathbf{v}^h)\|_{0,\Omega}^2 + \frac{\|\underline{b}\|_{0,\Omega}^2 C_{tr,B}}{\eta E} \|\underline{B}(\mathbf{v}^h)\|_{0,\Omega}^2 + \frac{6C_{tr,B}}{\eta^3 E} \|\underline{B}(\mathbf{v}^h)\|_{0,\Omega}^2 \\ &\quad + \frac{6h C_{tr,M}}{\eta^3 E} \|B_{nt}(\mathbf{v}^h)\|_{0,\Gamma}^2 + \frac{\eta^3 E C_{tr,u_\Gamma}}{6h^3} \|v_3^h\|_{0,\Gamma}^2 \\ &\leq (1 + C_{tr,A}) \|\mathbf{v}^h\|_A^2 + \left(1 + C_{tr,T} C_{inv,T} + \left(\frac{\eta^2}{6} \|\underline{b}\|_{0,\Omega}^2 + 1 + C_{tr,M} \right) C_{tr,B} \right) \|\mathbf{v}^h\|_B^2 \\ &\quad + \frac{\eta^3 EC_{pen,2}}{6h} \|\theta_n(\mathbf{v}^h)\|_{0,\Gamma}^2 + \frac{2\eta EC_{pen,1}}{h} \|\underline{v}^h\|_{0,\Gamma}^2 + \frac{\eta^3 E}{6h^3} (C_{pen,1} + C_{tr,u_\Gamma}) \|v_3^h\|_{0,\Gamma}^2 \\ &\leq \frac{1}{C_\ell} \left[\|\mathbf{v}^h\|_A^2 + \|\mathbf{v}^h\|_B^2 + \frac{\eta EC_{pen,1}}{h} \left(2\|\underline{v}^h\|_{0,\Gamma}^2 + \frac{\eta^2}{6h^2} \|v_3^h\|_{0,\Gamma}^2 \right) \right. \\ &\quad \left. + \frac{\eta^3 EC_{pen,2}}{6h} \|\theta_n(\mathbf{v}^h)\|_{0,\Gamma}^2 \right]. \end{aligned} \quad (6.97)$$

Now that we have demonstrated that $\|\cdot\|_{\mathcal{U}_{KLS}^h}$ is indeed a norm, we are able to prove the continuity, that is the boundedness, of the mesh-dependent bilinear form $a_{KLS}^h(\cdot, \cdot)$ in the following lemma.

Lemma 16. *The following continuity statement holds:*

$$a_{KLS}^h(\mathbf{v}^h, \mathbf{w}) \leq C_{cont, KLS} \|\mathbf{v}^h\|_{\mathcal{U}_{KLS}^h} \|\mathbf{w}\|_{\mathcal{U}_{KLS}^h} \quad (6.98)$$

for all $\mathbf{v}^h \in \mathcal{V}_{KLS}^h$ and \mathbf{w} such that $\mathbf{T}(\mathbf{w}) \in L^2(\Gamma_{D_1})$ and $B_{nn}(\mathbf{w}) \in L^2(\Gamma_{D_2})$.

Proof. To prove the continuity estimate, we first write:

$$\begin{aligned} a_{KLS}^h(\mathbf{v}^h, \mathbf{w}) &= a_{KLS}(\mathbf{v}^h, \mathbf{w}) - \int_{\Gamma_{D_2}} B_{nn}(\mathbf{w})\theta_n(\mathbf{v}^h) d\Gamma + B_{nt}(\mathbf{w})v_3^h \Big|_{\chi_C} - \int_{\Gamma_{D_1}} \underline{\mathbf{T}}(\mathbf{w}) \cdot \underline{\mathbf{v}}^h d\Gamma \\ &\quad - \int_{\Gamma_{D_1}} T_3(\mathbf{w})v_3^h d\Gamma - \int_{\Gamma_{D_2}} B_{nn}(\mathbf{v}^h)\theta_n(\mathbf{w}) d\Gamma + B_{nt}(\mathbf{v}^h)w_3 \Big|_{\chi_C} - \int_{\Gamma_{D_1}} \underline{\mathbf{T}}(\mathbf{v}^h) \cdot \underline{\mathbf{w}} d\Gamma \\ &\quad - \int_{\Gamma_{D_1}} T_3(v_3^h)w_3 d\Gamma + \frac{\eta EC_{pen,1}}{h} \left(2 \int_{\Gamma_{D_1}} \underline{\mathbf{w}} \cdot \underline{\mathbf{v}}^h d\Gamma + \frac{\eta^2}{6h^2} \int_{\Gamma_{D_1}} w_3 v_3^h d\Gamma \right) \\ &\quad + \frac{\eta^3 EC_{pen,2}}{6h} \int_{\Gamma_{D_2}} \theta_n(\mathbf{w})\theta_n(\mathbf{v}^h) d\Gamma. \end{aligned} \quad (6.99)$$

Observe we can bound:

$$\begin{aligned} a_{KLS}(\mathbf{v}^h, \mathbf{w}) &+ \frac{\eta EC_{pen,1}}{h} \left(2 \int_{\Gamma_{D_1}} \underline{\mathbf{w}} \cdot \underline{\mathbf{v}}^h d\Gamma + \frac{\eta^2}{6h^2} \int_{\Gamma_{D_1}} w_3 v_3^h d\Gamma \right) \\ &\quad + \frac{\eta^3 EC_{pen,2}}{6h} \int_{\Gamma_{D_2}} \theta_n(\mathbf{w})\theta_n(\mathbf{v}^h) d\Gamma \\ &\leq \|\mathbf{v}^h\|_{\mathcal{U}_{KLS}^h} \|\mathbf{w}\|_{\mathcal{U}_{KLS}^h}. \end{aligned} \quad (6.100)$$

Next, we bound the in-plane ersatz traction via

$$\begin{aligned} \int_{\Gamma_{D_1}} \underline{\mathbf{T}}(\mathbf{w}) \cdot \underline{\mathbf{v}}^h d\Gamma &\leq \|\underline{\mathbf{v}}^h\|_{0,\Gamma} \|\underline{\mathbf{T}}(\mathbf{w})\|_{0,\Gamma} \\ &\leq \sqrt{\frac{1}{h} \|\underline{\mathbf{v}}^h\|_{0,\Gamma}^2} \sqrt{h \|\underline{\mathbf{T}}(\mathbf{w})\|_{0,\Gamma}^2} \\ &\leq \|\mathbf{v}^h\|_{\mathcal{U}_{KLS}^h} \|\mathbf{w}\|_{\mathcal{U}_{KLS}^h} \end{aligned} \quad (6.101)$$

and the transverse component by

$$\begin{aligned}
\int_{\Gamma_{D_1}} T_3(\mathbf{w})v_3^h d\Gamma &\leq \|v_3^h\|_{0,\Gamma} \|T_3(\mathbf{w})\|_{0,\Gamma} \\
&\leq \sqrt{\frac{1}{h^3} \|v_3^h\|_{0,\Gamma}^2} \sqrt{h^3 \|T_3(\mathbf{w})\|_{0,\Gamma}^2} \\
&\leq \|\mathbf{v}^h\|_{\mathcal{U}_{KLS}^h} \|\mathbf{w}\|_{\mathcal{U}_{KLS}^h}.
\end{aligned} \tag{6.102}$$

The bending moment term is bounded via

$$\begin{aligned}
\int_{\Gamma_{D_2}} B_{nn}(\mathbf{w})\theta_n(\mathbf{v}^h) d\Gamma &\leq \|B_{nn}(\mathbf{w})\|_{0,\Gamma} \|\theta_n(\mathbf{v}^h)\|_{0,\Gamma} \\
&\leq \sqrt{h \|B_{nn}(\mathbf{w})\|_{0,\Gamma}^2} \sqrt{\frac{1}{h} \|\theta_n(\mathbf{v}^h)\|_{0,\Gamma}^2} \\
&\leq \|\mathbf{v}^h\|_{\mathcal{U}_{KLS}^h} \|\mathbf{w}\|_{\mathcal{U}_{KLS}^h}
\end{aligned} \tag{6.103}$$

and lastly, the boundary evaluation via

$$\begin{aligned}
B_{nt}(\mathbf{w})v_3^h \Big|_{\chi_C} &\leq \left(|B_{nt}(\mathbf{w})| \Big|_{\chi_C} \right) \left(|v_3^h| \Big|_{\chi_C} \right) \\
&\leq \sqrt{h^2 |B_{nt}(\mathbf{w})|^2 \Big|_{\chi_C}} \sqrt{\frac{1}{h^2} |v_3^h|^2 \Big|_{\chi_C}} \\
&\leq \|\mathbf{v}^h\|_{\mathcal{U}_{KLS}^h} \|\mathbf{w}\|_{\mathcal{U}_{KLS}^h}.
\end{aligned} \tag{6.104}$$

Clearly, these inequalities hold for their symmetric counterparts. Collecting these inequalities yields

$$a_{KLS}^h(\mathbf{v}^h, \mathbf{w}) \leq C_{cont,KLS} \|\mathbf{v}^h\|_{\mathcal{U}_{KLS}^h} \|\mathbf{w}\|_{\mathcal{U}_{KLS}^h} \tag{6.105}$$

with $C_{cont,KLS} = 9$.

□

Next, we prove the coercivity of the bilinear form with respect to the $\|\cdot\|_{\mathcal{U}_{KLS}^h}$ -norm in the following lemma.

Lemma 17. *The following coercivity statement holds:*

$$a_{KLS}^h(\mathbf{v}^h, \mathbf{v}^h) \geq C_{coer,KLS} \|\mathbf{v}^h\|_{\mathcal{U}_{KLS}^h}^2, \quad \forall \mathbf{v}^h \in \mathcal{V}_{KLS}^h \tag{6.106}$$

Proof. Let $\mathbf{v}^h \in \mathcal{V}_{KLS}^h$, $\varepsilon_1 > \max\left(2C_{tr,A}, 16\eta^2 C_{tr,B} \|\underline{b}\|_{0,\Omega}^2\right)$, $\varepsilon_2 > 8C_{tr,T}C_{inv,T}$, $\varepsilon_3 > 8C_{tr,B}$, $\varepsilon_4 > 8C_{tr,M}C_{tr,B}$, and observe that by Cauchy-Schwarz and Young's inequalities:

$$\int_{\Gamma_{D_1}} \underline{T}(\mathbf{v}^h) \cdot \underline{v}^h \, d\Gamma \leq \|\underline{v}^h\|_{0,\Gamma} \|\underline{T}(\mathbf{v}^h)\|_{0,\Gamma} \leq \frac{\eta E \varepsilon_1}{h} \|\underline{v}^h\|_{0,\Gamma}^2 + \frac{h}{4\eta E \varepsilon_1} \|\underline{T}(\mathbf{v}^h)\|_{0,\Gamma}^2 \quad (6.107)$$

and

$$\int_{\Gamma_{D_1}} T_3(\mathbf{v}^h) v_3^h \, d\Gamma \leq \|v_3^h\|_{0,\Gamma} \|T_3(\mathbf{v}^h)\|_{0,\Gamma} \leq \frac{\eta^3 E \varepsilon_2}{12h^3} \|v_3^h\|_{0,\Gamma}^2 + \frac{3h^3}{\eta^3 E \varepsilon_2} \|T_3(\mathbf{v}^h)\|_{0,\Gamma}^2. \quad (6.108)$$

Next, the moments and conjugate rotations

$$\int_{\Gamma_{D_2}} B_{nn}(\mathbf{v}^h) \theta_n(\mathbf{v}^h) \, d\Gamma \leq \|B_{nn}(\mathbf{v}^h)\|_{0,\Gamma} \|\theta_n(\mathbf{v}^h)\|_{0,\Gamma} \leq \frac{3h}{\eta^3 E \varepsilon_3} \|B_{nn}(\mathbf{v}^h)\|_{0,\Gamma}^2 + \frac{\eta^3 E \varepsilon_3}{12h} \|\theta_n(\mathbf{v}^h)\|_{0,\Gamma}^2. \quad (6.109)$$

Lastly, utilizing (5.20) and (5.21), we obtain the following estimate for the boundary evaluation:

$$\begin{aligned} B_{nt}(\mathbf{v}^h) v_3^h \Big|_{\chi_C} &\leq \left(\frac{3h^2}{\eta^3 E \varepsilon_4} \left| B_{nt}(\mathbf{v}^h) \right|_{\chi_C}^2 + \frac{\eta^3 E \varepsilon_4}{12h^2} \left| v_3^h \right|_{\chi_C}^2 \right) \\ &\leq \frac{3h C_{tr,M}}{\eta^3 E \varepsilon_4} \|B_{nt}(\mathbf{v}^h)\|_{0,\Gamma}^2 + \frac{\eta^3 E \varepsilon_4 C_{tr,u\Gamma}}{12h^3} \|v_3^h\|_{0,\Gamma}^2. \end{aligned} \quad (6.110)$$

Therefore, utilizing (6.107), (6.108), (6.109), (6.110), (5.15) through (5.21), (5.25), and for

$$C_{pen,1} > \frac{1}{2} + \max \left[2C_{tr,A}, 16\eta^2 C_{tr,B} \|\underline{b}\|_{0,\Omega}^2, 8(C_{tr,T}C_{inv,T} + C_{tr,M}C_{tr,B}C_{tr,u\Gamma}) \right] \quad (6.111)$$

and $C_{pen,2} > \frac{1}{2} + 8C_{tr,B}$, we have the following:

$$\begin{aligned}
a_{KLS}^h(\mathbf{v}^h, \mathbf{v}^h) &\geq \left\| \left\| \mathbf{v}^h \right\|_A \right\|^2 + \left\| \left\| \mathbf{v}^h \right\|_B \right\|^2 - 2 \int_{\Gamma_{D_2}} B_{nn}(\mathbf{v}^h) \theta_n(\mathbf{v}^h) \, d\Gamma - 2 B_{nt}(\mathbf{v}^h) v_3^h \Big|_{\chi_C} \\
&\quad - 2 \int_{\Gamma_{D_1}} \underline{T}(\mathbf{v}^h) \cdot \underline{v}^h \, d\Gamma - 2 \int_{\Gamma_{D_1}} T_3(\mathbf{v}^h) \cdot v_3^h \, d\Gamma \\
&\quad + \frac{\eta E C_{pen,1}}{h} \left(2 \|\underline{v}^h\|_{0,\Gamma}^2 + \frac{\eta^2}{6h^2} \|v_3^h\|_{0,\Gamma}^2 \right) + \frac{\eta^3 E C_{pen,2}}{6h} \|\theta_n(\mathbf{v}^h)\|_{0,\Gamma}^2 \\
&\geq \left\| \left\| \mathbf{v}^h \right\|_A \right\|^2 + \left\| \left\| \mathbf{v}^h \right\|_B \right\|^2 - \left(\frac{6h}{\eta^3 E \varepsilon_3} \|B_{nn}(\mathbf{v}^h)\|_{0,\Gamma}^2 + \frac{\eta^3 E \varepsilon_3}{6h} \|\theta_n(\mathbf{v}^h)\|_{0,\Gamma}^2 \right) \\
&\quad - \left(\frac{6h C_{tr,M}}{\eta^3 E \varepsilon_4} \|B_{nt}(\mathbf{v}^h)\|_{0,\Gamma}^2 + \frac{\eta^3 E \varepsilon_4 C_{tr,u\Gamma}}{6h^3} \|v_3^h\|_{0,\Gamma}^2 \right) \\
&\quad - \left(\frac{2\eta E \varepsilon_1}{h} \|\underline{v}^h\|_{0,\Gamma}^2 + \frac{h}{2\eta E \varepsilon_1} \|\underline{T}(\mathbf{v}^h)\|_{0,\Gamma}^2 \right) - \left(\frac{\eta^3 E \varepsilon_2}{6h^3} \|v_3^h\|_{0,\Gamma}^2 + \frac{6h^3}{\eta^3 E \varepsilon_2} \|T_3(\mathbf{v}^h)\|_{0,\Gamma}^2 \right) \\
&\quad + \frac{\eta E C_{pen,1}}{h} \left(2 \|\underline{v}^h\|_{0,\Gamma}^2 + \frac{\eta^2}{6h^2} \|v_3^h\|_{0,\Gamma}^2 \right) + \frac{\eta^3 E C_{pen,2}}{6h} \|\theta_n(\mathbf{v}^h)\|_{0,\Gamma}^2 \\
&\geq \left(1 - \frac{C_{tr,A}}{\varepsilon_1} \right) \left\| \left\| \mathbf{v}^h \right\|_A \right\|^2 + \frac{2\eta E}{h} (C_{pen,1} - \varepsilon_1) \|\underline{v}^h\|_{0,\Gamma}^2 + \frac{\eta^3 E}{6h} (C_{pen,2} - \varepsilon_3) \|\theta_n(\mathbf{v}^h)\|_{0,\Gamma}^2 \\
&\quad + \left(1 - \frac{2\eta^2 C_{tr,B} \|\underline{b}\|_{0,\Omega}^2}{\varepsilon_1} - \frac{C_{tr,T} C_{inv,T}}{\varepsilon_2} - \frac{C_{tr,B}}{\varepsilon_3} - \frac{C_{tr,M} C_{tr,B}}{\varepsilon_4} \right) \left\| \left\| \mathbf{v}^h \right\|_B \right\|^2 \\
&\quad + \frac{\eta^3 E}{6h^3} (C_{pen,1} - \varepsilon_2 - C_{tr,u\Gamma} \varepsilon_4) \|v_3^h\|_{0,\Gamma}^2 \\
&\geq \frac{1}{2} \left(\left\| \left\| \mathbf{v}^h \right\|_A \right\|^2 + \left\| \left\| \mathbf{v}^h \right\|_B \right\|^2 + \frac{\eta E C_{pen,1}}{h} \left(2 \|\underline{v}^h\|_{0,\Gamma}^2 + \frac{\eta^2}{6h^2} \|v_3^h\|_{0,\Gamma}^2 \right) \right. \\
&\quad \left. + \frac{\eta^3 E C_{pen,2}}{6h} \|\theta_n(\mathbf{v}^h)\|_{0,\Gamma}^2 \right) \\
&\geq C_{coer,KLS} \|\mathbf{v}^h\|_{\mathcal{U}_{KLP}^h}^2
\end{aligned} \tag{6.112}$$

where $C_{coer,KLS} = \frac{1}{2} \left(1 + \max \left[C_{tr,A}, C_{tr,T} C_{inv,T} + \left(\frac{\eta^2}{6} \|\underline{b}\|_{0,\Omega}^2 + 1 + C_{tr,M} \right) C_{tr,B}, \frac{C_{tr,u\Gamma}}{C_{pen,1}} \right] \right)^{-1}$

□

6.3.8 A Priori Error Estimates

Before proceeding with discretization-dependent approximation theorems, we have the following corollary to Theorem 3.

Corollary 18. *Let \mathbf{u} and \mathbf{u}^h denote the unique solutions of problems (6.79) and (6.91), respectively.*

Furthermore, suppose the hypotheses of Theorem 1 and Theorem 3 are satisfied. Then,

$$\|\mathbf{u} - \mathbf{u}^h\|_{\mathcal{U}_{KLP}^h} \leq \tilde{C}_{KLP} \inf_{\mathbf{w}^h \in \mathcal{U}_{KLS}^h} \|\mathbf{u} - \mathbf{w}^h\|_{\mathcal{U}_{KLS}^h}. \quad (6.113)$$

where

$$\tilde{C}_{KLS} = \left(18 + 19 \max \left[C_{tr,A}, C_{tr,T} C_{inv,T} + \left(\frac{\eta^2}{6} \|\underline{b}\|_{0,\Omega}^2 + 1 + C_{tr,M} \right) C_{tr,B}, \frac{C_{tr,u\Gamma}}{C_{pen,1}} \right] \right) \quad (6.114)$$

Proof. Recall Theorem 3 and the estimate provided therein. Then the result follows immediately by the continuity and coercivity constants defined in Lemma 16 and Lemma 17 and the consistency inherent to Nitsche's variational formulation for the Kirchhoff-Love plate. \square

6.4 Numerical Results

In this section, we demonstrate the effectiveness of Nitsche's formulation for the linearized Kirchhoff-Love shell formulation presented in previous sections. Note that we do not provide explicit examples for the linear-elastic membrane or Kirchhoff-Love plate since the Kirchhoff-Love shell encompasses both of these scenarios. In all of our examples, we employ uniform biquadratic, bicubic, and biquartic B-spline discretizations. Moreover, we present the so-called **shell obstacle course**, as presented in [11], as a validation of the discretization.

6.4.1 The Shell Obstacle Course

The shell obstacle course is comprised of three problems: (i) the Scordelis-Lo roof [5, 107], (ii) the pinched cylinder [44, 50, 78], and (iii) the pinched hemisphere [82, 84].

6.4.1.1 The Scordelis-Lo Roof

The Scordelis-Lo roof is a section of a cylindrical shell supported at its ends by a rigid diaphragm while the remaining boundary of the cylinder is free. The roof is subject to a uniform gravitational loading across the entire domain. By the symmetry of the problem, only one quarter

of the physical domain is modeled and symmetric boundary conditions are imposed accordingly. A more detailed problem configuration is provided in Figure 6.4.

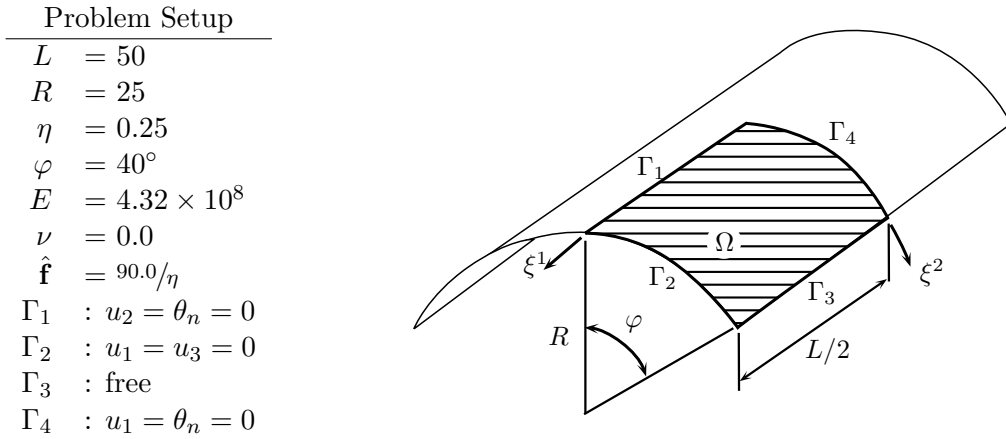


Figure 6.4: The Scordelis-Lo Roof problem setup and configuration.

The criterion for convergence is the vertical displacement of the free edge of the roof. The converged numerical solution from our discretization is $u = 0.3006$. This value is lower than $u = 0.3024$, that is reported in [5, 107], however it is in exact accordance with [72]. For this problem, numerical convergence is observed almost immediately for cubic and quartic B-splines while the quadratic counterpart exhibits locking on coarse meshes, as is shown in Figure 6.5.

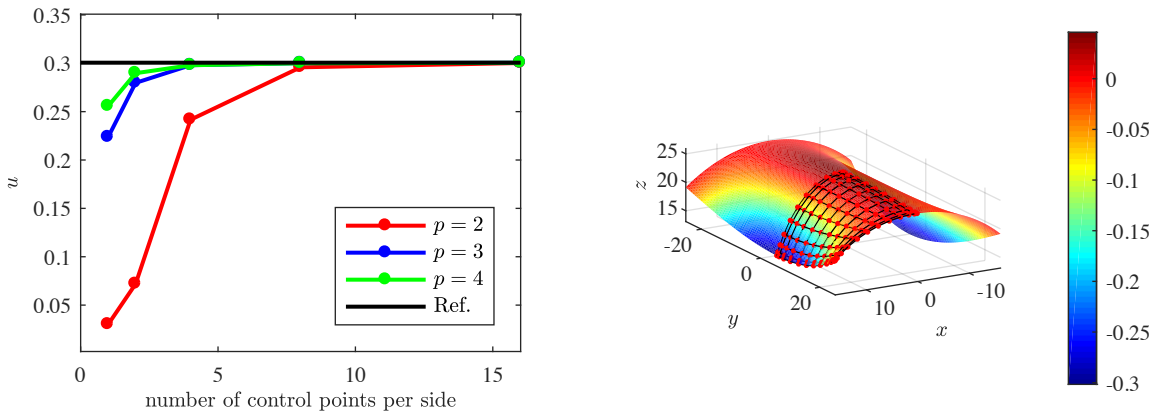


Figure 6.5: The Scordelis-Lo Roof displacement criterion is shown across the range of refinements considered in this paper (left). The z -displacement field is shown on the contour plot (right).

6.4.1.2 The Pinched Cylinder

The Pinched Cylinder problem is supported by rigid diaphragms at either end and subjected to two opposite point loads directed inward at the cylinder center. Once again, due to problem symmetry, only one eighth of the cylinder is modeled and symmetric boundary conditions are imposed accordingly. The problem setup and configuration is provided in Figure 6.6

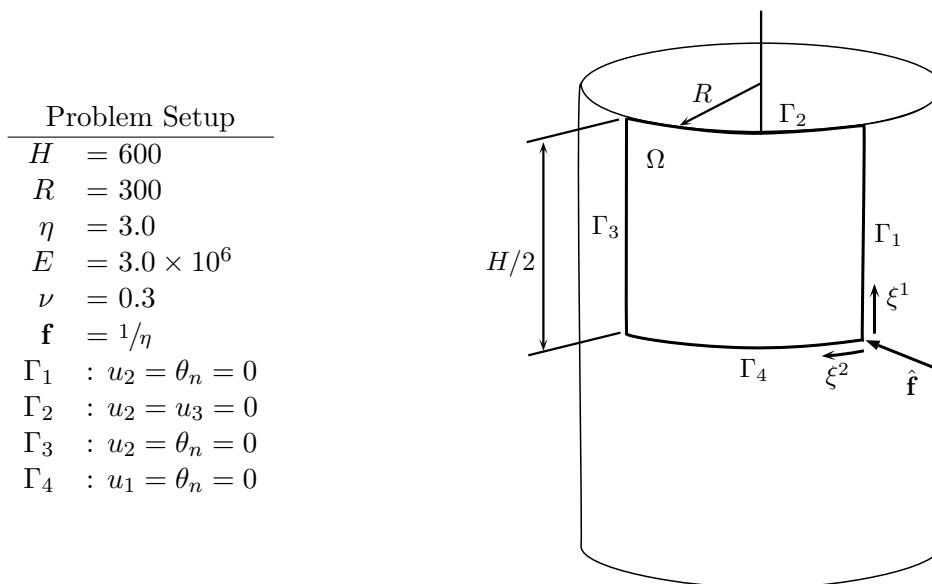


Figure 6.6: The Pinched Cylinder problem setup and configuration.

The criterion for convergence of this problem is once again a point displacement however in this instance it is at the point of load application. The reference displacement is $u = 1.8248 \times 10^{-5}$ as given in [44, 50, 78]. Convergence to this value is demonstrated for biquadratic, bicubic, and biquartic B-splines in Figure 6.7.

6.4.1.3 The Pinched Hemisphere

The Pinched Hemisphere problem is minimally-supported as to prevent rigid-body motion. The boundaries of the hemisphere are completely free and are subject to two opposing point loads directed either inwards or outwards. Once again, due to problem symmetry, only one quarter of the hemisphere is modeled and symmetric boundary conditions are imposed accordingly. The problem

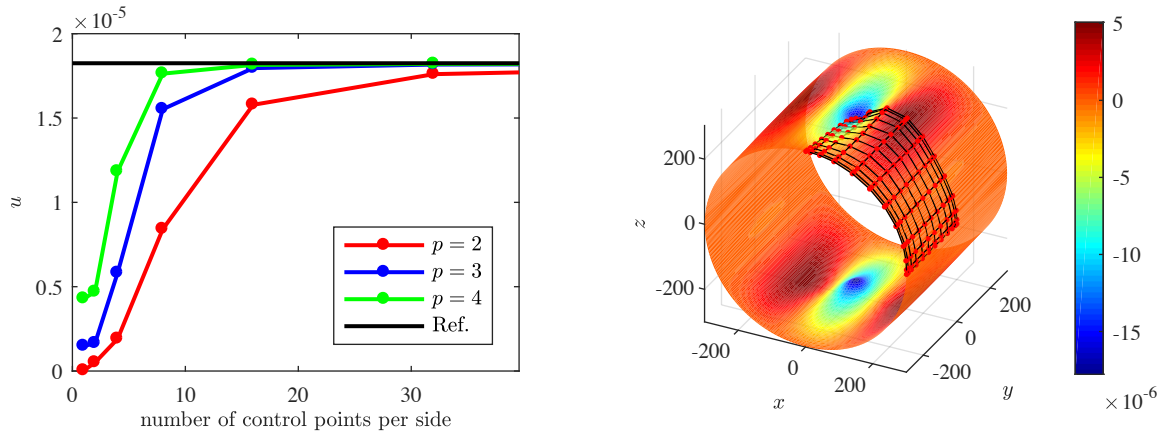


Figure 6.7: The Pinched Cylinder displacement criterion shown across the range of refinements considered in this paper (left). The y -displacement field is shown on the contour plot (right).

setup and configuration is provided in Figure 6.8

The criterion for convergence of this problem is once again a point displacement at the point of load application. The reference displacement is $u = 0.0924$ as given in [82, 84]. Convergence to this value is demonstrated for biquadratic, bicubic, and biquartic B-splines in Figure 6.9.

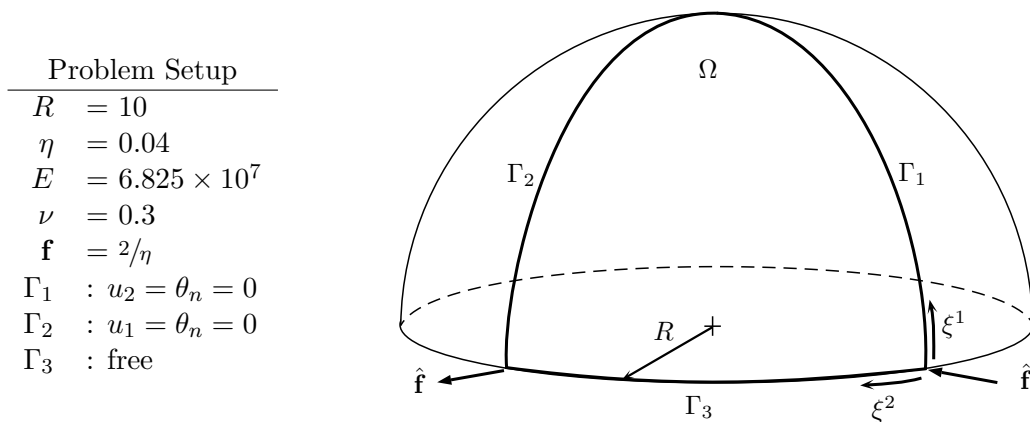


Figure 6.8: The Pinched Hemisphere problem setup and configuration.

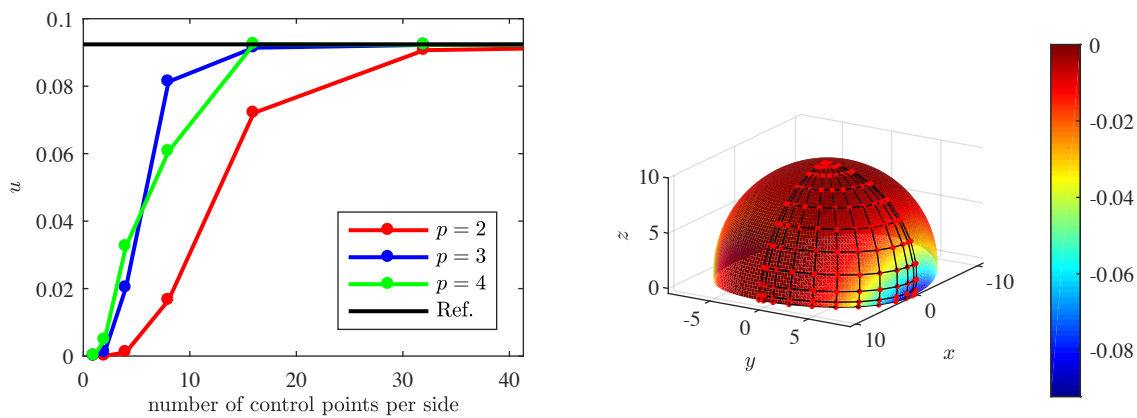


Figure 6.9: The Pinched Hemisphere displacement criterion shown across the range of refinements considered in this paper (left). The z -displacement field is shown on the contour plot (right). Note this is symmetric to the x -displacement field due to the symmetry of the loading configuration.

Chapter 7

Design Space Exploration

7.1 Parametric Partial Differential Equations & Families of Geometries

The seamless connection between CAD geometry and analysis in IGA allows us to define a unique relationship between **design parameters** and the corresponding CAD geometry. These parameters define the control points and weights associated with a geometric configuration. However it should be noted that, in general, control points are not individual design parameters to be tuned. Instead, we seek a reduced set of these design parameters which describe **features** and the overall shape of the design, in contrast to specific control point locations. For instance, these design parameters may be the radius of hole or fillet, the thickness of a load-bearing plate, or the Lamé parameters which relate stress and strain through a constitutive relationship.

Let us now formalize the above concepts. Namely, let us construct a **design space** $\mathcal{D} \subset \mathbb{R}^{d_\mu}$, where d_μ is the dimension of the parametric space associated with design parameters. We refer to each member of \mathcal{D} , denoted as $\boldsymbol{\mu} \in \mathcal{D}$, as a **design variable**, and it contains a selection of design parameters governing the material and geometric properties for a given design as discussed above. We assume throughout the dissertation that \mathcal{D} is a hyperrectangle, that is, a Cartesian product of intervals: $\mathcal{D} = (a_1, b_1) \times (a_2, b_2) \times \dots \times (a_{d_\mu}, b_{d_\mu})$. This will allow us to easily adopt existing sampling-based surrogate modeling approaches as shown in a later subsection. With the above terminology established, we connect a CAD geometry to the design space through the notion of a family of geometries:

Definition: Family of Geometries

A family of geometries $\{\Omega_\mu\}_{\mu \in \mathcal{D}}$ is a set of open domains $\Omega_\mu \subset \mathbb{R}^{d_\mu}$ defined from a family of geometric mappings:

$$\mathbf{x}_\mu(\xi) = \sum_i P_i(\mu) \hat{R}_i(\xi) \quad \forall \xi \in \hat{\Omega} \quad (7.1)$$

That is, $\Omega_\mu = \mathbf{x}_\mu(\hat{\Omega})$ for every $\mu \in \mathcal{D}$.

Note that in the above definition, we have implicitly defined the control mesh to be a function of the design variable. To make the concept of a family of geometries clear, consider the example of a Scordelis-Lo roof, as illustrated in Figure 7.1. The design variable:

$$\mu = (L, R, \varphi, t, E, \nu) \quad (7.2)$$

completely describes the Scordelis-Lo Roof family of geometries. In other words, we are able to generate the unique control points and weights as a function of the design variable (7.2).

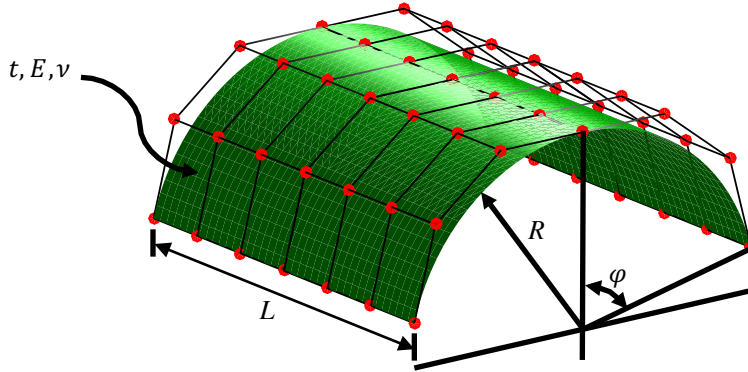


Figure 7.1: The Scordelis-Lo Roof Family

In **parametrized IGA for a family of geometries**, we consider the effect of changing geometry on the resulting solution. In particular, we parametrize the partial differential equation (2.5) in terms of the design variable μ :

$$\begin{aligned} \mathcal{L}(u(\mu); \mu) &= \mathcal{F}(\mu) \quad \forall x \in \Omega_\mu \\ \mathcal{B}(u(\mu); \mu) &= \mathcal{G}(\mu) \quad \forall x \in \partial\Omega_\mu \end{aligned} \quad (7.3)$$

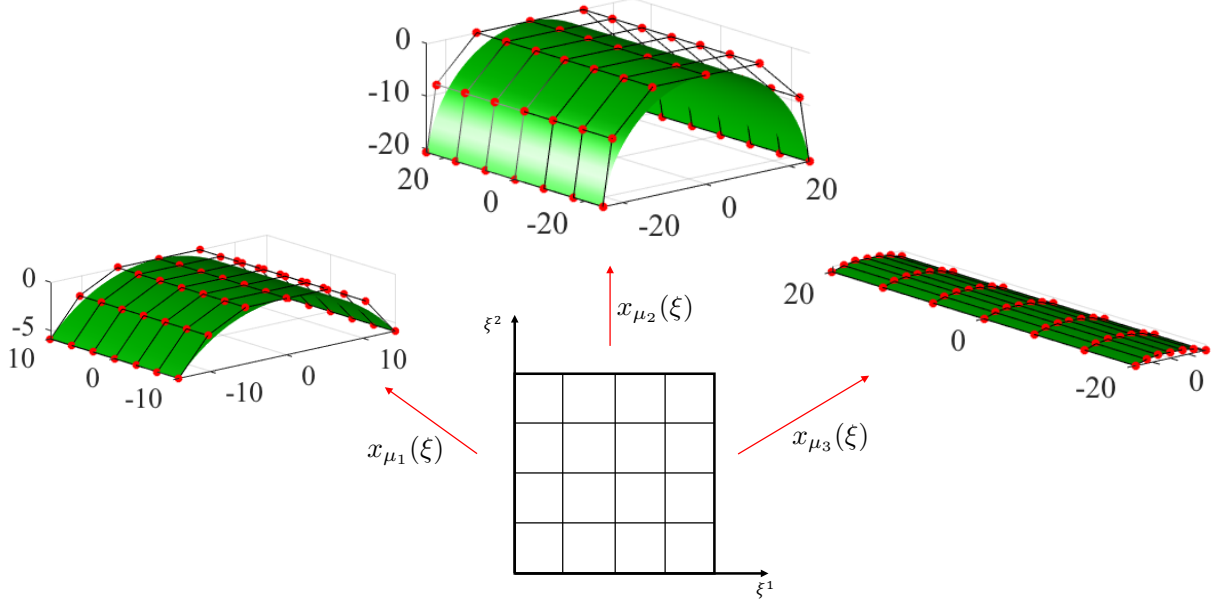


Figure 7.2: A representative sample of Scordelis-Lo Roof geometries belonging to the same family. Notice that after defining the appropriate mapping $\mathbf{x}_{\mu_i}(\boldsymbol{\xi})$, the same parametric domain can be mapped to various geometries seamlessly.

Leveraging the concepts (2.6) and (2.7), we claim that the discrete solution to such a problem can be expressed as:

$$\mathbf{u}^h(\mathbf{x}, \boldsymbol{\mu}) = \sum_{\mathbf{i}} \mathbf{d}_{\mathbf{i}}(\boldsymbol{\mu}) R_{\mathbf{i}}(\mathbf{x}) = \sum_{\mathbf{i}} \underbrace{\mathbf{d}_{\mathbf{i}}(\boldsymbol{\mu})}_{\text{unknown}} \underbrace{\hat{R}_{\mathbf{i}}(\mathbf{x}_{\boldsymbol{\mu}}^{-1}(\mathbf{x}))}_{\text{known}} \quad (7.4)$$

The effect of $\boldsymbol{\mu}$ on the physical basis functions is known through the isoparametric concept. With the concept of geometric families defined, the terms $\mathbf{d}_{\mathbf{i}}(\boldsymbol{\mu})$ in (7.4) are determined by a set of nonlinear algebraic equations:

$$\mathbf{R}(\boldsymbol{\mu}, \mathbf{d}(\boldsymbol{\mu})) = \mathbf{0} \quad \forall \boldsymbol{\mu} \in \mathcal{D} \quad (7.5)$$

where $\mathbf{R}(\boldsymbol{\mu}, \mathbf{d}(\boldsymbol{\mu}))$ is a vector of residuals and $\mathbf{d}(\boldsymbol{\mu})$ is a solution vector collecting the unknown control variables. In the linear setting, this system reduces to solving the system:

$$\mathbf{K}(\boldsymbol{\mu}) \mathbf{d}(\boldsymbol{\mu}) = \mathbf{F}(\boldsymbol{\mu}) \quad \forall \boldsymbol{\mu} \in \mathcal{D} \quad (7.6)$$

The discretized PDE systems (7.5) and (7.6) provides a vessel to explore the design space. Namely, for every $\boldsymbol{\mu}$, the solution $\mathbf{d}(\boldsymbol{\mu})$ is the parametric system response. However, every time $\boldsymbol{\mu}$ is changed, one must not only solve the system, but also assemble it. For an effective rapid design space exploration paradigm, we want to construct a framework for determining the solution for a family of geometries in a neighborhood about some nominal design, rather than for one particular design, so it is greatly desirable to reduce the computational expense of solving (7.5) and (7.6).

There exists two primary approaches to reduce this computational expense through the construction of suitable surrogate models:

1. **Dimensionality Reduction of the Spatial Approximation:** In this instance, a linear system of the form (7.6) for every parametric instance of $\boldsymbol{\mu}$ is assembled and solved. However, the associated computational expense is reduced by employing a reduced-order model. This approach utilizes techniques such as reduced basis methods [83] and proper orthogonal decompositions [95] for the surrogate model construction.
2. **Dimensionality Reduction of the Parametric Representation:** In this instance, rather than solving a linear system for every parametric instance of $\boldsymbol{\mu}$, we solve the full system (7.6) for a set $\{\boldsymbol{\mu}_i\}_i$ and extrapolate the obtained solutions throughout the design space to effectively construct a surrogate model.

In this dissertation, we consider the second approach listed above due to ease of implementation. More specifically, the second approach allows us to build sampling-based surrogate models using a wrapper about existing IGA simulation technologies. It should be mentioned that the parametrized analysis paradigm that we have presented here is quite difficult to implement within a classical finite element analysis framework. This is because changes to the geometry require a complete re-meshing within standard design-through-analysis platforms built on finite elements.

Consequently, most existing design space exploration environments allow users to visualize only quantities of interest such as max displacement, von Mises stress, or power consumption [71, 123]. By contrast, our environment allows users to visualize full system response.

We now transition to a discussion of surrogate modeling techniques including both sampling and construction.

7.2 Design Space Collocation for Parametrized IGA

In this section, we present a number of techniques of constructing a surrogate model for the solution manifold in parametrized IGA. To set the stage, recall that the displacement field in parametrized structural mechanics takes the form:

$$\mathbf{u}(\mathbf{x}, \boldsymbol{\mu}) = \sum_{\mathbf{i}} \mathbf{d}_{\mathbf{i}}(\boldsymbol{\mu}) R_{\mathbf{i}}(\mathbf{x})$$

The basis functions $R_{\mathbf{i}}(\mathbf{x})$ are known while the control variables $\mathbf{d}_{\mathbf{i}}(\boldsymbol{\mu})$ are unknown functions of the design parameters. In our surrogate modeling approach, we approximate the solution vector of (7.6) using a basis expansion of the form:

$$\mathbf{d}(\boldsymbol{\mu}) = \sum_{\mathbf{i}} \mathbf{c}_{\mathbf{i}} \Psi_{\mathbf{i}}(\boldsymbol{\mu})$$

where $\{\Psi_{\mathbf{i}}(\boldsymbol{\mu})\}_{\mathbf{i}}$ is a finite-dimensional set of orthogonal basis functions scaled by the coefficients $\mathbf{c}_{\mathbf{i}}$.

There are many suitable choices of basis functions but we only consider two herein. In particular, our choice of basis functions lie in the realms of **nodal** and **modal** manifold representations. A nodal paradigm considers the familiar **Lagrange basis**, which interpolates nodal data at sampling points while intermediate data is obtained through a linear combination of such basis functions scaled by their corresponding nodal values [6]. On the other hand, a modal representation considers a truncated spectral expansion of a function. An orthogonal polynomial series is first specified in which to represent the function. The modal coefficients are then associated with the terms in this series. Each coefficient quantifies the modal behavior intrinsic to the aggregate solution field. For

both the nodal and modal approaches, we employ parametric sampling to obtain approximations of the coefficients \mathbf{c}_i . In this manner, our surrogate modeling approach is non-intrusive in that our modeling methodology may be used as a “black box” in conjunction with existing IGA packages. This dramatically simplifies implementation as compared with intrusive approaches such as the parametric Galerkin method.

Before proceeding with the derivation of such polynomial surrogate models, we formally introduce the concept of a **multi-index**, since it greatly simplifies the notation in following sections and will establish a uniform language to be used consistently throughout this dissertation. A multi-index is an array of indices used to reference the dimensions present in a variable. Consider the multi-index $\mathbf{i} = (i_1, i_2, \dots, i_d)$. We can then enumerate a variable in several dimensions as $\boldsymbol{\mu}_i = (\mu_{i_1}, \mu_{i_2}, \dots, \mu_{i_d})$. It is often times convenient to introduce the concept of a multi-index norm. In this dissertation, the two norms of interest will be the **sup-norm** and **1-norm** given by:

$$\begin{aligned} \infty - \text{norm:} \quad & \|\mathbf{i}\|_\infty = \max_k |i_k| \\ \text{1-norm:} \quad & \|\mathbf{i}\|_1 = \sum_{k=1}^d |i_k| \end{aligned} \tag{7.7}$$

respectively. Moreover, after specification of a multi-index norm and a given non-negative integer k , we can define the following multi-index spaces:

$$\begin{aligned} \text{Isotropic:} \quad & \mathcal{P}_k^d := \left\{ \mathbf{i} \in (\mathbb{Z}^*)^d \mid 0 \leq \|\mathbf{i}\|_1 \leq k \right\} \\ \text{Tensor-product:} \quad & \mathcal{Q}_k^d := \left\{ \mathbf{i} \in (\mathbb{Z}^*)^d \mid 0 \leq \|\mathbf{i}\|_\infty \leq k \right\}. \end{aligned} \tag{7.8}$$

The meaning of this terminology will be made clear in a moment when we define polynomial spaces associated with these spaces of multi-indices. Note that these multi-index spaces are nested, specifically $\mathcal{P}_k^d \subseteq \mathcal{Q}_k^d$, and we can simply write summations and products over multivariate quantities using multi-index notation. For example, the tensor-product summation and product operations can be expressed compactly as:

$$\begin{aligned}
\text{Summation:} \quad & \sum_{\mathbf{i} \in \mathcal{Q}_\ell^d} f(\boldsymbol{\mu}_\mathbf{i}) = \sum_{i_1=1}^{\ell} \sum_{i_2=1}^{\ell} \dots \sum_{i_d=1}^{\ell} f(\mu_{i_1}, \mu_{i_2}, \dots, \mu_{i_d}) \\
\text{Product:} \quad & \prod_{\mathbf{i} \in \mathcal{Q}_\ell^d} f(\boldsymbol{\mu}_\mathbf{i}) = \prod_{i_1=1}^{\ell} \prod_{i_2=1}^{\ell} \dots \prod_{i_d=1}^{\ell} f(\mu_{i_1}, \mu_{i_2}, \dots, \mu_{i_d})
\end{aligned} \tag{7.9}$$

With the above multi-index notation established, we can now define what we mean by isotropic polynomial and tensor-product polynomial. Specifically, we define the respective spaces of isotropic and tensor-product polynomials of degree p for the domain $\mathcal{D} \subset \mathbb{R}^d$ via:

$$\begin{aligned}
\text{Isotropic:} \quad & \mathcal{P}_p(\mathcal{D}) := \left\{ f \in L^2(\mathcal{D}) \mid f(\boldsymbol{\mu}) = \sum_{\mathbf{i} \in \mathcal{Q}_p^d} f_{\mathbf{i}} \mu_1^{i_1} \mu_2^{i_2} \dots \mu_d^{i_d} \right\} \\
\text{Tensor-product:} \quad & \mathcal{Q}_p(\mathcal{D}) := \left\{ f \in L^2(\mathcal{D}) \mid f(\boldsymbol{\mu}) = \sum_{\mathbf{i} \in \mathcal{Q}_p^d} f_{\mathbf{i}} \mu_1^{i_1} \mu_2^{i_2} \dots \mu_d^{i_d} \right\}
\end{aligned} \tag{7.10}$$

At this juncture, it is not quite clear what we mean by “isotropic.” This is made clear by recognizing that if $f \in \mathcal{P}_p(\mathcal{D})$ and $\nu : \mathcal{D} \rightarrow \mathbb{R}^d$ is an affine mapping, then the composition mapping $g = f \circ \nu$ is also a member of $\mathcal{P}_p(\mathcal{D})$ ¹. Consequently, the space of isotropic polynomials is invariant under an affine change of coordinates. By contrast, this is not the case for the space of tensor-product polynomials. The concepts and formalism associated with constructing nodal and modal representations of the solution manifold from the tools discussed in heretofore are presented in the following sections.

7.2.1 Nodal Solution Manifold Representation

With a nodal manifold representation, we approximate the control variables as:

$$\mathbf{d}(\boldsymbol{\mu}) \approx \sum_{\mathbf{i}} \mathbf{d}(\boldsymbol{\mu}_\mathbf{i}) \mathcal{N}_\mathbf{i}(\boldsymbol{\mu}) \tag{7.11}$$

where $\{\boldsymbol{\mu}_\mathbf{i}\}_\mathbf{i}$ are a set of interpolation nodes and $\{\mathcal{N}_\mathbf{i}\}_\mathbf{i}$ are a set of interpolating polynomials satisfying:

¹ Here, we have used a slight abuse of notation in extending the domain of f to all of \mathbb{R}^d .

$$\mathcal{N}_{\mathbf{i}}(\boldsymbol{\mu}_{\mathbf{j}}) = \begin{cases} 1, & \text{if } \mathbf{i} \equiv \mathbf{j} \\ 0, & \text{otherwise} \end{cases} \quad (7.12)$$

where equivalence of multi-indices is understood in the component-wise sense, i.e., $i_k = j_k$ $k = 1, 2, \dots, d$. In the univariate setting, we build the interpolating polynomials from a set of $p + 1$ **unique** interpolation nodes $\{\mu_i\}_{i=1}^{p+1}$ which construct the Lagrange interpolants:

$$\mathcal{N}_i(\mu) = \prod_{\substack{j=1 \\ j \neq i}}^{p+1} \frac{\mu - \mu_j}{\mu_i - \mu_j} \quad (7.13)$$

For the multivariate setting, we must take a bit more care. First of all, we do not allow the interpolation nodes to be defined in an arbitrary manner. Instead, we enforce them to be defined via a tensor-product of one-dimensional sets of unique interpolation nodes. Then each interpolation node takes the form:

$$\boldsymbol{\mu}_{\mathbf{i}} = \left(\mu_{i_1}^{(1)}, \mu_{i_2}^{(2)}, \dots, \mu_{i_d}^{(d)} \right) \quad \forall \mathbf{i} \in \mathcal{Q}_p^d \quad (7.14)$$

for a desired tensor-product polynomial approximation of degree p . We build the corresponding interpolating polynomial as:

$$\mathcal{N}_{\mathbf{i}}(\boldsymbol{\mu}) = \bigotimes_{k=1}^d \mathcal{N}_{i_k}^{(k)}(\mu_k) = \bigotimes_{k=1}^d \prod_{\substack{j_k=1 \\ j_k \neq i_k}}^{p_k+1} \frac{\mu_k^{(k)} - \mu_{j_k}^{(k)}}{\mu_{i_k}^{(k)} - \mu_{j_k}^{(k)}} \quad (7.15)$$

Note that the solution coefficients $\mathbf{d}(\boldsymbol{\mu}_{\mathbf{i}})$ are the collocated values of the control variables at the interpolation nodes. Thus, they are obtained by running an IGA simulation for a select number of design instances.

The choice of interpolation nodes to use with such an interpolating scheme remains to be discussed. It is worth noting that an interpolatory representation of the solution manifold, such as the one described in this section, exhibits behavior dependent on the choice of sampling scheme. For example, a uniformly-distributed collection of collocation points results in a solution manifold suffering from the Runge phenomenon, providing acceptable function approximations in the interior

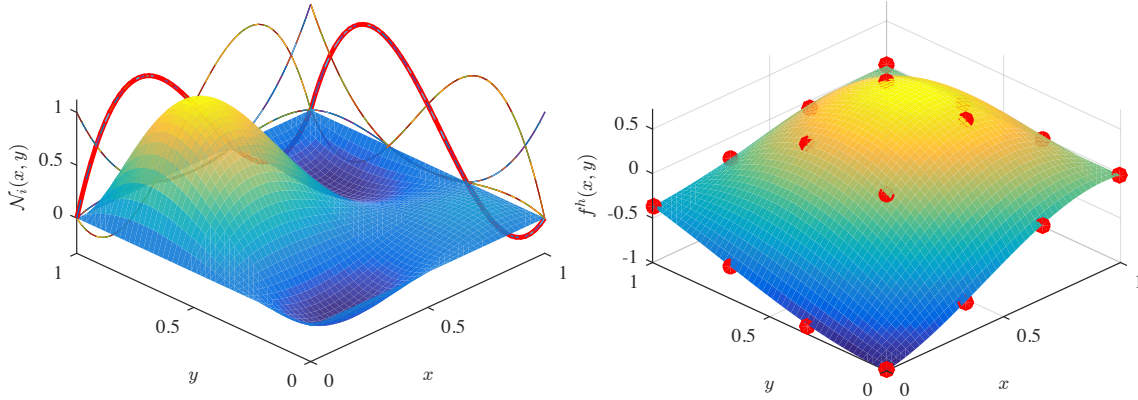


Figure 7.3: A representative tensor-product Lagrange interpolating basis function (left) and an interpolatory representation of the function $f(x, y) = \sin(\pi x) \sin(\pi y) - e^{-x^2 - 4y^2}$ using equispaced nodes and tensor-product Lagrange polynomials (right).

of the design space while exhibiting poor approximability near the boundaries. On the other hand, a Chebyshev distribution of sample points, where the node density is larger near the boundaries of the domain, distributes the error more uniformly throughout the surrogate solution manifold.

For the purposes of design space exploration, we consider the tensor-product Gauss-Legendre quadrature scheme for nodal collocation points. This selection is made due to the high-fidelity of the resulting surrogate model while minimizing the required number of points. In particular, the nodal expansion which interpolates the Gauss abscissa is equivalent to a spectral expansion in terms of a Legendre orthogonal polynomial series, maintaining the same fidelity therein [31].

Note that in using the above procedure, we have built an interpolating basis for the tensor-product approximation space $\mathcal{Q}_p(\mathcal{D})$. We can build an interpolating basis for the alternative multivariate approximation space $\mathcal{P}_p(\mathcal{D})$ in an analogous manner, but a stable choice of interpolation nodes for $\mathcal{P}_p(\mathcal{D})$ is not known at this time. One may also resort to other forms of multi-dimensional interpolation such as radial basis functions, but such an approach is beyond the scope of this dissertation.

7.2.2 Modal Solution Manifold Representation

With a modal manifold representation, we first write the control variables in terms of the infinite sum:

$$\mathbf{d}(\boldsymbol{\mu}) = \sum_{\|\mathbf{i}\|_{\infty} < \infty} \mathbf{a}_{\mathbf{i}} \mathcal{M}_{\mathbf{i}}(\boldsymbol{\mu}) \quad (7.16)$$

where $\{\mathbf{a}_{\mathbf{i}}\}_{\mathbf{i}}$ are a set of spectral coefficients defined as:

$$\mathbf{a}_{\mathbf{i}} = \int_{\mathcal{D}} \mathbf{W}(\boldsymbol{\mu}) \mathbf{d}_{\mathbf{i}}(\boldsymbol{\mu}) \mathcal{M}_{\mathbf{i}}(\boldsymbol{\mu}) d\mathcal{D} \quad (7.17)$$

and $\{\mathcal{M}_{\mathbf{i}}\}_{\mathbf{i}}$ are a set of orthonormal polynomial basis functions satisfying:

$$\langle \mathcal{M}_{\mathbf{i}}, \mathcal{M}_{\mathbf{j}} \rangle_w = \int_{\mathcal{D}} \mathbf{W}(\boldsymbol{\mu}) \mathcal{M}_{\mathbf{i}}(\boldsymbol{\mu}) \mathcal{M}_{\mathbf{j}}(\boldsymbol{\mu}) d\mathcal{D} = \begin{cases} 1, & \text{if } \mathbf{i} \equiv \mathbf{j} \\ 0, & \text{otherwise} \end{cases} \quad (7.18)$$

where $\langle \cdot, \cdot \rangle_w$ is the weighted L^2 inner product and $\mathbf{W}(\boldsymbol{\mu}) \geq 0$ is a pre-defined weighting function. A spectral representation of the solution manifold provides a characterization of the various sensitivities with respect to the design parameters. Namely, the average displacement throughout the design space is given by \mathbf{a}_0 while the magnitude of the following spectral coefficients, $\mathbf{a}_{\mathbf{i}}$, quantify the prominence of particular higher-order modes in the aggregate solution manifold. In this dissertation, we consider the case when $\mathbf{W}(\boldsymbol{\mu}) \equiv 1$, in which case the corresponding orthonormal basis functions coincide with tensor-product **Legendre polynomials**. For instance, when $\mathcal{D} = (-1, 1)^d$, we have that:

$$\mathcal{M}_{\mathbf{i}}(\boldsymbol{\mu}) = \bigotimes_{k=1}^d \mathcal{L}_{i_k}(\mu_k) \quad (7.19)$$

where $\{\mathcal{L}_n\}_{n=0}^{\infty}$ are the univariate Legendre polynomials.

In practice, our infinite sum representation must obviously be truncated after some finite number of terms, resulting in a computationally tractable surrogate model. We consider two such

approximations herein, an isotropic polynomial approximation and a tensor-product polynomial approximation. An isotropic polynomial approximation takes the form:

$$\mathbf{d}(\boldsymbol{\mu}) = \sum_{\mathbf{i} \in \mathcal{P}_p^{d_\mu}} \mathbf{a}_i \mathcal{M}_i(\boldsymbol{\mu}) \quad (7.20)$$

while a tensor-product polynomial approximation takes the form:

$$\mathbf{d}(\boldsymbol{\mu}) = \sum_{\mathbf{i} \in \mathcal{Q}_p^{d_\mu}} \mathbf{a}_i \mathcal{M}_i(\boldsymbol{\mu}) \quad (7.21)$$

Since $\mathcal{P}_p(\mathcal{D}) \subseteq \mathcal{Q}_p(\mathcal{D})$, the isotropic approximation includes less terms than the tensor-product approximation, but both isotropic and tensor-product approximations are **spectral** approximations exhibiting exponential convergence rates. Hence, the isotropic approximation is often preferred due to its comparatively lower computational expense.

From Figure 7.4, it is clear that such a modal representation cannot be interpreted analogously to an interpolation. In the latter case, exact function values are realized at collocation points whereas the former is a least-squares approximation to the function. Note that in order for us to recover both the isotropic and tensor-product approximations, we must compute the spectral coefficients:

$$\mathbf{a}_i = \langle \mathbf{d}, \mathcal{M} \rangle_w = \int_{\mathcal{D}} W(\boldsymbol{\mu}) \mathbf{d}(\boldsymbol{\mu}) \mathcal{M}_i(\boldsymbol{\mu}) d\mathcal{D} \quad (7.22)$$

This presents a challenge for two reasons: (i) We often do not know how to perform the integration analytically and (ii) we do not know the exact form of $\mathbf{d}(\boldsymbol{\mu})$ as it is the unknown we are trying to solve for. To overcome these issues, we turn to numerical quadrature. Briefly speaking, we approximate:

$$\mathbf{a}_i = \int_{\mathcal{D}} W(\boldsymbol{\mu}) \mathbf{d}(\boldsymbol{\mu}) \mathcal{M}_i(\boldsymbol{\mu}) d\mathcal{D} \approx \sum_{\mathbf{q}} \mathbf{d}(\boldsymbol{\mu}_{\mathbf{q}}) \mathcal{M}_i(\boldsymbol{\mu}_{\mathbf{q}}) w_{\mathbf{q}} \quad (7.23)$$

where $\{\boldsymbol{\mu}_{\mathbf{q}}\}_{\mathbf{q}}$ is a set of quadrature points and $\{w_{\mathbf{q}}\}_{\mathbf{q}}$ is a set of corresponding quadrature weights.

We refer to the resulting design space approximation as a *pseudospectral* approximation since

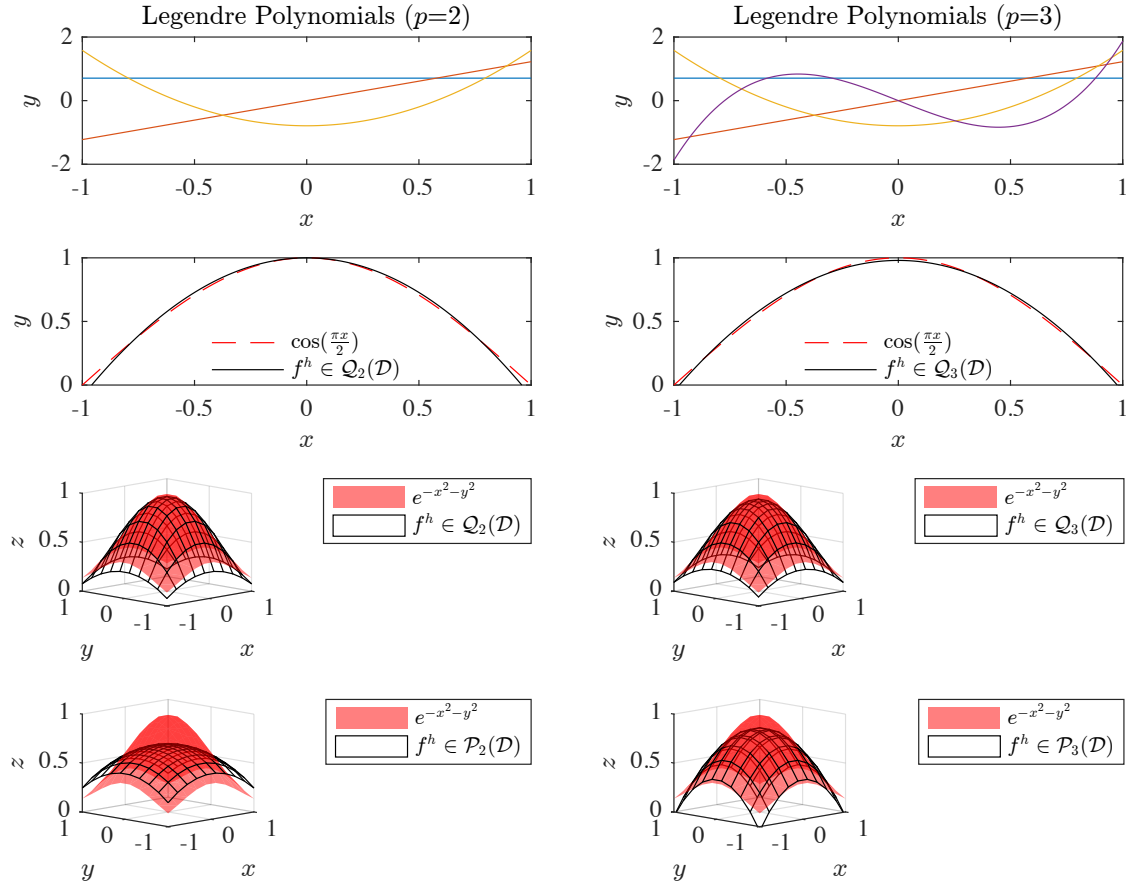


Figure 7.4: The 1st row of the figure shows the Legendre polynomial basis sets for $p = 2$ and $p = 3$. The 2nd row shows the 1-dimensional pseudospectral approximation of $f(x) = \cos(\pi x/2)$ using the above sets of Legendre polynomials, requiring 5 points and 9 points, respectively, for accurate integration using the univariate Clenshaw-Curtis quadrature rule over the domain $\mathcal{D} = (-1, 1)$. The 3rd row shows the pseudospectral representation of the function $f(x, y) = e^{-x^2-y^2}$ using a tensor-product Clenshaw-Curtis quadrature rule in a tensor-product Legendre basis, requiring 25 points and 81 points respectively, resulting in 2nd and 3rd degree tensor-product polynomial approximations over the domain $\mathcal{D} = (-1, 1)^2$. The 4th row shows the pseudospectral representation of the function $f(x, y)$ using a Delayed Smolyak Clenshaw-Curtis quadrature rule in the isotropic Legendre basis, requiring 13 points and 29 points respectively, resulting in 2nd and 3rd degree isotropic polynomial approximations over the domain $\mathcal{D} = (-1, 1)^2$.

the exact spectral coefficients have been approximated. With quadrature, we avoid the need for analytical integration and we also only need to determine $\mathbf{d}(\boldsymbol{\mu})$, that is, sample the solution space, at a set of quadrature points. In the next section, we provide an overview of quadrature schemes one may utilize including tensor-product quadrature and sparse quadrature.

7.2.3 Design Space Sampling and Numerical Integration

It remains to select sampling schemes and quadrature rules to recover the interpolated values in the nodal manifold representation and the spectral coefficients in the modal manifold representation. Our objective is to obtain sampling and quadrature schemes which not only lead to accurate surrogate models but are also computationally efficient. Since our selection of interpolation nodes in the nodal manifold representation follows a quadrature scheme, all of our schemes begin with a univariate quadrature rule which is then extended to the multivariate setting.

7.2.3.1 Univariate Quadrature

A general univariate quadrature scheme takes the form:

$$\mathcal{I}_w^1 f = \int_a^b W(x)f(x)dx \approx U_{n_q}^{(1)} f = \sum_{q=1}^{n_q} w_q f(x_q) \quad (7.24)$$

where (a, b) is the integration domain, $f : (a, b) \rightarrow \mathbb{R}$ is the function to be integrated, $W(x) \geq 0$ is a specified weighting function, n_q is the number of quadrature points, $\{x_q\}_{q=1}^{n_q}$ are the quadrature points, and $\{w_q\}_{q=1}^{n_q}$ are the quadrature weights. We have used the notation \mathcal{U}_{n_q} to denote a **univariate** scheme with n_q points. There are a great many number of univariate quadrature schemes to choose from, each with their own sets of pros and cons. We consider three herein: Gauss-Legendre quadrature [55], Clenshaw-Curtis quadrature [29], and Kronrod-Patterson quadrature [91]. The Gauss-Legendre scheme is ideal in that it employs a minimal number of quadrature points for a desired level of polynomial accuracy. On the other hand, the Clenshaw-Curtis and Kronrod-Patterson schemes exhibit a so-called nestedness property, to be described later, which alleviates the computational expense associated with an increase in the model polynomial fidelity in the multi-dimensional setting. Each of the three aforementioned schemes consist of not only one quadrature rule but rather a family of quadrature rules. We refer to the ℓ^{th} member of a given family as the ℓ^{th} level, and it contains n_ℓ quadrature points and weights and exhibits a polynomial degree accuracy of p_ℓ . That is, the quadrature rule \mathcal{U}_{n_ℓ} exactly integrates polynomials

of degree p_ℓ . Table 7.1 characterizes the Gauss-Legendre, Clenshaw-Curtis, and Kronrod-Patterson schemes and their properties.

Table 7.1: A comparison between the Gauss-Legendre, Clenshaw-Curtis, and Kronrod-Patterson quadrature schemes considered in this dissertation.

Univariate Scheme	Nested?	n_ℓ	p_ℓ
Gauss-Legendre	✗	ℓ	$2n_\ell - 1$
Clenshaw-Curtis	✓	$\begin{cases} 1, & \ell = 1 \\ 2^{\ell-1} + 1, & \ell \geq 2 \end{cases}$	$\begin{cases} n_\ell, & n_\ell \text{ even} \\ n_\ell + 1, & n_\ell \text{ odd} \end{cases}$
Kronrod-Patterson	✓	$2^\ell - 1$	$1/2(3n_\ell - 1)$

We are now ready to define what we mean by nested. Namely, a family of quadrature rules is **nested** if $\cup_{k=0}^{\ell-1} \{\mathbf{x}_q\}_k \subseteq \{\mathbf{x}_q\}_\ell$ where $\{\mathbf{x}_q\}_\ell$ is the set of quadrature nodes of level ℓ . This property will allow us to build highly efficient quadrature schemes in the multi-dimensional setting using the so-called Smolyak method.

7.2.3.2 Tensor-Product Multivariate Quadrature

We define a tensor-product multivariate quadrature rule as a tensor-product of univariate quadrature rules. In particular, given a set of n_ℓ -point univariate quadrature rules, $\{\mathcal{U}_{n_\ell}^{(i)}\}_{i=1}^d$, each associated with the ℓ^{th} level of a family of quadrature rules, we construct the multivariate rule:

$$\mathcal{F}_\ell^d f = \bigotimes_{i=1}^d \mathcal{U}_{n_\ell}^{(i)} f \quad (7.25)$$

for $f : \mathcal{D} \rightarrow \mathbb{R}$ where $\mathcal{D} \subset \mathbb{R}^d$ is a hyperrectangle. Then, to approximate the integral of a function, we write:

$$\begin{aligned} \mathcal{I}_W^d f &= \int_{\Omega} W_1(x_1)W_2(x_2) \cdots W_d(x_d) f(x_1, x_2, \dots, x_d) d\Omega \\ &\approx \mathcal{F}_\ell^d f = \sum_{i_1=1}^{n_\ell} \sum_{i_2=1}^{n_\ell} \cdots \sum_{i_d=1}^{n_\ell} w_{i_1} w_{i_2} \cdots w_{i_d} f(x_{i_1}, x_{i_2}, \dots, x_{i_d}) \end{aligned} \quad (7.26)$$

Figure 7.5 shows the tensor-product collocation schemes for Clenshaw-Curtis and Gauss-Legendre quadrature rules for two-dimensional integration.

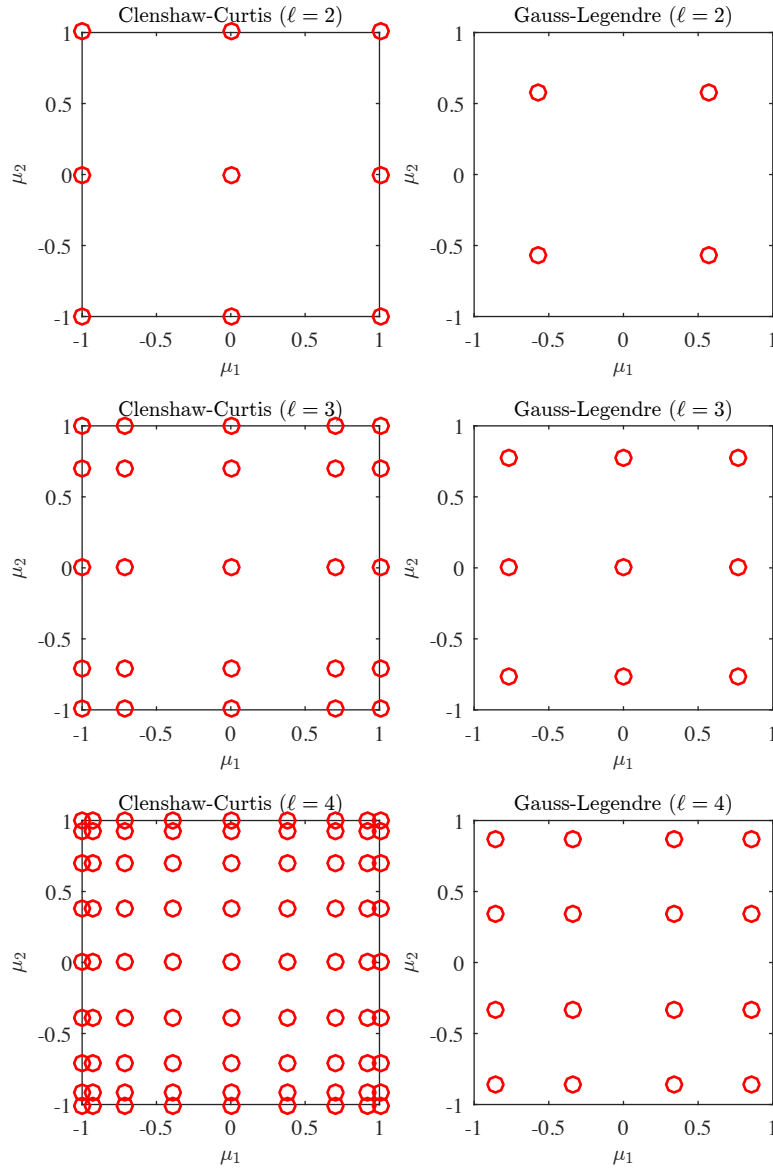


Figure 7.5: Two-dimensional tensor-product Clenshaw-Curtis (left) and Gauss-Legendre (right) quadrature rules for the integration domain $\mathcal{D} = (-1, 1)^2$. The ℓ^{th} -level Clenshaw-Curtis quadrature rule is capable of integrating $f \in \mathcal{Q}_{p_\ell}(\mathcal{D})$ with $p_\ell = 2^{\ell-1} + 1$ for $\ell > 1$ exactly while each Gauss-Legendre grid level ℓ is capable of integrating $f \in \mathcal{Q}_{p_\ell}(\mathcal{D})$ with $p_\ell = 2\ell - 1$ exactly.

Using tensor-product quadrature, we are able to obtain suitable interpolation points for the nodal manifold representation as well as suitable approximations of the spectral coefficients for both isotropic and tensor-product modal manifold approximations. In the nodal setting, we determine the polynomial order of the set of Lagrange basis functions by selecting the appropriate number

of collocation points, i.e., $p = n - 1 \geq 0$ where n is the number of univariate sample points. The selection of these points, and hence the polynomial order, are dictated by the error bound given by the Taylor series truncation error [6]. On the other hand, in the modal setting we seek to accurately represent the integrals defining the spectral coefficients using numerical integration:

$$\mathbf{a}_i = \int_{\mathcal{D}} W(\boldsymbol{\mu}) \mathbf{d}(\boldsymbol{\mu}) \mathcal{M}_i(\boldsymbol{\mu}) d\mathcal{D} \approx \mathcal{F}_\ell^d \mathbf{d} = \sum_{\mathbf{i} \in \mathcal{Q}_\ell^d} \mathbf{d}(\boldsymbol{\mu}_i) \mathcal{M}_i(\boldsymbol{\mu}_i) w_i. \quad (7.27)$$

In this case, we select ℓ such that $p_\ell = 2p$ where p is the desired polynomial degree of the modal manifold representation, i.e., $p = \max_{\mathbf{i}} \deg(\mathcal{M}_i)$. This has been shown to yield a stable and accurate numerical integration scheme [51, Chapter 4], and when $\mathbf{d}(\boldsymbol{\mu})$ is a tensor-product polynomial of degree p , the numerical integration scheme is exact.

Unfortunately it should be noted that a tensor-product quadrature rule suffers from the so-called **curse of dimensionality**. Particularly, each additional dimension, i.e. design parameter, causes an **exponential** increase in the number of required quadrature points. This sampling approach scales as $N_\ell = n_\ell^d$, where N_ℓ is the total number of collocation points for level ℓ , n_ℓ is the number of points associated with a univariate quadrature rule of level ℓ , and d is the dimension of the design space. Therefore, as the complexity of the design space grows, this approach quickly becomes intractable.

7.2.3.3 Sparse Multivariate Quadrature

To alleviate the curse of dimensionality associated with tensor-product quadrature, we consider sparse quadrature schemes obtained through the use of Smolyak sparse grids. Our objective is the construction of a numerical integration scheme capable of integrating a multi-dimensional **isotropic** polynomial with a minimal number of quadrature points. Recall that here isotropic refers to a polynomial with total degree $\|\mathbf{p}\|_1 \leq p$ for some $p \geq 0$. To begin, we define difference operators for each parametric dimension from a family of quadrature rules via:

$$\Delta_j^{(i)} = \begin{cases} \mathcal{U}_{n_1}^{(i)}, & \text{if } j = 1 \\ \mathcal{U}_{n_{j+1}}^{(i)} - \mathcal{U}_{n_j}^{(i)}, & \text{otherwise} \end{cases} \quad (7.28)$$

Then, the corresponding level ℓ Smolyak quadrature scheme is defined for $f : \mathcal{P} \rightarrow \mathbb{R}$ as:

$$\mathcal{S}_\ell^d f = \sum_{\boldsymbol{\alpha} \in \mathcal{P}_\ell^d} \bigotimes_{i=1}^d \Delta_{\alpha_i+1}^{(i)} f \quad (7.29)$$

The above quadrature rule is exact for at least all isotropic polynomials of degree less than or equal to p_ℓ , though it is not quite exact for tensor-product polynomials of degree p_ℓ . Consequently, Smolyak quadrature should be employed for isotropic polynomial approximations. However, as we shall see, Smolyak quadrature schemes employ far fewer quadrature points than tensor-product schemes.

It is often times convenient, especially for implementation, to represent the Smolyak scheme in terms of the univariate quadrature operators $\mathcal{U}_{n_\ell}^{(i)}$. After algebraic manipulation, we arrive at the representation:

$$\mathcal{S}_\ell^d f = \sum_{\ell \leq \|\mathbf{k}\|_1 \leq d+\ell-1} (-1)^{d+\ell-\|\mathbf{k}\|_1-1} \binom{d-1}{\|\mathbf{k}\|_1-\ell} \bigotimes_{i=1}^d \mathcal{U}_{n_{k_i}}^{(i)} f \quad (7.30)$$

From the above expression, we see that a Smolyak scheme is simply comprised of many tensor-product univariate quadrature schemes. If these schemes happen to exhibit nestedness, then there is an interlacing of quadrature points in between levels which provides additional accuracy with a minimal increase in required function evaluations. Consequently, we only consider nested quadrature families when building sparse quadrature rules for design space exploration.

As see in Table 7.1, the number of quadrature points n_ℓ and corresponding degree p_ℓ with the univariate Clenshaw-Curtis and Kronrod-Patterson schemes increases exponentially fast with the level ℓ . Unfortunately, this means this is also the case for Smolyak quadrature rules built from these families. This exponential growth per level is not ideal for application to design space exploration since we ultimately desire an economical, low-fidelity surrogate model. Fortunately, as presented

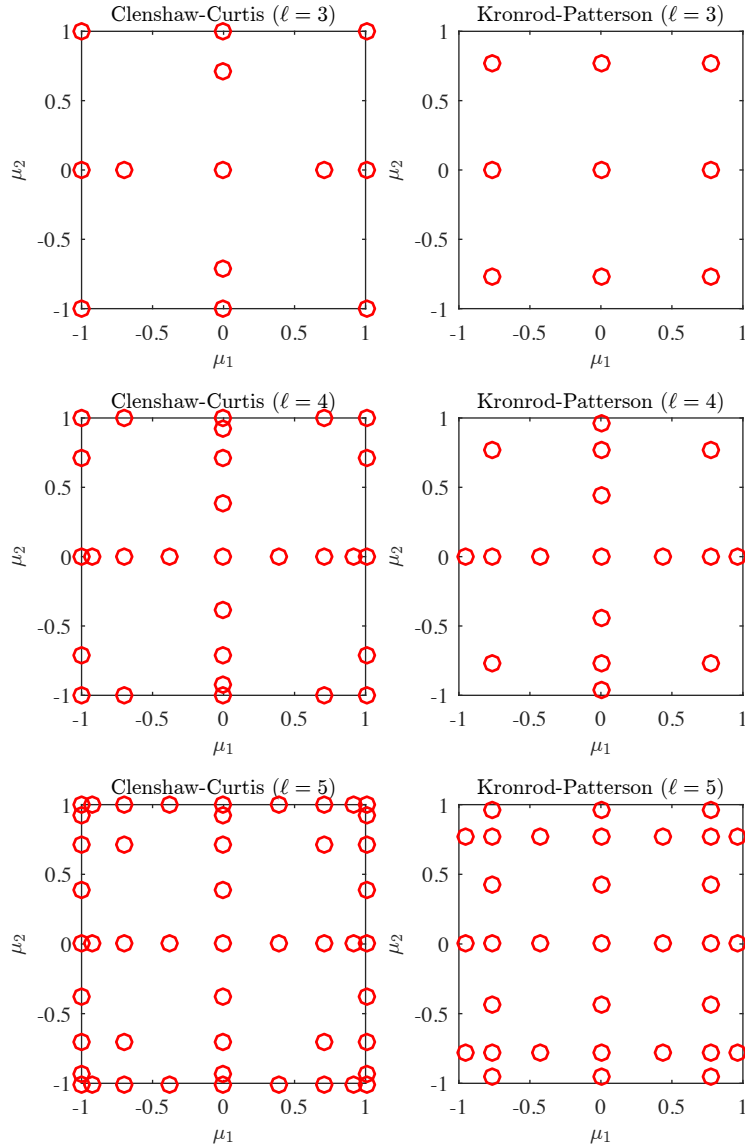


Figure 7.6: Smolyak collocation schemes for the delayed, two-dimensional Clenshaw-Curtis (left) and Kronrod-Patterson (right) quadrature rules for the integration domain $\mathcal{D} = (-1, 1)^2$. Both delayed Clenshaw-Curtis and Kronrod-Patterson grids are capable of integrating $f \in \mathcal{P}_{p_\ell}(\mathcal{D})$ with $p_\ell = 2\ell - 1$ exactly. Note that the nestedness of the Clenshaw-Curtis naturally permits Smolyak implementation, contrary to the Gauss-Legendre scheme which requires the Kronrod extension and Patterson's recursion.

in [92, 24], these exponentially-growing sequences can be delayed to slow the growth in required sampling data. In these delayed sequences, some of the quadrature rules are repeated to lower the rank of approximation and hence the required number of univariate quadrature points. With this

in mind, the **delayed Clenshaw-Curtis rule** is defined as:

$$\mathcal{U}_\ell^{CC,delayered} = \mathcal{U}_{k_\ell}^{CC}, \quad k_\ell = \begin{cases} 1, & \ell = 1 \\ \lceil \log_2(\ell - 1) \rceil + 1, & \ell > 1 \end{cases} \quad (7.31)$$

while the **delayed Kronrod-Patterson** univariate rule is defined as:

$$\mathcal{U}_\ell^{KP,delayered} = \mathcal{U}_{k_\ell}^{KP}, \quad \log_2\left(\frac{4\ell}{3}\right) \leq k_\ell \leq \log_2\left(\frac{8\ell - 1}{3}\right) \quad (7.32)$$

where, for simplicity of presentation, the subscripts ℓ and k_ℓ refer to the level rather than the number of quadrature points. Because of the presence of the logarithmic factors in the definitions of the delayed univariate rules, the number of quadrature points n_ℓ associated with the univariate sequences increases only linearly with the level ℓ . Consequently, the number of quadrature points n_ℓ associated with Smolyak quadrature schemes built from these sequences increases algebraically with the level ℓ . This is illustrated in Figure 7.6 which displays the Smolyak quadrature points for the delayed Clenshaw-Curtis and Kronrod-Patterson quadrature rules for levels $\ell = 3, 4, 5$.

It should be mentioned that the delayed Clenshaw-Curtis and Kronrod-Patterson sequences were constructed such that the associated Smolyak quadrature schemes built from these sequences exhibit a polynomial accuracy of $p_\ell \geq 2\ell - 1$ for $\ell \geq 1$, and for relatively low levels, $p_\ell = 2\ell - 1$. This guides the selection of sparse grid quadrature rules for the computation of spectral coefficients for isotropic polynomial coefficients. Recall that to accurately compute the coefficients for an isotropic polynomial of degree p , we should employ a quadrature rule with accuracy $2p$. Therefore, we can use a level $\ell = p + 1$ Smolyak quadrature scheme built from one of the two delayed sequences. With this in mind, and recalling the rules displayed in Figures 7.5 and 7.6, we see that these Smolyak quadrature schemes employ fewer quadrature points for a desired polynomial accuracy than their tensor-product counterparts, as contended earlier, and this reduction becomes far more dramatic with an increase in the dimensionality of the design space.

As a final remark, it is worth noting that the tensor-product quadrature scheme can be expressed in terms of the difference operators defining the Smolyak scheme. Namely, we have:

$$\mathcal{F}_\ell^d f = \sum_{\alpha \in \mathcal{Q}_\ell^d} \bigotimes_{i=1}^d \Delta_{\alpha_{i+1}}^{(i)} f = \bigotimes_{i=1}^d \mathcal{U}_{n_\ell}^{(i)} f \quad (7.33)$$

Consequently, the primary difference between the tensor-product and Smolyak schemes lies in the specification of the multi-index spaces \mathcal{P}_ℓ^d and \mathcal{Q}_ℓ^d .

7.2.4 Numerical Results

This section contains a selection of numerical examples illustrating the convergence behavior of the aforementioned methodology. In particular, we consider: (i) the Scordelis-Lo roof, (ii) a flat L-bracket, and (iii) an NREL 5MW wind turbine blade. Each subsection begins with a brief description of the methodologies discussed in previous sections with application to the problem under consideration. A convergence analysis is presented thereafter, where we will consider the effect of the polynomial order on the expansion to quantify the accuracy of our sampling-based surrogate modeling methodology as well as the effect of a change in the number of quadrature points, which assess the accuracy of the modal coefficients computed through the discrete integration. Lastly, we will numerically demonstrate the capability of design optimization facilitated through the design space exploration paradigm by maximizing or minimizing quantities of interest over a pre-specified design space for the Scordelis-Lo roof.

7.2.4.1 Scordelis-Lo Roof

Earlier in this dissertation, the Scordelis-Lo roof was introduced as a canonical shell code validation problem. Due to the relatively simple design-variable description of this shell, it is a premier problem choice for demonstrating the concepts presented in this dissertation. As such, we will study all aspects of our methodology using this problem, including: (i) the effectiveness of both nodal and modal solution manifold representations, (ii) the effectiveness of both isotropic and tensor-product polynomial approximations in the design space, and (iii) the accuracy of both tensor-product and sparse grid quadrature schemes as applied in design space exploration.

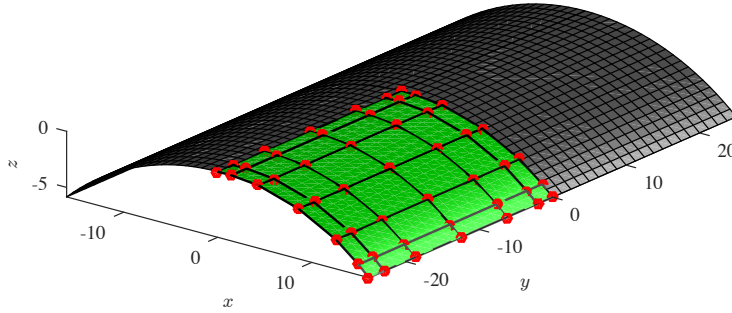


Figure 7.7: The computational domain of the Scordelis-Lo Roof. For sake of computational expense, only a quarter of the roof is modeled with symmetry boundary conditions. Therefore, refinement with respect to this geometry occurs only in this quadrant. This particular geometry has 16 elements.

7.2.4.2 Problem Formulation and Methodology

For the following discussion, the design space $\mathcal{D}_{\text{roof}} \subset \mathbb{R}^4$ is specified as:

$$\mathcal{D}_{\text{roof}} := \{\boldsymbol{\mu} = (L, R, t, \varphi) \mid 45 \leq L \leq 55, \quad 20 \leq R \leq 30, \quad .2 \leq t \leq .3, \quad 35^\circ \leq \varphi \leq 45^\circ\} \quad (7.34)$$

Note that this design space is restricted in the sense that $E = 550\text{MPa}$ and $\nu = 0.05$ are held fixed and moreover are not treated as design parameters, in comparison with our earlier discussion.

The computational domain used for analysis is shown in Figure 7.7. Due to the symmetry of the cylindrical shell geometry, only one quarter of the domain is analyzed. Homogeneous Dirichlet boundary conditions are applied to the cylindrical part of the free boundary while the remaining straight portion of the free boundary is unconstrained. Symmetry boundary conditions are applied by enforcing homogeneous normal derivatives, as well as zero in-plane displacement, across the symmetric boundary. The shell is loaded by a uniform gravitational field $\mathbf{g} = (0, 0, -90)^T$. Two tensor-product meshes of 16 and 64 elements are considered to assess convergence of the sampling-based surrogate modeling strategy under mesh refinement.

Both modal and nodal representations of the solution manifold to this design space are constructed with both tensor-product and sparse sampling. For ease of user interaction and demonstration, the results were compiled into a Graphical User Interface (GUI), which convey the properties

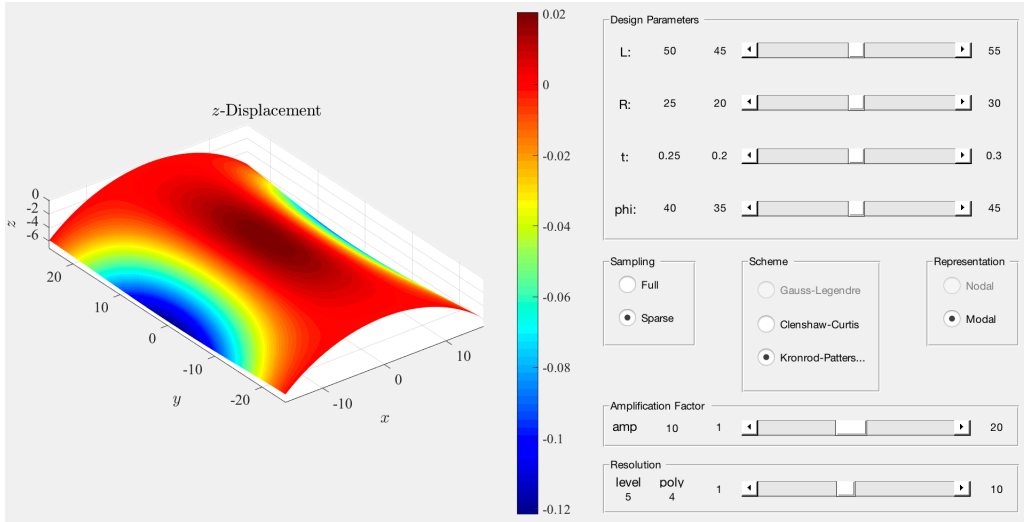


Figure 7.8: The “nominal” Scordelis-Lo roof geometry. A sparse, level 5 Kronrod-Patterson grid is used to compute the pseudospectral coefficients of the surrogate displacement field in the isotropic Legendre basis.

of this design approach in comparison to conventional design methodologies. Figures 7.8 and 7.9 below show screenshots of such a GUI.

7.2.4.3 Convergence Analysis

We continue our discussion by analyzing convergence behavior. In particular, we consider the error, $e^h = u_{IGA}^h - u_{surrogate}^h$, in both the L^2 and energy norms:

$$\|e^h\|_{0,\Omega}^2 = \int_{\Omega} |e^h|^2 d\Omega \quad \text{and} \quad \left\| \|e^h\|_A \right\|^2 + \left\| \|e^h\|_B \right\|^2 = a_{KLS}(e^h, e^h) \quad (7.35)$$

effectively assessing the accuracy of the displacement field and the strain energy, respectively. To ensure the accuracy of the figures presented, the L^2 and energy norms are computed for a total of 10 randomly-selected admissible geometries in the design space and then averaged. It should be noted that we do not compare our solution to the exact solution as we are only assessing the effectiveness of our surrogate modeling strategy. Instead, we are comparing the results obtained from our surrogate model to those obtained from IGA.

The first numerical test performed is shown in Table 7.2 below. In this instance, we use

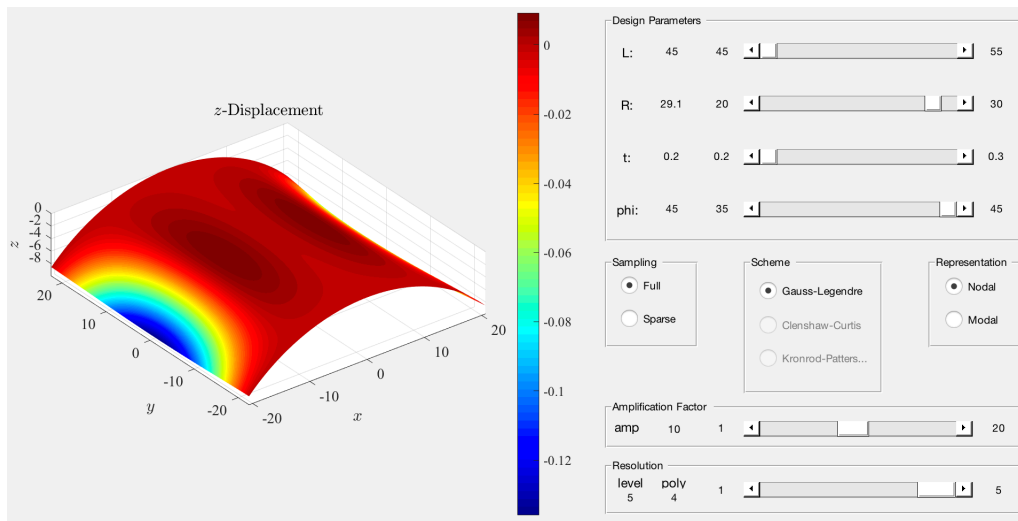


Figure 7.9: An admissible geometry to the design space specified above. In this particular example, a full (tensor-product), level 5 Gauss-Legendre grid is used to construct a nodal representation of the displacement field using a tensor-product Lagrange basis in the design space.

n_ℓ Gauss-Legendre quadrature nodes in each parametric direction to construct a tensor-product Lagrange polynomial of degree p_ℓ which interpolates the solution manifold at the Gauss-Legendre collocation points. From the table we see that the error decreases exponentially fast as the polynomial degree p_ℓ is increased. However, as the nodal manifold representation employs a tensor-product polynomial approximation in the design space, the number of required interpolation points increases very quickly with polynomial degree. Note moreover that the error behavior is the same for both the 16 element mesh and the 64 element mesh.

The second numerical test, shown in Table 7.3, uses a modal solution manifold representation with a tensor-product polynomial approximation in the design space. The pseudospectral coefficients are computed using the Gauss-Legendre quadrature scheme. Recall that in this case, the polynomial order of the basis function set is characterized as a tensor-product of univariate polynomial basis functions of degree $p_\ell = \ell - 1$. Again, we see that the error decreases exponentially fast as the polynomial degree p_ℓ is increased, and in fact, the reported errors in Tables 7.2 and 7.3 are nearly identical. Consequently, these nodal and modal approaches exhibit very similar behavior for tensor-product polynomial approximations of the solution manifold.

The last numerical test employs the sparse collocation framework through Smolyak grids, presented earlier. Both the delayed Kronrod-Patterson and delayed Clenshaw-Curtis Smolyak schemes are used to assess the numerical properties of the sparse modal representation of the solution manifold. The results are presented in Table 7.4 in which the aforementioned collocation schemes are employed to compute the pseudospectral coefficients for the sparse Legendre basis contained in $\mathcal{P}_p(\mathcal{D}_{\text{roof}})$.

In Table 7.4, we see that both the delayed Kronrod-Patterson and Clenshaw-Curtis schemes exhibit similar convergence rates as a function of level ℓ . However, the required number of quadrature points to achieve the same accuracy using Clenshaw-Curtis is approximately three times that of Kronrod-Patterson. For both rules, the error behavior is the same for both the 16 element mesh and the 64 element mesh.

It is also important to assess the accuracy of computation of the sparse pseudospectral coefficients. To determine this accuracy, the sparse coefficients of $\mathcal{P}_p(\mathcal{D}_{\text{roof}})$ are computed for $0 \leq p \leq 4$ using a tensor-product univariate quadrature rule, in contrast to the sparse quadrature rule used in Table 7.4. The results of this analysis are depicted in Table 7.5. From this table, we can see that the tensor-product Gauss-Legendre scheme overall performs better in the computation of the sparse pseudospectral coefficients in comparison to the sparse integration rule. However, the results are only marginally better but with a significant increase in computational cost. This suggests that the sparse rules can and should be employed in practice.

The results from Tables 7.2, 7.3, 7.4, and 7.5 are summarized in Figures 7.10 and 7.11. In Figure 7.10, the L^2 error is plotted against the required number of samples n_ℓ while Figure 7.11 depicts the Energy error against required number of samples. Once again, note that the tensor-product Gauss-Legendre quadrature scheme using a Nodal surrogate model produces similar results to its modal equivalent. Additionally, we see that the isotropic surrogate model with sparse quadrature performs similarly to the full sampling. With increasing design space dimensionality, we predict the attractiveness of sparse Kronrod-Patterson with an isotropic polynomial basis to be much more pronounced. This is due to the curse of dimensionality which will exponentially increase

the number of required function evaluations for a tensor-product quadrature rule.

7.2.4.4 Design Optimization and Comparison with Exact Optima

The design space exploration paradigm presented in this dissertation allows the user to pose a multi-constraint optimization problem, for which the solution can be approximated after the surrogate model has been constructed. In particular, we can specify an objective functional that is to be minimized through a constrained optimization routine. For example, consider the functional which combines the effects of midpoint displacement and root strain:

$$\mathcal{F}(\alpha_1, \alpha_2; \boldsymbol{\mu}) = \alpha_1 d_z(\boldsymbol{\mu}) + \alpha_2 \varepsilon_1(\boldsymbol{\mu}) \quad (7.36)$$

Here, ε_1 is the largest principle strain at the clamped end of the roof, d_z is the displacement of the midpoint of the free edge, and α_1, α_2 are weights which describe the significance of each quantity in the optimization routine.

Without our design space exploration framework, a functional such as the one above can be minimized, or maximized, through a constrained optimization code. However, each iteration in such a routine requires a complete system construction, assembly, and solve. In the design space exploration paradigm, each iteration is simply a function call to the surrogate model of the solution manifold that has been constructed. Although the output of the optimization routine in this context is an approximation to the true value, it provides a refined search window for additional, high-fidelity design space exploration tools to converge on the true optimum.

For the Scordelis-Lo roof, we employ a constrained optimization routine and compare results of a full system construction and solution to the design space exploration surrogate model. The design space is identical to that used in the previous sections and the initial guess to the optimization routine is a random geometry in this design space. For these simulations, we use the 64 element mesh and consider two surrogate models: (i) a tensor-product polynomial approximation interpolating the solution at Gauss-Legendre quadrature points, and (ii) a pseudospectral isotropic polynomial approximation where spectral coefficients are computed with the delayed Kronrod-

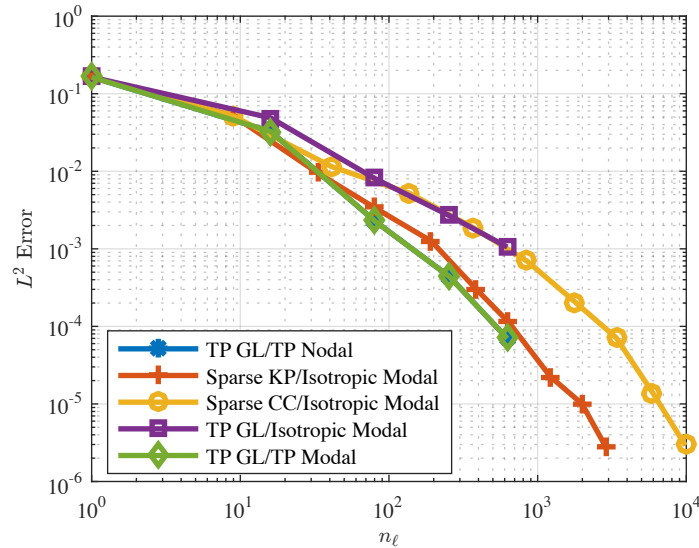


Figure 7.10: The L^2 error in the displacement field for the various surrogate models considered applied to the Scordelis-Lo roof problem. The first half of each legend entry refers to the sampling scheme employed while the second half refers to the surrogate model used. Note here that TP denotes “Tensor-Product”, GL denotes “Gauss-Legendre”, KP denotes “Kronrod-Patterson”, and CC denotes “Clenshaw-Curtis”. Additionally, “Nodal” indicates the use of the Lagrange polynomials as an interpolating basis while “Modal” denotes the use of the Legendre orthogonal polynomials.

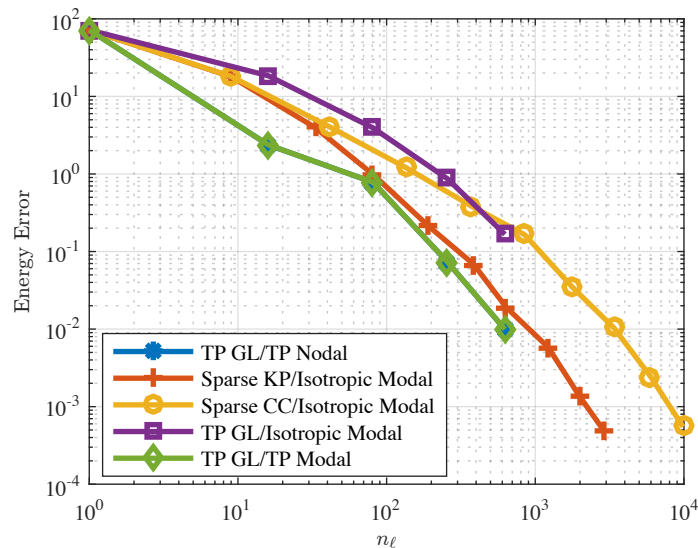


Figure 7.11: The energy error in the displacement field for the various surrogate models considered applied to the Scordelis-Lo roof problem. The first half of each legend entry refers to the sampling scheme employed while the second half refers to the surrogate model used. Note here that TP denotes “Tensor-Product”, GL denotes “Gauss-Legendre”, KP denotes “Kronrod-Patterson”, and CC denotes “Clenshaw-Curtis”. Additionally, “Nodal” indicates the use of the Lagrange polynomials as an interpolating basis while “Modal” denotes the use of the Legendre orthogonal polynomials.

Patterson quadrature rule. The results of this optimization routine are shown in Tables 7.6, 7.7, and 7.8.

For convergence criteria, we assert that the quantities of interest are within 1% of their true value. We observe that the interpolatory surrogate model converges to the optimal design location quickly in that it generally converges by $\ell = 2$, except for $(\alpha_1, \alpha_2) = (1, 0)$, where it converges by $\ell = 4$. On the other hand, the isotropic polynomial surrogate model converges to the optimal design location slower, typically by $\ell = 3$, except for $(\alpha_1, \alpha_2) = (2/3, 1/3)$. Recall however, that the computational expense associated with constructing the isotropic polynomial surrogate model is lower than the tensor-product polynomial approximation. We also consider the convergence of the surrogate model predicted max principal stress to that of the IGA solution. In the case of the interpolating surrogate model, note that the stress generally converges by $\ell = 3$, slightly slower than the rate of convergence to the optimal design location. In the case of the isotropic polynomial surrogate model, the max principal stress generally converges to the true value by $\ell = 5$.

7.2.5 Flat L-Bracket

We next consider application of our design space exploration framework to the analysis of a flat L-Bracket. The L-bracket is a linear-elastic model with a 17-dimensional design space, demonstrating the versatility of the proposed design space exploration framework. Moreover, full tensor-product sampling with either nodal or modal solution manifold representations is not feasible due to the high-dimensionality of this problem. For example, a linear, tensor-product pseudospectral or interpolatory model of the solution manifold would require $2^{17} = 131,072$ samples. Therefore, we resort to the sparse collocation schemes presented in previous sections, which capture the modes described by the total order of the underlying polynomial basis set. Additionally, the analysis model is constructed from 28 C^0 -continuous NURBS patches, demonstrating the applicability of this exploration framework in the multi-patch setting.

7.2.5.1 Problem Formulation and Methodology

Figure 7.12 below shows the design parameters for the L-Bracket as well as the patch layout used for analysis. Figure 7.13 below shows the boundary conditions and forcing used in the design space exploration problem. The mutli-patch model is discretized and refined to a 480-element mesh. Additionally, the holes described by a_1 and a_2 are constrained to zero displacement, effectively simulating a bolt. The remaining hole has an applied loading of $P = 30 \times 10^6$, directed upwards at a 45° angle and cosine-distributed across the boundary.

In reference to Figure 7.12, the design space of the L-bracket is is characterized by the design variable:

$$\mathcal{D}_L := \{\boldsymbol{\mu} = (M, N, L_1, H_3, R_f, a_1, e_1, t_{1h}, t_{1k}, a_2, e_2, t_{2h}, t_{2k}, a_3, e_3, t_{3h}, t_{3k}) \mid \boldsymbol{\mu} \in \mathbb{R}^{17}\} \quad (7.37)$$

which is comprised of the 17 design parameters associated with the L-bracket, as illustrated in Figure 7.12. We construct two design spaces of the form (7.37) for the L-Bracket geometry. The parameters defining the spaces are shown below.

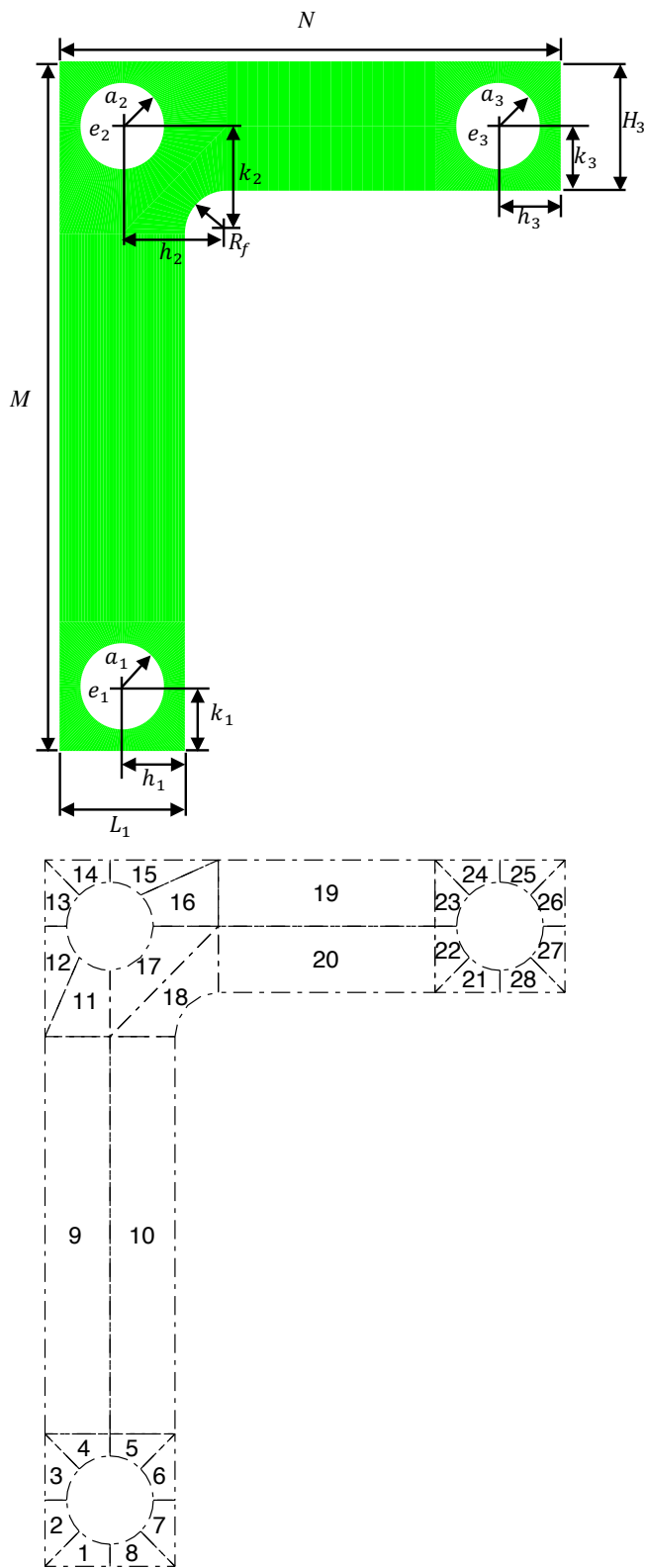


Figure 7.12: The design parameters associated with the Flat L-Bracket problem (left) and the patches associated with implementing a multi-patch isogeometric linear-elastic solver (right).

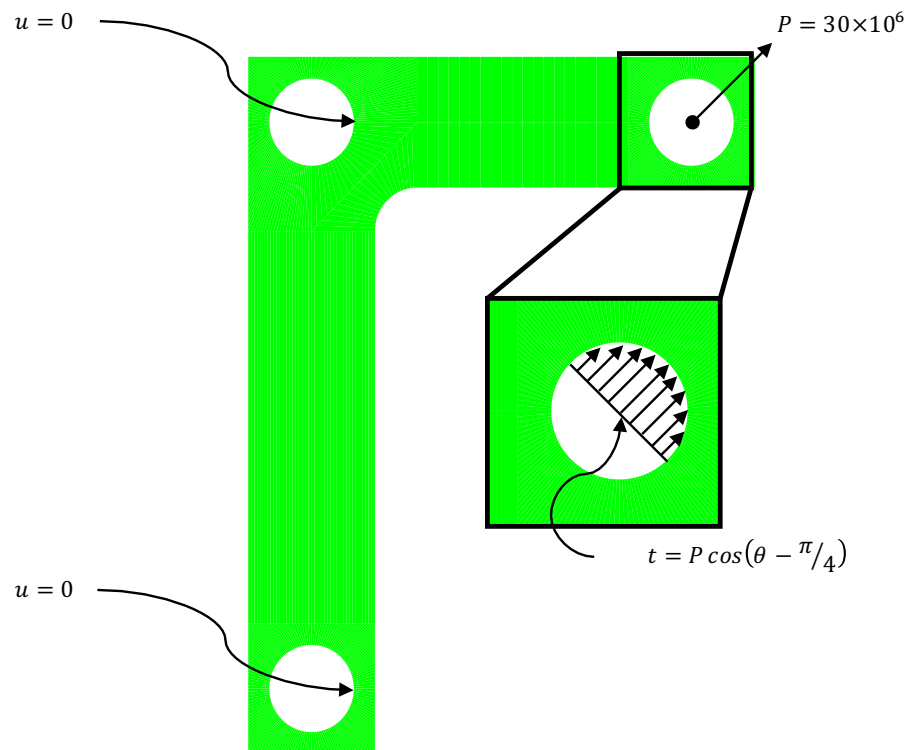


Figure 7.13: The boundary conditions and applied loading used in the L-Bracket problem. The lower and center L-Bracket holes are constrained with homogeneous Dirichlet boundary conditions. The loading on the remaining hole is cosine distributed for $-\pi/4 \leq \theta \leq 3\pi/4$ and is applied as a Neumann traction.

$$\mathcal{D}_{L,\text{minor}} = \left(\begin{array}{l} 5.5 \leq M \leq 6.5 \\ 3 \leq N \leq 4 \\ 1 \leq L_1 \leq 1.5 \\ 1 \leq H_3 \leq 1.5 \\ 0.15 \leq R_f \leq 0.25 \\ 0.15 \leq a_1 \leq 0.3 \\ 0 \leq e_1 \leq 0.2 \\ -0.2 \leq t_{1h} \leq 0.2 \\ -0.2 \leq t_{1k} \leq 0.2 \\ 0.15 \leq a_2 \leq 0.3 \\ 0 \leq e_2 \leq 0.2 \\ -0.2 \leq t_{2h} \leq 0.2 \\ -0.2 \leq t_{2k} \leq 0.2 \\ 0.15 \leq a_3 \leq 0.3 \\ 0 \leq e_3 \leq 0.2 \\ -0.2 \leq t_{3h} \leq 0.2 \\ -0.2 \leq t_{3k} \leq 0.2 \end{array} \right) \quad \mathcal{D}_{L,\text{extreme}} = \left(\begin{array}{l} 5.5 \leq M \leq 6.5 \\ 3 \leq N \leq 4 \\ 1 \leq L_1 \leq 1.5 \\ 1 \leq H_3 \leq 1.5 \\ 0.15 \leq R_f \leq 0.25 \\ 0.15 \leq a_1 \leq 0.35 \\ 0 \leq e_1 \leq 0.3 \\ -0.6 \leq t_{1h} \leq 0.6 \\ -0.6 \leq t_{1k} \leq 0.6 \\ 0.15 \leq a_2 \leq 0.35 \\ 0 \leq e_2 \leq 0.3 \\ -0.6 \leq t_{2h} \leq 0.6 \\ -0.6 \leq t_{2k} \leq 0.6 \\ 0.15 \leq a_3 \leq 0.35 \\ 0 \leq e_3 \leq 0.3 \\ -0.6 \leq t_{3h} \leq 0.6 \\ -0.6 \leq t_{3k} \leq 0.6 \end{array} \right)$$

The first design space is “minor” in the sense that the admissible design parameter perturbations lie in a localized neighborhood about a nominal design. The second design space is “extreme” since much larger perturbations and imperfections are admissible in this space. The two spaces are considered to assess the moderate dimensionality of the problem on the effectivity of the design space exploration paradigm. Representative geometries from these two design spaces are depicted in Figures 7.14 and 7.15 respectively.

To ensure that only sensical geometries live in these design spaces, we define the position of the L-Bracket holes’ center through a dimensionless design parameter which designates the percentage offset from the true center. The t_{ih} and t_{ik} , $i = 1, 2, 3$ parameters above define the hole offset via a

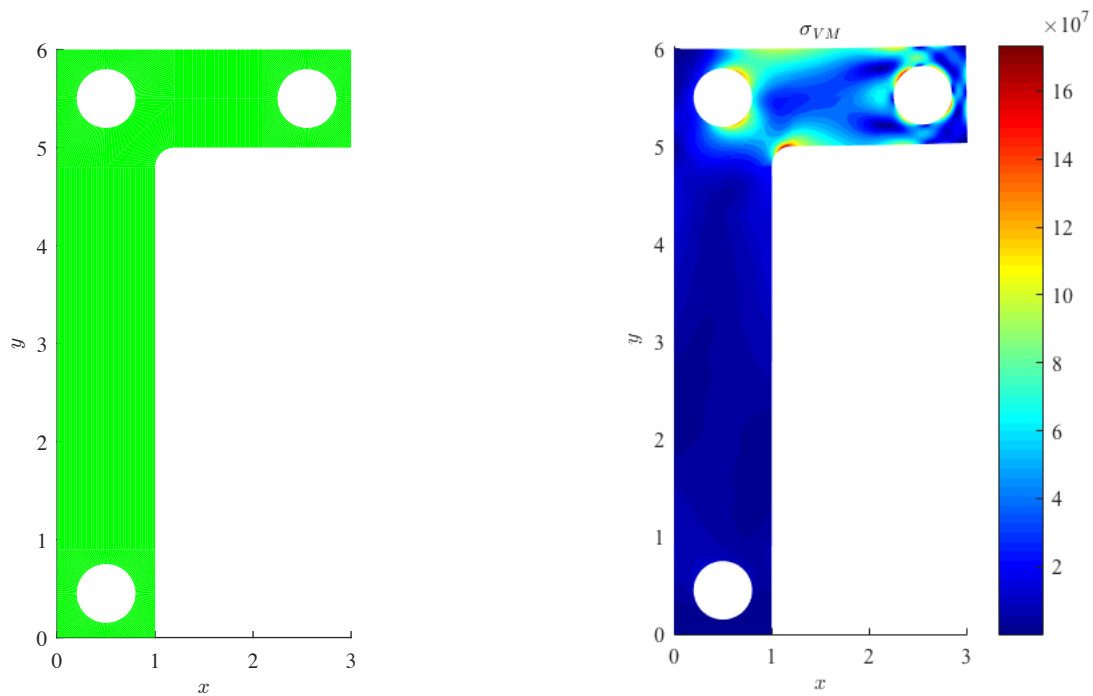


Figure 7.14: A sample geometry contained within $\mathcal{P}_{pl}(\mathcal{D}_{L,minor})$ (left) along with the resulting Von Mises stress field (right).

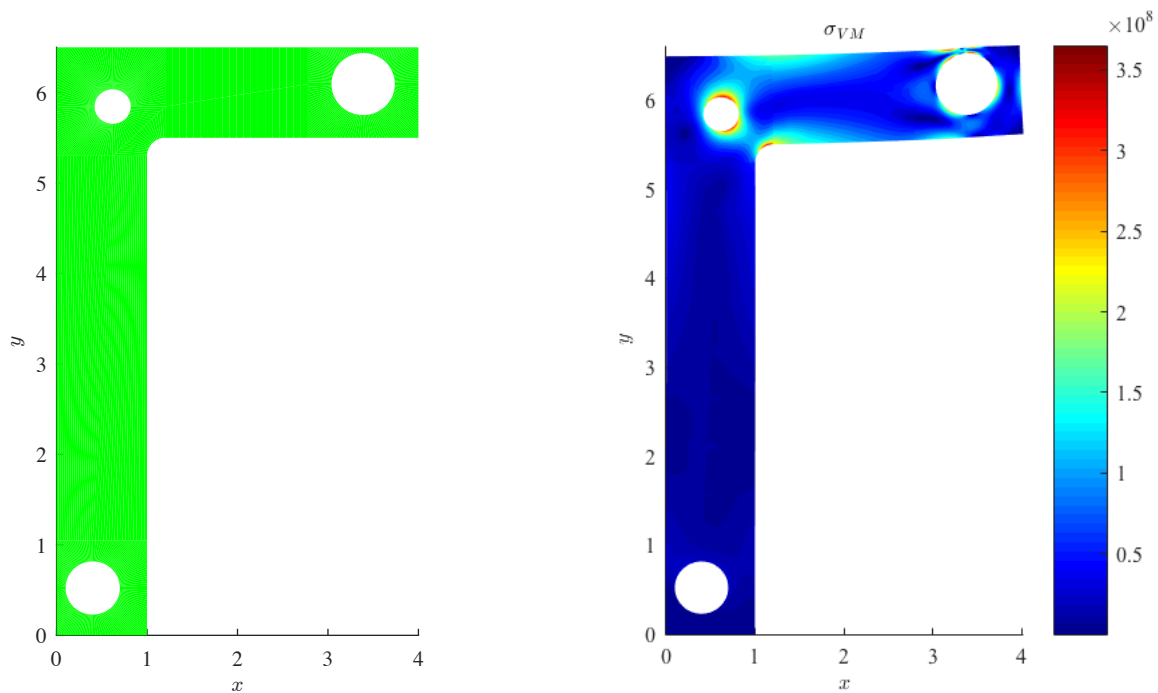


Figure 7.15: A sample geometry within $\mathcal{P}_{pl}(\mathcal{D}_{L,extreme})$ (left) along with the resulting Von Mises stress field (right).

convex combination of related design parameters, for example $h_1(t_{1h}) = (a_1 - L_1/2)t_{1h} + L_1/2$. The remaining quantities of k_1, h_2, k_2, h_3, k_3 , are defined in a similar manner.

It should be noted that the L-Bracket problem is motivated by the design space exploration problem of identifying suitable geometric tolerances for manufacturing. That is, one is often interested in the design question: **How large may we allow a set of tolerances to be without compromising performance?** Our framework allows one to address this question in a direct and efficient manner. Moreover, as well will see in the following chapter, we have devised an in-depth methodology for addressing this question.

7.2.5.2 Convergence Analysis

A convergence analysis is performed for the pseudospectral model of the solution manifold with the Flat L-Bracket. In particular, we measure the error in both the L^2 and energy-norms to assess the convergence of the displacement and strain energy fields, respectively. These norms are given by:

$$\|e^h\|_{0,\Omega}^2 = \int_{\Omega} |e^h|^2 d\Omega \quad \text{and} \quad \left\| \left\| e^h \right\| \right\|_A^2 = a_{LE}(e^h, e^h) \quad (7.38)$$

The results of the convergence analysis are shown below for the $\mathcal{D}_{L,\text{minor}}$ and $\mathcal{D}_{L,\text{extreme}}$ in Tables 7.9 and 7.10, respectively. To ensure the accuracy of the figures presented, the L^2 and energy norms are computed for a total of 10 randomly-selected admissible geometries in the design space and then averaged.

From these tables, we see that our surrogate modeling strategy quickly converges as the polynomial degree p_ℓ is increased. Similar to the Scordelis-Lo roof, the L^2 -error converges quicker than the energy error. The effectiveness of our surrogate modeling strategy is portrayed through these tables since quick convergence is seen for geometries in both $\mathcal{D}_{L,\text{minor}}$ and $\mathcal{D}_{L,\text{extreme}}$.

7.2.6 Wind Turbine Blade

As has been the theme of this dissertation, the inconsistent geometric descriptions used in design and analysis models constitute a significant rift in modern engineering work flows. While IGA addresses this issue fundamentally, many industrial design strategies remain disconnected and iterative, requiring repetitive user interaction. Typically, a designer first develops a CAD model using a particular software platform. The model can then be uploaded into a CAE platform to convert the geometry model information into mesh information suitable for analysis. Upon completing analysis, if the user wishes to change a design parameter, the entire process is repeated.

Previous work addressed this challenge by constructing a computational framework capable of performing NURBS-based parametric design, isogeometric analysis, and result visualization seamlessly in a single software environment. The framework is unique in that it is capable of utilizing complex, CAD-based geometric operations to generate parametric models for IGA. Basic heuristic methods were employed to perform optimization of a subset of design variables of an NREL 5MW wind turbine blade, a complex geometry defined by many design variables in [65]. However, given the seamlessness of the framework, it can be readily modified to incorporate design space discretization techniques, demonstrating the viability of such techniques for industrial applications.

7.2.6.1 Problem Formulation and Methodology

Here we consider application of our surrogate modeling methodology to the parametric design and analysis of an NREL 5MW wind turbine blade within the aforementioned design space exploration framework. Our goals are twofold: (i) to demonstrate that our surrogate modeling strategy seamlessly extends to the nonlinear and time-dependent settings and (ii) to demonstrate the effectiveness of our methodology in the context of an industrial-strength application.

Wind turbine blade geometries are typically defined by a set of parameters at discrete locations, or “stations,” along the length of the blade. The usual parameters are radial location of the section along the blade, chord length, airfoil shape, and twist degree. These parameters define

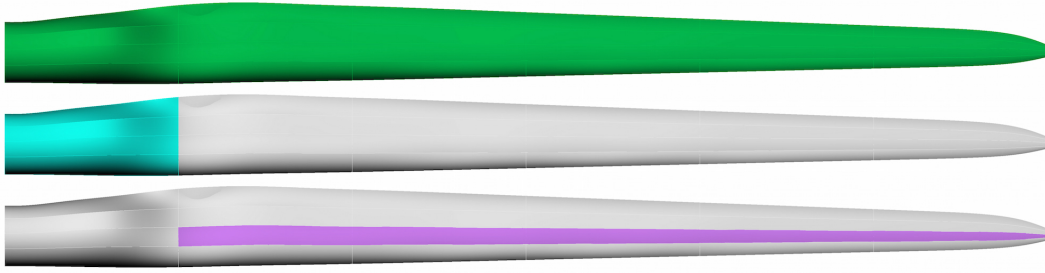


Figure 7.16: Simplified composite layup used for wind turbine optimization. Green color (top) indicates base uni-directional carbon across entire blade, blue color (middle) indicates root buildup of SNLTriax, and purple color (bottom) indicates spar cap region made up of additional uni-directional carbon.

the shape and orientation of each two-dimensional station in three-dimensional space; lofting all airfoil profiles produces a wind turbine blade shell geometry. In [69] a complete definition of a wind turbine blade geometry intended for use in 5MW offshore applications.

For this dissertation, all geometries are considered to have the same loading configuration. The root edge of the blade is clamped by eliminating all motion of the two innermost rings of control points, and a uniform flapwise traction of 250 Pa is applied in the reference configuration. The wind turbine blade is modeled as a nonlinear Kirchhoff-Love shell with a composite material model. A simplified composite layup is also used, shown in Figure 7.16. The blade is constructed primarily of a thin shell of uni-directional carbon, indicated by green, covering the entire blade, with additional uni-directional carbon thickness in the spar cap zone, indicated by purple, and buildup of SNLTriax on the root, indicated by blue. See [99] for details about material properties. Moreover, the T-spline analysis model is comprised of 1440 elements. From the traction loading, the shell model is iteratively solved until reaching its maximum tip displacement. The resulting displacement field in this state is the output which is used in our design space exploration surrogate modeling paradigm.

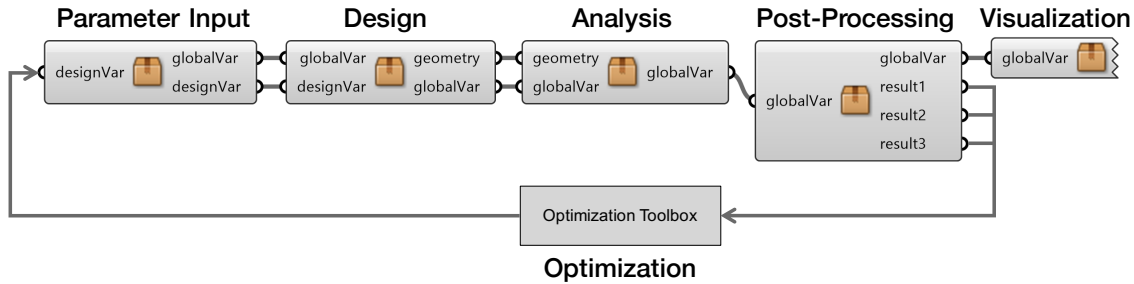


Figure 7.17: The basic layout of the isogeometric PDO framework, laid out in Grasshopper 3D, a visual programming plugin for Rhino, configured for iterative use.

7.2.6.2 Implementation

For implementation, we employed and extended an isogeometric Parametric Design Optimization (PDO) framework based on the CAD software Rhinoceros 3D (Rhino) [65]. Rhino has a NURBS-based geometry kernel, making it an attractive choice for IGA, and also features Grasshopper, a visual programming interface that enables parametric design within Rhino. The basic structure of the isogeometric PDO framework configured for iterative use is shown in Figure 7.17.

As Figure 7.17 demonstrates, each of the stages in the entire design and analysis work flow are contained within a single software platform. The rectangular components in Figure 7.17 are referred to as Grasshopper “clusters” and each contains a subset of predefined Grasshopper functions and C# scripting components. The “Design” cluster, for example, contains the appropriate geometric functions, such as point interpolation, curve rotation and translation, and lofts, necessary to construct a NURBS-based engineering model. The exact contents of the “Design” cluster will of course depend on the engineering application. The “Analysis” cluster contains functions that output the geometry, without performing meshing, and call the analysis code. The analysis code in these examples is IGA-based and seeks the midsurface displacement of a composite Kirchhoff-Love shell, originally formulated in [10] and reproduced in [65]. The results are then directly read and visualized within the Rhino viewport using the components inside the “Visualization” cluster.

The approach described above unites the paradigms of parametric design and high-fidelity FEA, allowing seamless design and analysis of complex engineering models within a single workspace.

Initial analysis stage



Design exploration stage

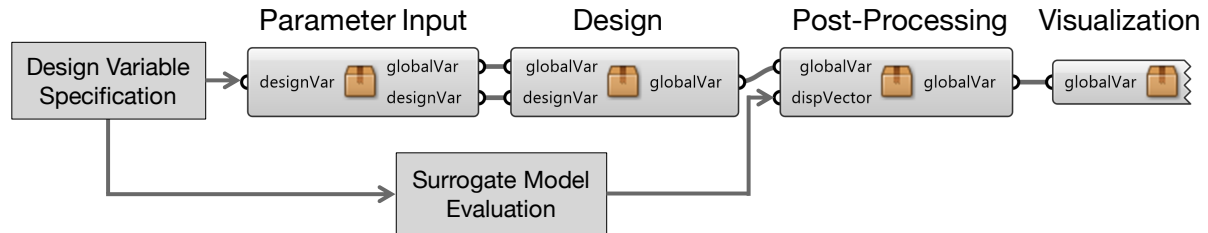


Figure 7.18: The isogeometric PDO framework configured for use with the design space exploration methodology, including analysis-heavy, iterative offline stage (top) and GUI-driven, rapidly evaluated design exploration stage (bottom).

In the configuration shown in Figure 7.17, however, the approach is limited in that it relies heavily on iteration. Hence, a designer cannot actively interrogate a particular point in the design space. Instead, once a point is selected, analysis results are available only after the entire structural analysis is completed.

In this work, the Grasshopper-based isogeometric PDO framework is reconfigured for use with the design space discretization methodology presented in the previous sections. As Figure 7.18 illustrates, the “Design” and “Analysis” clusters can first be used to automatically analyze the displacements $\mathbf{d}(\boldsymbol{\mu}_i)$ at a predetermined set of collocation points $\boldsymbol{\mu}_i$. This analysis information is then utilized to construct the surrogate model which approximates the solution manifold $\mathbf{d}(\boldsymbol{\mu})$. In particular, given a design variable $\boldsymbol{\mu}$, the associated displacement vector can be efficiently produced via evaluation of the solution manifold. As shown in Figure 7.18, this displacement vector is provided to the Grasshopper interface such that visualization of the solution, based on the original geometry’s position and nodal displacements, is performed. The designer can therefore use the GUI to select a design point of interest and quickly see the resultant geometry and any other post-processed results within the Rhino viewport, as shown in Figure 7.18.

We emphasize that, in the workflow demonstrated by Figure 7.18, only the initial, offline stage requires relatively computationally expensive finite element calculations. Once the results of these analyses have been used to construct the surrogate model however, a GUI can be used to rapidly explore the entirety of the design space and associated high-fidelity analysis results.

The NREL 5MW wind turbine blade in the PDO framework uses 19 radial locations, the parameters described in [69], each with independent chord lengths and airfoil cross-sections, to generate a turbine blade geometry. To reduce the dimensionality of the design space, we construct a quadratic B-spline with 4 parametric degrees of freedom which describes the chord line, c , as a function of radial position, r , as our design variable. Moreover, we do not consider the effect of varying airfoil cross-section on the displacement field and instead hold these nominal specifications constant. We define the turbine blade design space $\mathcal{D}_{\text{turb}} \subset \mathbb{R}^4$ via:

$$\mathcal{D}_{\text{turb}} := \{\boldsymbol{\mu} \in \mathbb{R}^4 \mid 9 \leq P_{5x} \leq 13, \quad 4.1 \leq P_{5y} \leq 4.7, \quad 22 \leq P_{7x} \leq 30, \quad 4.2 \leq P_{7y} \leq 4.6\}$$

where these parameters define the control variables \mathbf{P}_3 and \mathbf{P}_5 which describe the B-spline curve given by

$$c_{\boldsymbol{\mu}}(r) = \sum_{i=1}^8 \mathbf{P}_i(\boldsymbol{\mu}) N_i(r)$$

Figure 7.19 depicts the chord line of design space, $\mathcal{D}_{\text{turb}}$, for the wind turbine blade.

In addition to the design space presented in Figure 7.19, a representative set of geometries in this design space are shown in Figures 7.20 and 7.21. These figures demonstrate how altering the chord design parameter affects the resulting geometry.

7.2.6.3 Convergence Analysis

Similar to before, we perform a convergence analysis and assessment on the wind turbine blade using a nodal representation of the solution manifold. This choice of surrogate model was informed by the results of the Scordelis-Lo roof namely, a nodal surrogate modeling strategy is preferred for a low-dimensional design space. In particular, we measure the errors in the displacement

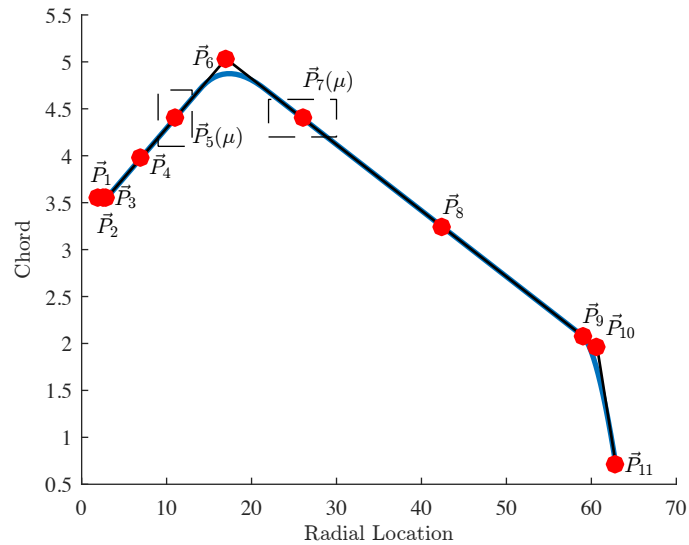


Figure 7.19: The chord line describing design space of an NREL 5MW wind turbine blade, $\mathcal{D}_{\text{turb}}$. The chord line as a function of radial location is constructed using a piecewise quadratic B-spline. The two red control points in the dashed box, P_5 and P_7 are the design parameters for the turbine blade, which are free to move within the box. The B-spline curve shown is the nominal configuration for the turbine blade.

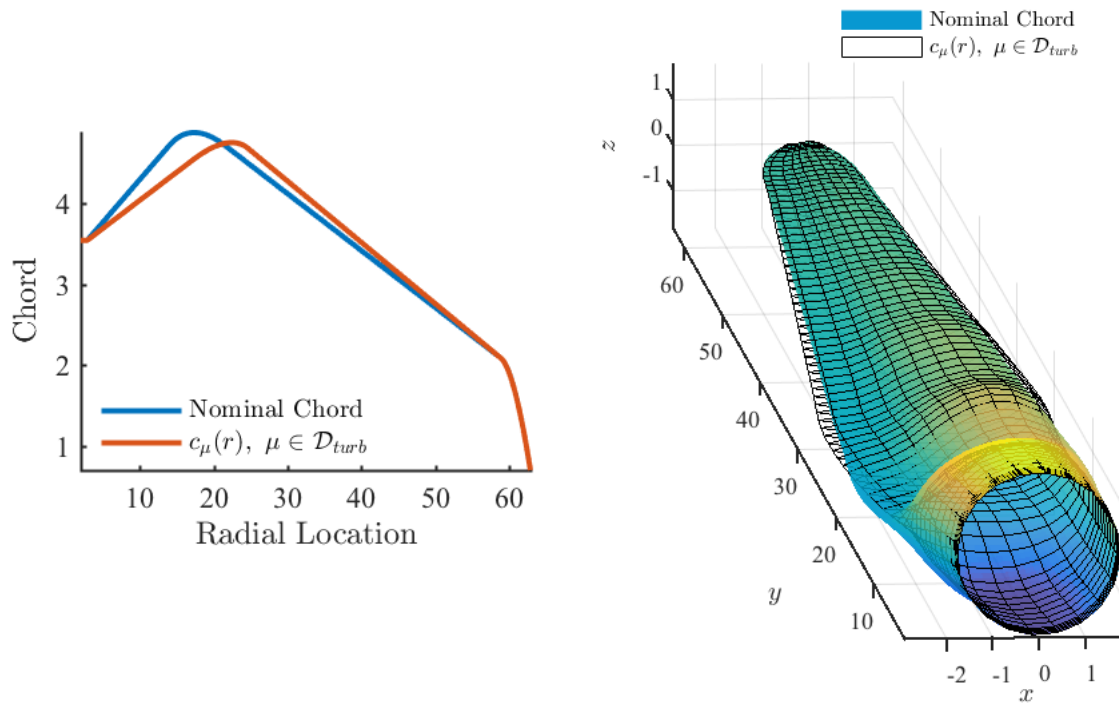


Figure 7.20: A sample geometry contained in $\mathcal{D}_{\text{turb}}$. This design has a tip wise shift in the maximal chord location.

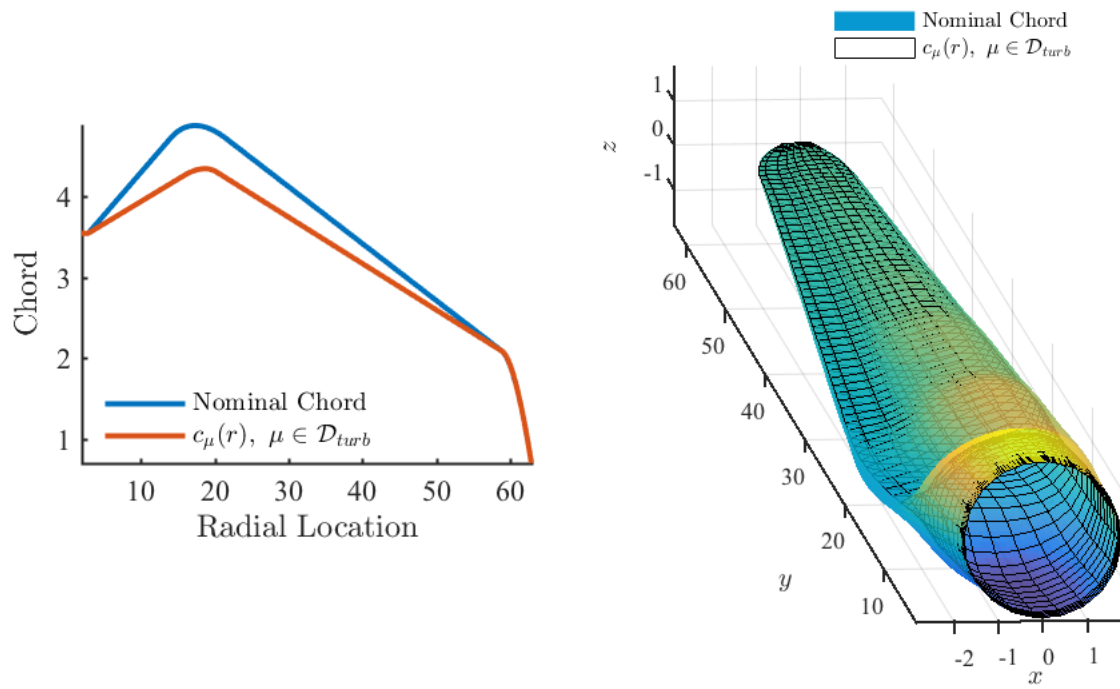


Figure 7.21: A sample geometry contained in \mathcal{D}_{turb} . This design has a smaller maximal chord location.

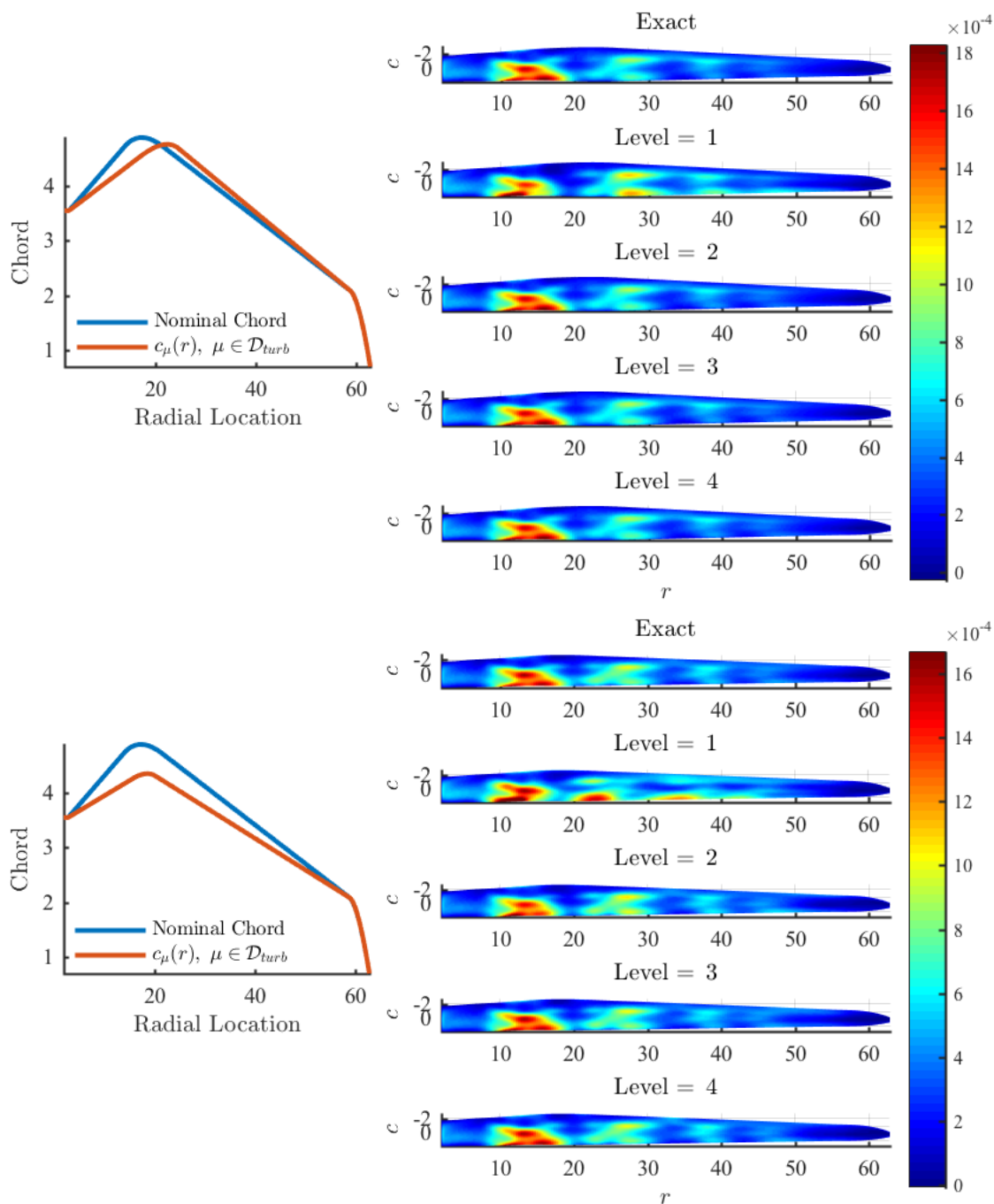


Figure 7.22: In the left plots, we present representative chord lines associated with geometries admissible to \mathcal{D}_{turb} . The blue lines correspond to the nominal turbine geometry while the red lines are the chord lines associated with a turbine geometry present in the design space under consideration. In the right column of plots, the corresponding strain fields for the exact IGA solution, as well as the nodal surrogate model for levels 1 through 4, are shown.

field and maximum in-plane strain field, both of which are measured in the L^2 -norm. For $e^h = u_{\text{IGA}}^h - u_{\text{surrogate}}^h$ and $\varepsilon(e^h) = \varepsilon(u_{\text{IGA}}^h) - \varepsilon(u_{\text{surrogate}}^h)$, these fields are given by:

$$\|e^h\|_{0,\Omega}^2 = \int_{\Omega} |e^h|^2 d\Omega \quad \text{and} \quad \|e^h\|_{\varepsilon}^2 = \|\varepsilon(e^h)\|_{0,\Omega}^2 \quad (7.39)$$

where the ε -norm is the L^2 -norm of the strain as defined in [73]. These norms effectively assess the accuracy of the surrogate model's capability of representing the displacement field as well as the corresponding strain field. Table 7.11 below depicts the convergence behavior of the nodal surrogate model constructed using the Lagrange polynomials with the tensor-product Gauss-Legendre sampling scheme.

We see that both the L^2 and ε errors decrease very quickly from the first level to the third level. In fact, both errors drop by over an order of magnitude from the first level to the third level. However, it should be noted that the convergence rates slow by the fourth level. This is because the coarse-scale solution behavior across the design space has been resolved while a high polynomial degree is required to accurately capture the remaining fine-scale solution features. Nonetheless, the average L^2 and ε errors are quite small and acceptable by the 4th level. In addition to the convergence table above, we present the strain fields for a representative set of turbine geometries present in $\mathcal{D}_{\text{turb}}$ in Figure 7.22. This figure demonstrates that our surrogate modeling strategy is very effective in resolving the solution fields of interest in nonlinear structural mechanics, namely the strain and stress fields.

Table 7.2: Results for the Scordelis-Lo roof with a Nodal solution manifold representation using a full tensor-product interpolation scheme with the Gauss-Legendre quadrature nodes. In the table below, ℓ is the level parameter, p_ℓ is the polynomial order of the Lagrange basis used to represent the solution manifold, n_ℓ is the number of interpolation points used to attain the specified representation, and n_{dof} is the number of basis functions in $\mathcal{Q}_{p_\ell}(\mathcal{D}_{\text{roof}})$.

Collocation Scheme	Number of Elements	ℓ	p_ℓ	n_{dof}	n_ℓ	Average L^2 error	Average Energy Error
Gauss-Legendre	16	1	0	1	1	1.6377×10^{-1}	7.1909×10^1
		2	1	16	16	3.2600×10^{-2}	2.3733
		3	2	81	81	2.2544×10^{-3}	7.8076×10^{-1}
		4	3	256	256	4.3639×10^{-4}	7.3727×10^{-2}
		5	4	625	625	6.9755×10^{-5}	9.9253×10^{-3}
	64	1	0	1	1	1.3030×10^{-1}	4.6528×10^1
		2	1	16	16	2.2413×10^{-2}	2.1955
		3	2	81	81	3.7941×10^{-3}	3.4959×10^{-1}
		4	3	256	256	5.2635×10^{-4}	1.0806×10^{-1}
		5	4	625	625	7.1170×10^{-5}	1.2703×10^{-2}

Table 7.3: Results for the Scordelis-Lo roof with a Modal solution manifold representation using a tensor-product Gauss-Legendre quadrature scheme for numerical computation of the pseudospectral coefficients. In the table below, ℓ is the level parameter, p_ℓ is the polynomial order of the Legendre basis used to represent the solution manifold, n_ℓ is the number of quadrature points used to attain the specified representation, and n_{dof} is the number of basis functions in $\mathcal{Q}_{p_\ell}(\mathcal{D}_{\text{roof}})$.

Quadrature Scheme	Number of Elements	ℓ	p_ℓ	n_{dof}	n_ℓ	Average L^2 error	Average Energy Error
Gauss-Legendre	16	1	0	1	1	1.6377×10^{-1}	7.1909×10^1
		2	1	16	16	3.2600×10^{-2}	2.3733
		3	2	81	81	2.2544×10^{-3}	7.8076×10^{-1}
		4	3	256	256	4.3639×10^{-4}	7.3727×10^{-2}
		5	4	625	625	6.9755×10^{-5}	9.9253×10^{-3}
	64	1	0	1	1	1.3030×10^{-1}	4.6528×10^1
		2	1	16	16	2.2413×10^{-2}	2.1955
		3	2	81	81	3.7941×10^{-3}	3.4959×10^{-1}
		4	3	256	256	5.2635×10^{-4}	1.0806×10^{-1}
		5	4	625	625	7.1170×10^{-5}	1.2703×10^{-2}

Table 7.4: Results for the Scordelis-Lo roof with a modal solution manifold representation using sparse, delayed Kronrod-Patterson and Clenshaw-Curtis schemes for the computation of the sparse pseudospectral coefficients in the isotropic Legendre basis. In the table below, ℓ denotes the level parameter, n_ℓ is the number of function evaluations required to accurately capture the pseudospectral coefficients, and n_{dof} is the number of basis functions in $\mathcal{P}_{pe}(\mathcal{D}_{roof})$.

Quadrature Scheme	Number of Elements	ℓ	n_{dof}	n_ℓ	Average L^2 error	Average Energy Error
Delayed Kronrod-Patterson	16	1	1	1	1.6377×10^{-1}	7.1909×10^1
		2	5	9	5.1812×10^{-2}	1.7968×10^1
		3	15	33	9.5744×10^{-3}	3.9784
		4	35	81	3.3485×10^{-3}	9.8703×10^{-1}
		5	70	193	1.2528×10^{-3}	2.1011×10^{-1}
		6	126	385	3.0431×10^{-4}	6.8352×10^{-2}
		7	210	641	1.1234×10^{-4}	1.8871×10^{-2}
		8	330	1217	2.2538×10^{-5}	5.8715×10^{-3}
		9	495	1985	1.0071×10^{-5}	1.3624×10^{-3}
		10	715	2881	2.7734×10^{-6}	4.9535×10^{-4}
	64	1	1	1	1.3030×10^{-1}	4.6528×10^1
		2	5	9	2.1879×10^{-2}	7.0638
		3	15	33	9.3368×10^{-3}	2.5295
		4	35	81	2.1281×10^{-3}	7.0158×10^{-1}
		5	70	193	6.4161×10^{-4}	1.2545×10^{-1}
		6	126	385	1.8277×10^{-4}	4.9450×10^{-2}
		7	210	641	7.4230×10^{-5}	8.9910×10^{-3}
		8	330	1217	1.9857×10^{-5}	3.5557×10^{-3}
		9	495	1985	8.4778×10^{-6}	6.4857×10^{-4}
		10	715	2881	2.3575×10^{-6}	2.9674×10^{-4}
Delayed Clenshaw-Curtis	16	1	1	1	1.6377×10^{-1}	7.1909×10^1
		2	5	9	5.1394×10^{-2}	1.8089×10^1
		3	15	41	1.1524×10^{-2}	4.0875
		4	35	137	5.2109×10^{-3}	1.1882
		5	70	369	1.8731×10^{-3}	3.8849×10^{-1}
		6	126	849	6.9447×10^{-4}	1.6440×10^{-1}
		7	210	1777	2.0808×10^{-4}	3.4681×10^{-2}
		8	330	3377	7.1409×10^{-5}	1.0398×10^{-2}
		9	495	5953	1.3878×10^{-5}	2.4518×10^{-3}
		10	715	9857	2.9136×10^{-6}	5.5005×10^{-4}
	64	1	1	1	1.3030×10^{-1}	4.6528×10^1
		2	5	9	2.4812×10^{-2}	7.2903
		3	15	41	6.8846×10^{-3}	3.1244
		4	35	137	3.6722×10^{-3}	7.7122×10^{-1}
		5	70	369	1.5087×10^{-3}	3.3838×10^{-1}
		6	126	849	3.1583×10^{-4}	1.0724×10^{-1}
		7	210	1777	1.0943×10^{-4}	4.3432×10^{-2}
		8	330	3377	8.2457×10^{-5}	7.9000×10^{-3}
		9	495	5953	1.0503×10^{-5}	2.0733×10^{-3}
		10	715	9857	2.0608×10^{-6}	3.4954×10^{-4}

Table 7.5: Results for the Scordelis-Lo roof with a modal solution manifold representation using an isotropic Legendre basis with a tensor-product univariate Gauss-Legendre quadrature scheme. In the table below, ℓ denotes the level parameter, n_ℓ is the number of function evaluations required to accurately capture the pseudospectral coefficients, and n_{dof} is the number of basis functions in $\mathcal{P}_{p_\ell}(\mathcal{D}_{\text{roof}})$.

Quadrature Scheme	Number of Elements	ℓ	n_{dof}	n_ℓ	Average L^2 error	Average Energy Error
Gauss-Legendre	16	1	1	1	1.6377×10^{-1}	7.1909×10^1
		2	5	16	4.8885×10^{-2}	1.8471×10^1
		3	15	81	8.0005×10^{-3}	3.9283
		4	35	256	2.6645×10^{-3}	8.6922×10^{-1}
		5	70	625	1.0542×10^{-3}	1.6657×10^{-1}
	64	1	1	1	1.3030×10^{-1}	4.6528×10^1
		2	5	16	2.4659×10^{-2}	7.4684
		3	15	81	7.2669×10^{-3}	2.2228
		4	35	256	2.0511×10^{-3}	5.7762×10^{-1}
		5	70	625	5.2271×10^{-4}	1.1514×10^{-1}

Table 7.6: Optimization of the functional presented in this section using the full IGA model throughout the design space.

Model	α_1	α_2	Optimal Design Parameters (L, R, t, φ)	Function Calls	σ_1	d_z	ε_1
Isogeometric Solution	1	0	(45, 20, 0.3, 45)	215	-841.1226	-0.0501	-0.3414
	$\frac{2}{3}$	$\frac{1}{3}$	(55, 30, 0.2, 38.35)	321	-1524.0956	-0.2687	-1.4085
	$\frac{1}{2}$	$\frac{1}{2}$	(55, 30, 0.2, 35)	243	-1644.8266	-0.3010	-1.4606
	$\frac{1}{3}$	$\frac{2}{3}$	(55, 30, 0.2, 35)	180	-1644.8448	-0.3010	-1.4606
	0	1	(55, 30, 0.2, 35)	150	-1644.9230	-0.3011	-1.4607

Table 7.7: Optimization of the functional presented in this section for varying level and α_i for a tensor-product, interpolating surrogate model.

Model	α_1	α_2	p	Optimal Design Parameters (L, R, t, φ)	Function Calls	σ_1	d_z	ε_1
Interpolatory with Gauss- Legendre	1	0	0	(45.7, 24, 0.3, 41.9)	5	-1564.7212	-0.1214	-0.6749
			1	(45, 20, 0.3, 35)	282	-873.3413	-0.0495	-0.3130
			2	(45, 20, 0.3, 35)	236	-902.2156	-0.0509	-0.3212
			3	(45, 20, 0.3, 45)	212	-840.5739	-0.0501	-0.3411
			4	(45, 20, 0.3, 45)	181	-841.1787	-0.0501	-0.3414
	$\frac{2}{3}$	$\frac{1}{3}$	0	(55, 30, 0.3, 45)	186	-947.7444	-0.1214	-0.8791
			1	(55, 30, 0.2, 37.05)	195	-1536.1837	-0.2698	-1.4058
			2	(55, 30, 0.2, 37.79)	176	-1530.2811	-0.2687	-1.4061
			3	(55, 30, 0.2, 38.46)	167	-1518.8445	-0.2674	-1.4051
			4	(55, 30, 0.2, 38.37)	187	-1523.7463	-0.2686	-1.4084
	$\frac{1}{2}$	$\frac{1}{2}$	0	(55, 30, 0.3, 45)	141	-947.7431	-0.1214	-0.8791
			1	(55, 30, 0.2, 35)	157	-1595.2322	-0.2903	-1.4453
			2	(55, 30, 0.2, 35)	132	-1639.3973	-0.2984	-1.4600
			3	(55, 30, 0.2, 35)	160	-1643.2761	-0.3006	-1.4591
			4	(55, 30, 0.2, 35)	178	-1645.0724	-0.3011	-1.4607
	$\frac{1}{3}$	$\frac{2}{3}$	0	(55, 30, 0.3, 45)	133	-947.7425	-0.1214	-0.8791
			1	(55, 30, 0.2, 35)	128	-1595.2309	-0.2903	-1.4453
			2	(55, 30, 0.2, 35)	154	-1639.4217	-0.2984	-1.4601
			3	(55, 30, 0.2, 35)	133	-1643.3374	-0.3006	-1.4591
			4	(55, 30, 0.2, 35)	139	-1645.1882	-0.3011	-1.4608
0	1	0	(55, 30, 0.3, 45)	123	-947.7419	-0.1214	-0.8791	
		1	(55, 30, 0.2, 35)	111	-1595.2319	-0.2903	-1.4453	
		2	(55, 30, 0.2, 35)	142	-1639.4180	-0.2984	-1.4601	
		3	(55, 30, 0.2, 35)	115	-1643.3302	-0.3006	-1.4591	
		4	(55, 30, 0.2, 35)	131	-1645.1909	-0.3011	-1.4608	

Table 7.8: Functional optimization for varying level and α_i for a sparse, isotropic surrogate model.

Model	α_1	α_2	ℓ	Optimal Design Parameters (L, R, t, φ)	Function Calls	σ_1	d_z	ε_1
Pseudospectral with Delayed Kronrod- Patterson	1	0	1	(47.4, 20, 0.2, 43.4)	5	-1620.7782	-0.1214	-0.6987
			2	(45, 20, 0.3, 45)	90	-525.6763	-0.0133	-0.2302
			3	(45, 20, 0.3, 35)	147	-815.8440	-0.0436	-0.2969
			4	(45, 20, 0.3, 45)	136	-813.3066	-0.0479	-0.3363
			5	(45, 20, 0.3, 45)	140	-847.3026	-0.0507	-0.3431
			6	(45, 20, 0.3, 45)	125	-840.7822	-0.0501	-0.3413
			7	(45, 20, 0.3, 45)	136	-841.3068	-0.0501	-0.3414
			8	(45, 20, 0.3, 45)	162	-841.0824	-0.0501	-0.3414
			9	(45, 20, 0.3, 45)	148	-841.1001	-0.0501	-0.3414
			10	(45, 20, 0.3, 45)	133	-841.1252	-0.0501	-0.3414
	$\frac{2}{3}$	$\frac{1}{3}$	1	(55, 30, 0.3, 45)	126	-947.7444	-0.1214	-0.8791
			2	(55, 30, 0.2, 45)	88	-1333.4704	-0.2011	-1.2796
			3	(55, 30, 0.2, 41.56)	113	-1408.0096	-0.2360	-1.3363
			4	(55, 30, 0.2, 39.22)	123	-1493.7329	-0.2607	-1.3921
			5	(55, 30, 0.2, 38.56)	150	-1518.9885	-0.2675	-1.4071
			6	(55, 30, 0.2, 38.37)	130	-1524.1443	-0.2687	-1.4087
			7	(55, 30, 0.2, 38.35)	106	-1524.0718	-0.2687	-1.4085
			8	(55, 30, 0.2, 38.35)	95	-1524.2580	-0.2687	-1.4086
			9	(55, 30, 0.2, 38.35)	131	-1524.1108	-0.2687	-1.4085
			10	(55, 30, 0.2, 38.36)	129	-1524.1015	-0.2687	-1.4085
	$\frac{1}{2}$	$\frac{1}{2}$	1	(55, 30, 0.3, 45)	165	-947.7431	-0.1214	-0.8791
			2	(55, 30, 0.2, 45)	90	-1333.4712	-0.2011	-1.2796
			3	(55, 30, 0.2, 36.39)	108	-1521.7261	-0.2737	-1.3933
			4	(55, 30, 0.2, 35)	150	-1623.7197	-0.2969	-1.4484
			5	(55, 30, 0.2, 35)	127	-1641.9099	-0.3005	-1.4600
			6	(55, 30, 0.2, 35)	133	-1644.2682	-0.3009	-1.4603
			7	(55, 30, 0.2, 35)	143	-1644.8948	-0.3011	-1.4607
			8	(55, 30, 0.2, 35)	101	-1644.9328	-0.3011	-1.4607
			9	(55, 30, 0.2, 35)	127	-1644.9215	-0.3011	-1.4607
			10	(55, 30, 0.2, 35)	110	-1644.9249	-0.3011	-1.4607
	$\frac{1}{3}$	$\frac{2}{3}$	1	(55, 30, 0.3, 45)	143	-947.7425	-0.1214	-0.8791
			2	(55, 30, 0.2, 45)	91	-1333.4715	-0.2011	-1.2796
			3	(55, 30, 0.2, 35)	117	-1541.9198	-0.2823	-1.4008
			4	(55, 30, 0.2, 35)	99	-1623.9744	-0.2970	-1.4485
			5	(55, 30, 0.2, 35)	107	-1641.9102	-0.3005	-1.4600
			6	(55, 30, 0.2, 35)	97	-1644.2650	-0.3009	-1.4603
			7	(55, 30, 0.2, 35)	118	-1644.9110	-0.3011	-1.4607
			8	(55, 30, 0.2, 35)	109	-1644.9338	-0.3011	-1.4607
			9	(55, 30, 0.2, 35)	92	-1644.9182	-0.3011	-1.4607
			10	(55, 30, 0.2, 35)	99	-1644.9260	-0.3011	-1.4607
0	1	1	(55, 30, 0.3, 45)	144	-947.7419	-0.1214	-0.8791	
		2	(55, 30, 0.2, 45)	127	-1333.4718	-0.2011	-1.2796	
		3	(55, 30, 0.2, 35)	95	-1541.9196	-0.2823	-1.4008	
		4	(55, 30, 0.2, 35)	110	-1623.9775	-0.2970	-1.4485	
		5	(55, 30, 0.2, 35)	102	-1641.9127	-0.3005	-1.4600	
		6	(55, 30, 0.2, 35)	98	-1644.2677	-0.3009	-1.4603	
		7	(55, 30, 0.2, 35)	126	-1644.9140	-0.3011	-1.4607	
		8	(55, 30, 0.2, 35)	109	-1644.9364	-0.3011	-1.4607	
		9	(55, 30, 0.2, 35)	120	-1644.9208	-0.3011	-1.4607	
		10	(55, 30, 0.2, 35)	132	-1644.9289	-0.3011	-1.4607	

Table 7.9: Results for the Flat L-Bracket with a modal solution manifold representation of the $\mathcal{D}_{L,\text{minor}}$ using the sparse, delayed Kronrod-Patterson with an isotropic Legendre basis. In the table below, ℓ denotes the level parameter, n_{dof} are the number of basis functions contained in $\mathcal{P}_{p_\ell}(\mathcal{D}_{L,\text{minor}})$ and n_ℓ are the number of function evaluations required to accurately capture the pseudospectral coefficients.

Collocation Scheme	Number of Elements	ℓ	n_{dof}	n_ℓ	Average L^2 error	Average Energy Error
Kronrod-Patterson	480	1	1	1	2.3589×10^{-5}	1.3782×10^2
		2	18	35	5.3034×10^{-6}	4.8530×10^1
		3	171	579	1.4566×10^{-6}	1.7515×10^1
		4	1140	6087	4.9801×10^{-7}	3.5950

Table 7.10: Results for the Flat L-Bracket with a modal solution manifold representation of the $\mathcal{D}_{L,\text{extreme}}$ using the sparse, delayed Kronrod-Patterson with an isotropic Legendre basis. In the table below, ℓ denotes the level parameter, n_{dof} are the number of basis functions contained in $\mathcal{P}_{p_\ell}(\mathcal{D}_{L,\text{extreme}})$ and n_ℓ are the number of function evaluations required to accurately capture the pseudospectral coefficients.

Collocation Scheme	Number of Elements	ℓ	n_{dof}	n_ℓ	Average L^2 error	Average Energy Error
Kronrod-Patterson	480	1	1	1	1.9409×10^{-5}	2.3368×10^2
		2	18	35	9.9425×10^{-6}	1.0326×10^2
		3	171	579	4.0818×10^{-6}	5.2883×10^1
		4	1140	6087	1.4370×10^{-6}	2.2798×10^1

Table 7.11: Results for an NREL 5MW with a nodal discretization of the design space using tensor-product Gauss-Legendre nodes. These results use 10 randomly chosen design variables and compares the isogeometric solution to the solution predicted by the nodal surrogate design space representation. In the table below, ℓ denotes the level parameter, n_{dof} are the number of basis functions contained in $\mathcal{Q}_{p_\ell}(\mathcal{D}_{\text{turb}})$ and n_ℓ are the number of function evaluations.

Collocation Scheme	Number of Elements	ℓ	n_{dof}	n_ℓ	Average L^2 error	Average ε Error
Gauss-Legendre	1440	1	1	1	3.8484×10^{-1}	3.0465×10^{-3}
		2	16	16	5.2918×10^{-2}	3.3269×10^{-4}
		3	81	81	2.1019×10^{-2}	1.4241×10^{-4}
		4	256	256	9.0516×10^{-3}	9.7949×10^{-5}

Chapter 8

Physics-Informed Tolerance Allocation

The problem considered emanates naturally from the aforementioned isogeometric design space exploration methodology presented in Chapter 7. In contrast to the design space exploration framework, rather than a full-system response, we are instead interested in the **system performance** $\mathcal{Q}(\boldsymbol{\mu})$, a scalar-valued function which provides a quantity of interest, e.g. maximum stress, maximum displacement, etc., as a function of design. Although we ground this topic in examples pertaining to the elastic problems considered in Chapters 6.1, 6.2, and 6.3, the methodology can easily be extended to a wide array of parametric partial differential equations.

8.1 Problem Statement

We are particularly interested in controlling allowable geometric deviations such that the design conforms to a prescribed performance constraint, which we denote $\mathcal{Q}_{\text{allow}}$. In the spirit of classical tolerance practices, we define the **tolerance variable** $\boldsymbol{\tau} \in \mathbb{R}_+^{d_\mu}$ which employs a performance-based tolerance about a **nominal design**, which we denote $\hat{\boldsymbol{\mu}} \in \mathbb{R}^{d_\mu}$. In this instance, any varied geometry about the nominal design can be represented via the relationship $\tilde{\boldsymbol{\mu}} = \hat{\boldsymbol{\mu}} \pm \boldsymbol{\tau}$. We wish to determine an optimal tolerance $\hat{\boldsymbol{\tau}} \in \mathbb{R}_+^{d_\mu}$ such that for all $\tilde{\boldsymbol{\mu}}$ with $|\hat{\mu}_i - \tilde{\mu}_i| \leq \tau_i$ for $i = 1, 2, \dots, d_\mu$, it follows that $\mathcal{Q}(\tilde{\boldsymbol{\mu}}) \leq \mathcal{Q}_{\text{allow}}$. However, since we are no longer concerned with a single design but rather a space of designs, we must define the **tolerance hyperrectangle** centered at $\hat{\boldsymbol{\mu}}$ by:

$$\mathcal{D}_{\hat{\boldsymbol{\mu}}}(\boldsymbol{\tau}) := \left\{ \boldsymbol{\mu} \in \mathbb{R}^{d_\mu} : |\mu_i - \hat{\mu}_i| \leq \tau_i, i = 1, 2, \dots, d_\mu \right\}. \quad (8.1)$$

This hyperrectangle formally characterizes the space of designs which deviate from a nominal design $\hat{\boldsymbol{\mu}}$ within some threshold $\boldsymbol{\tau}$. Note that sequences of hyperrectangles of this type are in fact nested. In particular, given some $\hat{\boldsymbol{\mu}}$ and tolerance variables $\boldsymbol{\tau}_1, \boldsymbol{\tau}_2$ such that if $(\boldsymbol{\tau}_1)_i \leq (\boldsymbol{\tau}_2)_i$ for $i = 1, 2, \dots, d_\mu$, it necessarily follows that $\mathcal{D}_{\hat{\boldsymbol{\mu}}}(\boldsymbol{\tau}_1) \subseteq \mathcal{D}_{\hat{\boldsymbol{\mu}}}(\boldsymbol{\tau}_2)$.

The quantity $\mathcal{Q}(\boldsymbol{\mu})$ provides a characteristic of only one design. Instead, we would like to understand the behavior of this quantity over an entire space of designs, in particular the space of designs within a specified tolerance hyperrectangle. This necessitates the direct manipulation of the tolerance variable $\boldsymbol{\tau}$, rather than the design variable $\boldsymbol{\mu}$. Therefore, we define the **performance measure** $\mathcal{G}(\boldsymbol{\tau})$ which will be used as our constraint in the optimization problem:

$$\mathcal{G}(\boldsymbol{\tau}) := \max_{\boldsymbol{\mu} \in \mathcal{D}_{\hat{\boldsymbol{\mu}}}(\boldsymbol{\tau})} \mathcal{Q}(\boldsymbol{\mu}) \tag{8.2}$$

elucidating the equivalent constraint on the tolerance variable of $\mathcal{G}(\boldsymbol{\tau}) \leq \mathcal{Q}_{\text{allow}}$. That is, all candidate tolerance variables in our selection procedure must satisfy the criterion that the “worst-case” design within the corresponding tolerance hyperrectangle must be in compliance with the performance constraint.

There are a variety of approaches to arrive at an optimal tolerance variable, which we refer to herein as $\hat{\boldsymbol{\tau}}$, satisfying the above criteria. For our applications, it is desirable that $\hat{\boldsymbol{\tau}}$ be maximal with respect to some measure, denoted $\mathcal{F}(\boldsymbol{\tau})$, which we refer to colloquially herein as the tolerance measure. Moreover, it is preferable that the choice of the tolerance measure will ultimately provide the most flexibility in design as well as inform design considerations such as cost or manufacturability. With the appropriate mathematical formalism in place, we can pose our general optimization problem:

Given $\hat{\boldsymbol{\mu}} \in \mathbb{R}_+^{d_\mu}$, find $\hat{\boldsymbol{\tau}}$ such that

$$\hat{\boldsymbol{\tau}} = \underset{\boldsymbol{\tau} \in \mathcal{T}_{\text{allow}}}{\operatorname{argmax}} \mathcal{F}(\boldsymbol{\tau}) \quad \text{where} \quad \mathcal{T}_{\text{allow}} := \left\{ \boldsymbol{\tau} \in \mathbb{R}_+^{d_\mu} : \mathcal{G}(\boldsymbol{\tau}) \leq \mathcal{Q}_{\text{allow}} \right\} \quad (8.3)$$

With this problem formulation, there are four outstanding concerns:

1. Each function call to $\mathcal{G}(\boldsymbol{\tau})$ is a demanding optimization over $\boldsymbol{\mu}$, how do we mitigate this seemingly unavoidable computational expense?
2. How do we construct the tolerance “search space” $\mathcal{T}_{\text{allow}}$ in a computationally feasible, yet exhaustive manner?
3. Our choice of $\mathcal{F}(\boldsymbol{\tau})$ may dramatically affect the resulting $\hat{\boldsymbol{\tau}}$, what is an appropriate choice for this measure?
4. How do we arrive at $\hat{\boldsymbol{\tau}}$, the solution to the optimization problem Eq. (8.3) which we have outlined above?

We address these issues in the following subsections and present our solutions to each.

8.1.1 A Low-Rank, Separated Representation for System Performance

Recall Eq. (8.2), the worst-case constraint function over a tolerance hyperrectangle. Given a tolerance variable $\boldsymbol{\tau}$, $\mathcal{G}(\boldsymbol{\tau})$ searches the corresponding tolerance hyperrectangle for the entry which maximizes the performance constraint $\mathcal{Q}(\boldsymbol{\mu})$, a rather costly optimization procedure. This is due to the necessity of a global system construction and subsequent solve of the isogeometric discretization for each $\boldsymbol{\mu}$. Moreover, this computational cost is only compounded in optimization routines over the tolerance variable, in which $\mathcal{G}(\boldsymbol{\tau})$ must be evaluated several times. The goal of this subsection is to construct an economical and numerically stable model for the quantity $\mathcal{Q}(\boldsymbol{\mu})$.

To alleviate this inherent computational expense, we resort to constructing a surrogate model to $\mathcal{Q}(\boldsymbol{\mu})$, analogous to those considered in [14]. However, the nodal and modal surrogate models

considered therein suffer from the notorious curse of dimensionality, where a linear increase in model fidelity demands an exponential increase in required sample realizations. Additionally, high-fidelity orthogonal polynomial expansions are comprised of many terms, consequently increasing computational expense for each evaluation. Furthermore, the cardinality of these orthogonal polynomial basis sets in moderate dimensions present stability concerns in floating-point arithmetic. Therefore, we instead adopt a technique emanating from the uncertainty quantification community known as a **low-rank, separated representation**. That is, a representation of the form:

$$\mathcal{Q}(\boldsymbol{\mu}) \approx \tilde{\mathcal{Q}}_{r,p}(\boldsymbol{\mu}) = \sum_{\ell=1}^r s_{\ell} \mathcal{G}_{\ell,p}(\boldsymbol{\mu}) \quad \text{where} \quad \mathcal{G}_{\ell,p}(\boldsymbol{\mu}) = \prod_{i=1}^{d_{\mu}} g_{\ell,p}^i(\mu_i) \quad (8.4)$$

for a surrogate model to $\mathcal{Q}(\boldsymbol{\mu})$. The separation rank, r , is chosen to be relatively small, mitigating the stability and economic concerns presented above while the polynomial degree p is chosen sufficiently large to effectively resolve nonlinearities. The coefficients s_{ℓ} are constants which enforce any normalization preferences e.g. $\|g_{\ell,p}^i\| = 1$. These basis functions provide a better approximation to $\mathcal{Q}(\boldsymbol{\mu})$ at the expense of the orthogonality that is ensured by an orthogonal polynomial series. Determining the basis set $\{g_{\ell,p}^i(\mu_i)\}_{\ell=1}^r$ for $i = 1, 2, \dots, d_{\mu}$ is a nonlinear optimization problem with various solution approaches as outlined in [15, 42]. One approach utilizes an alternating least-squares routine, e.g. see [75, 20, 34, 111], which minimizes the usual least-squares error between N data points $\{(\boldsymbol{\mu}^{(j)}, \mathcal{Q}^{(j)})\}_{j=1}^N$ and the minimizer $\tilde{\mathcal{Q}}_{r,p}(\boldsymbol{\mu})$:

$$\|\{(\boldsymbol{\mu}^{(j)}, \mathcal{Q}^{(j)})\}_{j=1}^N - \tilde{\mathcal{Q}}_{r,p}(\boldsymbol{\mu}^{(j)})\|^2 = \sum_{j=1}^N (\mathcal{Q}^{(j)} - \tilde{\mathcal{Q}}_{r,p}(\boldsymbol{\mu}^{(j)}))^2 \quad (8.5)$$

where $\boldsymbol{\mu}^{(j)} = (\mu_1^{(j)}, \mu_2^{(j)}, \dots, \mu_{d_{\mu}}^{(j)})$ and $\mathcal{Q}^{(j)} = \mathcal{Q}(\boldsymbol{\mu}^{(j)})$. This is accomplished by determining the coefficients $c_{\ell,j}^i$ in an orthogonal polynomial expansion, e.g. the Legendre polynomials, of the form:

$$g_{\ell,p}^i(\mu_i) \approx \sum_{j=1}^{M_{\ell}} c_{\ell,j}^i \mathcal{L}_{j,p}(\mu_i), \quad i = 1, 2, \dots, d_{\mu}, \quad \ell = 1, 2, \dots, r \quad (8.6)$$

effectively approximating the non-polynomial basis function set. Alternative approaches for determining the coefficients $c_{\ell,j}^i$ exist, including compressive sensing [122, 127] and adding regularization terms to the error [117, 42]. Moreover, other orthogonal polynomials, e.g. Hermite, may be employed to consequently induce a non-uniform weighting on the sample space. Note that this representation is particularly appealing for our purposes due to the variety of existing optimization algorithms for determining $\mathcal{G}(\boldsymbol{\tau})$ from function representations of this form, e.g. [100]. Additionally, the low-rank nature of these separated representations affords its numerically stable and economical evaluation, since they are comprised of relatively few terms in comparison to potentially thousands in the interpolatory or spectral counterpart.

8.1.2 Construction of the Tolerance Search Space

The question of over which space to construct the surrogate model, that is $\mathcal{T}_{\text{allow}}$, naturally arises after the presentation of our surrogate model construction strategy. Constructing this space too expansively will render $\tilde{\mathcal{Q}}_{r,p}(\boldsymbol{\mu})$ a poor approximation of the true performance constraint $\mathcal{Q}(\boldsymbol{\mu})$ while a conservative construction of $\mathcal{T}_{\text{allow}}$ will limit our tolerance allocation capabilities. Given certain regularity and smoothness assumptions on the performance constraint $\mathcal{Q}(\boldsymbol{\mu})$, we can convert the problem of sizing the tolerance search space $\mathcal{T}_{\text{allow}}$ into a set of d_μ , one-dimensional root-finding problems. In particular, we define $q_i(\mu) := \mathcal{Q}(\hat{\boldsymbol{\mu}} + \mu \mathbf{e}_i)$. Then, if $q_i(\mu) \in C^1$, we can assert that $(\mathcal{T}_{\text{allow}})_i = |\mu_i^* - \hat{\mu}_i|$ where:

$$\mu_i^* = \underset{\mu}{\operatorname{argmin}} \frac{1}{2} |\mu - \hat{\mu}_i|^2 \quad \text{such that} \quad \begin{cases} q_i(\mu) & = \mathcal{Q}_{\text{allow}} \\ \frac{dq_i(\mu)}{d\mu} \cdot \operatorname{sgn}(\mu - \hat{\mu}_i) & > 0 \end{cases} \quad (8.7)$$

for $i = 1, 2, \dots, d_\mu$. We rigorously ground this concept in the following proposition:

Proposition 19. *The tolerance hyperrectangle $\mathcal{T}_{\text{allow}}$ with dimensions defined by Eq. (8.7) contains all solutions to Eq. (8.3).*

Proof. Suppose $\exists \boldsymbol{\tau}^*$ satisfying Eq. (8.3) such that $\mathcal{G}(\boldsymbol{\tau}^*) = \mathcal{Q}_{\text{allow}}$ but $\tau_i^* > (\mathcal{T}_{\text{allow}})_i$ for some $i \in [1, d_\mu]$. Then by the monotonicity asserted by Eq. (8.7) it follows that for some $\boldsymbol{\tau} \in \mathcal{T}_{\text{allow}}$:

$$\mathcal{Q}_{\text{allow}} = \mathcal{G}(\boldsymbol{\tau}^*) \geq \mathcal{G}(\boldsymbol{\tau}) = \mathcal{Q}_{\text{allow}}$$

In the case of a strict inequality, the contradiction is apparent. However in the case of equality, $\mathcal{G}(\boldsymbol{\tau}^*) = \mathcal{G}(\boldsymbol{\tau})$ implies that $\frac{dq_i(\mu_i^*)}{d\mu} (\mu_i^* - \hat{\mu}_i) \leq 0$ due to monotonicity, contradicting the condition presented in Eq. (8.7). \square

We have thus far presented a methodology for sizing the **upper bounds**, $\boldsymbol{\tau}_{\text{max}}$, of the tolerance hyperrectangle. However, in practice it may be desirable to additionally enforce lower bounds $\boldsymbol{\tau}_{\text{min}}$, ensuring that boundary solutions to Eq. (8.3) still allocate some prescribed minimum, nonzero tolerance to every design parameter. The only requirement in this case is that $\mathcal{G}(\boldsymbol{\tau}_{\text{min}}) \leq \mathcal{Q}_{\text{allow}}$, where, in the case of equality $\boldsymbol{\tau}_{\text{min}} = \hat{\boldsymbol{\tau}}$. Moreover, assignment of $\boldsymbol{\tau}_{\text{min}}$ does not affect the aforementioned construction of $\boldsymbol{\tau}_{\text{max}}$.

8.1.3 Tolerance Measures

In Section 8.2 section of this dissertation, we consider the following three tolerance measures for optimization. Each measure is used to emulate the cost, or inverse of cost in the instance of the first two measures, associated with each tolerance. Intuitively, the more flexibility each tolerance parameter has, the lower the associated cost, e.g. if τ_i is large, manufacturing costs will be low given the loose tolerance. The tolerance measures presented in this section are by no means exhaustive. However, they are perhaps the most relevant for the applications considered herein while also demonstrating the versatility of our methodology with respect to matters of design interest. For a list containing several other tolerance measures that are considered in practice, refer

to [27, 13, 79, 115, 38].

1. The first measure considered, $\mathcal{F}_1(\boldsymbol{\tau})$, is perhaps the simplest choice.

$$\mathcal{F}_1(\boldsymbol{\tau}) := \sum_{i=1}^{d_\mu} \tau_i \quad (8.8)$$

Note that, $\mathcal{F}_1(\boldsymbol{\tau}) \equiv \|\boldsymbol{\tau}\|_1$. Intuitively, the selection of this tolerance functional will maximize the total tolerance available while complying to the performance constraint. However this choice may lead to the sparsest solution in the presence of large discrepancies in the magnitudes of design parameter sensitivities.

2. The second measure considered, $\mathcal{F}_\mu(\boldsymbol{\tau})$, leverages the design variable sensitivities informed through the performance measure surrogate model since the weighting: $\alpha_i = |\partial_{\mu_i}(\hat{\boldsymbol{\mu}})|$ accounts for design parameter sensitivities revealed through the surrogate model.

$$\mathcal{F}_\mu(\boldsymbol{\tau}) := \sum_{i=1}^{d_\mu} \left| \frac{\partial Q}{\partial \mu_i}(\hat{\boldsymbol{\mu}}) \right| \tau_i \quad (8.9)$$

With this selection, design parameters which are the most sensitive to perturbations are given prevalence in the optimization routine.

3. The third and final measure considered, $\mathcal{F}_{-1}(\boldsymbol{\tau})$, is a more drastic weighting than the previous two. In particular, this measure will “isotropize” the allocated tolerance since maximal values of the contours lie along the vector of ones.

$$\mathcal{F}_{-1}(\boldsymbol{\tau}) := \left(\sum_{i=1}^{d_\mu} \frac{1}{\tau_i} \right)^{-1} \quad (8.10)$$

Moreover, this measure coerces tolerance values away from the axes which, in the scenario without minimum-allocated tolerances, prevents “wall solutions” from occurring.

8.1.4 Manifold Traversal

The feasible region $\mathcal{T}_{\text{allow}}$ in the optimization problem Eq. (8.3) in fact describes a connected, immersed manifold of codimension one, embedded in a d_μ -dimensional space, specifically,

$$\mathcal{M} := \left\{ \boldsymbol{\tau} \in \mathbb{R}_+^{d_\mu} : \mathcal{G}(\boldsymbol{\tau}) = \mathcal{Q}_{\text{allow}} \right\}. \quad (8.11)$$

The nestedness of the tolerance hyperrectangles granted by our construction ensures that this manifold is monotonically increasing. Moreover in some instances, this manifold is also convex suggesting an ascent-based optimization routine will excel. Classical optimization routines cannot be directly employed, since each point of the manifold belongs to a different linear space. However, many of these algorithms have been generalized to a manifold setting [2, 103] which are well-suited for our optimization problem by introducing an affine connection between linear spaces. Common to these algorithms is that for every iteration i , a linear space is constructed about the point $\boldsymbol{\tau}_i$, namely the tangent space $T_{\boldsymbol{\tau}_i}\mathcal{M}$. If we define $\mathcal{N}(\boldsymbol{\tau}) := \text{span}\{\nabla_{\boldsymbol{\tau}}\mathcal{G}(\boldsymbol{\tau})\}$, then it follows that $T_{\boldsymbol{\tau}}\mathcal{M} = \mathcal{N}(\boldsymbol{\tau})^\perp$, necessitating the computation of $\nabla_{\boldsymbol{\tau}}\mathcal{G}(\boldsymbol{\tau}_i)$ in an efficient and accurate manner. Moreover, since $\mathcal{G}(\boldsymbol{\tau})$ is an implicitly-defined manifold with potentially sharp gradients, finite-difference approaches lack robustness in this regard. Instead, we resort to an analytic gradient by first defining the set of candidate $\boldsymbol{\mu}$ -maximizers which define $\mathcal{G}(\boldsymbol{\tau})$, $\mathcal{K}(\boldsymbol{\tau}) := \{\boldsymbol{\mu} \in \mathcal{D}_{\hat{\boldsymbol{\mu}}}(\boldsymbol{\tau}) : \mathcal{Q}(\boldsymbol{\mu}) = \mathcal{G}(\boldsymbol{\tau})\}$. The gradient is then given by:

$$\frac{\partial \mathcal{G}}{\partial \tau_i}(\boldsymbol{\tau}^*) = \begin{cases} \max_{\substack{\boldsymbol{\mu} \in \mathcal{K}(\boldsymbol{\tau}^*) \\ |\mu_i - \hat{\mu}_i| = \tau_i^*}} \frac{\partial \mathcal{Q}}{\partial \mu_i}(\boldsymbol{\mu}) \cdot \text{sgn}(\mu_i - \hat{\mu}_i), & \mathcal{K}(\boldsymbol{\tau}) \neq \emptyset \\ 0, & \mathcal{K}(\boldsymbol{\tau}) = \emptyset \end{cases} \quad (8.12)$$

Necessarily, $\mathbb{R}^{d_\mu} = \mathcal{N}(\boldsymbol{\tau}) \oplus T_{\boldsymbol{\tau}}\mathcal{M}$ for every $\boldsymbol{\tau} \in \mathcal{M}$. Let $\{\mathbf{t}_i\}_{i=1}^{d_\mu-1} \in \mathbb{R}^{d_\mu}$ denote an orthonormal basis of $T_{\boldsymbol{\tau}}\mathcal{M}$ and define $\mathbf{T} = [\mathbf{t}_1 | \mathbf{t}_2 | \cdots | \mathbf{t}_{d_\mu-1}]$. Then for every $\boldsymbol{\tau} \in \mathbb{R}^{d_\mu}$, there exists $b \in \mathbb{R}$ and $\boldsymbol{\xi} \in \mathbb{R}^{d_\mu-1}$ such that $\boldsymbol{\tau} = \boldsymbol{\eta} + b\hat{\mathbf{n}}$ where $\hat{\mathbf{n}} = \mathcal{G}(\boldsymbol{\tau})/\|\mathcal{G}(\boldsymbol{\tau})\|$ and $\boldsymbol{\eta} = \mathbf{T}\boldsymbol{\xi}$. Intuitively, $\hat{\mathbf{n}}$ is the manifold normal at $\boldsymbol{\tau}$ and $\boldsymbol{\eta}$ is a vector in the tangent space with coordinates $\boldsymbol{\xi}$ in the \mathbf{T} basis.

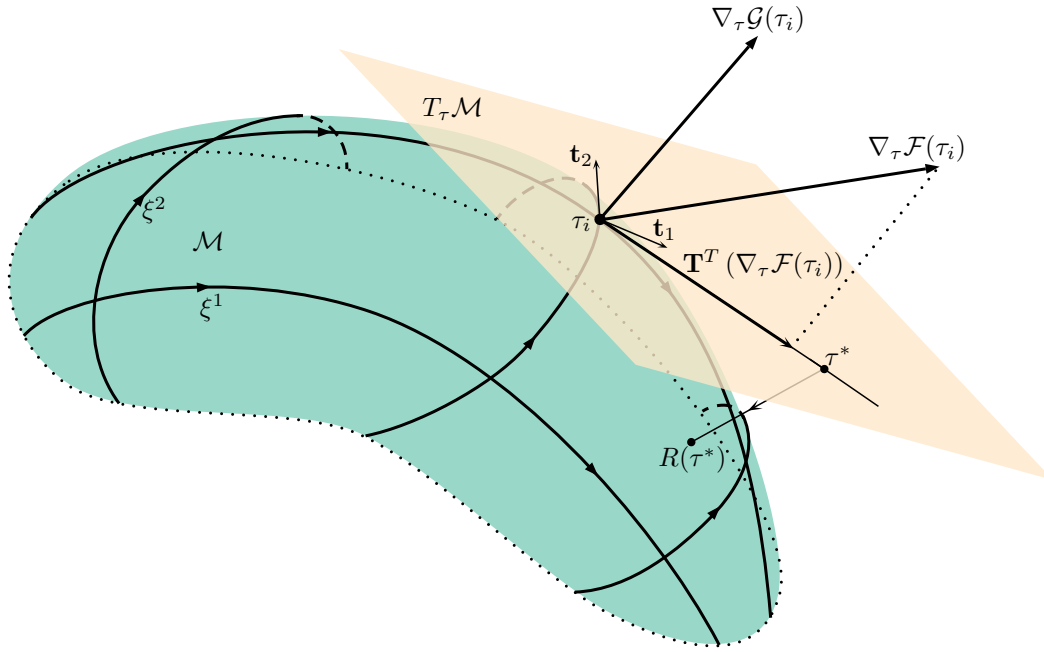


Figure 8.1: An example manifold with a graphical illustration of the differential geometric tools presented in this section.

It is through this decomposition that we are capable of performing manifold optimization solely in terms of tangent-space entities. Then, we project $\nabla\mathcal{F}(\boldsymbol{\tau})$ into the tangent space which provides the direction of steepest ascent. An illustration of such a manifold, along with the necessary differential geometric tools to perform optimization, are shown in Fig. 8.1.

Any finite traversal in $T_{\boldsymbol{\tau}}\mathcal{M}$ away from $\boldsymbol{\tau}$ will no longer reside in the manifold due to the lack of a covariant gradient in the definition our tangent space basis. Moreover, we are unable to readily define the necessary Christoffel symbols because the manifold is implicitly defined. Therefore, we resort to determining an operator which transforms elements of $T_{\boldsymbol{\tau}_i}\mathcal{M}$ into elements of \mathcal{M} . A smooth mapping $R: T\mathcal{M} \rightarrow \mathcal{M}$, colloquially referred to as a **retraction** in the manifold optimization community, is well suited for our purposes and is formalized in the following definition. For further details, the reader is referred to [3, 112].

Definition 1. A smooth mapping $R : T\mathcal{M} \rightarrow \mathcal{M}$ is said to be a **retraction** if it satisfies the following properties. Let $R_\tau = R|_{T_\tau\mathcal{M}}$ denote the restriction of R to $T_\tau\mathcal{M}$.

(i) $R_\tau(\mathbf{0}_\eta) = \tau$ where $\mathbf{0}_\eta$ is the zero element of $T_\tau\mathcal{M}$.

(ii) $DR_\tau(\mathbf{0}_\eta) = id_{T_\tau\mathcal{M}}$ where $id_{T_\tau\mathcal{M}}$ is the identity mapping on $T_\tau\mathcal{M}$, e.g. $DR_\tau(\mathbf{0}_\eta)[\xi] = \xi$

A **retractor** induces a retraction provided it satisfies Definition 1. A retraction operation is an approximation to the Riemannian exponential map, that is, a local parametrization of \mathcal{M} in a neighborhood of $\tau \in \mathcal{M}$ in terms of tangent-space entities η . There are several retractors available which are classified depending on their approximation capability of the Riemannian exponential map. In particular, a retractor is referred to as 1st-order if it approximates the Riemannian exponential map to the first order and similarly, it is 2nd-order retractor if it agrees with this map up to second order. Retractor classifications are thoroughly discussed in [3] and the reader is referred here for further details. For our purposes we use the first-order retractor:

$$\mathbf{v}_\tau(\eta) = \begin{cases} (\tau + \eta) - \tau_{\min}, & \mathcal{G}(\tau + \eta) \geq \mathcal{Q}_{\text{allow}} \\ \tau_{\max} - (\tau + \eta), & \mathcal{G}(\tau + \eta) < \mathcal{Q}_{\text{allow}} \end{cases} \quad (8.13)$$

Note that this retractor doesn't exactly satisfy the definitions of Definition 1. However, it is shown in [3, Definition 4.1, Theorem 4.2] that if $R_\tau(\mathbf{0}_\eta)$ is **transverse** to $T_\tau\mathcal{M}$, that is $R_\tau(\mathbf{0}_\eta) \cap T_\tau\mathcal{M} = \mathbf{0}_\eta$, $R_\tau(\eta)$ is indeed a retraction. This retraction operator plays a pivotal role in our algorithm as well as many others in the manifold optimization community since it enables the evaluation of the objective functional on the manifold solely through the tangent-space coordinates. This feature elucidates an equivalent formulation of the optimization problem Eq. (8.3) namely,

$$\hat{\tau} = \operatorname{argmax}_{\eta \in T\mathcal{M}} \mathcal{F}(R(\eta)) = \operatorname{argmax}_{\xi \in \mathcal{M}} \hat{\mathcal{F}}(\xi) \quad (8.14)$$

Note here that the feasible region $\mathcal{T}_{\text{allow}}$ is now implicitly embedded in the restriction $\eta \in T\mathcal{M}$, and similarly $\xi \in \mathcal{M}$. The function $\hat{\mathcal{F}}(\xi)$ denotes the pullback of \mathcal{F} through the retraction R , i.e. the objective functional in terms of the curvilinear manifold coordinates $\xi \in \mathcal{M}$, or more specifically

$\hat{\mathcal{F}}_{\tau}(\xi)$ for the restricted pullback associated with R_{τ} . Additionally, property (ii) of Definition 1 facilitates the vector-transport of η along ξ through the differentiated retraction operator:

$$\mathcal{T}_{\xi}\eta = \nabla_{\xi}R(\eta). \quad (8.15)$$

This ability enables vector-field differentiation in terms of manifold coordinates through an affine connection between nearby tangent spaces. With the introduction of the aforementioned entities, we are now capable of introducing the manifold ascent algorithm. Herein we consider two algorithms for manifold ascent: (i) bound-constrained manifold gradient ascent and (ii) bound-constrained manifold conjugate gradients. As is with the Euclidean setting, the manifold gradient ascent algorithm suffers from slow convergence in the presence of large disparity between eigenvalues; the manifold conjugate gradients algorithm somewhat restores the expected convergence rates. Next, we provide pseudocode for the manifold traversal in efforts to algorithmically combine the aforementioned entities in a computationally tractable manner.

8.1.5 Algorithm Pseudocode

Manifold traversal begins with an initial guess, $\tau_0 \in \mathcal{M}$ which may be obtained in a manner analogous to retraction. In our algorithm we begin at the origin, or τ_{\min} , and construct a ray from this point along the direction of $\nabla_{\tau}\mathcal{F}(\tau_{\min})$, or $\nabla_{\tau}\mathcal{F}(\mathbf{0})$. We then traverse this ray until the point of manifold intersection, τ_0 , the initial guess to start the gradient ascent or conjugate gradients algorithm. Heretofore, the remainder of the algorithm is iterative until convergence. Therefore for the sake of generality, we employ the notation of τ_i throughout the remainder of this discussion.

At the point τ_i , we compute $\nabla\mathcal{G}(\tau_i)$ through (8.12), providing us the normal director to \mathcal{M} at the point τ_i . Thereafter, we construct a basis to the tangent space $T_{\tau_i}\mathcal{M}$ by determining the orthogonal complement of $\nabla\mathcal{G}(\tau_i)$. With the construction of a basis for the tangent space, we then project $\nabla\mathcal{F}$ into the tangent bundle to obtain the steepest ascent direction and hence the direction for the line search. In the case of conjugate gradients, there are additional terms in the ascent direction which are informed through previous iterates of the algorithm. A line search is

then performed over this search direction, between wall boundaries, and the maximal value is set to τ_{i+1} . This line search process utilizes the retraction operation since every function evaluation on the manifold is equivalent to an evaluation of a retracted tangent-space entity.

Note that in every step of the algorithm when constructing $T_{\tau_i}\mathcal{M}$, we must employ a check which will determine if τ_i lies on a boundary of the hyperrectangle. If so, then we check if $\nabla\mathcal{F}$ has increasing normal derivative out of the hyperrectangle. If both of these conditions are met, the components of the tangent basis which exit the hyperrectangle are set to zero, effectively projecting the manifold trace onto the tolerance hyperrectangle boundary. The monotonicity of the manifold ensures that this component has been maximized and no further optimization in that direction is necessary. Note that the first iteration of conjugate gradients is simply gradient ascent and every new “boundary projection” effectively restarts the conjugate gradients algorithm, this flag is denoted by CG in the algorithm pseudocode.

Algorithm 1 Manifold retraction operation

```

1: function MANIFOLDRETRACTION( $\tau_0, \eta$ )
2:   if  $\mathcal{G}(\tau_0 + \eta) \geq \mathcal{Q}_{\text{allow}}$  then                                     ▷  $\tau_0 + \eta$  is above manifold
3:      $\mathbf{v} = (\tau_0 + \eta) - \tau_{\text{min}}$                                        ▷ Retractor per Eq. (8.13)
4:   else                                                                     ▷  $\tau_0 + \eta$  is below manifold
5:      $\mathbf{v} = \tau_{\text{max}} - (\tau_0 + \eta)$                                        ▷ Retractor per Eq. (8.13)
6:   end if
7:    $\tau_{\mathbf{v}}(s) = s\mathbf{v} + (\tau_0 + \eta)$                                      ▷ Line from tangent space along retractor to manifold
8:   Find  $s^*$  such that  $\mathcal{G}(\tau_{\mathbf{v}}(s^*)) = \mathcal{Q}_{\text{allow}}$                        ▷ Determine manifold intersection
9:   return  $\tau_{\mathbf{v}}(s^*)$ 
10: end function

```

8.2 Numerical Tests

In the following section, we apply the aforementioned methodology to the setting of linear elasticity. We consider a suite of problems including: (i) a plate with hole parametrized by two design parameters, (ii) a plate with hole parametrized by six design parameters, (iii) an L-Bracket parametrized by 17 design parameters. These problems are chosen to demonstrate the robustness and effectiveness of the algorithm with respect to dimensionality over complex and intricate

Algorithm 2 Build tangent space

```

1: function BUILD_TANGENT_SPACE( $\boldsymbol{\tau}_0, \boldsymbol{\tau}_{\min}, \boldsymbol{\tau}_{\max}$ )
2:   CG = 1
3:    $\mathbf{T} = [\nabla_{\boldsymbol{\tau}} \mathcal{G}(\boldsymbol{\tau}_0)]^\perp$  ▷  $\mathbf{T} = [\mathbf{t}_1 | \mathbf{t}_2 | \dots | \mathbf{t}_{d_\mu - 1}]$ 
4:   for  $k = 1, 2, \dots, d_\mu$  do
5:     if  $(\boldsymbol{\tau}_0)_k == (\boldsymbol{\tau}_{\min})_k$  or  $(\boldsymbol{\tau}_0)_k == (\boldsymbol{\tau}_{\max})_k$  then ▷ Check if  $\boldsymbol{\tau}_0$  is on wall
6:       if  $\mathcal{F}(\mathbf{t}_k) \cdot \mathbf{n}_k \geq 0$  then ▷  $\mathbf{n}_k$  is unit outward normal to wall  $k$ .
7:         CG = 0 ▷ New wall intersection
8:         for  $m = 1, 2, \dots, d_\mu - 1$  do
9:            $\mathbf{T}_{km} = 0$  ▷ Project out  $k^{\text{th}}$  component of search
10:        end for
11:      end if
12:    end if
13:  end for
14:  return  $[\mathbf{T}, \text{CG}]$ 
15: end function

```

Algorithm 3 Bound-constrained manifold gradient ascent

```

1: function MANIFOLD_GRADIENT_ASCENT( $\boldsymbol{\tau}_0, \boldsymbol{\tau}_{\min}, \boldsymbol{\tau}_{\max}$ )
2:    $i = 0$ 
3:   while  $i < N$  do
4:      $\mathbf{T} = \text{BUILD\_TANGENT\_SPACE}(\boldsymbol{\tau}_i, \boldsymbol{\tau}_{\min}, \boldsymbol{\tau}_{\max})$  ▷ Get tangent space to  $\boldsymbol{\tau}_i$ 
5:      $\mathbf{v} = \mathbf{T}^T \nabla \mathcal{F}(\boldsymbol{\tau}_i)$  ▷ Project  $\nabla \mathcal{F}(\boldsymbol{\tau}_i)$  into tangent space
6:      $j_\ell = \underset{j > 0}{\operatorname{argmin}} |v_j / (\boldsymbol{\tau}_{\min})_j|$  ▷ Index of first ray intersection with lower bound
7:      $j_u = \underset{j > 0}{\operatorname{argmin}} |v_j / (\boldsymbol{\tau}_{\max})_j|$  ▷ Index of first ray intersection with upper bound
8:     Set  $\alpha_\ell = v_{j_\ell} / (\boldsymbol{\tau}_{\min})_{j_\ell}$  ▷ Lower bound of search
9:     Set  $\alpha_u = v_{j_u} / (\boldsymbol{\tau}_{\max})_{j_u}$  ▷ Upper bound of search
10:    Find  $\alpha^* = \underset{\alpha_\ell \leq \alpha \leq \alpha_u}{\operatorname{argmax}} \mathcal{F}(R_{\boldsymbol{\tau}_i}(\alpha \mathbf{v}))$  ▷ Line search for optimal step in ascent direction
11:     $\boldsymbol{\tau}_{i+1} = \alpha^* \mathbf{v} + \boldsymbol{\tau}_i$  ▷ Compute  $\boldsymbol{\tau}_{i+1}$ 
12:     $i = i + 1$  ▷ Increment counter
13:  end while
14: end function

```

Algorithm 4 Bound-constrained manifold nonlinear conjugate gradients

```

1: function MANIFOLDCONJUGATEGRADIENTS( $\boldsymbol{\tau}_0, \boldsymbol{\tau}_{\min}, \boldsymbol{\tau}_{\max}$ )
2:    $i = 0$ 
3:    $\text{CG} = 0$  ▷ First iteration is gradient ascent
4:   while  $i < N$  do
5:      $[\mathbf{T}^{(i)}, \text{CG}] = \text{BUILDTANGENTSPACE}(\boldsymbol{\tau}_i, \boldsymbol{\tau}_{\min}, \boldsymbol{\tau}_{\max})$  ▷ Get  $\mathbf{T}$  and check for new wall
6:     intersection
7:      $\mathbf{v}^{(i)} = (\mathbf{T}^{(i)})^T \nabla \mathcal{F}(\boldsymbol{\tau}_i)$  ▷ Project  $\nabla \mathcal{F}(\boldsymbol{\tau}_i)$  into tangent space
8:     if  $\text{CG}$  and  $i > 1$  then
9:        $[\mathbf{T}^{(i-1)}, \text{CG}] = \text{BUILDTANGENTSPACE}(\boldsymbol{\tau}_{i-1}, \boldsymbol{\tau}_{\min}, \boldsymbol{\tau}_{\max})$  ▷ Get  $\mathbf{T}^{(i-1)}$ 
10:       $\mathbf{v}^{(i-1)} = (\mathbf{T}^{(i-1)})^T \nabla \mathcal{F}(\boldsymbol{\tau}_{i-1})$  ▷ Project  $\nabla \mathcal{F}(\boldsymbol{\tau}_{i-1})$  into tangent space
11:       $\mathbf{v}^{(i)} = \mathbf{v}^{(i)} + \beta_i \mathcal{T}_{\alpha_{i-1} \mathbf{v}^{(i-1)}}(\mathbf{v}^{(i-1)})$  ▷ Add vector transport to search direction
12:    end if
13:     $j_\ell = \operatorname{argmin}_{j>0} |\mathbf{v}_j / (\boldsymbol{\tau}_{\min})_j|$  ▷ Index of first ray intersection with lower bound
14:     $j_u = \operatorname{argmin}_{j>0} |\mathbf{v}_j / (\boldsymbol{\tau}_{\max})_j|$  ▷ Index of first ray intersection with upper bound
15:    Set  $\alpha_\ell = \mathbf{v}_{j_\ell} / (\boldsymbol{\tau}_{\min})_{j_\ell}$  ▷ Lower bound of search
16:    Set  $\alpha_u = \mathbf{v}_{j_u} / (\boldsymbol{\tau}_{\max})_{j_u}$  ▷ Upper bound of search
17:    Find  $\alpha^* = \operatorname{argmax}_{\alpha_\ell \leq \alpha \leq \alpha_u} \mathcal{F}(R_{\boldsymbol{\tau}_i}(\alpha \mathbf{v}))$  ▷ Line search for optimal step in ascent direction
18:     $\boldsymbol{\tau}_{i+1} = \alpha^* \mathbf{v} + \boldsymbol{\tau}_i$  ▷ Compute  $\boldsymbol{\tau}_{i+1}$ 
19:     $i = i + 1$  ▷ Increment counter
20:  end while
21: end function

```

geometric configurations.

In each of our numerical tests, we will begin by constructing the appropriately-sized tolerance hyperrectangle as discussed in the previous subsection. From here, we are capable of building surrogate models over a variety of polynomial degrees and ranks using the separated representation methodology presented in an earlier section. These models are constructed from a database of realizations from uniformly-distributed Monte Carlo samples corresponding to geometries which reside in the predetermined hyperrectangle. Both the mean

$$\|\mathbf{e}_{r,p}\|_{\text{M}} := \frac{1}{N_c} \sum_{i=1}^{N_c} \left| \frac{\mathcal{Q}_{\text{exact},i} - \tilde{\mathcal{Q}}_{r,p}(\boldsymbol{\mu}_i)}{\mathcal{Q}_{\text{exact},i}} \right| \quad (8.16)$$

and maximum

$$\|\mathbf{e}_{r,p}\|_{\infty} := \max_{1 \leq i \leq N_c} \left| \frac{\mathcal{Q}_{\text{exact},i} - \tilde{\mathcal{Q}}_{r,p}(\boldsymbol{\mu}_i)}{\mathcal{Q}_{\text{exact},i}} \right| \quad (8.17)$$

relative errors in the surrogate models, as a function of polynomial degree and separation rank, are considered in this section. Here, N_c is the number of compared samples, none of which are used in the construction of $\tilde{\mathcal{Q}}_{r,p}(\boldsymbol{\mu})$. The average relative error provides a notion of surrogate model convergence while the maximum error is the pointwise quantity we wish to accurately capture, since the “worst member” in the set of designs indicates compliance to the system performance. Tables containing these errors will be presented and leveraged in our choice of surrogate model construction. Moreover, our proposed methodology allows the user to effectively “tune” the surrogate model to be within their desired fidelities through this approach.

Throughout these numerical tests, we allocate tolerances while considering the effect of design parameter variations on the maximum stress at specified areas, effectively characterizing part failure. In the two-dimensional case, we also consider the total strain energy of the design configuration, providing a notion of overall geometric stiffness. To assess the algorithm’s effectiveness, we consider the three following measures throughout our numerical results. First, we consider

$$\boldsymbol{\epsilon}_{r,p} = \hat{\boldsymbol{\tau}} - \boldsymbol{\tau}_{r,p} \quad (8.18)$$

which is the **error** between the obtained tolerance of a low-fidelity surrogate model and the **true optimal** value, which comes from either a dense sampling or a high-fidelity surrogate model. In particular, we examine $\|\boldsymbol{\epsilon}_{r,p}\|_\infty$ which, in cases where the manifold is indeed convex, we expect convergence with respect to this measure. However, this is generally not the case therefore we also consider

$$\varphi_A(\boldsymbol{\tau}_{r,p}) = \frac{|\mathcal{F}_A(\hat{\boldsymbol{\tau}}) - \mathcal{F}_A(\boldsymbol{\tau}_{r,p})|}{\mathcal{F}_A(\hat{\boldsymbol{\tau}})} \quad (8.19)$$

which is the relative error in the objective functional with respect to the **true optimal** value. If $A = 1$, this corresponds to the 1-norm, Eq. (8.8), if $A = \boldsymbol{\mu}$, this corresponds to the $\boldsymbol{\mu}$ -norm, Eq. (8.9), and if $A = -1$, this corresponds to the -1 -norm, Eq. (8.10). Since this is the objective functional, we can expect some sort of convergence with respect to this measure. However, the non-convexity in the general setting does not guarantee convergence, since local optima may exist throughout the manifold. Therefore in this case, we lastly consider the following measure

$$\gamma_A(\boldsymbol{\tau}_{r,p}) = \frac{|\mathcal{Q}_{A,\text{allow}} - \mathcal{G}_A(\boldsymbol{\tau}_{r,p})|}{\mathcal{Q}_{A,\text{allow}}} \quad (8.20)$$

that is the relative error in the constraint functional with respect to the performance constraint. If $A = SE$, this corresponds to the strain energy measure, and if $A = M$, this corresponds to the maximum stress measure, as defined in (8.22). This measure assess the convergence of the surrogate model to the the true model in the optimization routine. We do expect convergence with respect to this measure, since it is our manifold definition. Before proceeding with the presentation of numerical results, we briefly discuss the linear-elastic theory, in its parametric form, which is employed throughout the remainder of this section.

8.2.1 Application to Linear Elasticity

From the solution vector \underline{u} to (6.14), we can construct the surrogate models to the aforementioned system performances we consider throughout the numerical tests. In particular:

$$\begin{array}{cc} \text{Maximum Stress} & \text{Strain Energy} \\ \hline \mathcal{Q}_M(\boldsymbol{\mu}) = \max_{\boldsymbol{\xi} \in \mathcal{P}} \underline{\underline{\sigma}}(\mathbf{x}_\mu(\boldsymbol{\xi}); \boldsymbol{\mu}) & \mathcal{Q}_{SE}(\boldsymbol{\mu}) = \int_{\Omega_\mu} \underline{\underline{\sigma}}(\mathbf{x}_\mu; \boldsymbol{\mu}) : \underline{\underline{\varepsilon}}(\mathbf{x}_\mu; \boldsymbol{\mu}) \, d\Omega_\mu \end{array} \quad (8.21)$$

for a set $\mathcal{P} \subset \hat{\Omega}$ specified a priori. Moreover, the corresponding performance measures are given by

$$\begin{array}{ll} \text{Maximum Stress:} & \mathcal{G}_M(\boldsymbol{\tau}) = \max_{\boldsymbol{\mu} \in \mathcal{D}_{\hat{\boldsymbol{\mu}}}(\boldsymbol{\tau})} \mathcal{Q}_M(\boldsymbol{\mu}) \\ \text{Strain Energy:} & \mathcal{G}_{SE}(\boldsymbol{\tau}) = \max_{\boldsymbol{\mu} \in \mathcal{D}_{\hat{\boldsymbol{\mu}}}(\boldsymbol{\tau})} \mathcal{Q}_{SE}(\boldsymbol{\mu}) \end{array} \quad (8.22)$$

Finally, analogous to Eq. (8.3), we have in this setting the following optimization problem:

Linear Elasticity Tolerance Allocation

Given $\hat{\boldsymbol{\mu}}$, find $\hat{\boldsymbol{\tau}}$ such that

$$\hat{\boldsymbol{\tau}} = \operatorname{argmax}_{\boldsymbol{\tau} \in \mathcal{T}_{\text{allow}}} \mathcal{F}(\boldsymbol{\tau}) \quad \text{where} \quad \mathcal{T}_{\text{allow}} := \left\{ \boldsymbol{\tau} \in \mathbb{R}^{d_\mu} : \mathcal{G}_A(\boldsymbol{\tau}) \leq \mathcal{Q}_{\text{allow}} \right\} \quad (8.23)$$

where $A = M$ or SE in the case of maximum stress and strain energy, respectively.

8.2.2 Two-dimensional plate with hole

In this section we consider the plate with hole problem with loading and boundary conditions as depicted in Fig. 8.2. We consider the design parameters of horizontal and vertical translations of the hole which we denote μ_h and μ_k , respectively, which are depicted in Fig. 8.2. Moreover, we consider the effects of variations in hole placement on (i) the maximum Von-Mises stress occurring at either the top or bottom of the hole and (ii) the strain energy of the plate configuration. The nominal configuration of this problem is with the hole centered in the plate:

$$\hat{\boldsymbol{\mu}} = \begin{pmatrix} \hat{\mu}_h \\ \hat{\mu}_k \end{pmatrix} = \begin{pmatrix} 0 \\ 0 \end{pmatrix}$$

The height and width of the plate is 1.5 with a circular hole radius of 0.35. The corresponding Von-Mises stress distribution is shown in Fig. 8.2. The plate with hole is a 512-element, multi-patch isogeometric analysis model parametrized with quadratic NURBS functions. This choice of analysis model accurately represents the circular hole and additionally provides a natural parametric modeling framework for obtaining quantities of interest as a function of design variable.

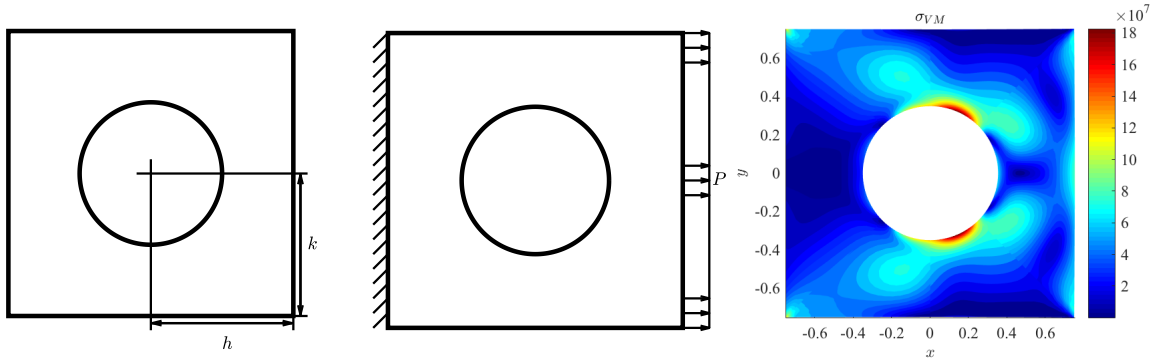


Figure 8.2: (left) Two-dimensional plate with hole geometric configuration where variations of the horizontal and vertical positions of the hole are considered. (center) The loading and boundary conditions associated with the plate with hole problem. A uniform loading of $P = 30 \text{ MPa}$ is applied to the right and the left side of the plate has zero-displacement boundary conditions. (right) Von Mises stress distribution in the plate with hole in the nominal configuration.

This problem is thoroughly investigated since, due to the low-dimensional nature of the problem, an “exact” optimal tolerance is obtainable through a dense sampling of the design space. Through this approach, we are capable of comparing the accuracy of the tolerance obtained through the aforementioned algorithms to this optimum as a function of polynomial degree and rank of the chosen surrogate.

The process begins by tolerance hyperrectangle sizing in accordance with the techniques described in Section 8.1.2. The sizing process was accomplished using the performance constraints of $Q_{M,\text{allow}} = 210 \text{ MPa}$, corresponding to approximately a 10% deviation from the nominal stress, and $Q_{SE,\text{allow}} = 760 \text{ kJ}$, which corresponds to approximately a 10% deviation from the nominal strain

energy. Since we consider two separate quantities of interest, we must size two hyperrectangles according to this methodology. In the two-dimensional case, no nonzero minimum tolerance was prescribed. Given the nominal geometric configuration of the two-dimensional plate with hole, namely a width and height of 1.5, hole radius of 0.35, and no eccentricity, this corresponds to the feasible domain defined by:

$$\boldsymbol{\tau}_{\max, \text{M}} = \begin{pmatrix} \tau_{h, \max, \text{M}} \\ \tau_{k, \max, \text{M}} \end{pmatrix} = \begin{pmatrix} 0.263\mu_H \\ 0.098\mu_L \end{pmatrix}, \quad \boldsymbol{\tau}_{\max, \text{SE}} = \begin{pmatrix} \tau_{h, \max, \text{SE}} \\ \tau_{k, \max, \text{SE}} \end{pmatrix} = \begin{pmatrix} 0.153\mu_H \\ 0.156\mu_L \end{pmatrix}$$

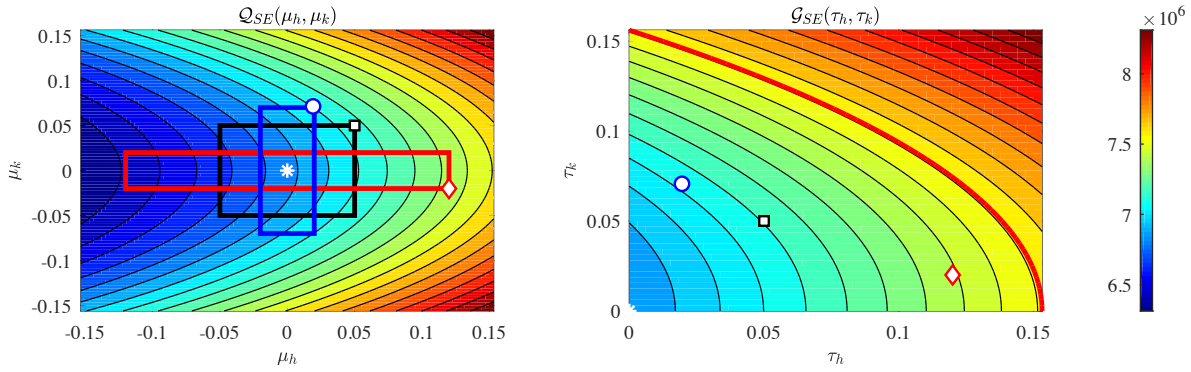
Note that these quantities are **relative** in that they are percentage deviations as a function of the nominal plate width μ_H and plate height μ_L . Moreover, both scenarios utilized the origin as the minimum allocable tolerance, i.e. $\boldsymbol{\tau}_{\min} = \mathbf{0}$.

To proceed with a demonstration of our methodology, we then construct a surrogate model to the aforementioned quantities of interest. This was accomplished by constructing separated representations of the system performances presented in Eq. (8.21). Determining the appropriate polynomial degree and rank amounts to performing a survey of these parameters and selecting the model which suits the desired fidelity. A set of $N = 100$ Monte-Carlo samples were used in the construction of these surrogate models and their relative accuracy is computed using an additional $N_c = 500$ samples not used in the model construction. Table 8.1 portrays this survey and moreover exhibit the convergence of the separated representations with respect to the polynomial degree and rank of the expansion. Due to the least-squares nature of the separated representations, we only expect convergence in an L^2 -sense. However, the smoothness associated with these response surfaces additionally provides convergence in Eq. (8.16) and Eq. (8.17).

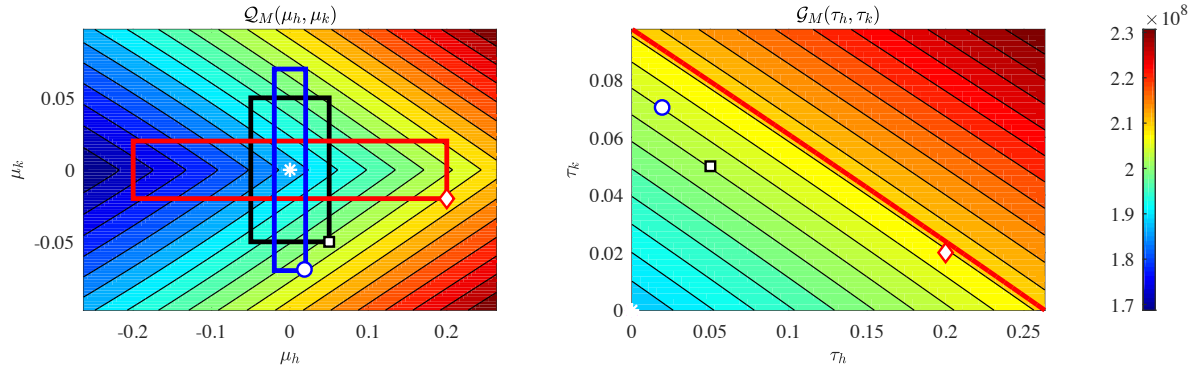
With the construction of the surrogate models to Eq. (8.21), we are capable of employing our tolerance allocation algorithm. For this two-dimensional problem, a dense sampling was used to obtain an exact optimum tolerance and the following results reflect this choice. Fig. 8.3 depicts the response surfaces from the surrogate for the system performances of strain energy and the maximum stress between the top and bottom of the hole as well as their corresponding performance measures restricted to the preconditioned tolerance hyperrectangle. Additionally, there are three

Table 8.2: Tolerance values obtained using a dense sampling of the tolerance hyperrectangle. These values are treated as the “exact” optima and are used in our subsequent results. Bold numbers indicate values lying on the boundary of the hyperrectangle.

	Strain Energy			Maximum Stress		
	$\mathcal{F}_1(\boldsymbol{\tau})$	$\mathcal{F}_\mu(\boldsymbol{\tau})$	$\mathcal{F}_{-1}(\boldsymbol{\tau})$	$\mathcal{F}_1(\boldsymbol{\tau})$	$\mathcal{F}_\mu(\boldsymbol{\tau})$	$\mathcal{F}_{-1}(\boldsymbol{\tau})$
$\hat{\tau}_h$	0.114	0.153	0.100	0.263	0.263	0.100
$\hat{\tau}_k$	0.081	0.000	0.093	0.061	0.000	0.061



(a) (left) A contour plot of the strain energy and (right) the performance measure $\mathcal{G}_{SE}(\tau_h, \tau_k)$.



(b) (left) A contour plot of the maximum stress and (right) the performance measure $\mathcal{G}_M(\tau_h, \tau_k)$.

Figure 8.3: The white asterisk at $\mu_h = 0$ and $\mu_k = 0$ denotes the nominal configuration of the two-dimensional plate with hole problem. The three colored rectangles depict three different tolerance hyperrectangles, $\boldsymbol{\tau}^{(i)}$, with hollow markers indicate the location where the maximum of the restricted system performance $\mathcal{Q}(\mu_h, \mu_k)|_{\mathcal{D}_{\hat{\mu}}(\boldsymbol{\tau}^{(i)})}$ is attained. The red contour line denotes the loci of $\boldsymbol{\tau}$, that is the immersed manifold, such that $\mathcal{G}(\tau_h, \tau_k) = \mathcal{Q}_{\text{allow}}$. Refer to the online article for the colorized figure.

degree and rank of the surrogate model. As is clearly demonstrated, the accuracy of the obtained tolerance behaves similar to the accuracy in the surrogate model construction. Note that the

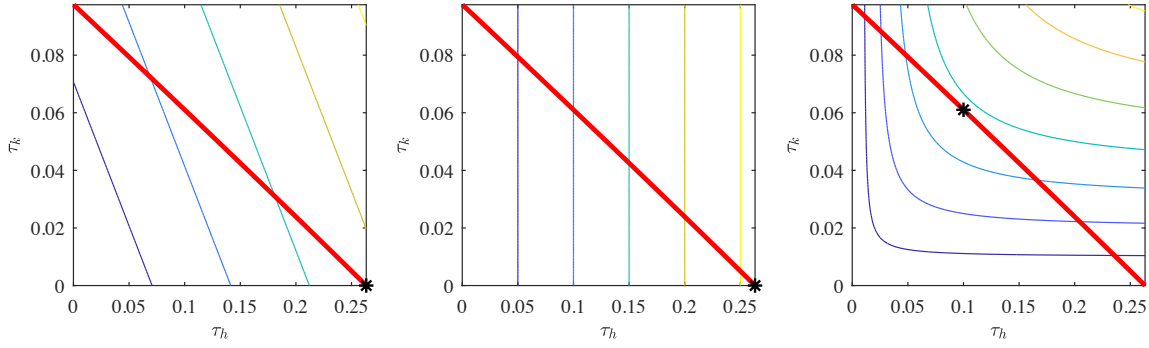


Figure 8.4: The one-dimensional manifold corresponding to the level set of $\mathcal{G}(\boldsymbol{\tau}) = \mathcal{Q}_{\text{allow,SE}}$ for strain energy with (left) the tolerance measure $\mathcal{F}_1(\boldsymbol{\tau})$, (center) the tolerance measure $\mathcal{F}_\mu(\boldsymbol{\tau})$, and (right) the tolerance measure $\mathcal{F}_{-1}(\boldsymbol{\tau})$. The black asterisk denotes the location of $\hat{\boldsymbol{\tau}}$ with respect to this norm.

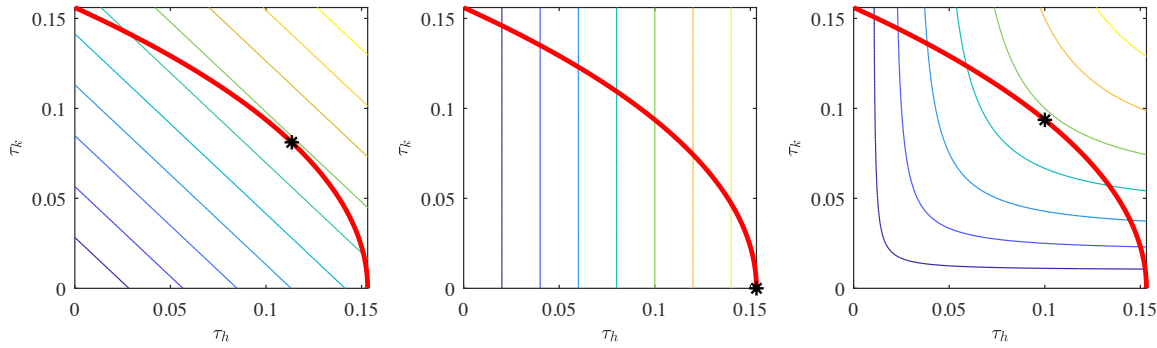


Figure 8.5: The one-dimensional manifold corresponding to the level set of $\mathcal{G}(\boldsymbol{\tau}) = \mathcal{Q}_{\text{allow,M}}$ for maximum stress with (left) the tolerance measure $\mathcal{F}_1(\boldsymbol{\tau})$, (center) the tolerance measure $\mathcal{F}_\mu(\boldsymbol{\tau})$, and (right) the tolerance measure $\mathcal{F}_{-1}(\boldsymbol{\tau})$. The black asterisk denotes the location of $\hat{\boldsymbol{\tau}}$ with respect to this norm.

optimal tolerances for maximum stress in both the 1-norm and the derivative-weighted norm are identical and reside on the tolerance hyperrectangle boundary. On the other hand, the -1 -norm has an isotropized tolerance which is almost centered in the tolerance hyperrectangle. In these tables, the error in the obtained tolerance is presented in the maximum norm, the cost of the optimal tolerance, and the cost of the obtained tolerance. However, this is not the only important factor to be considered in this analysis, the accuracy of the surrogate model, i.e. the manifold approximation, is crucial for robustness since this is how the algorithm distinguishes the true optimal tolerance from others present in the implicitly defined manifold. The columns n_{GA} and n_{CG} are the number

of iterations until the increase in allocated tolerance size is within 10^{-6} or until the algorithm detects the wall intersection for all dimensions of the manifold.

Table 8.3: Errors and convergence behavior of the tolerance allocation algorithm for the 1-norm.

r	p	n_{GA}	n_{CG}	$\ \epsilon_{r,p}\ _\infty$	$\varphi_1(\tau_{r,p})$	$\gamma_{SE}(\tau_{r,p})$	n_{GA}	n_{CG}	$\ \epsilon_{r,p}\ _\infty$	$\varphi_1(\tau_{r,p})$	$\gamma_M(\tau_{r,p})$
0		-	-	-	-	-	-	-	-	-	-
1	1	2	2	7.462e-2	2.459e-1	6.568e-2	3	3	6.479e-4	2.455e-3	6.728e-4
	2	3	3	2.311e-3	1.108e-3	1.664e-4	3	3	4.102e-3	1.583e-2	1.626e-3
	3	3	3	1.657e-3	1.324e-3	1.836e-4	4	4	3.156e-14	1.199e-13	5.677e-16
2	1	2	2	7.462e-2	2.375e-1	6.371e-2	3	3	5.437e-4	2.061e-3	5.646e-4
	2	3	3	8.492e-4	3.030e-4	3.764e-5	3	3	2.695e-3	1.034e-2	1.068e-3
	3	3	3	1.130e-4	5.113e-5	5.322e-6	3	3	2.477e-4	9.417e-4	9.812e-5
	4	3	3	9.023e-5	7.823e-6	2.463e-6	3	3	3.156e-14	1.199e-13	5.677e-16
3	2	3	3	8.271e-4	3.090e-4	3.862e-5	3	3	2.568e-3	9.850e-3	1.017e-3
	3	3	3	1.212e-4	3.745e-5	3.520e-6	3	3	3.156e-14	1.199e-13	5.677e-16
	4	3	3	7.976e-5	9.094e-6	2.631e-6	3	3	3.156e-14	1.199e-13	5.677e-16
	5	3	3	7.949e-5	1.056e-5	3.720e-8	3	3	3.156e-14	1.199e-13	5.677e-16
4	3	3	3	1.242e-4	2.410e-5	1.759e-6	3	3	1.274e-4	4.840e-4	5.045e-5
	4	3	3	8.051e-5	1.060e-5	2.830e-6	3	3	3.156e-14	1.199e-13	5.677e-16
	5	3	3	7.938e-5	1.024e-5	7.970e-8	3	3	3.156e-14	1.199e-13	5.677e-16
	6	3	3	7.845e-5	1.092e-5	1.019e-8	3	3	3.156e-14	1.199e-13	5.677e-16

Table 8.4: Errors and convergence behavior of the tolerance allocation algorithm for the μ -norm.

r	p	n_{GA}	n_{CG}	$\ \epsilon_{r,p}\ _\infty$	$\varphi_\mu(\tau_{r,p})$	$\gamma_{SE}(\tau_{r,p})$	n_{GA}	n_{CG}	$\ \epsilon_{r,p}\ _\infty$	$\varphi_\mu(\tau_{r,p})$	$\gamma_M(\tau_{r,p})$
0		-	-	-	-	-	-	-	-	-	-
1	1	3	3	4.963e-2	4.792e-1	3.397e-2	3	3	6.479e-4	2.391e-3	6.728e-4
	2	8	8	1.769e-2	2.307e-5	1.329e-3	3	3	4.102e-3	1.583e-2	1.626e-3
	3	9	9	1.558e-2	3.295e-5	1.030e-3	4	4	3.156e-14	1.156e-13	5.677e-16
2	1	3	3	4.984e-2	4.822e-1	3.410e-2	3	3	5.437e-4	2.013e-3	5.646e-4
	2	9	9	1.097e-2	2.323e-5	5.111e-4	3	3	2.695e-3	1.034e-2	1.068e-3
	3	12	12	2.481e-3	3.165e-7	2.618e-5	3	3	2.477e-4	9.417e-4	9.812e-5
	4	13	13	1.581e-3	1.003e-7	1.065e-5	3	3	3.156e-14	1.161e-13	5.677e-16
3	2	9	9	1.095e-2	1.087e-5	5.087e-4	3	3	2.568e-3	9.850e-3	1.017e-3
	3	12	12	2.615e-3	9.234e-7	2.908e-5	3	3	3.156e-14	1.163e-13	5.677e-16
	4	13	13	1.324e-3	6.480e-8	7.474e-6	3	3	3.156e-14	1.162e-13	5.677e-16
	5	14	14	5.283e-4	1.636e-9	1.199e-6	3	3	3.156e-14	1.161e-13	5.677e-16
4	3	12	12	2.575e-3	2.547e-6	2.821e-5	3	3	1.274e-4	4.840e-4	5.045e-5
	4	13	13	1.308e-3	5.513e-8	7.290e-6	3	3	3.156e-14	1.162e-13	5.677e-16
	5	14	14	5.263e-4	1.060e-9	1.190e-6	3	3	3.156e-14	1.161e-13	5.677e-16
	6	14	14	3.716e-4	3.150e-9	5.961e-7	3	3	3.156e-14	1.161e-13	5.677e-16

Table 8.5: Errors and convergence behavior of the tolerance allocation algorithm for the -1 -norm.

r	p	n_{GA}	n_{CG}	$\ \epsilon_{r,p}\ _\infty$	$\varphi_{-1}(\tau_{r,p})$	$\gamma_{SE}(\tau_{r,p})$	n_{GA}	n_{CG}	$\ \epsilon_{r,p}\ _\infty$	$\varphi_{-1}(\tau_{r,p})$	$\gamma_M(\tau_{r,p})$
0	-	-	-	-	-	-	-	-	-	-	-
1	1	2	2	2.908e-2	1.303e-1	2.322e-2	3	3	2.322e-3	1.081e-2	1.126e-3
	2	4	4	9.884e-4	6.032e-3	8.173e-4	3	3	5.294e-4	2.545e-3	2.517e-4
	3	4	4	2.881e-4	1.545e-3	2.032e-4	3	3	1.098e-3	6.728e-3	7.024e-4
2	1	2	2	2.483e-2	1.176e-1	2.024e-2	3	3	8.215e-4	6.452e-4	1.035e-4
	2	4	4	1.062e-3	3.874e-3	5.193e-4	3	3	9.725e-4	5.157e-3	5.882e-4
	3	4	4	2.810e-4	2.710e-4	2.648e-5	3	3	3.815e-4	1.530e-4	3.920e-5
	4	4	4	1.975e-5	6.544e-5	2.025e-5	3	3	3.138e-4	3.604e-5	2.646e-5
3	2	4	4	1.140e-3	4.623e-3	6.235e-4	3	3	9.528e-4	5.186e-3	5.915e-4
	3	4	4	5.129e-4	3.360e-4	3.547e-5	3	3	3.730e-4	1.583e-4	3.978e-5
	4	4	4	1.320e-4	6.357e-4	7.673e-5	3	3	3.035e-4	4.272e-5	2.720e-5
	5	4	4	3.208e-5	1.927e-4	1.562e-5	3	3	3.053e-4	1.355e-5	2.401e-5
4	3	4	4	2.054e-4	6.705e-4	8.161e-5	3	3	3.764e-4	1.722e-4	4.130e-5
	4	4	4	2.382e-4	6.842e-4	8.332e-5	3	3	3.036e-4	4.447e-5	2.739e-5
	5	4	4	2.434e-5	2.293e-4	2.068e-5	3	3	3.055e-4	1.451e-5	2.411e-5
	6	4	4	8.573e-6	8.146e-5	1.700e-7	3	3	3.037e-4	7.077e-6	2.331e-5

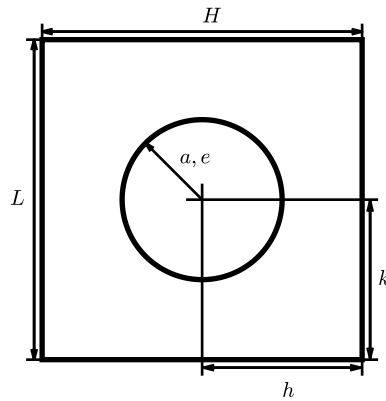


Figure 8.6: Six-dimensional plate with hole geometric configuration where variations of the horizontal and vertical positions of the hole, plate height and width, and hole radius and eccentricity are considered.

8.2.3 Six-dimensional plate with hole

In this section, we consider an identical plate with hole problem as the previous section shown in Fig. 8.2 however we include 4 additional design parameters. These include plate width, height, hole radius, hole eccentricity, and the previously-presented horizontal and vertical hole offsets. The nominal configuration of the six-dimensional plate with hole problem is

$$\begin{array}{c|cccccc}
& \hat{\mu}_H & \hat{\mu}_L & \hat{\mu}_h & \hat{\mu}_k & \hat{\mu}_a & \hat{\mu}_e \\
\hline
\text{nom.} & 1.5 & 1.5 & 0 & 0 & 0.35 & 0
\end{array} \tag{8.24}$$

Moreover, using the same performance constraint of $\mathcal{Q}_{M,\text{allow}} = 210\text{MPa}$ corresponds to an approximate allowable deviation of 10% in the maximum stress. Univariate root-finding with this performance constraint constructs the feasible domain for the six-dimensional plate with hole. Therefore, the feasible domain is given by:

$$\begin{array}{c|cccccc}
& \hat{\tau}_H & \hat{\tau}_L & \hat{\tau}_h & \hat{\tau}_k & \hat{\tau}_a & \hat{\tau}_e \\
\hline
\text{min} & 0.25 & 0.231 & 0.263\mu_H & 0.098\mu_L & 0.034 & 0.3 \\
\text{max} & 0.025 & 0.023 & 0.026\mu_H & 0.010\mu_L & 0.003 & 0.03
\end{array} \tag{8.25}$$

Note that similar to the two-dimensional case, τ_h and τ_k are **relative** tolerances, namely percentage deviations from the center. However, in contrast to the two-dimensional case, the parameters used in its definition are themselves design parameters, particularly, μ_H and μ_L .

From here, we are capable of constructing the surrogate model via separated representations over a set of Monte-Carlo samples. For the six-dimensional plate with hole problem, we used 1500 samples and once again performed a survey over various polynomial degrees and ranks until a desired surrogate model fidelity was obtained. The results of this survey are shown in Table 8.6 where the surrogate models' accuracies are determined by comparison to an additional set of 500 samples not used in the construction of the surrogate model. As expected, the higher-dimensionality of this problem necessitates the use of larger polynomial degrees and separation rank for comparable accuracy to the two-dimensional setting. Regardless, as depicted in the results, the methodology is still capable of representing the true response surface with excellent precision in a relatively few number of samples as well as low polynomial degrees and rank.

To assess the algorithm's convergence behavior, we construct a high-fidelity SR from 1500 samples of rank 20 and degree 4 to approximate $\hat{\tau}$. This SR gives $\|\mathbf{e}\|_M = 4.837e - 5$ and $\|\mathbf{e}\|_\infty = 3.649e - 4$. The high-fidelity approximations to the optimal tolerances, which are treated as the

Table 8.6: The maximum stress surrogate modeling errors for the six-dimensional plate with hole problem constructed from $N = 1500$ samples and $N_c = 500$.

p	$r = 1$	$r = 2$	$r = 3$	$r = 4$	$r = 5$	$r = 6$
$\ \mathbf{e}_{r,p}\ _\infty$	4.918e-1					
0	4.918e-1					
1	1.503e-1	8.576e-2				
2	1.370e-1	3.982e-2	2.069e-2			
3	1.420e-1	3.664e-2	1.853e-2	8.061e-3		
4		3.774e-2	1.886e-2	1.234e-2	1.023e-2	
5			1.907e-2	1.303e-2	1.129e-2	4.686e-3
6				1.374e-2	1.012e-2	5.192e-3
7					1.055e-2	4.804e-3
8						3.908e-3
$\ \mathbf{e}_{r,p}\ _M$	1.047e-1					
0	1.047e-1					
1	2.788e-2	1.832e-2				
2	2.159e-2	7.559e-3	3.355e-3			
3	2.169e-2	7.563e-3	3.243e-3	1.416e-3		
4		7.661e-3	3.278e-3	2.000e-3	1.127e-3	
5			3.297e-3	2.033e-3	1.114e-3	5.916e-4
6				2.066e-3	1.167e-3	6.155e-4
7					1.221e-3	6.481e-4
8						6.330e-4

“exact” optimal over the various $\mathcal{G}(\boldsymbol{\tau})$ and $\mathcal{F}(\boldsymbol{\tau})$ are presented in Table 8.7.

Tables 8.8, 8.9, and 8.10 depict the effectiveness of our algorithm with respect to polynomial degree and rank of the surrogate model. In these tables, the error in the obtained tolerance is presented in the maximum norm, the cost of the optimal tolerance, and the cost of the obtained tolerance. However, this is not the only important factor to be considered in this analysis, the accuracy of the surrogate model, i.e. the manifold approximation, is crucial for robustness since this is how the algorithm distinguishes the true optimal tolerance from others present in the implicitly defined manifold. The columns n_{GA} and n_{CG} are the number of iterations until the increase in allocated tolerance size is within 10^{-6} or until the algorithm detects the wall intersection for all dimensions of the manifold.

8.2.4 17-dimensional L-Bracket

For the L-Bracket, we use a performance constraint of $\mathcal{Q}_{M,\text{allow}} = 260$ MPa which corresponds to an approximate allowable deviation of 10% in the maximum stress located at the top of the fillet.

Table 8.7: Tolerance values obtained using a rank 20, degree 4 SR constructed from 7500 samples of the maximum stress between the top and bottom of the plate with hole. These values are treated as the “exact” optima and are used in our subsequent results. Bold numbers indicate values lying on the boundary of the hyperrectangle.

	$\mathcal{F}_1(\boldsymbol{\tau})$	$\mathcal{F}_\mu(\boldsymbol{\tau})$	$\mathcal{F}_{-1}(\boldsymbol{\tau})$
$\hat{\tau}_H$	0.073	0.050	0.044
$\hat{\tau}_L$	0.058	0.080	0.032
$\hat{\tau}_h$	0.088	0.080	0.035
$\hat{\tau}_k$	0.010	0.010	0.023
$\hat{\tau}_a$	0.003	0.003	0.013
$\hat{\tau}_e$	0.117	0.030	0.136

Table 8.8: Errors and convergence behavior of the tolerance allocation algorithm for the 1-norm.

r	p	n_{GA}	n_{CG}	$\ \boldsymbol{\epsilon}_{r,p}\ _\infty$	$\varphi_1(\boldsymbol{\tau}_{r,p})$	$\gamma_M(\boldsymbol{\tau}_{r,p})$
	0	-	-	-	-	-
1	1	69	53	1.857e-2	1.720e-1	9.439e-3
	2	78	25	3.088e-2	8.062e-2	9.840e-3
	3	79	27	2.665e-2	8.111e-2	9.882e-3
	1	73	54	1.306e-2	1.229e-1	3.746e-3
2	2	82	23	3.304e-2	4.604e-2	5.922e-3
	3	83	23	2.974e-2	3.583e-2	4.703e-3
	4	81	24	3.916e-2	4.985e-2	6.306e-3
	2	83	59	3.903e-3	3.281e-2	3.925e-3
3	3	85	60	2.977e-3	1.807e-2	2.328e-3
	4	85	60	3.103e-3	1.991e-2	2.525e-3
	5	85	60	3.098e-3	2.132e-2	2.673e-3
	3	86	61	3.049e-3	1.094e-2	1.302e-3
4	4	86	61	3.391e-3	8.553e-3	1.068e-3
	5	88	60	4.338e-3	5.455e-3	7.665e-4
	6	87	61	4.291e-3	2.801e-3	4.764e-4
	4	88	62	3.809e-3	2.394e-3	3.132e-4
5	5	88	62	3.814e-3	3.252e-3	4.292e-4
	6	87	62	3.738e-3	3.911e-3	5.049e-4
	7	88	62	3.703e-3	2.895e-3	3.555e-4
	5	88	62	4.089e-3	2.716e-4	2.573e-5
6	6	88	62	4.162e-3	6.215e-4	6.912e-7
	7	88	62	4.146e-3	9.188e-4	4.253e-5
	8	88	62	3.931e-3	1.062e-3	1.677e-4

The loading and boundary conditions associated with this problem are shown in Fig. 8.2. Univariate root-finding with this performance constraint constructs the feasible domain. In this example, we consider 17 design parameters which together completely describe an L-Bracket geometry, as depicted in Fig. 8.7. The analysis model is comprised of 28 NURBS patches for a total of 1792

Table 8.9: Errors and convergence behavior of the tolerance allocation algorithm for the μ -norm.

r	p	n_{GA}	n_{CG}	$\ \epsilon_{r,p}\ _\infty$	$\varphi_\mu(\tau_{r,p})$	$\gamma_M(\tau_{r,p})$
0		-	-	-	-	-
1	1	>100	82	2.698e-1	1.774e-1	4.194e-2
	2	>100	>100	2.616e-1	9.630e-2	1.277e-2
	3	>100	98	2.598e-1	1.172e-1	1.331e-2
2	1	33	22	1.398e-2	1.417e-1	1.570e-2
	2	29	21	6.005e-3	5.504e-2	5.043e-3
	3	29	22	4.661e-3	4.389e-2	4.004e-3
	4	30	21	5.764e-3	5.902e-2	5.672e-3
3	2	29	19	3.986e-3	3.291e-2	3.143e-3
	3	29	19	2.288e-3	1.525e-2	1.518e-3
	4	29	19	2.794e-3	1.694e-2	1.627e-3
	5	29	20	2.534e-3	2.018e-2	1.982e-3
4	3	28	19	1.781e-3	9.068e-3	8.758e-4
	4	29	19	9.338e-4	6.433e-3	6.957e-4
	5	28	20	1.087e-3	2.824e-3	3.928e-4
	6	28	19	7.918e-4	3.853e-4	1.429e-4
5	4	28	20	7.466e-4	3.510e-3	2.860e-4
	5	29	20	6.914e-4	4.599e-3	4.073e-4
	6	29	19	4.488e-4	4.502e-3	4.077e-4
	7	29	21	1.052e-3	4.078e-3	3.331e-4
6	5	28	20	7.449e-4	2.902e-4	4.453e-5
	6	28	20	7.188e-4	3.603e-4	7.333e-5
	7	28	22	8.143e-4	2.831e-4	1.011e-4
	8	29	17	2.477e-2	2.276e-3	9.222e-5

elements. The nominal configuration is given by:

	$\hat{\mu}_M$	$\hat{\mu}_N$	$\hat{\mu}_{L_1}$	$\hat{\mu}_{H_3}$	$\hat{\mu}_{R_f}$	$\hat{\mu}_{a_1}$	$\hat{\mu}_{e_1}$	$\hat{\mu}_{h_1}$	$\hat{\mu}_{k_1}$	$\hat{\mu}_{a_2}$	$\hat{\mu}_{e_2}$	$\hat{\mu}_{h_2}$	$\hat{\mu}_{k_2}$	$\hat{\mu}_{a_3}$	$\hat{\mu}_{e_3}$	$\hat{\mu}_{h_3}$	$\hat{\mu}_{k_3}$
nom.	6	3.5	1.25	1.25	.2	.25	0	0	0	.25	0	0	0	.25	0	0	0

(8.26)

and through this parametrization, the feasible domain is given by:

	$\hat{\tau}_M$	$\hat{\tau}_N$	$\hat{\tau}_{L_1}$	$\hat{\tau}_{H_3}$	$\hat{\tau}_{R_f}$	$\hat{\tau}_{a_1}$	$\hat{\tau}_{e_1}$	$\hat{\tau}_{h_1}^*$	$\hat{\tau}_{k_1}^*$	$\hat{\tau}_{a_2}$	$\hat{\tau}_{e_2}$	$\hat{\tau}_{h_2}^*$	$\hat{\tau}_{k_2}^*$	$\hat{\tau}_{a_3}$	$\hat{\tau}_{e_3}$	$\hat{\tau}_{h_3}^*$	$\hat{\tau}_{k_3}^*$
min	.5	.21	.25	.07	.04	.1	.3	.6	.6	.04	.3	.57	.47	.03	.3	.6	.6
max	.05	.021	.025	.007	.004	.01	.03	.06	.06	.004	.03	.057	.047	.003	.03	.06	.06

(8.27)

Note that, similar to the cases of the two-dimensional and six-dimensional plate with hole problems, the hole offsets are parametrized as **relative** quantities. For example, $\hat{\tau}_{h_1, \max} = 0.6$ corresponds to a **maximum allowable horizontal hole deviation of 60% of the parameter μ_{L_1}** . All quantities in this feasible region with a * denote relative quantities. However, as the

Table 8.10: Errors and convergence behavior of the tolerance allocation algorithm for the -1 -norm.

r	p	n_{GA}	n_{CG}	$\ \epsilon_{r,p}\ _\infty$	$\varphi_{-1}(\tau_{r,p})$	$\gamma_M(\tau_{r,p})$
0		-	-	-	-	-
1	1	>100	>100	1.697e-2	1.514e-1	3.500e-3
	2	>100	>100	7.262e-2	6.173e-2	6.260e-3
	3	>100	>100	8.475e-3	4.499e-2	5.440e-3
2	1	>100	>100	1.453e-2	1.373e-1	1.846e-3
	2	>100	>100	1.213e-2	5.940e-2	7.157e-3
	3	>100	>100	1.233e-2	5.273e-2	6.224e-3
	4	>100	>100	1.035e-2	5.445e-2	6.523e-3
3	2	>100	>100	3.080e-3	3.624e-2	4.342e-3
	3	>100	>100	5.614e-2	4.055e-2	3.727e-3
	4	>100	>100	1.897e-3	3.227e-2	3.891e-3
	5	>100	>100	5.219e-3	3.483e-2	4.085e-3
4	3	>100	>100	1.254e-3	1.243e-2	1.440e-3
	4	>100	>100	2.028e-3	1.368e-2	1.567e-3
	5	>100	>100	2.091e-2	1.607e-2	1.358e-3
	6	>100	>100	2.477e-2	1.711e-2	1.398e-3
5	4	>100	>100	2.366e-4	6.225e-3	7.327e-4
	5	>100	>100	5.134e-4	7.612e-3	8.839e-4
	6	>100	>100	4.924e-4	8.294e-3	9.653e-4
	7	>100	>100	2.142e-4	6.807e-3	7.946e-4
6	5	>100	>100	4.009e-3	3.799e-3	3.356e-4
	6	>100	>100	4.160e-3	4.955e-3	4.670e-4
	7	>100	>100	1.620e-3	4.479e-3	4.777e-4
	8	>100	>100	2.569e-4	4.664e-3	5.443e-4

design complexity grows, as well as the interaction between the design parameters, the expression for these quantities are not as elegant which is why they are omitted.

To assess the algorithm's convergence behavior, we construct a high-fidelity SR from 13500 samples of rank 20 and degree 4 to approximate $\hat{\tau}$. This SR gives $\|\mathbf{e}\|_M = 1.926e - 4$ and $\|\mathbf{e}\|_\infty = 1.120e - 3$. The high-fidelity approximations to the optimal tolerances over the considered $\mathcal{G}(\tau)$ and $\mathcal{F}(\tau)$ are presented in Table 8.12.

Table 8.11: The maximum stress surrogate modeling errors for the six-dimensional plate with hole problem constructed from $N = 13500$ samples and $N_c = 500$.

	p	$r = 9$	$r = 10$	$r = 11$	$r = 12$	$r = 13$	$r = 14$	$r = 15$	$r = 16$
$\ \mathbf{e}_{r,p}\ _\infty$	1	1.529e-1				1.093e-1			
	2	7.284e-3	4.351e-3			4.882e-3	6.154e-3		
	3		3.877e-3	3.611e-3			3.028e-3	2.314e-3	
	4			3.445e-3	3.561e-3			3.797e-3	3.721e-3
	5				3.630e-3				2.662e-3
$\ \mathbf{e}_{r,p}\ _M$	1	1.309e-2				1.320e-2			
	2	1.056e-3	9.822e-4			9.246e-4	9.397e-4		
	3		5.101e-4	4.677e-4			3.162e-4	2.827e-4	
	4			4.697e-4	4.030e-4			3.427e-4	3.305e-4
	5				4.072e-4				2.720e-4

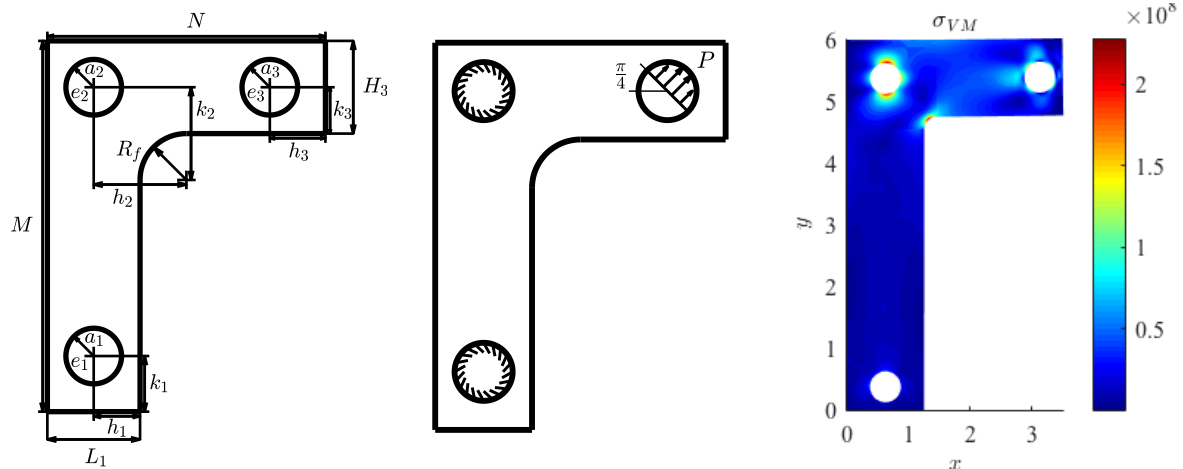


Figure 8.7: (left) The 17-dimensional L-Bracket configuration where the various design parameters are shown. (center) The loading and boundary conditions associated with the L-Bracket problem. A uniform bearing pressure of $P = 30$ MPa is applied to the top-right hole while the other two holes have zero-displacement boundary conditions. (right) Von Mises stress distribution in the L-Bracket in the nominal configuration.

Table 8.12: Tolerance values obtained using a rank 20, degree 4 SR constructed from 7500 samples. These values are treated as the “exact” optima and are used in our subsequent results. Bold numbers indicate values lying on the boundary of the hyperrectangle.

	$\mathcal{F}_1(\tau)$	$\mathcal{F}_\mu(\tau)$	$\mathcal{F}_{-1}(\tau)$
$\hat{\tau}_M$	0.348	0.056	0.050
$\hat{\tau}_N$	0.021	0.021	0.022
$\hat{\tau}_{L_1}$	0.025	0.036	0.028
$\hat{\tau}_{H_3}$	0.007	0.007	0.008
$\hat{\tau}_{R_f}$	0.004	0.004	0.006
$\hat{\tau}_{a_1}$	0.100	0.010	0.012
$\hat{\tau}_{e_1}$	0.030	0.030	0.033
$\hat{\tau}_{h_1}$	0.600	0.060	0.067
$\hat{\tau}_{k_1}$	0.600	0.060	0.067
$\hat{\tau}_{a_2}$	0.004	0.004	0.006
$\hat{\tau}_{e_2}$	0.071	0.030	0.034
$\hat{\tau}_{h_2}$	0.057	0.167	0.063
$\hat{\tau}_{k_2}$	0.047	0.047	0.053
$\hat{\tau}_{a_3}$	0.003	0.003	0.005
$\hat{\tau}_{e_3}$	0.300	0.030	0.034
$\hat{\tau}_{h_3}$	0.060	0.090	0.060
$\hat{\tau}_{k_3}$	0.594	0.060	0.068

Table 8.13: Errors and convergence behavior of the tolerance allocation algorithm for the 1-norm.

r	p	n_{GA}	n_{CG}	$\ \epsilon_{r,p}\ _\infty$	$\varphi_1(\tau_{r,p})$	$\gamma_M(\tau_{r,p})$
9	1	66	62	4.931e-1	2.690e-2	3.334e-3
	2	>100	>100	2.700e-1	4.591e-2	1.468e-4
10	2	>100	>100	2.700e-1	5.045e-2	2.244e-4
	3	>100	74	5.340e-1	1.094e-3	2.271e-4
11	3	>100	>100	5.340e-1	1.381e-1	2.021e-4
	4	>100	76	3.228e-1	1.112e-1	6.753e-5
12	4	>100	>100	2.043e-1	6.775e-2	1.370e-4
	5	>100	69	2.700e-1	3.035e-2	1.029e-4
13	1	66	61	4.978e-1	2.670e-2	3.277e-3
	2	>100	42	2.953e-1	6.408e-2	2.531e-5
14	2	>100	>100	3.279e-1	4.571e-2	9.149e-5
	3	>100	>100	2.700e-1	8.513e-2	6.960e-5
15	3	>100	31	4.318e-1	1.013e-1	1.043e-4
	4	>100	38	3.754e-1	7.107e-2	1.457e-4
16	4	>100	93	2.983e-1	3.304e-2	1.165e-4
	5	70	24	4.972e-1	9.811e-3	2.646e-4

Table 8.14: Errors and convergence behavior of the tolerance allocation algorithm for the μ -norm.

r	p	n_{GA}	n_{CG}	$\ \epsilon_{r,p}\ _\infty$	$\varphi_\mu(\tau_{r,p})$	$\gamma_M(\tau_{r,p})$
9	1	49	11	4.695e-2	1.091e-1	2.984e-3
	2	>100	7	1.317e-1	1.459e-2	1.575e-4
10	2	82	6	3.026e-2	9.584e-3	1.877e-4
	3	54	7	3.799e-2	5.495e-4	1.985e-4
11	3	62	7	4.082e-2	1.681e-2	1.966e-4
	4	56	7	3.876e-2	6.594e-3	4.562e-5
12	4	82	7	3.026e-2	1.394e-2	1.175e-4
	5	>100	7	4.103e-2	1.195e-2	1.910e-4
13	1	49	11	4.705e-2	1.084e-1	2.929e-3
	2	79	7	3.026e-2	1.457e-2	1.391e-5
14	2	57	8	3.372e-2	4.805e-3	6.746e-5
	3	75	8	3.430e-2	3.823e-2	5.397e-5
15	3	>100	7	1.144e-2	3.984e-3	3.428e-5
	4	81	7	3.026e-2	9.893e-3	1.133e-4
16	4	62	7	7.662e-2	2.871e-3	7.815e-5
	5	>100	7	1.716e-2	3.503e-3	2.313e-4

Table 8.15: Errors and convergence behavior of the tolerance allocation algorithm for the -1 -norm.

r	p	n_{GA}	n_{CG}	$\ \epsilon_{r,p}\ _\infty$	$\varphi_{-1}(\tau_{r,p})$	$\gamma_M(\tau_{r,p})$
9	1	>100	>100	1.178e-2	1.214e-1	3.728e-3
	2	65	13	8.653e-3	4.721e-3	1.048e-4
10	2	>100	10	6.578e-3	2.737e-3	1.458e-4
	3	>100	13	3.514e-2	5.525e-3	1.675e-4
11	3	>100	4	8.075e-3	1.819e-3	1.534e-4
	4	43	9	8.075e-3	1.816e-3	3.380e-6
12	4	>100	8	8.075e-3	5.857e-3	6.364e-5
	5	>100	6	2.047e-2	3.132e-4	8.808e-5
13	1	>100	>100	1.264e-2	1.207e-1	3.672e-3
	2	>100	7	2.000e-2	7.108e-4	7.152e-5
14	2	25	16	7.454e-3	4.759e-3	5.788e-6
	3	32	7	5.623e-3	1.305e-3	9.865e-6
15	3	21	12	7.815e-3	3.915e-3	1.101e-5
	4	>100	8	3.190e-2	1.298e-3	4.391e-5
16	4	>100	4	1.532e-2	2.906e-3	4.544e-6
	5	40	7	5.924e-3	2.901e-4	1.157e-4

Chapter 9

Multigrid Methods

The purpose of this chapter is to present a scalable and robust methodology for obtaining the numerical solution to the PDEs presented in this dissertation. As mesh resolution increases, so does computational complexity necessitating the solver technologies capable of outperforming direct solvers for large systems. For this purpose, we resort to geometric multigrid methods whose computational complexity scales as $\mathcal{O}(N \log N)$ where N is the number of degrees of freedom in the discrete system, in contrast to $\mathcal{O}(N^3)$ for direct solvers. The mathematical exposition of geometric multigrid methods in this section is rather brief, since much of it is well-known. The primary focus is on the extension of the concepts of prolongation and restriction operators to the isogeometric setting, since this is the relevant contribution. For reference, the reader is referred to [19] in regards to the analysis and implementation of standard multigrid methods.

9.1 Fundamentals of Isogeometric Multigrid Methods

We begin by reviewing the basics of geometric multigrid methods. We limit our discussion to the V-cycle algorithm, though our approach can also be applied within a W-cycle or Full Multigrid framework [19].

Assume that we have a sequence of nested isogeometric meshes that have been obtained through knot insertion, a technique discussed in detail in the next subsection. We denote the discrete displacement spaces associated with this sequence as $\{\mathbf{V}_\ell\}_{\ell=0}^{n_\ell}$ where n_ℓ is the number of

levels, and we note that:

$$\mathbf{V}_0 \subset \mathbf{V}_1 \subset \dots \subset \mathbf{V}_{n_\ell} \quad (9.1)$$

Level $\ell = 0$ corresponds to the coarsest mesh while level $\ell = n_\ell$ corresponds to the finest mesh. The action of knot insertion not only allows for NURBS refinement, but it also provides the intergrid transfer operators associated with a geometric multigrid method. Namely, we can build prolongation operators:

$$P_\ell^v : \mathbf{V}_\ell \rightarrow \mathbf{V}_{\ell+1}$$

for $\ell = 0, \dots, n_\ell - 1$. We encode the action of these prolongation operators in the matrix \mathbf{P}_ℓ^v such that the following refinement operation holds:

$$\mathbf{N}_{i,\ell}^v(\boldsymbol{\xi}) = \sum_j [\mathbf{P}_\ell^v]_{ji} R_{j,\ell+1}(\boldsymbol{\xi}) \quad (9.2)$$

for $\ell = 0, \dots, n_\ell - 1$ where $\{\mathbf{R}_{i,\ell}\}_{i=1}^{n_{v,\ell}}$ denotes the displacement NURBS basis functions associated with level ℓ . Moreover, the degrees of freedom associated with displacement field on the ℓ^{th} level can be transferred to the the $(\ell + 1)^{\text{st}}$ level via the expressions:

$$\mathbf{u}_{\ell+1} = \mathbf{P}_\ell^v \mathbf{u}_\ell \quad (9.3)$$

As is standard with a Galerkin formulation, restriction operators are constructed as the adjoint or transpose of the prolongation operators, namely $R_{\ell+1}^v = (P_\ell^v)^*$ and $\mathbf{R}_{\ell+1}^v = (\mathbf{P}_\ell^v)^T$ for $\ell = 0, \dots, n_\ell - 1$. The corresponding restriction matrix for level ℓ is given by $\mathbf{R}_{\ell+1} = (\mathbf{P}_\ell)^T$.

We need a few more ingredients before stating the multigrid V-cycle algorithm for our discretization scheme. First of all, we need to form the matrix system associated with the finest level, $\mathbf{K}\mathbf{U} = \mathbf{F}$. We then form the system matrices associated with coarser levels via the relation $\mathbf{K}_\ell = \mathbf{R}_{\ell+1} \mathbf{K}_{\ell+1} \mathbf{P}_\ell$ for $\ell = 0, \dots, n_\ell - 1$ where $\mathbf{K}_{n_\ell} = \mathbf{K}$. Second of all, we need to choose a smoother

for each level ℓ which we encode in a smoothing matrix \mathbf{S}_ℓ , and we need to select a number of pre-smoothing steps ν_1 and post-smoothing steps ν_2 . Typically, Jacobi or Gauss-Seidel smoothers are employed though other variants are used to exploit PDE-level or matrix-level structures, e.g. [30]. Third of all, we need to choose a suitable initial guess \mathbf{U} for the solution on the finest level. Then, one V-cycle corresponds to a single call of the form $\text{MGV}(n_\ell, \mathbf{U}, \mathbf{F})$ to the recursive function defined below [19].

Algorithm 5 Multigrid V-Cycle Algorithm

```

1: function MGV( $\ell, \mathbf{U}, \mathbf{F}$ )
2:   if  $\ell = 0$  then
3:      $\mathbf{vd} = \mathbf{K}_\ell^{-1}\mathbf{F}$  ▷ Exact System Solution
4:   else
5:     for  $i = 1$  to  $\nu_1$  do
6:        $\mathbf{U} \leftarrow \mathbf{U} + \mathbf{S}_\ell^{-1}(\mathbf{F} - \mathbf{K}_\ell\mathbf{U})$  ▷ Pre-Smoothing
7:     end for
8:      $\mathbf{G} = \mathbf{R}_\ell(\mathbf{F} - \mathbf{K}_\ell\mathbf{U})$  ▷ Restriction of Residual to Coarse Grid
9:      $\Delta\mathbf{U} = \mathbf{0}$  ▷ Coarse Grid Correction Initialization
10:    MGV( $\ell - 1, \Delta\mathbf{U}, \mathbf{G}$ ) ▷ Coarse Grid Correction Evaluation
11:     $\mathbf{U} \leftarrow \mathbf{U} + \mathbf{P}_{\ell-1}\Delta\mathbf{U}$  ▷ Update of Solution
12:    for  $i = 1$  to  $\nu_2$  do
13:       $\mathbf{U} \leftarrow \mathbf{U} + \mathbf{S}_\ell^{-1}(\mathbf{F} - \mathbf{K}_\ell\mathbf{U})$  ▷ Post-Smoothing
14:    end for
15:  end if
16: end function

```

Note that the solution \mathbf{U} is updated within the algorithm stated above. Hence, additional V-cycles simply correspond to additional calls of the form $\text{MGV}(n_\ell, \mathbf{U}, \mathbf{F})$. We now proceed with explicitly outlining the construction of the necessary intergrid transfer operators in the isogeometric setting.

The primary goal of knot insertion is to enrich the underlying parametric basis by providing additional functions while leaving the geometry and parameterization unchanged. The process of knot insertion is to insert an additional knot, $\xi_0 \in (\xi^1, \xi^{n+p+1})$ into the existing knot vector, Ξ , resulting in the **extended** knot vector $\bar{\Xi}$ namely,

$$\begin{aligned}
\Xi &= \{\xi^1, \xi^2, \dots, \xi^k, \xi^{k+1}, \dots, \xi^{n+p+1}\} \\
\bar{\Xi} &= \{\bar{\xi}^1 = \xi^1, \bar{\xi}^2 = \xi^2, \dots, \bar{\xi}^k = \xi^k, \bar{\xi}^{k+1} = \xi^0, \bar{\xi}^{k+2} = \xi^{k+1}, \dots, \bar{\xi}^{m+p+1} = \xi^{n+p+1}\}
\end{aligned} \tag{9.4}$$

where m is the number of basis functions after knot refinement. Now, for each knot we insert, we expect the addition of a new basis function to the parametric domain. Thus, we seek to find a relationship between the two bases, before and after knot insertion, of the form

$$R_{i,p}(\xi) = \sum_{j=1}^m T_{ji}^p \bar{R}_{j,p}(\bar{\xi})$$

In particular, an expression for the old basis in terms of the new, enriched basis. While performing the knot insertion operation, we wish to preserve geometry and since we are adding additional basis functions, we expect the the control points which describe the geometry to change as well. Therefore, we require a relationship between the old control points \mathbf{P}_i and the new control points \mathbf{Q}_i . This is accomplished by recognizing that the geometric mapping transforms via

$$\mathbf{C}(\xi) = \sum_{i=1}^n \mathbf{P}_i R_i(\xi) = \sum_{i=1}^n \mathbf{P}_i \left(\sum_{j=1}^m T_{ji}^p \bar{R}_{j,p}(\bar{\xi}) \right) = \sum_{j=1}^m \left(\sum_{i=1}^n T_{ji}^p \mathbf{P}_i \right) \bar{R}_{j,p}(\bar{\xi}) = \sum_{j=1}^m \mathbf{Q}_j \bar{R}_{j,p}(\bar{\xi})$$

From the above derivations we see that in terms of operators,

$$\underline{R}_p = (\mathbf{T}^p)^T \underline{\bar{R}}_p \quad \text{and} \quad \underline{\mathbf{Q}} = \mathbf{T}^p \underline{\mathbf{P}}$$

hence \mathbf{T}^p is an $m \times n$ array. We can find an explicit expression for \mathbf{T}^p by first noting that the support of the newly-inserted B-spline basis function is compactly-supported in the parametric domain such that $\bar{N}_{k,p}(\bar{\xi}) \neq 0$ for $\bar{\xi} \in [\xi_{k-p}, \xi_{k+1}]$. Therefore, only the old basis functions in this knot interval are affected by the knot insertion operation. Moreover, the construction of the operator resembles the Cox-deBoor recursion relationship:

$$T_{ji}^k = \frac{\bar{\xi}^{j+k} - \xi^i}{\xi^{j+k} - \xi^i} T_{ji}^{k-1} + \frac{\xi^{i+k+1} - \bar{\xi}^{j+k}}{\xi^{i+k+1} - \xi^{i+1}} T_{ji}^{k-1},$$

for $k = 1, \dots, p$ with

$$T_{ji}^0 = \begin{cases} 1, & \bar{\xi}^j \in [\xi^i, \xi^{i+1}) \\ 0, & \text{else} \end{cases}$$

Note that for each inserted knot, a new operator T_α is constructed which governs the relationship between the knot vectors before and after insertion. Moreover, the complete refinement operator for B-spline control points after repeated knot insertion is given by $\mathbf{T} = \mathbf{T}_\alpha \mathbf{T}_{\alpha-1} \cdots \mathbf{T}_1$. Now, since all geometric manipulations of the NURBS entity must occur in projective space, we must account for the NURBS weighting. With this in mind, we can define the prolongation operator for isogeometric analysis on NURBS via:

$$\mathbf{P} = \mathbf{W}_f^{-1} \mathbf{T} \mathbf{W}_c$$

where the coarse-weighting \mathbf{W}_c and fine-weighting \mathbf{W}_f matrices are defined via

$$\mathbf{W}_c = \begin{bmatrix} w_1^c & 0 & \dots & 0 \\ 0 & w_2^c & \dots & 0 \\ \vdots & \vdots & \ddots & \vdots \\ 0 & 0 & \dots & w_n^c \end{bmatrix} \quad \text{and} \quad \mathbf{W}_f = \begin{bmatrix} w_1^f & 0 & \dots & 0 \\ 0 & w_2^f & \dots & 0 \\ \vdots & \vdots & \ddots & \vdots \\ 0 & 0 & \dots & w_m^f \end{bmatrix}$$

It is clear that performing a prolongation operation amounts to first transferring the control points to projective space, performing the refinement operation, and then returning the control points to n -dimensional space. Before proceeding to implementation, there are a few points to make note of. First, the prolongation operator (and knot insertion) operator for d -dimensional geometric entities is formed via tensor product, ie.

$$\mathbf{P} = \mathbf{P}_1 \otimes \mathbf{P}_2 \otimes \dots \otimes \mathbf{P}_d$$

The other concern is the restriction operator, which is almost the transpose of the knot insertion operator with compensation for the projective space transformation, namely the NURBS weights

$$\mathbf{R} = \mathbf{P}^T = \mathbf{W}_c \mathbf{T}^T \mathbf{W}_f^{-1}$$

Lastly, we define the coarse-grid operator via the Galerkin condition

$$\mathbf{A}^{2h} = \mathbf{R}\mathbf{A}^h\mathbf{P}$$

With the above discussions, we are ready to implement an isogeometric multigrid solver on various PDEs. The examples we present only consider Kirchhoff-Love Plates 6.2, as they are compelling results for a fourth-order operator. Although the simple geometric multigrid method we've discussed is naturally applicable to the linear-elastic membrane 6.1, we do not consider it since superior performance of such a method on Laplace-type operators is well-known. Finally, we do not consider results of this method on the Kirchhoff-Love shells 6.3 because often times they suffer from membrane locking, as was demonstrated in the shell obstacle course displacement criterion, i.e. Figure 6.5, Figure 6.7, and Figure 6.9. This is problematic as the coarse-grid correction will not inform the fine resolution displacement field through prolongation, the crux of an effective multigrid method.

9.2 Numerical Tests

We now present a series of numerical tests illustrating the effectiveness of our proposed multigrid framework. The first test is a simply-supported rectangular Kirchhoff-Love plate with uniform downward loading. The exact solution to this problem is known and used as an assessment of convergence. Figure 9.1 contains a table displaying the number of V-cycles required to reduce the error by 10^6 , along with the corresponding average convergence factor during this process, for various numbers of degrees of freedom. For each V-cycle, one pre and post smoothing step is employed using the Gauss-Seidel smoother. From the figure, we observe that the number of iterations required for error reduction is independent of the number of levels. Figure 9.2 demonstrates the convergence of the numerical solution with mesh refinement if a full multigrid algorithm is employed for system solution. From the figure, we observe the convergence is optimal with respect to mesh refinement. That is, the error decays like N^{-2} , where N is the number of degrees of freedom.

DOFs	V-cycles	Convergence Factor
16	9	0.211
25	10	0.241
49	9	0.203
121	9	0.213
361	10	0.229
1225	10	0.226

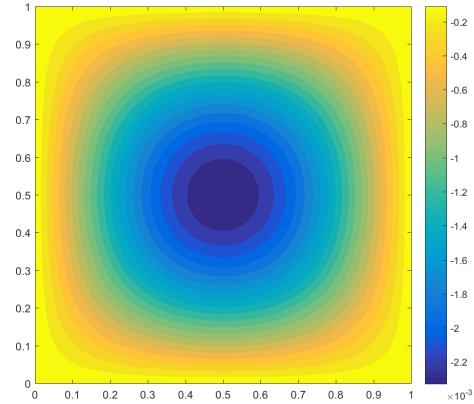


Figure 9.1: Convergence behavior and displacement plot for the rectangular Kirchhoff-Love plate system using a $V(1, 1)$ scheme.

DOFs	Error	Convergence Rate
16	2.879e-05	-
25	3.698e-06	4.5985
49	3.863e-07	3.3568
121	6.404e-08	1.988
361	3.528e-09	2.6519
1225	4.781e-10	1.6358

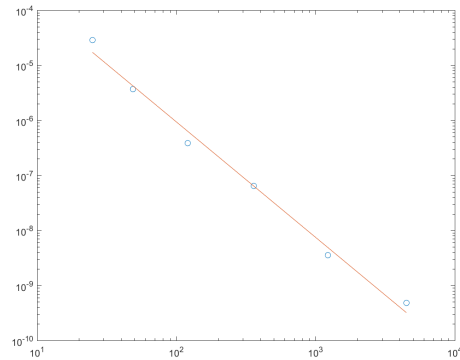


Figure 9.2: Convergence rates and plot of $\|e\|_{L^2}$ at various levels of refinement for the rectangular Kirchhoff-Love plate using FMG(1,1,1) scheme.

Our second test is a simply-supported parallelogram Kirchhoff-Love plate with uniform downward loading. As opposed to the first test, the exact solution to this test exhibits singularities in the obtuse corners which inhibit convergence. Figure 9.3 contains a table displaying the number of V-cycles required to reduce the error by 10^6 , along with the corresponding average convergence factor during this process, for various numbers of degrees of freedom. The V-cycles for this problem are identical to the rectangular plate case. From the figure, we observe that the number of iterations required for error reduction is asymptotically independent of the number of levels, though the number of iterations required for convergence for this problem is larger than the number required

for the first problem. This deterioration is a consequence of the singularities present in the exact solution.

DOFs	V-cycles	Convergence Factor
16	6	0.092
25	13	0.341
49	39	0.699
121	65	0.808
361	82	0.845
1225	86	0.851

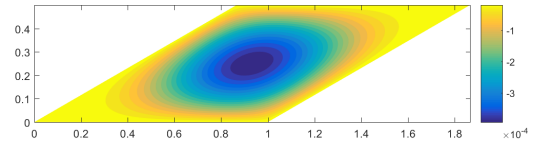


Figure 9.3: Convergence behavior and displacement plot for the parallelogram Kirchhoff-Love plate system using a $V(1, 1)$ scheme.

Chapter 10

Conclusion

In this dissertation, we have presented a novel framework for the propagation and control of geometric variation in engineering structural design and analysis. The dissertation began with an exposition of isogeometric analysis which is the primary analysis paradigm employed throughout the dissertation. This selection was made for several reasons, the first and foremost being the natural parametric modeling environment provided through this analysis methodology. In addition, the arbitrary continuity of the NURBS basis is capable of exactly representing a variety of common engineering features, such as fillets and holes, as well as providing a high-quality and a high-order, accurate solution field. The parametric modeling framework granted through the isogeometric paradigm played a pivotal role in the construction of a rapid and efficient design space exploration tool as well as an algorithm for a physics-informed tolerance allocation procedure. Moreover, the arbitrary continuity of NURBS basis functions allowed for a direct, primal formulation and implementation of the Kirchhoff-Love shell equations, the major structural setting considered throughout the dissertation.

Following the exposition on the fundamentals of isogeometric analysis, we provided a brief discussion of differential geometry which is crucial for the analysis and derivations of the Kirchhoff-Love shell equations. We introduced the fundamental concepts and methodologies required for arriving at a physically-consistent variational formulation. We grounded these concepts in the physical principles of continuum mechanics where the Green-Lagrange strain tensor was linearized and thereafter used in the derivation of strain fields for a linear-elastic membrane, the Kirchhoff-

Love plate, and the agglomeration of these two settings over a curved manifold, the Kirchhoff-Love shell. Before proceeding to the detailed derivations and analyses of these three physical problems, we provided a brief discussion of the functional analysis tools used for obtaining a high-order accurate numerical method resulting in a symmetric, positive-definite discrete system through Nitsche's method. With these tools in place, we were then able to discuss the physics of the structural problems considered throughout this dissertation.

The design space exploration framework and tolerance allocation procedure was set in the context of linear elastic membranes, Kirchhoff-Love plates, and Kirchhoff-Love shells. To this end, we provided a detailed derivation and analysis of these three physical problems through Nitsche's method. For all three problems, we began with deriving the work and energy of the physical systems and through the Euler-Lagrange equations, we obtained a variational principle. Through this weak formulation, we were able to infer an underlying strong form in each setting which provided the physically-consistent boundary integral terms and in the setting of the Kirchhoff-Love plate and shell, this resulted in a modified shearing term known as the "ersatz" force relating tangential boundary derivatives to the displacement field which was shown to be equivalent to a tangential boundary integration. After deriving Nitsche's formulation for the three problems, we demonstrated consistency, symmetry, continuity, and coercivity of the bilinear form and subsequently provided an a priori error estimate guaranteeing optimal convergence rates of the approximation error by a bound on the interpolation error. With the exposition of these physical problems in place, we were then able to discuss the first major application considered in this dissertation, design space exploration.

The framework for rapid and efficient design space exploration based on a combination of IGA and smart sampling. Although the methodology was presented in the context of structural mechanics, the modeling paradigm is agnostic in terms of its range of applicability. Moreover, this framework provides a means for obtaining an approximation to the full-system response whereas state-of-the-art approaches only provide exploration capability for quantities of interest present in the solution field. Various sampling techniques were considered where tensor-product grids provided

a high-fidelity representation of the solution space for low-dimensional problems and Smolyak-style sparse grids were effective in alleviating the curse of dimensionality in solution fields comprised of a few dominant displacement mode shapes for high-dimensional problems. Both nodal and modal representations of the solution manifold were considered through the use of interpolating polynomial basis functions and pseudospectral expansions. The methodology was demonstrated to be effective in exploring the design spaces of the Scordelis-Lo roof, a Flat L-Bracket, and an NREL 5MW wind turbine blade.

In short, the following conclusions were drawn through the numerical experiments conducted in this dissertation:

1. In general, both nodal and modal solution manifold representations provide the same fidelity of the surrogate model per degree of freedom and at the same computational cost for the case of tensor-product polynomial design space discretizations. However, the nodal representation performed slightly better than modal in terms of solution accuracy. This is due to numerical integration errors incurred while computing the pseudospectral coefficients through numerical integration.
2. In the case where the solution is inherently sparse with little cross-derivative information, isotropic polynomial design space discretizations out-performed tensor-product polynomial design space discretizations in terms of accuracy versus cost. In the case where cross-derivative fidelity is necessary, as in the example of the Scordelis-Lo roof, the tensor-product discretization performed better.
3. Both tensor-product and sparse quadrature rules were considered for sampling the design space and numerical integration. Tensor-product quadrature rules were more effective at computing the pseudospectral coefficients as expected, however computing the resulting approximation error through both approaches generally maintained the same order of magnitude. As the sparse rules are considerably cheaper, it is recommended that they be used in practice.

4. For high-dimensional problems, as in the example of the Flat L-Bracket, isotropic design space discretizations perform well in conjunction with sparse quadrature rules while tensor-product design space discretizations are not feasible due to the curse of dimensionality.
5. In all cases, Kronrod-Patterson achieved a higher accuracy per computational cost in comparison to Clenshaw-Curtis.

Overall, we found that the design space exploration methodology was an excellent and economical solution for problems with solution manifolds that have inherently “smooth” characteristics. In other words, solution manifolds which have a response dominated by global feature manipulation were the most effective in this framework. This was exemplified in the cases of the Scordelis-Lo roof, the Flat L-Bracket, and an NREL 5MW wind turbine blade, where the solution manifold is comprised of a sparse set of displacement modes. The appropriate combination and scaling of these modes, afforded through the methodologies presented throughout this dissertation, resulted in an accurate approximation to the exact displacement profile.

It should be remarked, however, that our the methodology is not quite as effective in representing “rough” solution fields which have a response dominated by localized features. In particular, it does not work well for problems with solution manifolds that are discontinuous or have discontinuous derivatives which are associated with, for instance, bifurcations. This is due to the fact that we have essentially considered a p -adaptive design space exploration paradigm in this dissertation. In future work, the issue of solution manifold “roughness” will be addressed through dimension-adaptive refinement procedures. In particular, extending our framework to an hp -adaptive framework may remedy the issue of roughness by effectively splitting the design space along discontinuous and non-differentiable loci. Note that hp methods based on isotropic design space mesh refinement suffer from the curse of dimensionality in a tensor-product setting [36]. However, employing this refinement protocol with anisotropic refinement will alleviate these concerns [54, 23]

The methodology presented in this dissertation also lays the foundation for a plethora of research topics from shape optimization to geometric uncertainty quantification, analogous to those

presented in [63, 105, 94, 90, 35, 124, 126]. Future work will leverage the surrogate modeling methodology presented herein for stochastic problems, where classic uncertainty quantification tools and techniques are readily available. In this setting, the design parameters can be interpreted as random variables which capture inherent modeling and manufacturing uncertainties. This lends to the notion of a stochastic geometric family which can be used to quantify the impact of tolerances on engineering designs, namely how geometric uncertainties in design propagate through the solution manifold. Similar ideas have been considered in the field of shape uncertainty quantification, on the analysis of random domains, such as those presented in [62, 33, 46]. Additionally, tools such as compressed sensing shows promise in obtaining coefficients to high-order modes, and consequently an increase in surrogate model fidelity, without incurring additional sampling expense in solution fields which are inherently sparse [41, 60].

This dissertation highlights several outstanding limitations which the authors plan to tackle in a future dissertation. First, the separated representation methodology used for surrogate model construction provides an excellent tool for efficient and accurate surrogate modeling with respect to **smooth** system responses to smooth changes in design variables. However in many practical scenarios, the responses are not expected to be smooth, e.g. in the scenario where the **location** of maximum stress changes in a discontinuous fashion with respect to a continuous change in design parameter. Utilizing a continuity-adaptive basis, rather than globally-smooth Legendre polynomials, for SR construction may remedy this issue and provide a means for attaining a tolerance allocation methodology which is capable of ensuring a conformity to geometrically-global, point-wise, worst-case performance criteria. Second, extending this framework to incorporate multiple constraint functionals would be a beneficial contribution in a variety of scenarios. For example, a physical system requiring conformity to a maximum stress and a maximum displacement can be ensured through a performance-based tolerance allocation routine of this form. Lastly, although worst-case tolerance allocation provides a measure of design conformity with respect to **every** design within the prescribed tolerance, this is arguably too restrictive since, probabilistically speaking, the absolute worst-case scenario is extremely unlikely to occur in practice. To this end, we propose

changing the constraint functional from a pointwise metric to one that is statistical. In particular, a metric which ensures that, given a probability density function, the designs contained within the prescribed tolerance hyperrectangle conform to the performance constraint in a statistically-average sense with respect to the provided probability density function.

In this dissertation, we have also presented a novel tolerance allocation methodology which is suitable for geometric design configurations parametrized with moderate dimensionality. This approach naturally emanates from design space exploration techniques and parametric modeling paradigms. Although the methodology was presented in this dissertation in the setting of linear elasticity, it is overall agnostic with respect to the underlying physical model and performance constraints considered. Provided with a parametric PDE, a user is capable of allocating design tolerances based on prescribed performance constraints by solving a nested sequence of optimization problems posed over an immersed manifold of codimension 1. We have presented both gradient ascent and conjugate gradient algorithms for performing optimization along this manifold to ultimately arrive at a tolerance for which all designs within the solution satisfy the prescribed performance constraint. Numerical results presented, which included the plate with hole parametrized with two design parameters, the plate with hole parametrized with six design parameters, and the L-Bracket parametrized with 17 design parameters, demonstrate that this methodology is robust up to moderate dimensionality. However there is an incurred increase in computational expense due to the offline, separated representation construction, which requires a larger set of sample realizations to obtain a desired surrogate model fidelity.

The final key to the effectiveness of our design space exploration and tolerance allocation capabilities is rapid sampling strategies. Since the primary means of mitigating the computational expense associated with these design space exploration and tolerance allocation tools relies on surrogate modeling, it is expected and understood that providing a larger set of sample realizations will result in a high-quality and accurate surrogate model. To this end, it is crucial to design techniques for obtaining these samples in a rapid manner. The Nitsche formulations considered result in a symmetric, positive-definite system which is ideal for fast and robust linear solvers.

Bibliography

- [1] M. Abramowitz and I. Stegun. Handbook of Mathematical Functions. Dover Publications, 1965.
- [2] P-A Absil, Robert Mahony, and Rodolphe Sepulchre. Optimization algorithms on matrix manifolds. Princeton University Press, 2009.
- [3] P-A Absil and Jérôme Malick. Projection-like retractions on matrix manifolds. SIAM Journal on Optimization, 22(1):135–158, 2012.
- [4] Andreas Apostolatos, Robert Schmidt, Roland Wüchner, and Kai-Uwe Bletzinger. A Nitsche-type formulation and comparison of the most common domain decomposition methods in isogeometric analysis. International Journal for Numerical Methods in Engineering, 97(7):473–504, 2014.
- [5] D. G. Ashwell. Strain elements with applications to arches, rings and cylindrical shells. In Finite Elements for Thin Shells and Curved Members. John Wiley and Sons New York, 1976.
- [6] K. E. Atkinson. An Introduction to Numerical Analysis. Wiley, 1978.
- [7] I. Babuška, F. Nobile, and R. Tempone. A stochastic collocation method for elliptic partial differential equations with random input data. SIAM Journal on Numerical Analysis, 45(3):1005–1034, 2007.
- [8] Y. Bazilevs, L. Beirão da Veiga, J. A. Cottrell, T. J. R. Hughes, and G. Sangalli. Isogeometric analysis: approximation, stability, and error estimates for h-refined meshes. Mathematical Models and Methods in Applied Sciences, 16(07):1031–1090, 2006.
- [9] Y. Bazilevs, V. M. Calo, J. A. Cottrell, J. A. Evans, T. J. R. Hughes, S. Lipton, M. A. Scott, and T. W. Sederberg. Isogeometric analysis using t-splines. Computer Methods in Applied Mechanics and Engineering, 199(5):229–263, 2010.
- [10] Y. Bazilevs, M.-C. Hsu, J. Kiendl, R. Wüchner, and K.-U. Bletzinger. 3D simulation of wind turbine rotors at full scale. Part II: Fluid–structure interaction modeling with composite blades. IJNMF, 65:236–253, 2011.
- [11] Ted Belytschko, Henryk Stolarski, Wing Kam Liu, Nicholas Carpenter, and Jame S.J. Ong. Stress projection for membrane and shear locking in shell finite elements. Computer Methods in Applied Mechanics and Engineering, 51(1):221 – 258, 1985.

- [12] P. Benner, A. Onwunta, and M. Stoll. Low-rank solution of unsteady diffusion equations with stochastic coefficients. SIAM/ASA Journal on Uncertainty Quantification, 3(1):622–649, 2015.
- [13] G. BENNETT and L. C. GUPTA. Least-cost tolerances—i. International Journal of Production Research, 8(1):65–74, 1970.
- [14] J Benzaken, A. J. Herrema, M.-C. Hsu, and J. A. Evans. A rapid and efficient isogeometric design space exploration framework with application to structural mechanics. Computer Methods in Applied Mechanics and Engineering, 316:1215–1256, 2017.
- [15] Gregory Beylkin, Jochen Garcke, and Martin J Mohlenkamp. Multivariate regression and machine learning with sums of separable functions. SIAM Journal on Scientific Computing, 31(3):1840–1857, 2009.
- [16] G. Blatman and B. Sudret. An adaptive algorithm to build up sparse polynomial chaos expansions for stochastic finite element analysis. Probabilistic Engineering Mechanics, 25(2):183–197, 2010.
- [17] M. J. Borden, M. A. Scott, J. A. Evans, and T. J. R. Hughes. Isogeometric finite element data structures based on bézier extraction of nurbs. International Journal for Numerical Methods in Engineering, 87(1-5):15–47, 2011.
- [18] Louis Brand. Vector and Tensor Analysis. John Wiley & Sons, Inc., New York, 1947.
- [19] William L Briggs, Steve F McCormick, et al. A multigrid tutorial, volume 72. Siam, 2000.
- [20] Rasmus Bro. Parafac. tutorial and applications. Chemometrics and intelligent laboratory systems, 38(2):149–171, 1997.
- [21] J. Burkardt. Clenshaw curtis quadrature rules. Available at https://people.sc.fsu.edu/~jburkardt/cpp_src/clenshaw_curtis_rule/clenshaw_curtis_rule.html.
- [22] J. Burkardt. Gauss-kronrod quadrature rules. Available at https://people.sc.fsu.edu/~jburkardt/m_src/kronrod/kronrod.html.
- [23] J. Burkardt. The combining coefficient for anisotropic sparse grids. Interdisciplinary Center for Applied Mathematics & Information Technology Department, Virginia Tech, 2010.
- [24] J. Burkardt. Slow exponential growth for clenshaw curtis sparse grids, 2012.
- [25] James V Burke, Adrian S Lewis, and Michael L Overton. A robust gradient sampling algorithm for nonsmooth, nonconvex optimization. SIAM Journal on Optimization, 15(3):751–779, 2005.
- [26] D. Chapelle and K. J. Bathe. The Finite Element Analysis of Shells - Fundamentals. Computational Fluid and Solid Mechanics. Springer, 2003.
- [27] Kenneth W. Chase. Tolerance allocation methods for designers, 1999.
- [28] F. Cirak, M. Ortiz, and P. Schröder. Subdivision surfaces: a new paradigm for thin-shell finite-element analysis. International Journal for Numerical Methods in Engineering, 47(12):2039–2072, 2000.

- [29] C. W. Clenshaw and A. R. Curtis. A method for numerical integration on an automatic computer. Numerische Mathematik, 2(1):197–205, 1960.
- [30] Christopher Coley, Joseph Benzaken, and John A Evans. A geometric multigrid method for isogeometric compatible discretizations of the generalized stokes and oseen problems. Numerical Linear Algebra with Applications, 25(3):e2145, 2018.
- [31] P. G. Constantine, M. S. Eldred, and E. T. Phipps. Sparse pseudospectral approximation method. Computer Methods in Applied Mechanics and Engineering, 229:1–12, 2012.
- [32] J. A. Cottrell, T. J. R. Hughes, and Y. Bazilevs. Isogeometric Analysis: Toward Integration of CAD and FEA. Wiley Publishing, 1st edition, 2009.
- [33] M. Dambrine, H. Harbrecht, and B. Puig. Computing quantities of interest for random domains with second order shape sensitivity analysis. ESAIM: Mathematical Modelling and Numerical Analysis, 49(5):1285–1302, 2015.
- [34] Lieven De Lathauwer, Bart De Moor, and Joos Vandewalle. On the best rank-1 and rank-(r_1, r_2, \dots, r_n) approximation of higher-order tensors. SIAM Journal on Matrix Analysis and Applications, 21(4):1324–1342, 2000.
- [35] M. C. Delfour and J.-P. Zolésio. Shapes and Geometries. Society for Industrial and Applied Mathematics, second edition, 2011.
- [36] L. Demkowicz. Computing with hp-Adaptive Finite Elements: Volume 1 One and Two Dimensional Elliptic and Maxwell problems. CRC Press, 2006.
- [37] Zhonghai Ding. A proof of the trace theorem of Sobolev spaces on Lipschitz domains. Proceedings of the American Mathematical Society, 124(2):591–600, 1996.
- [38] Z. Dong, W. Hu, and D. Xue. New production cost-tolerance models for tolerance synthesis. Journal of Engineering for Industry, 116(2):199–206, 05 1994.
- [39] A. Doostan, R. G. Ghanem, and J. Red-Horse. Stochastic model reduction for chaos representations. Computer Methods in Applied Mechanics and Engineering, 196(37):3951–3966, 2007.
- [40] A. Doostan and H. Owhadi. A non-adapted sparse approximation of pdes with stochastic inputs. Journal of Computational Physics, 230(8):3015–3034, 2011.
- [41] A. Doostan and H. Owhadi. A non-adapted sparse approximation of pdes with stochastic inputs. Journal of Computational Physics, 230(8):3015–3034, 2011.
- [42] Alireza Doostan, AbdoulAhad Validi, and Gianluca Iaccarino. Non-intrusive low-rank separated approximation of high-dimensional stochastic models. Computer Methods in Applied Mechanics and Engineering, 263:42–55, 2013.
- [43] M. R. Dörfel, B. Jüttler, and B. Simeon. Adaptive isogeometric analysis by local h-refinement with t-splines. Computer methods in applied mechanics and engineering, 199(5):264–275, 2010.
- [44] Eduardo N Dvorkin and Klaus-Jürgen Bathe. A continuum mechanics based four-node shell element for general non-linear analysis. Engineering computations, 1(1):77–88, 1984.

- [45] Anand Embar, John Dolbow, and Isaac Harari. Imposing Dirichlet boundary conditions with Nitsche's method and spline-based finite elements. International Journal for Numerical Methods in Engineering, 83(7):877–898, 2010.
- [46] K. Eppler, H. Harbrecht, and R. Schneider. On convergence in elliptic shape optimization. SIAM Journal on Control and Optimization, 46(1):61–83, 2007.
- [47] John A. Evans and Thomas J. R. Hughes. Explicit trace inequalities for isogeometric analysis and parametric hexahedral finite elements. Numerische Mathematik, 123(2):259–290, Feb 2013.
- [48] Lawrence C. Evans. Partial Differential Equations, volume 19 of Graduate Studies in Mathematics. AMS, Providence, Rhode Island, 1998.
- [49] Sonia Fernández-Méndez and Antonio Huerta. Imposing essential boundary conditions in mesh-free methods. Computer Methods in Applied Mechanics and Engineering, 193(12):1257 – 1275, 2004. Meshfree Methods: Recent Advances and New Applications.
- [50] W Flugge. Stresses in Shells. Springer, Berlin, 1960.
- [51] B. Fornberg. A Practical Guide to Pseudospectral Methods, volume 1. Cambridge university press, 1998.
- [52] B. Ganapathysubramanian and N. Zabaras. Sparse grid collocation schemes for stochastic natural convection problems. Journal of Computational Physics, 225:652–685, 2007.
- [53] T. Gerstner and M. Griebel. Numerical integration using sparse grids. Numerical algorithms, 18(3-4):209–232, 1998.
- [54] T. Gerstner and M. Griebel. Dimension-adaptive tensor-product quadrature. Computing, 71(1):65–87, 2003.
- [55] G. H. Golub and J. H. Welsch. Calculation of gauss quadrature rules. Mathematics of computation, 23(106):221–230, 1969.
- [56] R. Douglas Gregory and Frederic Y. M. Wan. Decaying states of plane strain in a semi-infinite strip and boundary conditions for plate theory. Journal of Elasticity, 14(1):27–64, Mar 1984.
- [57] M. Grigoriu. Parametric models for samples of random functions. Journal of Computational Physics, 297:47 – 71, 2015.
- [58] Yujie Guo and Martin Ruess. Nitsche's method for a coupling of isogeometric thin shells and blended shell structures. Computer Methods in Applied Mechanics and Engineering, 284:881 – 905, 2015. Isogeometric Analysis Special Issue.
- [59] S. Güzey, B. Cockburn, and H. K. Stolarski. The embedded discontinuous Galerkin method: application to linear shell problems. International Journal for Numerical Methods in Engineering, 70(7):757–790, 2007.
- [60] J. Hampton and A. Doostan. Compressive sampling of polynomial chaos expansions: Convergence analysis and sampling strategies. Journal of Computational Physics, 280:363–386, 2015.

- [61] Isaac Harari and Thomas J.R. Hughes. What are C and h?: Inequalities for the analysis and design of finite element methods. Computer Methods in Applied Mechanics and Engineering, 97(2):157 – 192, 1992.
- [62] H. Harbrecht. On output functionals of boundary value problems on stochastic domains. Mathematical Methods in the Applied Sciences, 33(1):91–102, 2010.
- [63] J. Haslinger and R. A. E. Mäkinen. Introduction to Shape Optimization. Society for Industrial and Applied Mathematics, 2003.
- [64] B. Heling, A. Aschenbrenner, M.S.J. Walter, and S. Wartzack. On connected tolerances in statistical tolerance-cost-optimization of assemblies with interrelated dimension chains. Procedia CIRP, 43:262 – 267, 2016. 14th CIRP CAT 2016 - CIRP Conference on Computer Aided Tolerancing.
- [65] A. J. Herrema, N. M. Wiese, C. N. Darling, A. Krishnamurthy, B. Ganapathysubramanian, and M.-C. Hsu. A framework for parametric design optimization using isogeometric analysis. CMAME, 2016. In review.
- [66] M.-C. Hsu, C. Wang, A. J. Herrema, D. Schillinger, A. Ghoshal, and Y. Bazilevs. An interactive geometry modeling and parametric design platform for isogeometric analysis. Computers & Mathematics with Applications, 70(7):1481–1500, 2015.
- [67] T. J. R. Hughes. The Finite Element Method: Linear Static and Dynamic Finite Element Analysis. Courier Corporation, 2012.
- [68] T. J. R. Hughes, J. A. Cottrell, and Y. Bazilevs. Isogeometric analysis: Cad, finite elements, nurbs, exact geometry and mesh refinement. Computer methods in applied mechanics and engineering, 194(39):4135–4195, 2005.
- [69] J. Jonkman, S. Butterfield, W. Musial, and G. Scott. Definition of a 5-MW reference wind turbine for offshore system development. Technical Report NREL/TP-500-38060, National Renewable Energy Laboratory, Golden, CO, 2009.
- [70] V. Kaarnioja et al. Smolyak quadrature. 2013.
- [71] A. B. Kahng, B. Li, L.-S. Peh, and K. Samadi. Orion 2.0: A fast and accurate noc power and area model for early-stage design space exploration. In Proceedings of the conference on Design, Automation and Test in Europe, pages 423–428. European Design and Automation Association, 2009.
- [72] J. Kiendl, K.-U. Bletzinger, J. Linhard, and R. Wüchner. Isogeometric shell analysis with kirchhoff–love elements. Computer Methods in Applied Mechanics and Engineering, 198(49):3902–3914, 2009.
- [73] Josef Kiendl, Ming-Chen Hsu, Michael C.H. Wu, and Alessandro Reali. Isogeometric kirchhoff–love shell formulations for general hyperelastic materials. Computer Methods in Applied Mechanics and Engineering, 291:280 – 303, 2015.
- [74] G. Kirchhoff. Über das Gleichgewicht und die Bewegung einer elastischen Scheibe. Journal für die reine und angewandte Mathematik, 40:51–88, 1850.

- [75] Pieter M Kroonenberg and Jan De Leeuw. Principal component analysis of three-mode data by means of alternating least squares algorithms. Psychometrika, 45(1):69–97, 1980.
- [76] D. Laurie. Calculation of gauss-kronrod quadrature rules. Mathematics of Computation of the American Mathematical Society, 66(219):1133–1145, 1997.
- [77] X. Li, J. Zheng, T. W. Sederberg, T. J. R. Hughes, and M. A. Scott. On linear independence of t-spline blending functions. Computer Aided Geometric Design, 29(1):63–76, 2012.
- [78] G. M. Lindberg, M. D. Olson, and G. R. Cowper. New developments in the finite element analysis of shells. Quarterly Bulletin of the Division of Mechanical Engineering and The National Aeronautical Establishment, 4:1–38, 1969.
- [79] A. Sanz Lobera, M. Villeta López, and M. A. Sebastián Pérez. Comparative research among costtolerance models used in mechanical manufacturing. AIP Conference Proceedings, 1181(1):254–265, 2009.
- [80] A. E. H. Love. The small free vibrations and deformation of a thin elastic shell. Philosophical Transactions of the Royal Society of London A: Mathematical, Physical and Engineering Sciences, 179:491–546, 1888.
- [81] A. E. H. Love. A treatise on the mathematical theory of elasticity, volume 1. Cambridge University Press, 1892.
- [82] Richard H MacNeal and Robert L Harder. A proposed standard set of problems to test finite element accuracy. Finite elements in analysis and design, 1(1):3–20, 1985.
- [83] A. Manzoni, F. Salmoiraghi, and L. Heltai. Reduced basis isogeometric methods (rb-iga) for the real-time simulation of potential flows about parametrized naca airfoils. Computer Methods in Applied Mechanics and Engineering, 284:1147–1180, 2015.
- [84] Leslie Sydney Denis Morley and A. J. Morris. Conflict between finite elements and shell theory. In Finite element methods in the commercial environment : Papers Presented at the Second World Congress on Finite Element Methods. Robinson and Associates, 23-27 October 1978.
- [85] H. N. Najm. Uncertainty quantification and polynomial chaos techniques in computational fluid dynamics. Annual Review of Fluid Mechanics, 41:35–52, 2009.
- [86] L. W.-T. Ng and M. S. Eldred. Multifidelity uncertainty quantification using nonintrusive polynomial chaos and stochastic collocation. In Proceedings of the 14th AIAA Non-Deterministic Approaches Conference, number AIAA-2012-1852, Honolulu, HI, volume 43, 2012.
- [87] J. Nitsche. Über ein Variationsprinzip zur Lösung von Dirichlet-Problemen bei Verwendung von Teilräumen, die keinen Randbedingungen unterworfen sind. Abhandlungen aus dem Mathematischen Seminar der Universität Hamburg, 36(1):9–15, Jul 1971.
- [88] F. Nobile, R. Tempone, and C. G. Webster. An anisotropic sparse grid stochastic collocation method for partial differential equations with random input data. SIAM Journal on Numerical Analysis, 46(5):2411–2442, 2008.

- [89] F. Nobile, R. Tempone, and C. G. Webster. A sparse grid stochastic collocation method for partial differential equations with random input data. SIAM Journal on Numerical Analysis, 46(5):2309–2345, 2008.
- [90] A. Novruzi and M. Pierre. Structure of shape derivatives. Journal of Evolution Equations, 2(3):365–382, 2002.
- [91] T. N. L. Patterson. The optimum addition of points to quadrature formulae. Mathematics of Computation, 22(104):847–856, 1968.
- [92] K. Petras. Smolyak cubature of given polynomial degree with few nodes for increasing dimension. Numerische Mathematik, 93(4):729–753, 2003.
- [93] L. Piegl and W. Tiller. The NURBS Book. Springer Science & Business Media, 2012.
- [94] O. Pironneau. Optimal shape design for elliptic systems. Springer Science & Business Media, 2012.
- [95] S. S. Ravindran. A reduced-order approach for optimal control of fluids using proper orthogonal decomposition. International journal for numerical methods in fluids, 34(5):425–448, 2000.
- [96] M.T. Reagan, H.N. Najm, B.J. Debusschere, O.P. Le Maître, O.M. Knio, and R. G. Ghanem. Spectral stochastic uncertainty quantification in chemical systems. Combustion Theory and Modelling, 8(3):607–632, 2004.
- [97] H. Reid. Clenshaw curtis quadrature, 2014. Available at <http://homerreid.dyndns.org/teaching/18.330/Notes/ClenshawCurtis.pdf>.
- [98] Eric Reissner. Reflections on the Theory of Elastic Plates. Applied Mechanics Reviews, 38(11):1453–1464, Nov 1985.
- [99] B. R. Resor. Definition of a 5MW/61.5m wind turbine blade reference model. Technical Report SAND2013-2569, Sandia National Laboratories, Albuquerque, NM, 2013.
- [100] Matthew J. Reynolds, Gregory Beylkin, and Alireza Doostan. Optimization via separated representations and the canonical tensor decomposition. Journal of Computational Physics, 348:220 – 230, 2017.
- [101] M. Ruess, D. Schillinger, Y. Bazilevs, V. Varduhn, and E. Rank. Weakly enforced essential boundary conditions for NURBS-embedded and trimmed NURBS geometries on the basis of the finite cell method. International Journal for Numerical Methods in Engineering, 95(10):811–846, 2013.
- [102] Martin Ruess, Dominik Schillinger, Ali I. Özcan, and Ernst Rank. Weak coupling for isogeometric analysis of non-matching and trimmed multi-patch geometries. Computer Methods in Applied Mechanics and Engineering, 269:46 – 71, 2014.
- [103] Hiroyuki Sato and Toshihiro Iwai. A new, globally convergent riemannian conjugate gradient method. Optimization, 64(4):1011–1031, 2015.

- [104] D. E. Schiavazzi, A. Doostan, G. Iaccarino, and A. L. Marsden. A generalized multi-resolution expansion for uncertainty propagation with application to cardiovascular modeling. Computer Methods in Applied Mechanics and Engineering, 2016.
- [105] V. H. Schulz. A riemannian view on shape optimization. Foundations of Computational Mathematics, 14(3):483–501, 2014.
- [106] Larry Schumaker. Spline Functions: Basic Theory. Cambridge Mathematical Library. Cambridge University Press, 3 edition, 2007.
- [107] A. C. Scordelis and K. S. Lo. Computer analysis of cylindrical shells. Journal of the American Concrete Institute, 61(5):539–562, May 1964.
- [108] M. A. Scott, M. J. Borden, C. V. Verhoosel, T. W. Sederberg, and T. J. R. Hughes. Isogeometric finite element data structures based on bézier extraction of t-splines. International Journal for Numerical Methods in Engineering, 88(2):126–156, 2011.
- [109] M. A. Scott, X. Li, T. W. Sederberg, and T. J. R. Hughes. Local refinement of analysis-suitable t-splines. Computer Methods in Applied Mechanics and Engineering, 213:206–222, 2012.
- [110] T. W. Sederberg, J. Zheng, A. Bakenov, and A. Nasri. T-splines and t-nurccs. In ACM transactions on graphics (TOG), volume 22, pages 477–484. ACM, 2003.
- [111] Alberto Sibileau, Ferdinando Auricchio, Simone Morganti, and Pedro Díez. Explicit parametric solutions of lattice structures with proper generalized decomposition (pgd). Computational Mechanics, Jan 2018.
- [112] Steven T Smith. Optimization techniques on riemannian manifolds. 1994.
- [113] S. A. Smolyak. Quadrature and interpolation formulas for tensor products of certain classes of functions. In Dokl. Akad. Nauk SSSR, volume 4, page 123, 1963.
- [114] Gilbert Strang and George J. Fix. An Analysis of the Finite Element Method, volume 212. Prentice-Hall, Englewood Cliffs, New Jersey, 1973.
- [115] G. H. Sutherland and B. Roth. Mechanism design: Accounting for manufacturing tolerances and costs in function generating problems. Journal of Engineering for Industry, 97(1):283–286, 02 1975.
- [116] L. N. Trefethen. Is gauss quadrature better than clenshaw-curtis? SIAM review, 50(1):67–87, 2008.
- [117] Abdoulahad Validi. Low-rank separated representation surrogates of high-dimensional stochastic functions: Application in bayesian inference. J. Comput. Phys., 260:37–53, March 2014.
- [118] F. Vidal-Codina, N.-C. Nguyen, M. B. Giles, and J. Peraire. A model and variance reduction method for computing statistical outputs of stochastic elliptic partial differential equations. Journal of Computational Physics, 297:700–720, 2015.
- [119] J. Waldvogel. Fast construction of the fejer and clenshaw–curtis quadrature rules. BIT Numerical Mathematics, 46(1):195–202, 2006.

- [120] Frederic Y. M. Wan. Stress boundary conditions for plate bending. International Journal of Solids and Structures, 40(16):4107–4123, 2003. A Special Issue in honour of Arthur. W. Leissa on his 70th Birthday.
- [121] T. Warburton and J. S. Hesthaven. On the constants in hp-finite element trace inverse inequalities. Computer Methods in Applied Mechanics and Engineering, 192(25):2765 – 2773, 2003.
- [122] Stephen J Wright, Robert D Nowak, and Mário AT Figueiredo. Sparse reconstruction by separable approximation. IEEE Transactions on Signal Processing, 57(7):2479–2493, 2009.
- [123] Y. Xie, G. H. Loh, B. Black, and K. Bernstein. Design space exploration for 3d architectures. ACM Journal on Emerging Technologies in Computing Systems (JETC), 2(2):65–103, 2006.
- [124] Dongbin Xiu and George Em Karniadakis. Modeling uncertainty in steady state diffusion problems via generalized polynomial chaos. Computer methods in applied mechanics and engineering, 191(43):4927–4948, 2002.
- [125] Dongbin Xiu and George Em Karniadakis. The wiener–askey polynomial chaos for stochastic differential equations. SIAM journal on scientific computing, 24(2):619–644, 2002.
- [126] Dongbin Xiu and George Em Karniadakis. Modeling uncertainty in flow simulations via generalized polynomial chaos. Journal of computational physics, 187(1):137–167, 2003.
- [127] Junfeng Yang and Yin Zhang. Alternating direction algorithms for ℓ_1 -problems in compressive sensing. SIAM journal on scientific computing, 33(1):250–278, 2011.